A sublimation technique for high-precision $\delta^{13}C$ on CO_2 and CO_2 mixing ratio from air trapped in deep ice cores

Jochen Schmitt

Dissertation zur Erlangung des Grades

Dr. rer. nat.

vorgelegt dem
Fachbereich Geowissenschaften
der Universität Bremen

Bremerhaven, Oktober 2006

Stiftung Alfred-Wegener-Institut für Polar- und Meeresforschung
in der Helmholtz-Gemeinschaft

A sublimation technique for high-precision $\delta^{13}C$ on CO_2 and CO_2 mixing ratio from air trapped in deep ice cores

Gutachter:
Prof. Dr. Heinz Miller
Prof. Dr. Kai-Uwe Hinrichs

Stiftung Alfred-Wegener-Institut für Polar- und Meeresforschung
in der Helmholtz-Gemeinschaft

Contents

Zusammenfassung

Das Eis der polaren Eisschilde stellt das einzige direkte Archiv dar, um Informationen über die Zusammensetzung der Atmosphäre in der Vergangenheit zu erhalten. Bereits seit mehr als 10 Jahren weiß man durch Analyse von antarktischen Eiskernen, wie z.B. dem Vostok Eiskern, dass die Konzentration des Treibhausgases CO_2 zwischen Eiszeiten und Warmzeiten periodisch schwankte. Während der letzten vier Eiszeiten lag die CO_2 Konzentration um etwa 90 ppmv niedriger als zu warmen Klimaperioden. Überraschend war die hohe Korrelation der CO_2 Konzentration mit der Temperatur. Mit Hilfe des Dome C Eiskerns, der im Rahmen des europäischen Projekts für Eiskernbohrungen in der Antarktis (EPICA) erbohrt wurde, kann nun die Entwicklung der CO_2 Konzentration bis zu 650 000 Jahre in die Vergangenheit zurückverfolgt werden. Die steuernden Prozesse für die markanten CO_2 Schwankungen auch quantitativ zu beschreiben, ist für die Paläoklimaforschung von überragender Bedeutung. Dieses Prozessverständnis ist die Grundvoraussetzung, um Vorhersagen über die zukünftige Entwicklung der atmosphärischen CO_2 Konzentration treffen zu können. Eine entscheidende Schlüsselinformation zur Beantwortung der offenen Fragen, wie atmosphärisches CO_2 auf Veränderungen im globalen Kohlenstoffkreislaufs reagiert, bietet das Verhältnis der stabilen Kohlenstoffisotope im CO_2 ($\delta^{13}C$). Jedoch blieb aufgrund von methodischen Schwierigkeiten die Analyse von $\delta^{13}C$ in Eiskernen auf den oberen Kernabschnitt beschränkt. Darüber hinaus sind die bisher gewonnen $\delta^{13}C$ Daten aufgrund der Messungenauigkeit und ihrer zeitlicher Auflösung schwierig zu interpretieren. Ferner wurde kürzlich an den EPICA Eiskernen eine hohe Variabilität des $\delta^{13}C$ Signals auf der Zentimeterskala gemessen, die nicht mit atmosphärischen Veränderungen in Einklang zu bringen ist.

Diese Doktorarbeit stellt ein neuartiges Analyseverfahren vor, mit dem es möglich ist, eingeschlossene Luft aus Eiskernen quantitativ zu extrahieren und an dieser $\delta^{13}C$ mit Hilfe einer Kopplung aus Gaschromatographie und Isotopenverhältnismassenspektrometrie in hoher Präzision zu bestimmen. Weiterhin kann mit diesem Verfahren die Konzentration von CO_2 an der gleichen Eisprobe bestimmt werden. Mit dieser neuen Analysetechnik gelingt es, die methodischen Schwierigkeiten der bisherigen Analyseverfahren zu überwinden. Durch Verwendung einer neuartigen Sublimationstechnik wurde eine nahezu vollständige Extraktionsausbeute erreicht, was für die genaue Bestimmung von $\delta^{13}C$ an tiefen, klathratisierten Eiskernproben Vorraussetzung ist. Da die Sublimationstechnik für Blaseneis und Klathrateis gleichermaßen geeignet ist, kann erstmals ein Eiskern in seiner gesamten Länge mit einem einzigen Analyseverfahren auf $\delta^{13}C$ und die CO_2 Konzentration analysiert werden. Somit erübrigt sich der kritische Schritt, die Extraktionsbedingungen an die Eiszusammensetzung anzupassen. Von einer Eiskernprobe mit einem Gewicht von ca. 30 g werden während der kontinuierlichen Sublimation fünf einzelne Teilproben separat gesammelt. Dies erlaubt es, fünf getrennte Messungen pro Eiskernprobe durchzuführen, was einer Probenmenge von ca. 6 g Eis pro Teilprobe ent-

spricht; oder einer extrahierten Luftmenge von etwa 0.5 ml STP. Diese Menge ist um eine bis zwei Größenordnungen geringer als bei früheren Verfahren zur $\delta^{13}C$ Bestimmung. Das schrittweise Sammeln von fünf Teilproben während der kontinuierlichen Gasextraktion ermöglicht es, den Sublimationsprozess zu überwachen und mögliche unerwünschte Effekte zu identifizieren. Bisherige Methoden zur $\delta^{13}C$ Analyse nutzen mechanische Extraktionsverfahren, bei denen die eingeschlossene Luft in einem einzigen Schritt freigesetzt wird. Folglich liefern bisherige Verfahren nur Informationen über diesen Analyseschritt und erlauben darüber hinaus keine weitere Prozessinformation. Durch Anwendung einer gaschromatographischen Probenaufreinigung vor der eigentlichen massenspektrometrischen Messung, können isobare Störkomponenten wie N_2O, organische Verbindungen und Verunreinigungen durch die Bohrflüssigkeit sicher von CO_2 abgetrennt werden. Dies war bislang nicht möglich. Die Richtigkeit und Genauigkeit des Analyseverfahrens wurde mit Hilfe von Luftstandards verifiziert. Diese können der Extraktionsapparatur kontinuierlich zugeführt werden und simulieren so die Analyse von Eiskernproben so nah wie möglich. Luftstandards können mit einer Genauigkeit von 0.06‰ auf ihren $\delta^{13}C$ Wert und mit 1.5 ppmv auf ihre CO_2 Konzentration analysiert werden. Die erzielte Leistungsfähigkeit des Verfahrens erlaubt es, die $\delta^{13}C$ Änderungen, die mit den beobachteten Änderungen der CO_2 Konzentration in der Vergangenheit verknüpft sind, aufzulösen.

An ausgewählten Tiefenintervallen des EPICA Dronning Maud Land Eiskerns wurden Wiederholungsmessungen mit dem Ziel durchgeführt, die kürzlich gefundenen kleinskaligen $\delta^{13}C$ Fluktuationen mit dem neuen Verfahren zu verifizieren. Die hierbei gemessene Reproduzierbarkeit für eng benachbarte Eiskernproben beträgt 0.06‰, folglich die gleiche Streuung, die auch bei der Analyse von Luftstandards gemessen wurde. Aus diesen Resultaten lässt sich ableiten, dass die postulierte kleinskalige $\delta^{13}C$ Fluktuation im Eis mit diesem Verfahren nicht bestätigt werden kann. Weiterhin sind die gemessenen CO_2 Konzentrationen in guter Übereinstimmung mit publizierten Werten, die mit mechanischen Extraktionsmethoden erzielt wurden. Die gute Übereinstimmung der CO_2 Konzentration mit bisherigen Messungen unterstützt die Eignung der Methode zur richtigen Bestimmung auch von $\delta^{13}C$ in Eiskernen. Diese vorliegende Studie zeigt, dass die neu entwickelte Kopplung aus Sublimationsextration-Gaschromatographie-Isotopenverhältnismassenspektrometrie geeignet ist, die Änderung in der $\delta^{13}C$ Signatur aufgrund von Verschiebungen im globalen Kohlenstoffkreislauf nachzuweisen.

Thesis summary

Glacier ice from polar ice sheets represents the only direct archive to retrieve information about the composition of the paleoatmosphere. From deep Antarctic ice cores like Vostok it is known for more than a decade that the concentration of the greenhouse gas CO_2 periodically varied between glacials and interglacials and its variations are strikingly correlated with temperature. During the glacials the CO_2 concentration was about 90 ppmv lower than during the warm interglacials. With the Dome C ice core drilled within the European Project for Ice Coring in Antarctica (EPICA) the CO_2 concentration record now covers the last 650,000 years. The task to quantitatively understand the processes behind these observed CO_2 changes is of outstanding importance not only for the paleo climate community, but also to predict the CO_2 concentration in the future. One crucial key to unravel the open questions about the coupling of the atmospheric CO_2 concentration with the dynamics of the global carbon cycle is the stable carbon isotope ratio of CO_2 ($\delta^{13}C$). Methodological constraints have, so far, restricted the $\delta^{13}C$ analysis from ice cores to the uppermost core section. Moreover, the available $\delta^{13}C$ data sets are difficult to interpret as accuracy and temporal resolution are insufficient and a large centimeter scale variability of $\delta^{13}C$ was recently measured on the EPICA ice cores, which cannot be explained by atmospheric fluctuations.

This thesis introduces a new analytical method allowing a quantitative extraction of air from small ice core samples coupled to a high precision gas chromatography-isotope ratio mass spectrometry system to determine $\delta^{13}C$ on the released CO_2. Additionally, this technique precisely determines the CO_2 concentration on the same ice sample. This new technique makes it possible to surmount major analytical limitations and shortcomings encountered during previous studies. Using a unique sublimation technique a nearly complete gas extraction has been achieved which represents a prerequisite for high-precision $\delta^{13}C$ analysis in deep clathrate ice. As the sublimation technique is equally suitable to analyze bubble and clathrate ice, this new method allows for the first time to measure $\delta^{13}C$ values and the CO_2 concentration on the entire length of an ice core without adapting the extraction to changing ice conditions. From one ice core sample weighing ~30 g five individual sub-samples are collected separately during the continuous sublimation to yield five measurements per ice core sample. This corresponds to ~6 g ice per sub-sample or an amount of roughly 0.5 mL STP of extracted air, i.e. 1-2 orders of magnitude less than in previous conventional ice core $\delta^{13}C$ analyses. A stepwise collection of five sub-samples during the ongoing extraction makes it possible to derive valuable process information during the sublimation. With the previous mechanical extraction techniques applied for $\delta^{13}C$ analysis, the enclosed air is extracted all at once, thus, the information is provided only from one single step. Applying a gas chromatographic sample clean-up prior to the mass spectrometric measurement, isobaric interferences like N_2O, organic compounds, and drill fluid contaminants can be separated from CO_2, which was not possible so far. The accuracy and precision of the method was verified with whole air reference standards, which can be introduced to the extraction apparatus and closely mimic the sample analysis. Air standards can be analyzed with a precision of 0.06‰ for $\delta^{13}C$, and 1.5 ppmv for the CO_2 concentration. The achieved performance enables to resolve the natural $\delta^{13}C$ variability connected with the observed CO_2 concentration changes in the past.

On selected depth intervals on the EPICA Dronning Maud Land ice core sample replicates were measured to reproduce the recently reported small-scale $\delta^{13}C$ scatter. The measurement reproducibility of $\delta^{13}C$ obtained from adjacent ice samples is on average 0.06‰, thus, the same precision as for air standards. There is no evidence for an assumed small-scale $\delta^{13}C$ variability within the ice itself. Additionally, the CO_2 concentrations measured on the same samples are in line with results from previous studies using mechanical extraction devices. The achieved accuracy of the CO_2 concentration measurement supports the method's suitability to correctly analyze $\delta^{13}C$ in ice cores. As a conclusion of this study, the developed sublimation extraction-gas chromatography-isotope ratio mass spectrometry system is suitable to trace the paleoatmospheric $\delta^{13}C$ changes caused by the dynamics of the global carbon cycle.

1 Introduction

Long before carbon dioxide (CO_2) made its way into the current Global Change discussion, the Swedish chemist Svante Arrhenius already thought about its climatic effect (*Arrhenius,* 1896). This was decades prior to the rapid atmospheric CO_2 rise caused by human activities and long before measurement techniques were developed to track this rise. He pointed out that atmospheric gases like CO_2 selectively absorb radiation and thus considerably increase the Earth's temperature by up to 15 °C. Without this so called natural greenhouse effect the Earth would not be inhabitable as we know it. At this time, Arrhenius already speculated whether the ice ages could have been related to reduced CO_2 concentrations.

Two iconic figures have shaped the public awareness of the current increase of the atmospheric CO_2 concentration. First, the so called 'Mauna Loa curve' (Fig. 1-1) from direct atmospheric CO_2 measurements on Hawaii, started 1959 under the initiative of Charles D. Keeling documenting its steady rise (*Keeling and Whorf,* 2000). This curve is unique since it is the longest data set from direct atmospheric CO_2 concentration measurements. It unequivocally documents the continuous rise from 315 ppmv[1] in 1959 when the measurements were started to 380 ppmv in 2005.

The second iconic figure is the 'Vostok record' (*Petit et al.,* 1999) allowing to look back at

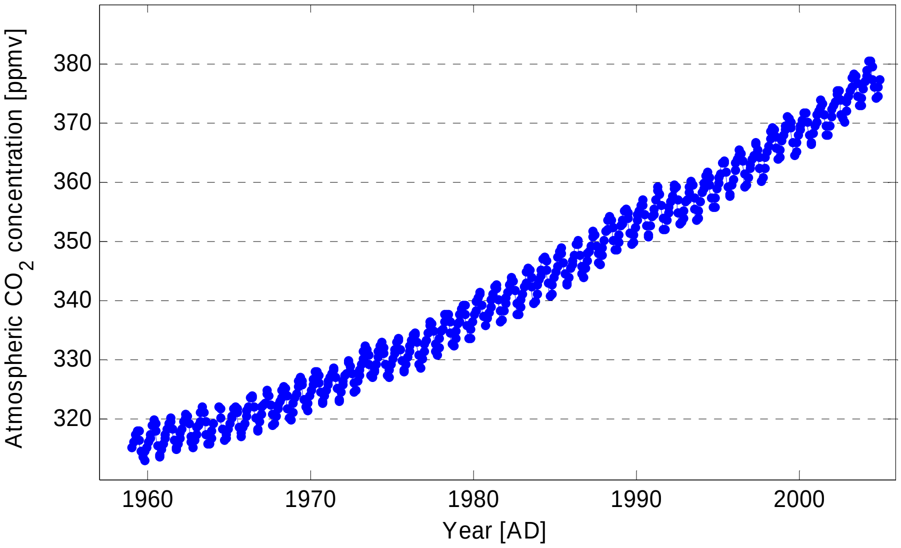

Figure 1-1 Increase of atmospheric CO_2 since first measurements started at Mauna Loa station, Hawaii (*Keeling and Whorf,* 2000). During the last 45 years the CO_2 concentration rose from 315 to 380 ppmv with an average annual increase of 1.4 ppmv year^{-1}. This translates to roughly 7 Pg[2] CO_2 per year added to the atmosphere by direct (fossil fuel burning) or indirect (land use change) emissions. Besides this long term trend attributed to human activity, the record shows an annual cycle, which reflects the seasonal imbalance of the net carbon uptake and release by the terrestrial biosphere.

---

[1] 1 ppmv = 1 part per million by volume or mole fraction

[2] Pg =10^{15} grams and equivalent to Gigatons (Gt)

four glacial cycles of CO_2 and climate history (Fig. 1-2). Within the perspective of the last 400,000 years it became obvious that the current level of 380 ppmv was unprecedented. The mean value of the last 10,000 years (corresponding to the Holocene) was 270 ppmv. During ice ages the CO_2 level was considerably lower and dropped to almost 180 ppmv during the coldest periods. The 'Vostok record' shows an intimate coupling of the CO_2 concentration and δD[3], which is a proxy[4] for the Antarctic temperature. These two pieces of information certainly influenced society and politics and boosted international efforts like the IPCC (Intergovernmental Panel on Climate Change) and the Kyoto protocol trying to slow down the CO_2 increase in the future.

For the scientific community the task remained to explain the enigmatic glacial/interglacial

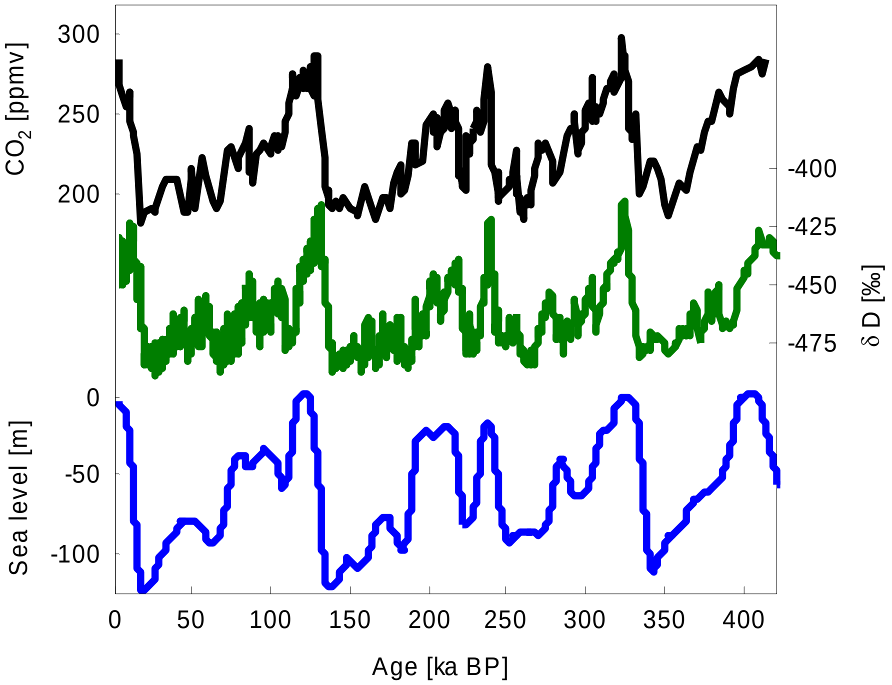

Figure 1-2 Compilation of the Vostok CO_2 concentrations and δD as a proxy for local air temperature (*Petit et al.,* 1999) and the changes in global sea level relative to the present level (*Bintanja et al.,* 2005). To a first approximation, sea level changes reflect the volume of ocean water bound in continental ice sheets during the ice ages. Note that in this figure time is on a the geologic time scale and therefore runs from right to left, thus, opposite to the direction in Figure 1-1; time is given in years before present (BP), which is defined at 1950 Anno Domini (AD). CO_2 minima were reached approximately when the sea level was at a minimum, hence, the extent of the continental ice sheets were at a maximum. Vice versa, highest CO_2 levels were found during interglacials during the high stands of the sea level. The evolution of the local temperature (as deduced from δD) follows this overall picture and points to a strong coupling of the climate and the carbon cycle. On a finer time scale leads and lags and a non-linear behavior of the system is clearly visible.

---

[3] δD is the isotopic ratio of ^2H (or Deuterium) to ^1H measured on H_2O to derive a measure of the precipitation temperature at a site (δD is often used as equivalent to $\delta^{18}O$).

[4] A proxy is a measurable parameter, i.e. δD in precipitation, from which a target environmental information like annual temperature can be deduced.

CO_2 riddle and to extend the records further back in time. The new results have added well resolved CO_2 data of the next two older glacial/interglacial climate cycles to the four cycles already investigated from the Vostok ice core. These two cycles are characterised by considerably lower temperature maxima during interglacials, but with similar temperatures during glacial periods. As the same climate-CO_2 relation was found valid even under these quite different climate cycles, the established picture of a close climate-CO_2 relation was strongly confirmed.

Within the scientific community a broad consensus exists about the temporal evolution of the past's atmospheric CO_2 concentration. In contrast, for the underlying processes and feedback loops and the question of what drives what, things are different (*Broecker and Peng,* 1987; *Toggweiler,* 1999; *Archer et al.,* 2000; *Köhler et al.,* 2005a). Only recently, *Köhler et al* (2005a) were able to propose a global carbon cycle scenario, which is able to quantitatively account for the observed CO_2 changes. While the different processes contributing to the glacial/interglacial CO_2 change seem now to be recognized, their individual contribution, however, may vary depending on the scenario.

Another, additional constraint on the carbon cycle dynamics is provided by studies on the isotopic signature of CO_2 in the past, which so far remained rudimentary (*Friedli et al.,* 1986; *Indermühle et al.,* 1999; *Smith et al.,* 1999; *Fischer et al.,* 2003). This thesis presents a new methodological attempt to gain new high precision $\delta^{13}C$ data on CO_2 from deep ice cores. Understanding atmospheric CO_2 concentration on glacial/interglacial timescales is challenging, and also a prerequisite to assess its future behaviour, which is on top of the Global Change agenda.

1.1 The global carbon cycle

The main characteristic of atmospheric CO_2 is its rapid exchange with both the ocean and the terrestrial biosphere. Note that the carbonate sediments of the Earth crust constitute the largest carbon reservoir. Although its reservoir size of 48,000,000 Pg C dwarfs the ocean (39,000 Pg C), the exchange rate due to weathering on land or sedimentation/dissolution balance within the ocean are relatively small (both around 0.2 Pg C year^{-1}) compared to the ocean and biosphere fluxes. Nevertheless, the interplay of carbonate precipitation in the surface ocean and its dissolution in the abyss constitutes the carbon and alkalinity equilibrium of the ocean on longer time scales. To bring the three most dynamic carbon reservoirs (ocean, biosphere, and atmosphere) into relation, a first step is to compare the corresponding reservoir sizes. The reservoir of the terrestrial biosphere, where carbon is stored mainly in soils and plant biomass, is by a factor of 3 larger than the carbon content of the preindustrial atmosphere. In case of the ocean, with its main inorganic species bicarbonate and carbonate, the carbon reservoir size is by a factor of 65 larger than the atmosphere (*Sigman and Boyle,* 2000). Physical, chemical and biological processes link the biosphere and the ocean with the atmosphere and determine its budget. The main processes and fluxes between these reservoirs are illustrated in a simple sketch of the global carbon cycle (Fig. 1-3).

The largest annual carbon gross flux occurs between the terrestrial biosphere and the atmosphere, which amounts to around 120 Pg. Prior to the recent human influence, the two opposing fluxes, photosynthesis and respiration/degradation, were almost balanced. The second largest flux is the gas exchange of the ocean's surface with the atmosphere, where the outgassing of CO_2 from the warm tropical waters is in balance with the net uptake into cold wa-

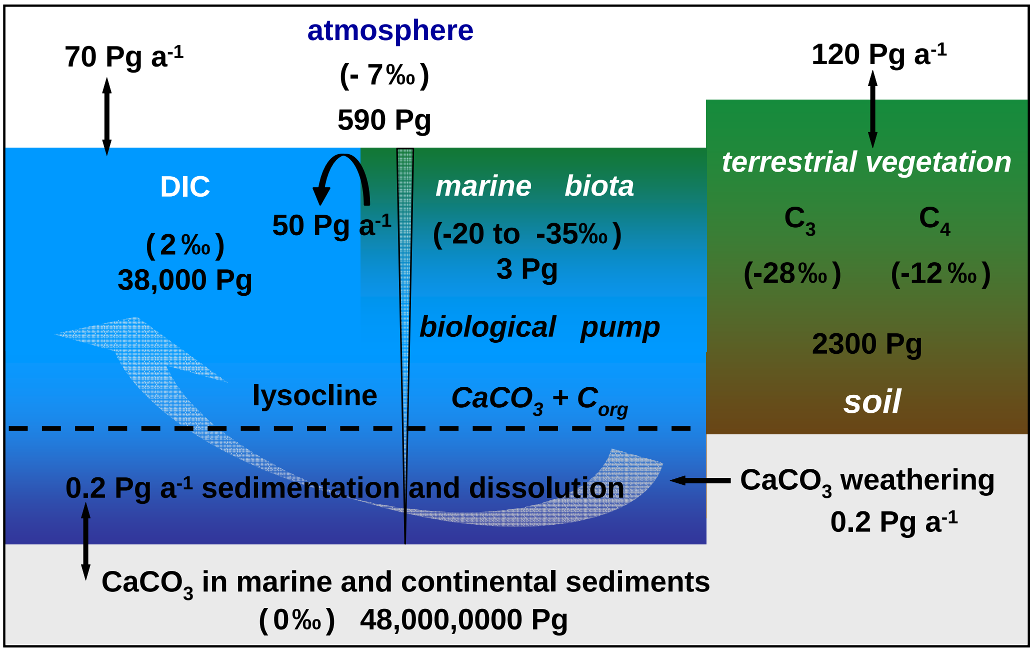

Figure 1-3 A simple sketch of the global carbon cycle showing the earth's crust main reservoirs, their annual exchange fluxes, and in brackets their isotopic composition ($\delta^{13}C$). Although sedimentary calcium carbonate ($CaCO_3$) constitutes the largest carbon pool, the exchange rate with the three more dynamic reservoirs (ocean, biosphere and atmosphere) is marginal. In contrast, the smallest carbon reservoir, the atmosphere rapidly exchanges with both the surface ocean and the terrestrial biosphere. The carbon flux associated with the terrestrial biosphere is highly variable on a seasonal time scale with a net uptake during the main growing season during the northern summer and CO_2 release between fall and spring (see Fig. 1-4 for details). In contrast, the exchange fluxes ocean/atmosphere are regionally separated with the tropics releasing CO_2 while the high northern latitudes are a CO_2 sink. Within the ocean the marine biosphere drives the biological carbon pump transferring organic and inorganic carbon to deeper ocean layers. The oceanic circulation (grey arrow) again redistributes the accumulated carbon and brings it back to the surface ocean/atmosphere system. Basically, the ratio of the carbon export from surface to the deep ocean by biological and physical processes to the strength of carbon redistribution by circulation sets the atmospheric CO_2 and $\delta^{13}C$ level. Each of the main reservoirs is characterized by a distinct carbon isotopic composition, which results from isotopic fractionation due to fluxes among the reservoirs. Arrows denote annual fluxes.

ters at high latitudes. Within the surface ocean the marine biota produces a mixture of organic carbon rich soft tissue biomass and inorganic carbonate shells. While the estimated actual carbon stock is only 3 Pg, this relatively small amount of marine biota has a high turnover rate and the marine annual production of organic carbon sums up to ~50 Pg. A large proportion is rapidly mineralized within the surface water and only ~10 Pg are exported to deeper layers (*Schlitzer,* 2002). On its way down from the productive surface layer to the deep sea, mineralization of organic carbon and dissolution of inorganic carbonate takes place. The biologically induced carbon export from the surface ocean to deeper layers is called the biological pump. Its action leads to an effective enrichment of dissolved inorganic carbon (DIC is the sum of dissolved CO_2, HCO_3^-, and CO_3^{2-}) with increasing water depth.

A marked geochemical feature of the deep ocean is the lysocline, the water depth where calcium carbonate becomes undersaturated and the progressive dissolution of the calcareous shells sets in. The action of the global ocean currents (the thermohaline circulation) balances the successive accumulation of carbon in the deep ocean as the enriched deep water is transported to upwelling regions, which release CO_2 back to the atmosphere. Modelling experiments by *Brovkin et al.* (2002) showed that the marine biologic cycle in total has a capacity to mediate about 2400 Pg carbon by remineralisation of organic carbon.

1.2 Stable carbon isotopes and fractionation processes

As shown in Figure 1-3 the reservoirs not only exchange carbon in large quantities, but each reservoir has a distinct carbon isotopic composition. This is due to the fact that exchange processes between one reservoir and another discriminate between the carbon isotopes. Carbon has two stable isotopes: ^{12}C which is the most abundant with 98.9% and ^{13}C with an abundance of only 1.1%. The isotopic variations measured in natural samples are rather small, therefore differences in the isotopic ratios are usually reported in permil (‰) relative to a standard using the δ-notation:

$$\delta^{13}C = \left[\frac{R_{sample} - R_{standard}}{R_{standard}}\right] \cdot 1000 \; [‰] \qquad (1-1)$$

with

$$R = \frac{^{13}C}{^{12}C} \qquad (1-2)$$

and

R_{sample} : isotopic ratio of the sample
$R_{standard}$: isotopic ratio of the standard

The current reference standard for stable carbon isotope analysis is the Vienna Pee Dee Belemnite (VPDB). As the original reference material from the Belemnite of the Pee Dee Formation in South Carolina (PDB) was exhausted, its $^{13}C/^{12}C$ ratio of 0.011237 measured by *Craig* (1957) was assigned to the new VPDB standard NBS19 (*Allison et al.,* 1995).

Fluxes from one reservoir to another, e.g. from A to B, are always connected with an isotopic fractionation or discrimination. Fractionation among isotopes are either induced kinetically or during equilibrium processes (*Young et al.,* 2002). Kinetic fractionations are often related to physical transport effects and are generally observed during diffusion, whereby the lighter molecules diffuse faster than the heavier ones. Equilibrium fractionations are involved among chemical species, e.g. between CO_3^{2-}, HCO_3^- and dissolved CO_2, and during phase changes, e.g. gas-liquid equilibrium. The fractionation factor α is defined as

$$\alpha_{A \rightarrow B} = \frac{R_A}{R_B} \qquad (1-3)$$

As natural fractionation processes are generally small, the absolute number of α is near 1, thus, a more convenient way to report isotopic fractionation uses ε instead of α.

$$\varepsilon = (\alpha - 1) \times 1000 \; [‰] \qquad (1-4)$$

In both cases the degree with which two or more isotopes are fractionated is mass dependent. In rare cases, like photochemical reactions of ozone in the stratosphere, mass independent fractionations occur and influence the oxygen isotope distribution of O_3, CO_2 and N_2O (e.g. *Röckmann et al.,* 2001). During most natural processes kinetic and equilibrium fractionations occur simultaneously. As isotope effects are additive, it is convenient to calculate the net fractionation at certain conditions. For many processes the dependencies of the isotopic fractionation on temperature, pressure and other parameters are either calculated by thermodynamics or by empiric relations.

In case of the primary production of terrestrial plants, the additive effect of many consecutive steps during the photosynthesis discriminates the heavier isotope ^{13}C against ^{12}C. As a consequence, plants are isotopically depleted with respect to the heavier isotope. The degree with which plants discriminate carbon isotopes is primarily species dependent (C_3, C_4 and CAM[5] pathway (*O'Leary,* 1981)), but also influenced by environmental parameters. The overall process of photosynthesis of C_3 plants discriminates against ^{13}C with a fractionation factor of about -20‰ (*Lloyd and Farquhar,* 1994). Given an atmospheric $\delta^{13}C$ value of -8‰, the biomass of C_3 plants as a typical $\delta^{13}C$ value of -28‰. As the removed carbon has a light signa-

---

[5] The abbreviations C_3 and C_4 denote the number of carbon atoms of the first intermediate product built during the photosynthesis. CAM is the abbreviation of Crassulacean Acid Metabolism.

ture, in turn, the remaining CO_2 in the atmosphere gets isotopically enriched in ^{13}C. The basis for this is the isotopic mass balance, which can be formulated in its simplest form as a two reservoir system as follows:

$$C_{mixture} \cdot \delta^{13}C_{mixture} = C_{reservoir\ A} \cdot \delta^{13}C_{reservior\ A} + C_{reservoir\ B} \cdot \delta^{13}C_{reservior\ B} \qquad (1-5)$$

with C_i the amount of carbon for the *reservoirs A* or *B* and the *mixture*, and $\delta^{13}C_i$ the respective isotopic composition of the reservoirs and the composition of the mixture.

The effect of isotopic fractionation during photosynthesis and the mass balance principle can be observed from the plant level to the landscape level, and most strikingly, on the global scale as shown in Figure 1-4. Basically, the annual waxing and waning of the terrestrial biosphere can be followed at three measurement stations. As most of the primary production from plants is located in the high latitudes of the Northern Hemisphere, the annual carbon cycle is most pronounced at Barrow station (71°N) compared to Mauna Loa (19°N) and South Pole (90°S). During peak photosynthesis in summer, large amounts of CO_2 are removed from the atmosphere visible by the marked dip in the CO_2 concentration (lower panel). In parallel, the atmosphere gets isotopically enriched by almost 0.8‰ (upper panel) as predicted by the mass balance. The annual gross fluxes of the terrestrial photosynthesis amount to ~120 Pg carbon (*Ciais et al.,* 1997). Due to this rapid turnover of the atmospheric CO_2 a $\delta^{13}C$ signal can be quickly diluted within the larger carbon pools, especially in the surface ocean.

Contrary to the isotopic fractionation between the terrestrial biosphere and the atmosphere, for the ocean/atmosphere exchange it is the ocean, which is 'heavier' in $\delta^{13}C$ and the atmosphere, which is 'lighter' (see Fig. 1-3). Here, the temperature dependent fractionation of the carbon isotopes is dominated by the carbonate chemistry of the ocean and the diffusive transfer of CO_2 from air to water and vice versa (*Mook,* 1986). In contrast to the pronounced seasonal exchange fluxes of the terrestrial biosphere/atmosphere system, the seasonality of the ocean/atmosphere exchange fluxes is less pronounced. However, on time scales of decades and millennia, it is the ocean who dictates the atmospheric CO_2 level and its $\delta^{13}C$ value. For the latter, the main factors are the temperature dependent isotopic fractionation during the ocean/atmospheric gas exchange. Secondly, the vertical $\delta^{13}C$ gradient within the ocean, which is introduced by the biological pump and depends on the quantity of the marine export production and the $\delta^{13}C$ value of the exported biomass.

From this simplistic view on the global carbon cycle it can be deduced that knowing the temporal changes of a reservoir's size and its isotopic composition can provide valuable information about the underlying processes and fluxes. In other words, if we have access to archives storing these information, we can identify and quantitatively describe the mechanisms driving the major CO_2 fluctuations in the past (e.g. during glacial/interglacial cycles).

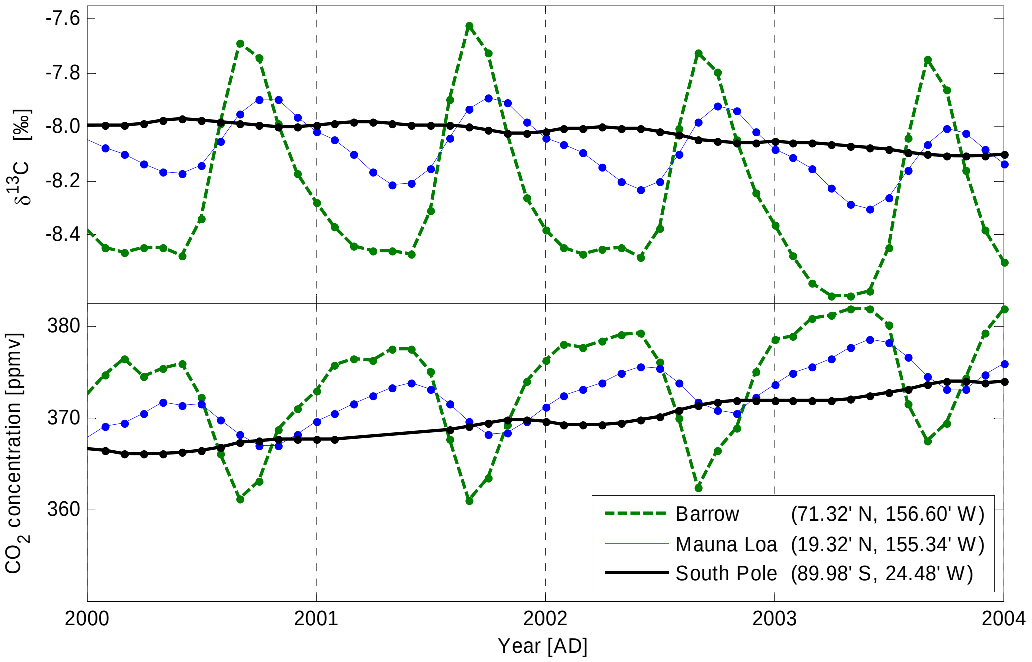

Figure 1-4 Time series of direct atmospheric $\delta^{13}C$ and CO_2 concentration measurements at three stations covering four years to illustrate the isotopic fractionation during photosynthesis and the concept of the isotopic mass balance. The northernmost station, Barrow, is characterized by the highest annual amplitudes: 0.8‰ for $\delta^{13}C$ and 15 ppmv for the atmospheric CO_2 concentration. This pattern reflects the net carbon fixation by plants, which are mainly located in the Northern Hemisphere and the imprint of the associated isotopic fractionation. As the maxima of the net carbon fluxes of photosynthesis and respiration are not synchronous, the isotopic fractionation during carbon fixation perturbs the atmosphere $\delta^{13}C$ value. Going south, i.e. away from the main source of the signal, the seasonal amplitude at the Mauna Loa station is already attenuated. At the South Pole, the seasonal amplitude has almost vanished since limited interhemispheric mixing prevents the northern signal to penetrate further southwards. The Southern Hemisphere itself lacks large land masses with equivalents to the boreal forest biomes like in Eurasia. Nevertheless, a phase lag of 6 months visible for the $\delta^{13}C$ maxima reflects the imprint of the southern biosphere on the atmosphere of the Southern Hemisphere. Large CO_2 gross fluxes between the atmosphere and the surface ocean further reduce the amplitude. The general trend towards more negative $\delta^{13}C$ values and increasing CO_2 concentration reflects the anthropogenic CO_2 emissions of isotopically depleted carbon. The data shown are taken from the NOAA/CMDL[6] monitoring station network (Pieter Tans, NOAA, http://www.cmdl.noaa.gov).

1.3 Reconstructing atmospheric $\delta^{13}C$ in the past

Since decades carbon isotopic information has been available from the ocean as the largest of the three dynamic carbon reservoirs (e.g. *Curry et al.,* 1988; *Spero and Lea,* 2002; *Broecker and Clark,* 2003; *Hodell et al.,* 2003). These information were derived from carbonate shells

---

[6] Climate Monitoring and Diagnostics Laboratory of the National Oceanic and Atmospheric Administration

from a large suite of marine sediment cores, which further allow to reconstruct a broad spectrum of physical, chemical, and biological parameters of the ocean in the past ($\delta^{18}O$, alkenones, boron isotopes, salinity etc.). Therefore, physical oceanographers and the associated modelling community proposed several hypotheses how the ocean might have controlled the atmospheric CO_2 concentration in the past (e.g. *Broecker and Peng,* 1987; *Toggweiler,* 1999; *Archer et al.,* 2000; *Sigman and Boyle,* 2000; *Stephens and Keeling,* 2000; *Köhler et al.,* 2005a).

Only recently, *Ruddiman* (2003) brought up the hypothesis that mankind might have influenced the atmospheric CO_2 concentration already for thousand of years due to substantial land use changes. The point of this discussion is that the level of the CO_2 concentration throughout the pre-industrial Holocene was not constant, but dropped from an early maximum of almost 270 ppmv around 11 ka BP to a minimum of 260 ppmv at 8 ka BP (*Indermühle et al.,* 1999; *Monnin et al.,* 2001; *Monnin et al.,* 2004). Afterwards, CO_2 was continuously rising with a minor decrease during the period of the 'Little Ice Age' (around 15th to 18th century) and eventually sharply increased after the industrial revolution at around 1750 AD (*Siegenthaler et al.,* 2005a). Interestingly, this unexplained rise in the preindustrial CO_2 concentration is unique for the Holocene. For older interglacials (marine isotope stages (MIS) 5, 7, 9) this rise was not observed in the CO_2 ice core records (*Petit et al.,* 1999; *Siegenthaler et al.,* 2005b).

An intense discussion followed whether this CO_2 increase was already induced by human activities, by natural changes in the terrestrial biosphere, or whether an internal equilibration of the ocean/sediment system was responsible (e.g. *Joos et al.,* 2004; *Claussen et al.,* 2005; *Ruddiman,* 2005; *Broecker and Stocker,* 2006). *Broecker and Clark* (2003) summarized arguments in favor of the ocean as the dominant driving mechanism, but left the answer open by stating: *"Only when a convincing ^{13}C record for atmospheric CO_2 has been generated will it be possible to make this distinction*."

Attempts to obtain such a record either from proxies or direct ice core archives have been made for more then 30 years. Beginning in the 1970s, $\delta^{13}C$ was measured on tree rings from C_3 plants to trace back the atmospheric $\delta^{13}C$ depletion caused by fossil fuel burning and anthropogenic land use changes (*Francey,* 1981; *Arens et al.,* 2000). Due to the large isotopic fractionation of plants using the C_3 pathway, the data was highly scattered and not reliable due to vital and climatic effects influencing the photosynthetic discrimination (*Francey and Farquhar,* 1982). C_4 plants are principally more suitable to obtain an unbiased atmospheric $\delta^{13}C$ record. This is due to the fact that the C_4 pathway discriminates carbon isotopes only little. Based on this idea, *Marino et al.* (1992) presented $\delta^{13}C$ values from plant remains of a single C_4 species. However, this assumption was challenged (*Buchmann et al.,* 1996 and references therein) and the attempt to reconstruct atmospheric $\delta^{13}C$ from plant proxies was abandoned.

An inherent drawback for using terrestrial $\delta^{13}C$ proxies becomes apparent when looking at the large seasonal $\delta^{13}C$ cycles of the atmosphere itself (shown in Fig 1-4). The seasonal $\delta^{13}C$ amplitude at potential locations for a terrestrial $\delta^{13}C$ proxy is of the same order of magnitude (~0.5‰) as the entire $\delta^{13}C$ variability expected for glacial/interglacial time scales (*Smith et al.,* 1999, see Fig. 1-7). As the net carbon fixation of plants is highly variable throughout the year, any climatic shift influencing this temporal distribution of carbon fixation will induce a bias in the atmospheric $\delta^{13}C$ data. The prerequisite of a reliable atmospheric archive spanning large time scales is that the stored information represents an unbiased value of the past's atmospheric composition. This implies that the underlying process with which an ideal archive records annual mean values is not a function of short term fluctuations. Such conditions are realized for the air bubble archives in ice cores that constitute the only direct archives for atmospheric gases. CO_2 trapped in ice cores can be considered representative of the whole troposphere of at least the hemisphere in which the drill site is located. As shown above (Fig. 1-4) the seasonal $\delta^{13}C$ fluctuations for high southern latitudes (station South Pole) are largely attenuated. Further, air mixing by diffusion within the firn column and the slow bubble enclosure process removes any short term fluctuations and the enclosed air in the ice core represents air samples with an age distribution of many decades.

During the last 25 years analytic efforts were not only made to analyze the CO_2 concentration of the trapped air in ice cores, but also on its carbon isotopic composition (*Friedli et al.,* 1984; *Friedli et al.,* 1986; *Leuenberger et al.,* 1992; *Francey et al.,* 1999; *Indermühle et al.,* 1999; *Smith et al.,* 1999; *Leuenberger et al.,* 2003; *Eyer,* 2004). However, problems within the analyzed ice itself and analytical hurdles have prevented scientists so far to generate long and well resolved high precision $\delta^{13}C$ data sets like the ones available for the CO_2 concentration. The early $\delta^{13}C$ measurements on the Siple Dome ice core from *Friedli et al.* (1986) cover only the last two centuries (Fig. 1-5). However, this record provided strong evidence that the recent rise of the atmospheric CO_2 concentration is related to carbon emissions carrying an isotopically 'light' $\delta^{13}C$ signal (~-25‰). This $\delta^{13}C$ signature matches both the carbon isotopic composition of fossil fuels and the organic carbon found in terrestrial soils and plants. Both sources emit carbon in large quantities by human activities either directly due to burning of fossil fuels or indirectly due to land use changes (e.g. conversion of forests into crop lands). Later measurements on the Law Dome ice core were able to establish a well defined preindustrial atmospheric $\delta^{13}C$ level of around -6.4‰ (*Francey et al.,* 1999). The large amount of isotopically light anthropogenic carbon emitted during the last 200 years is diluting the original atmospheric $\delta^{13}C$ signal. The simultaneous decrease in $\delta^{13}C$ with increasing CO_2 concentrations caused by the addition of a light carbon source to the atmospheric carbon pool is called the Suess effect[7]. Prior to the anthropogenic CO_2 increase starting around 1750 AD, the global carbon cycle was relatively stable according to the Law Dome record (Fig. 1-5) showing only minor variability in $\delta^{13}C$ and in the CO_2 concentration (see lower panel of Fig. 1-6 for a wider perspective of the Holocene CO_2 evolution).

The first $\delta^{13}C$ data from the glacial period were retrieved from the Byrd ice core (*Leuenberger et al.,* 1992), but the measured data set does not provide the temporal resolution to allow a reconstruction of the carbon cycle of the glacial period (Fig. 1-7). Nevertheless, the Byrd data showed that the $\delta^{13}C$ signature of the glacial atmosphere was on average 0.3±0.2‰ isotopically lighter than during the Holocene (*Leuenberger et al.,* 1992). This is in line with the general assumption that during the cold periods the carbon reservoir of the terrestrial biosphere was reduced as large areas in the Northern Hemisphere were covered with continental ice sheets or permafrost. The amount of organic carbon stored in these areas during the interglacials is assumed to be released into the atmosphere/ocean system, thus, decreasing its $\delta^{13}C$

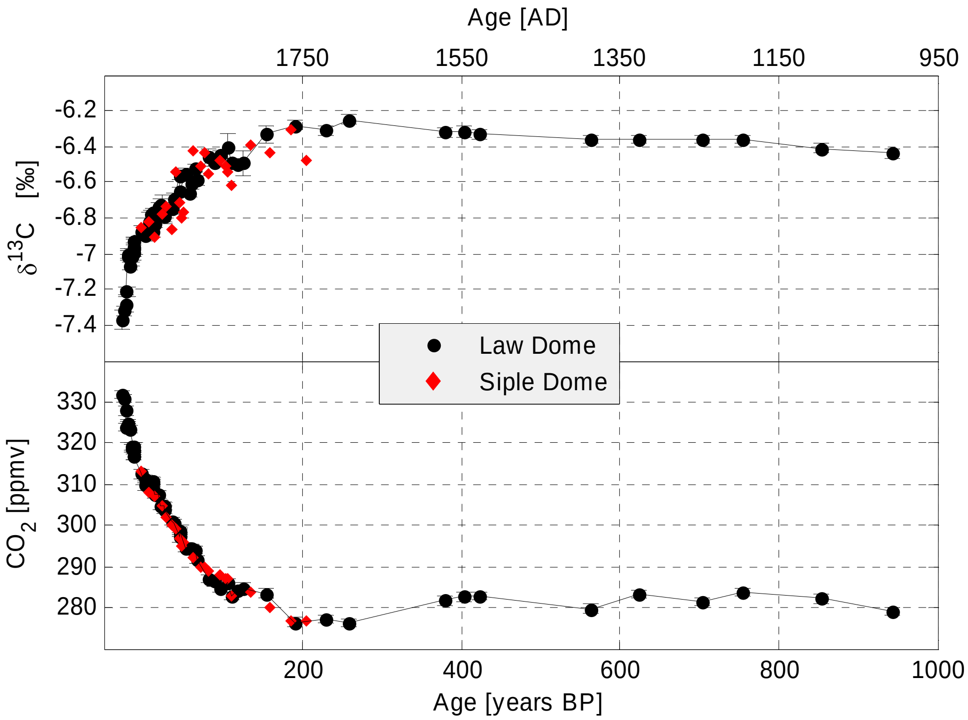

Figure 1-5 Compilation of $\delta^{13}C$ values and CO_2 concentrations from two Antarctic ice cores covering the last 1000 years (top panel showing $\delta^{13}C$ and the lower panel the respective CO_2 concentration measured on the same core). Note the two different time axes (AD and BP) valid for both records. The results from the Siple Dome core (*Friedli et al.,* 1986) were measured on large ice samples of ~700 g with a precision of 0.1‰ for $\delta^{13}C$ and 3 ppmv for the CO_2 concentration and the records starts with the onset of the marked CO_2 rise. More precise and covering also the preindustrial period is the Law Dome record (*Francey et al.,* 1999) with a precision of mostly 0.025-0.05‰ for $\delta^{13}C$ and 1.2 ppmv for the CO_2 concentration for ~1kg ice samples.

---

[7] named after H.E. Suess. The Suess effect denotes the dilution of the atmospheric ^{14}C and ^{13}C concentration due to the emission of 'old' carbon from fossil fuels, devoid of ^{14}C and as also isotopically depleted in $\delta^{13}C$.

signature. A more detailed picture emerged from the two $\delta^{13}C$ data sets measured on the Taylor Dome ice core, showing millennial scale $\delta^{13}C$ variability within the Holocene (*Indermühle et al.,* 1999) and especially during the deglaciation between 18 and 10 ka BP (*Smith et al.,* 1999) summarized in Figure 1-6 and 1-7. Due to the low temporal resolution and limited analytical precision of 0.085‰ many questions remained unanswered. To improve the temporal resolution within the Holocene and extending the $\delta^{13}C$ record further into the glacial period, recently *Eyer* (2004) measured two highly resolved $\delta^{13}C$ records on the EPICA ice cores (Dronning Maud Land: EDML; Dome C: EDC). As shown in Figure 1-6, the highly resolved EDML Holocene $\delta^{13}C$ record (*Eyer,* 2004) deviates from the $\delta^{13}C$ values from Taylor Dome (*Indermühle et al.,* 1999). Even when large dating errors between the two ice cores were taken into account, it is difficult to align these records. Especially for the time interval older than 6 ka BP the $\delta^{13}C$ average for EDML is ~0.3‰ isotopically lighter compared to the Taylor Dome data, however the analytical scatter in the *Eyer* (2004) data is quite considerable. Slightly better is the agreement of the Holocene part of the EDC $\delta^{13}C$ record with Taylor Dome shown in Figure 1-7.

Based on this overview on the previous $\delta^{13}C$ data sets, two major issues need special attention: First, the $\delta^{13}C$ ice core records cover only the Holocene and the younger part of the gla-

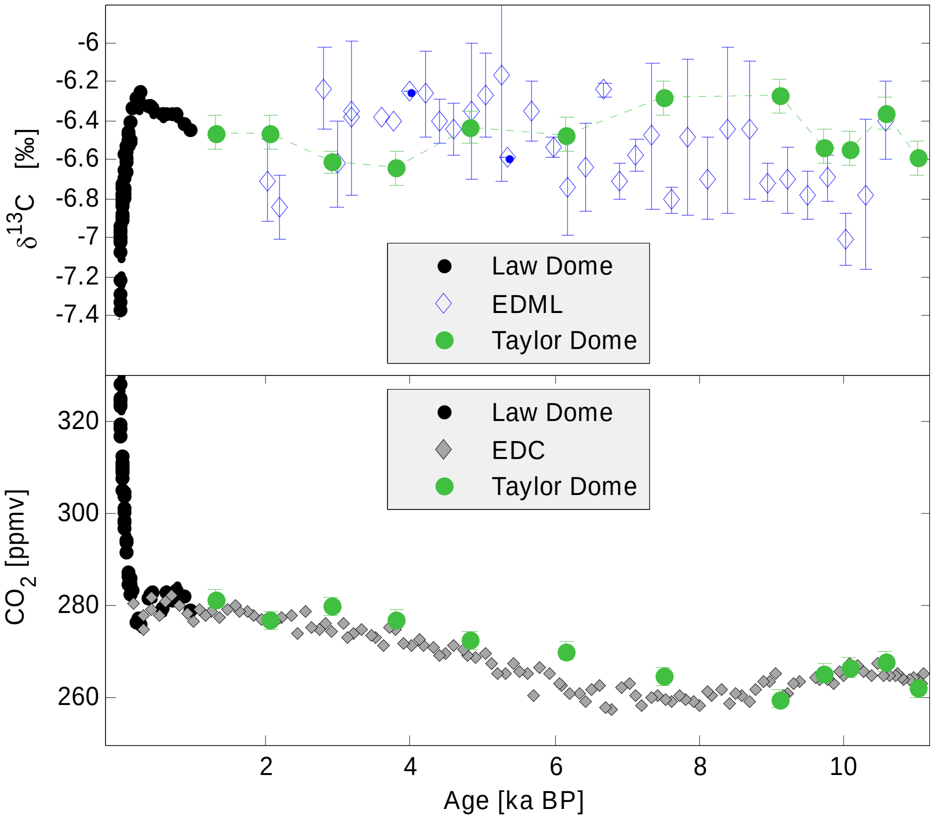

Figure 1-6 Compilation of $\delta^{13}C$ values and CO_2 concentrations covering the Holocene period. Top panel: $\delta^{13}C$ data from Law Dome, (black circles, *Francey et al.,* 1999), EDML (blue diamonds, *Eyer,* 2004), Taylor Dome (green circles, *Indermühle et al.,* 1999). Lower panel: CO_2 records from Law Dome (black circles, *Francey et al.,* 1999), EDC (grey diamonds, 2004), Taylor Dome (green circles, *Indermühle et al.,* 1999).

cial period. Secondly, discrepancies of the absolute $\delta^{13}C$ values are visible among the different data sets and especially the EDML record shows a high variability on very short time scales.

The first issue results from the fact that all previous studies used mechanical devices to extract the air trapped in the ice core samples. Usually, only the upper 700 meters of an ice core, where air exists in bubbles, are unproblematic for mechanical extraction devices. At deeper layers, air is tightly bound within the ice crystal and forms clathrate hydrates from which the gases are difficult to extract. Although *Eyer* (2004) conducted $\delta^{13}C$ measurements on this so called clathrate ice on the EDC core, the obtained results were more scattered (see EDC $\delta^{13}C$

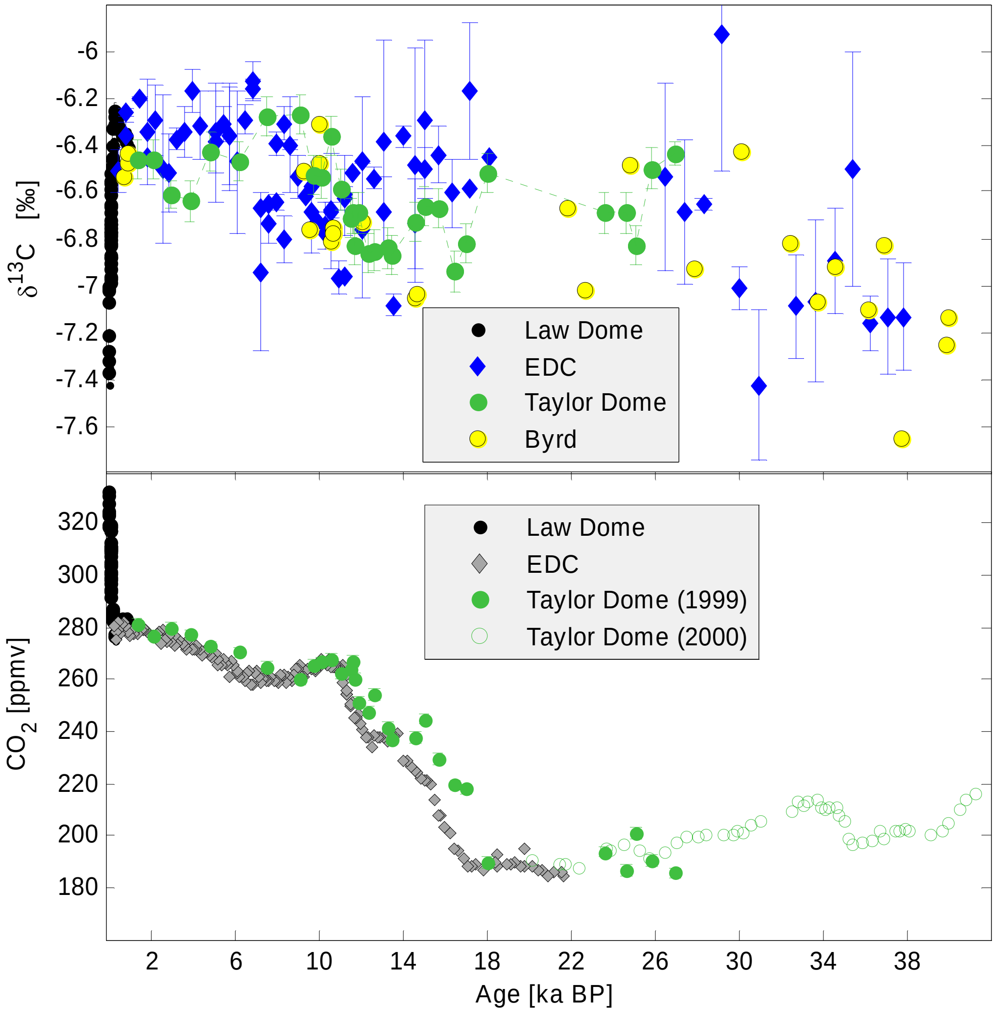

Figure 1-7 Compilation of $\delta^{13}C$ data and CO_2 concentrations reaching back to the glacial period. Top panel: $\delta^{13}C$ data from Law Dome (black circles, *Francey et al.,* 1999), EDC (blue diamonds, *Eyer,* 2004), Taylor Dome (green circles, *Indermühle et al.,* 1999; *Smith et al.,* 1999) and from the Byrd ice core (yellow circles, *Leuenberger et al.,* 1992). Lower panel CO_2 records from Law Dome (black circles, *Francey et al.,* 1999), EDC (grey diamonds, *Monnin et al.,* 2001; *Monnin et al.,* 2004), 'Taylor Dome (1999)' (green circles, *Indermühle et al.,* 1999; *Smith et al.,* 1999) is the corresponding CO_2 data to the $\delta^{13}C$ values, and the open green circles the 'Taylor Dome (2000)' data measured by *Indermühle et al.* (2000) extending the record further back in time.

data in Fig. 1-7 for the time period older than 12 ka BP). He reported isotopic effects during the extraction, which were ascribed to the nonquantitative gas recovery. Since the fractionation process associated with incomplete recovery is not yet understood, the scatter increased with depth (Fig. 1-7). As almost 90% of the entire climatic history of an ice core is enclosed in clathrate ice, a quantitative extraction technique for the $\delta^{13}C$ analysis is therefore compulsory.

Secondly, while the $\delta^{13}C$ data recently measured on the EDC core (*Eyer,* 2004) generally agree with the Taylor Dome record (*Indermühle et al.,* 1999; *Smith et al.,* 1999) as shown in Figure 1-7, the EDML $\delta^{13}C$ record (*Eyer,* 2004) has little resemblance with the Taylor Dome record (Fig. 1-5). Remarkable is the higher scatter of the EDML $\delta^{13}C$ record with 0.23‰ compared to 0.12‰ for the EDC record (*Eyer,* 2004). This is puzzling since the latter results were obtained from the same laboratory using the identical measurement technique and protocol. Hence, problems due to differences in the applied analysis technique, the referencing and correcting scheme should be excluded. Consequently, either the observed $\delta^{13}C$ difference between EDML and EDC lies in the ice itself, which would somehow challenge the approach to yield accurate $\delta^{13}C$ values from ice cores, or an up to now undetected analytical effect might account for this discrepancy. Without exception, all previous studies reported on the issue that organic impurities (e.g. from drill fluid) disturb the mass spectrometric measurement during sample analysis. In addition, different approaches were chosen to correct for the isobaric interference of N_2O in the mass spectrometric analysis, which affects $\delta^{13}C$ by a few tens of ‰.

Based on the experiences from the previous approaches to measure $\delta^{13}C$ on ice core samples, the objective of this work was to develop a new analysis technique to fulfil the following criteria:

- Quantitative extraction of air from the entire length of an ice core
- Use of a gas chromatographic sample clean-up to exclude interferences due to contamination from drill fluid
- Separation of N_2O from CO_2 prior to the mass spectrometric measurement
- Drastic reduction of the sample size
- Parallel determination of the CO_2 concentration at a high precision (<2 ppmv) on the same ice sample to identify a possible contamination within the ice itself or during the analysis
- A precision of ~0.05‰ to resolve the small variations connected with the global carbon cycle dynamics

This work represents the first effort to fulfil all these criteria. To this end, a new sublimation extraction for $\delta^{13}C$ on CO_2 in ice core samples coupled to a gas chromatography-isotope ratio mass spectrometry method has been developed. This new methodology, its analytical set-up and uncertainty as well as first measurements on Antarctic ice core samples are described within this work.

This work is structured as follows: In Chapter 2 physical and chemical processes are described which lead to a deviation of the measured $\delta^{13}C$ composition compared to the atmospheric value. Chapter 3 presents the development and performance of the analysis system for measuring $\delta^{13}C$ and the CO_2 concentration on ice core samples. In Chapter 4 first ice core results of this new analysis technique are shown and compared with previous ice core studies. In the Appendix a paper entitled 'On the application and interpretation of Keeling plots in paleo climate research – Deciphering $\delta^{13}C$ of atmospheric CO_2 measured in ice cores' is presented. This paper is a collaborative work with Peter Köhler and Hubertus Fischer and is submitted to *Biogeosciences*.

2 Processes affecting $\delta^{13}C$ of the ice core gas archive

In the following chapter known processes are summarized which may lead to a deviation of the measured $\delta^{13}C$ compared to the atmospheric values during the time the air was trapped within the ice. In order to ultimately interpret the measured $\delta^{13}C$ data in terms of changes of the global carbon cycle, these effects have to be identified and quantified.

These processes mainly fall into two classes: First, physical processes within the firn column and during the close-off process, as well as the formation of clathrate-hydrates from air bubbles. Secondly, chemical reactions adding extra CO_2 after the air was trapped within the ice. In contrast to the physical processes, this so called in-situ production of CO_2 is less understood and as yet cannot be easily corrected for as is the case for the physical ones (*Anklin et al.,* 1995; *Barnola,* 1999; *Tschumi and Stauffer,* 2000).

2.1 Physical processes

Most physical processes relevant for CO_2 and $\delta^{13}C$ measured on ice cores are related to molecular transport processes occurring in the firn, i.e. gravitative settling, thermal diffusion, and ordinary diffusion. In the first paragraphs, the basic structural properties of this special medium are introduced since they constitute the boundary conditions for these diffusion processes. On this basis, each diffusive process is then treated separately. However, these processes are interrelated in that both gravitative settling and thermal diffusion create concentration gradients, whereas ordinary diffusion attenuates these gradients until a steady state equilibrium is established. Formally, this is expressed in the following differential equation combining these driving forces (*Severinghaus et al.,* 2001):

$$\frac{\partial C}{\partial t} = \frac{\partial}{\partial z}\left(D_{eff}(z,T) \left[\underbrace{\frac{\partial C}{\partial z}}_{\substack{\text{ordinary}\\ \text{diffusion}}} - \underbrace{\frac{\Delta m g}{RT}}_{\substack{\text{gravitative}\\ \text{settling}}} + \underbrace{\Omega \frac{dT}{dz}}_{\substack{\text{thermal}\\ \text{diffusion}}} \right] \right) \qquad (2-1)$$

with C the isotopic composition of a gas species (e.g. $\delta^{13}C$), t the time, z the depth, D_{eff} the effective molecular diffusivity of a gas species in firn, and T the temperature. The parameters of the gravitative settling term are: Δm the mass difference between two species, g the acceleration due to gravitation, and R the ideal gas constant. The parameter Ω denotes the thermal diffusion sensitivity, which is specific for each gas and has to be determined experimentally (*Severinghaus et al.,* 2001). Details are explained in the respective paragraphs.

2.1.1 Firn structure

The zone on top of an ice sheet is known as firn and is both porous and permeable. For Antarctica its thickness can vary from 50 to 150 m, primarily depending on local climate parameters like mean accumulation rate[8] and mean annual temperature (*Kaspers et al.,* 2004). To be suitable as an uncompromised gas archive for CO_2, surface melting during summer has to be excluded as CO_2 readily dissolves in melt water (*Stauffer et al.,* 2002). Therefore, the following description of the physical processes within the firn column is restricted to cold sites in central Greenland or Antarctica with dry snow conditions.

Fresh snow has low densities and is highly porous, but is quickly reworked mechanically by wind and settling. Sublimation processes driven by daily and seasonal temperature cycles further reduce the surface area and snow is transformed to firn (Fig. 2-1). By these processes

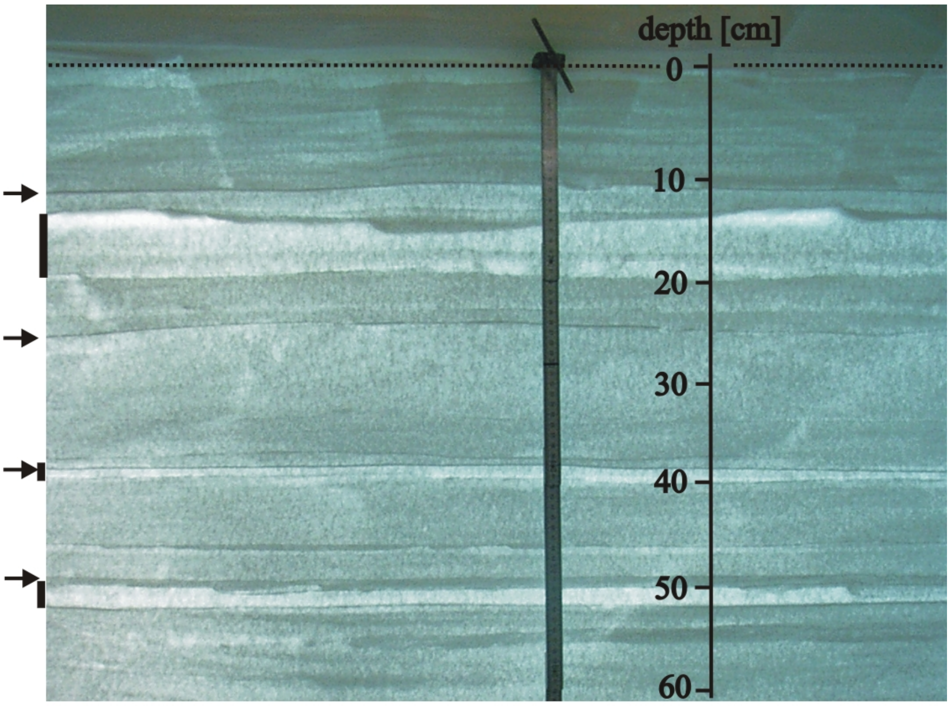

Figure 2-1 Snow pit at Kohnen station (75°00'S, 00°04'E, at 2882 m above sea level) showing the upper 60 cm, roughly four years of the stratigraphic sequence of snow fall or accumulation events. The dashed line marks the original surface at 08.02.2004. Bright, translucent layers consist of loose material with lower densities than adjacent layers (marked with bars). These layers represent depth hoar horizons formed by water vapor transport within the upper 20 cm induced by seasonal temperature gradients. The thin features well pronounced at 11, 24, 39, and 49 cm mark crusts of only a few mm consisting of densely packed snow (marked with an arrow). They form either due to wind action (wind crust) or when a consolidated surface is exposed to solar radiation between two deposition events. This small-scale heterogeneity in surface snow properties partially survives during the firnification process comprising around 800 years at this site. These surface features later modulate the lock-in process and the depth of the non-diffusive zone and the effects during the bubble close-off.

---

[8] the accumulation rate on a glacier is the net mass balance gain in snow throughout a year. It results from added snowfall minus loss due to melt or sublimation and horizontal mass transfer due to wind drift. Since the accumulation rate is highly variable between years, the mean of several years is used for characterization.

distinctive layers form which ultimately determine how and when air is trapped within the ice. With progressive accumulation of snow layers on top, growing ice crystals are deformed and by sintering and creep this compaction increases the firn density, in turn the porosity gradually decreases. Ongoing creep finally traps air in bubbles.

2.1.2 Gas transport properties within the firn column

The firn column (Fig. 2-2) can be separated into three zones according to the prevailing type of air movement (*Sowers et al.,* 1992). First, the so called convective zone, which is advectively well mixed with the overlaying atmosphere due to pressure differences, e.g. wind pumping (*Colbeck,* 1989). This zone generally comprises the upper 1 to 10 meters of the firn column, but might be thicker under special climatic conditions such as in low accumulation

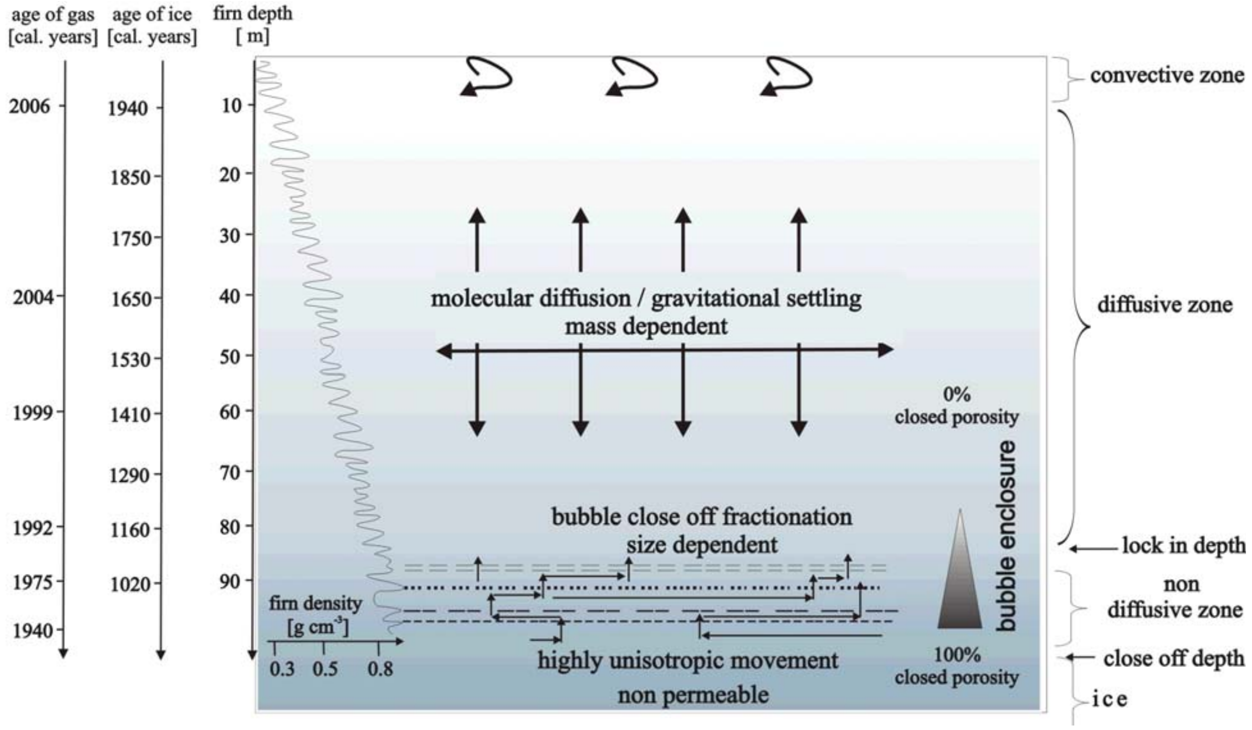

Figure 2-2 Scheme of physical processes occurring in the firn column with depth and age values for ice and gas representative for the drill site Kohnen station. The density increases from ~0.3±0.2 g cm^{-3} at the top to ~0.8±0.05 g cm^{-3} at the firn-ice transition. Ages of the firn air were derived during the field campaign 2005/2006 (K. Weiler and J. Freitag, personal communication, 2006) by firn air pumping. Gas ages were derived by comparing the measured CO_2 concentration profile with the known anthropogenic CO_2 rise. The convective zone contains air from the year of sampling due to rapid mixing. Then gas ages steadily increase with depth due to decreasing effective diffusivities of the porous firn. In the diffusive zone, gas transport is mainly by molecular diffusion and the gas species and their isotopes fractionate due to the Earth's gravitational field. In the region of 80 to 90 m, where most of the bubbles close-off and trap firn air, the mean gas age is 15 to 20 years. Below this depth the gas ages rapidly increase as prevailing diffusive mixing is shifted to a unidirectional expulsion of air within the non-diffusive zone. As the age of the ice at this depth is around 850 years (*Traufetter et al.,* 2004), a large Δ-age off-set has to be considered when gas records are compared with records measured on the ice phase.

sites or “megadune” regions (*Kawamura et al.,* 2006 and references therein). Large annual temperature cycles lead to thermal fractionation processes which are only transient and generally do not effect the processes below. The simultaneous occurrence of advective mixing in conjunction with the observed isotopic gradients due to thermal diffusion do not necessarily contradict each other because molecular diffusivity of gases in shallow firn is rather fast (1m^2 day^{-1}; for details see *Schwander et al.* (1988)). If convective mixing, i.e. the effective vertical eddy diffusivity, exceeds this value, isotopic fractionation due to thermal diffusion does not occur (*Severinghaus et al.,* 2003).

Secondly, the diffusive zone, where the isotopic and elemental composition of the air is altered by molecular diffusion. This zone generally comprises 50 to 100 m depending on the accumulation rate and the annual temperature of the site. In contrast to the convective zone, here diffusive processes are persistent over longer time scales (years to decades) as annual temperature cycles or advective mixing do not reach the diffusion zone. The main driving forces are gravitative settling and vertical concentration and temperature gradients.

Thirdly, a non diffusive zone of several meters, where unrestricted vertical gas exchange and diffusion finally cease at the lock-in depth. In contrast, horizontal gas movement remains active along permeable layers. This is due to contrasting differences in vertical firn permeability. Certain layers become nearly impermeable and restrict vertical diffusion, but allow expulsion of air at confined leaks from underlying, still permeable layers. The actual depth and extension of this zone strongly depends on the anisotropy of the seasonal snow and firn layers and is primarily generated by the accumulation and wind regime of the site. New methodic attempts to analyze the three dimensional firn structure and to derive effective gas transport parameters are currently developed, but so far the firn’s anisotropic structure has not been implemented in models (*Freitag et al.,* 2002).

2.1.3 Enclosure process, age distribution and Δ-age

Figure 2-2 further shows that the bubble enclosure is a continuous process, and bubbles trap firn air over a wide depth interval starting in the lower diffusive zone. Generally, this happens when the density of a firn layer exceeds a threshold, the critical density of around 0.83 g cm^{-3}. This density is reached at different depths for different firn layers according to the seasonal layering (*Freitag et al.,* 2004). Further, a fraction of bubbles closes-off earlier than this critical density. Consequently, the trapped air in an ice sample has not a discrete age, but can be described with a characteristic age distribution. For the drill site EDML, Siegenthaler et al. (2005a) report a mean age distribution of 59±5 years (half height of the distribution) shown in Figure 2-3. This age distribution acts like a low pass filter and atmospheric fluctuations with frequencies time scales of years to decades are attenuated in their amplitude (*Spahni et al.,* 2003). For atmospheric gases with rapidly changing concentrations, like methane, this leads to a considerable loss of information at drill sites with low accumulation, hence, broad age distributions. In contrast atmospheric CO_2 changes are generally less rapid, because the large reservoir of the surface ocean already smoothes out fast CO_2 fluctuations.

Due to the firn's permeability the firn air is in contact with the free atmosphere and therefore the enclosed air at a certain depth is always younger than the surrounding ice (Fig. 2-2). The mean age and the width of the age distribution of the firn air increases nonlinearly with depth. The parameter describing how efficient the vertical gas transport within the firn column can operate is the effective diffusivity, D_{eff}, introduced in Eqn. 2-1. With increasing depth, firn density increases (Fig. 2-2) and in turn the remaining pore space volume, or porosity decreases. Not only the volume of the gas phase decreases with depth, but also the shape of the pore space changes. Pores become more and more elongated and tortuous, therefore molecular gas transport becomes less efficient. D_{eff} accounts for this reduction in pore volume and increased tortuosity, and can be approximated from the diffusivity of a gas species in free air, reduced by the available open pore space and tortuosity. Note that since the diffusion velocity of gases is inversely proportional to the relative molecular mass, different gas species have different mean ages at a certain depth (*Rommelaere et al.,* 1997). In case of the pair CO_2 and CH_4 with masses 44 and 16, the lighter molecule methane diffuses 30% faster than CO_2 , accordingly their corresponding mean ages vary at a certain depth (*Schwander et al.,* 1993). For CO_2 at the EDML drill site the mean gas age at the lock-in depth of 88 m was determined to be about 15 years for the current climatic conditions (Weiler et al., GRL 2006, submitted). At this depth the age of the ice approaches around 850 years.

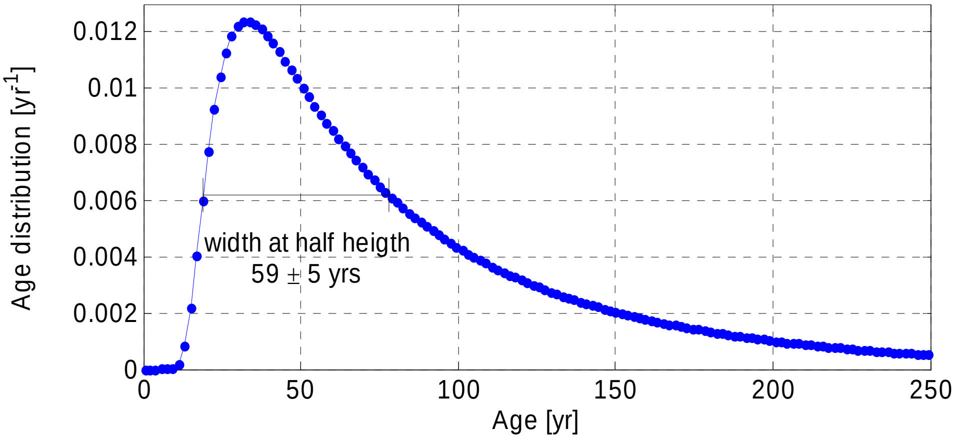

Figure 2-3 Age distribution for CO_2 of enclosed air bubbles at the EDML drill site. For the modeling current conditions were used as input parameters. The age distribution is normalized to have an area of 1 and the width at half height was calculated 59±5 years, for details see *Siegenthaler et al.* (2005a), data provided by Renato Spahni.

Therefore, in addition to the age distribution an age difference (Δ-age) between ice and air at a certain depth has to be calculated. For the EDML core Δ-age is around 825 years for Holocene conditions (*Siegenthaler et al.,* 2005a). The age distribution and Δ-age are strongly dependent on accumulation rate and annual temperature of a site and can vary spatially over an order of magnitude throughout Antarctica (*Kaspers et al.,* 2004). Knowing the precise Δ-age is central for deciphering leads and lags concerning changes in temperature and CO_2.

2.1.4 Separation of gases and isotopes due to gravitation

In the absence of turbulence, a gas mixture subject to a gravitational field will tend to unmix by a process known as gravitational settling. The heavier isotope species or gas component preferentially accumulates at the bottom and light components at the top of a column. A steady state is reached in which gravitational settling in one direction is balanced by diffusion along a concentration gradient in the other direction. The isotopic enrichment at the bottom of the firn column (lock-in depth) can be calculated by applying the barometric equation:

$$\delta = \left(e^{\frac{\Delta mgz}{RT}} - 1 \right) \cdot 1000\ [‰] \quad \cong \quad \frac{\Delta mgz}{RT} \cdot 1000\ [‰] \qquad (2-2)$$

with Δm the absolute mass difference between two gas species, T the mean annual firn temperature, z the diffusive column height (total firn column height minus convective zone and non diffusive zone). For the conditions currently prevailing at the EDML site (mean annual temperature = -45 °C, and diffusive column height around 80 m) the enrichment is pretty well known and is 0.45‰ for $\Delta m = 1$ g mol^{-1} (*Landais et al.,* 2006). Analogue to the isotopic enrichment, gravitative settling results in an increase of the CO_2 mixing ratio as well. Assuming Holocene conditions with 280 ppmv, air at close-off depth is 1.8 ppmv enriched in CO_2 compared to the atmosphere (with $\Delta m = 15.2$ g mol^{-1} for the mass difference between CO_2 and the average mass of air).

Climatic conditions during glacial times considerably deviated from the current ones, i.e. temperature and precipitation were considerably lower and so was the firn structure and the diffusive column height, and hence the gravitational enrichment with depth.

To overcome the lack of information on the past diffusive column height, δ^{15}N of the trapped atmospheric N_2 can be analyzed and be used to correct for the gravitational fractionation of CO_2. Nitrogen has a mean atmospheric residence time in the order of hundred thousand years and its isotopic composition can be assumed constant for this approach (*Mariotti,* 1983). As shown above, the isotopic fractionation effect of a gas species due to gravitation is a function of the absolute difference in mass. Hence, the mass difference for $^{13}CO_2$ with the mass 45 and

$^{12}CO_2$ with mass 44 is 1, the same is true for $^{15}N^{14}N$ with mass 29 and $^{14}N^{14}N$ with mass 28. Consequently, δ^{15}N values can be directly used to correct the gravitational effect on δ^{13}C. According to δ^{15}N measurements from the EDML core, the diffusive column height might have been reduced during the Last Glacial Maximum (LGM). Isotopic fractionation due to gravitation was only 0.39‰, instead of the Holocene level of 0.44‰ (*Landais et al.,* 2006).
In addition to this empiric approach, coupled firn densification and diffusion models are used to calculate the diffusive column height of the firn (*Goujon et al.,* 2003) . According to Eqn. 2-2, additional to the diffusive column height, the mean annual temperature is needed. It can be derived from δ^{18}O or δD of the ice itself by using the spatial relation of annual temperature and isotopic composition of the precipitation (*Jouzel et al.,* 2003).

2.1.5 Diffusion along a thermal gradient

A gas mixture within a temperature gradient undergoes thermal fractionation that accumulates the heavier isotopes preferably at the cooler side, whereas lighter isotopes preferentially accumulate at the warmer side. The same is true for a pair of gas species, e.g. O_2/N_2. In a constant temperature gradient, a steady state is reached in which thermal diffusion in one direction is balanced by diffusion along a concentration gradient in the other direction. This effect is called thermal diffusion and is due to the sensitivity of intermolecular forces during collision of molecules and atoms (*Severinghaus et al.,* 2001; *Grachev and Severinghaus,* 2003 for methodic details). The isotopic fractionation due to this effect amounts to:

$$\delta = \left[\left(\frac{T_t}{T_b} \right)^{\alpha_T} - 1 \right] \cdot 1000 \; [‰] \quad \cong \quad \Omega \Delta T \qquad (2-3)$$

where ΔT is the temperature difference between the top (T_t) and the bottom (T_b) of the diffusive column, α_T is the thermal diffusion constant and Ω the thermal diffusion sensitivity (in ‰ °C $^{-1}$). The thermal diffusion sensitivity Ω of a gas species is measured as the observed fractionation divided by an applied temperature difference. Ω and α_T are temperature dependent. For some gases Ω was determined experimentally and values range from 0.015‰ °C^{-1} for δ^{15}N and 0.025‰ °C^{-1} for δ^{18}O at 255 K and atmospheric pressure (*Grachev and Severinghaus,* 2003). Until now, no data was published for the corresponding effect on the stable carbon isotopes of CO_2. However, the values for the other gases suggest, that the magnitude of thermal diffusion has to be critically considered also during the analytical procedure. In the turbulent atmosphere the effect of thermal diffusion as well as gravitational settling is not observable since temperature differences induce convective motion of the air, which destroys any fractionation. Only an exceptionally stable atmospheric inversion at a special topographic setting recently allowed to detect thermal diffusion in the atmosphere (*Adachi et al.,* 2006). Porous media like extended sand dunes and firn columns are able to suppress convection due to small pore diameter and tortuous pore space geometry. In these cases thermal diffusion can affect the isotopic composition of the gases involved (*Severinghaus et al.,* 1996). The required temperature gradient within a firn column results from its thermal inertia producing temperature differences of up to 20 °C within the upper 5 m (*Severinghaus et al.,* 2001). Most pronounced are the large seasonal temperature cycles typical for the interior of polar ice caps, which affect, however, only the upper few meters of the firn column. In contrast, thermal diffusion can sometimes involve the entire firn column. A prominent application of this effect is the identification and quantification of rapid temperature changes in the Northern Hemisphere from Greenland ice cores (*Severinghaus et al.,* 1998). As the effect of thermal diffusion in the firn column requires rapid and large changes (several degrees in annual mean temperature in 1000 years (*Caillon et al.,* 2001)) an influence on $\delta^{13}C$ measured on ice cores is only minor (*Kawamura et al.,* 2006). Similarly to the gravitation effect on $\delta^{13}C$, the influence of thermal diffusion can be principally corrected with $\delta^{15}N$ and ratios of noble gas isotopes. To do this, gas specific thermal diffusivity constants have to be used and the effect of gravitation separated from thermal diffusion (*Severinghaus et al.,* 2001).

2.1.6 Diffusion along a concentration gradient

According to Fick's law, the diffusive flux of a gas species along a concentration gradient can be described as follows:

$$F = -D\frac{dC}{dx} \qquad (2-4)$$

where *F* the net flux and *dC/dx* the concentration gradient in direction of diffusion and *D* the diffusion constant. The latter is proportional to the inverse of the square root of the molecular mass. This relation results form the fact that all molecules of a gas mixture have the same kinetic energy ($E=1/2mv^2$). Consequently, gas species or isotopes with a lower mass move faster and have higher diffusion constants. If the diffusion involves the movement of one gas species through a second, here A for relevant gas species of CO_2 and B for air, molecular masses have to be replaced by their reduced masses, denoted with μ:

$$\mu = \frac{m_A \cdot m_B}{m_A + m_B} \qquad (2-5)$$

In case of the diffusion of CO_2 molecules in air (mean mass 29 g mol^{-1}) the isotopic fractionation, $^{13}\alpha$, for the stable carbon isotopes of CO_2 can be written as follows:

$$^{13}\alpha = \frac{D_{^{13}CO_2}}{D_{^{12}CO_2}} = \sqrt{\frac{m_A^* + m_B}{m_A^* \cdot m_B} \quad \frac{m_A \cdot m_B}{m_A + m_B}} = \sqrt{\frac{45+29}{45 \cdot 29} \quad \frac{44 \cdot 29}{44+29}} = 0.9956 \qquad (2-6)$$

with $^{13}\alpha$ the fractionation factor for the pair $^{13}CO_2$ and $^{12}CO_2$ with masses 45 (m_A^*) and 44 (m_A), respectively. In delta notation a fractionation factor of $^{13}\alpha = 0.9956$ translates into an isotopic depletion of 4.4‰.

The two processes described above, gravitative settling and thermal diffusion, create vertical gradients both in the concentration and in isotopic composition. Further, vertical gradients within the diffusive firn column occur when the ambient atmospheric composition changes and the signal slowly propagates downward into the firn column. In either case, ordinary diffusion reduces these gradients until a steady state equilibrium is being established according to Eqn. 2-1

With the exception of the current anthropogenic CO_2 rise, natural changes in the atmospheric CO_2 concentration are marginal in view of the mean age of the firn air. Within the Holocene, maximum changes were observed during the Little Ice Age reaching 3 ppmv CO_2 per 100 years (*Siegenthaler et al.,* 2005a). For the most rapid CO_2 increases during the end of the last ice age, CO_2 increase rates of 1-2 ppmv per 100 years were reported (*Monnin et al.,* 2001). Although these data were derived from Antarctic ice cores from low accumulation sites and consequently also broad age distributions smoothing the original signal, rapid CO_2 fluctuations are unlikely due to the equilibrium with the surface ocean. This gentle behavior of the atmospheric CO_2 concentration due to 'buffering' with the large reservoir surface ocean is known from modeling studies (e.g. *Köhler et al.,* 2005b). Therefore, diffusion effects due to natural changes of the ambient CO_2 on the isotopic composition of CO_2 are minor compared to the gravitational effect. However, for the rapid CO_2 rise during the last 50 years this has to be taken into account. According to *Trudinger et al.* (1997), the effect caused by the large CO_2 concentration gradient currently found within the firn column is as high as 0.1‰.

2.1.7 Processes during bubble close-off

Contrary to the three processes described above, where diffusion takes place in the gas phase, the following phenomenon deals with diffusion through the ice lattice. Elemental ratios in air pumped out of polar firn layers near the firn-ice transition show systematic enrichments of Ne/N_2, O_2/N_2 and Ar/N_2 (*Huber et al.,* 2006; *Severinghaus and Battle,* 2006). In turn, air extracted from already closed-off bubbles is relatively depleted. This unexpected depletion in O_2/N_2 ratios was recognized early, when O_2/N_2 ratios were measured with the aim to gain information about the strength of the photosynthetic oxygen production (*Bender et al.,* 1994 and references therein). The O_2/N_2 depletion was found to be systematic and cyclical and although the underlying mechanism remained obscure, the fractionation effect was exploited for dating issues (*Bender,* 2002). Only recently, the effect of gas fractionation during bubble close-off gained more attention and can now be described as a special diffusion process through the ice lattice (*Huber et al.,* 2006; *Severinghaus and Battle,* 2006). In contrast to gas phase diffusion, here the mass of the species is not a relevant parameter, but rather its diameter. Large atoms, like Kr and Xe, are not affected by this process, however, the small atoms He and Ne are subject to considerable losses. Below a critical diameter of 3.6 Å[9], gas molecules and atoms migrate through the lattice and are partially lost to the firn air and are therefore relatively depleted within the bubble. The dependency of the measured loss with diameter is strongly nonlinear (*Severinghaus and Battle,* 2006).

Analogue to the preferential gas loss during the bubble close-off, a similar diffusion process through the ice matrix is present during the storage of ice cores after drilling, which causes further off-sets for the gas composition, e.g. for N_2/O_2 (*Bender,* 2002)[10].

CO_2 has a molecular diameter of 3.94 Å, thus, should lie on the safe side of this size criterion. The values for the diameters are collision diameters, derived form viscosity experiments. Note that besides collision diameters, kinetic sieving diameters are used in the field of studying diffusion and permeation through porous membranes. Here, the effective diameter of CO_2 (3.3 Å) is smaller than for N_2 (3.6 Å) and CO_2 preferentially passes inorganic membranes (*Yeom et al.,* 2000 and references therein).

To derive effective diameters for a given process, both the dimension of the gas of interest, but also for the second collision partner, in our case the ice lattice, have to be considered. The data basis for effective diameters is sparse, therefore, the conclusion that CO_2 is not affected by this process has yet to be proven. Firn air measurements near the close-off zone did not indicate any effect on the CO_2 concentration. However, in contrast to other gases like O_2, N_2, and the noble gases, for which a relative enrichment against a fairly stable background concentration can be detected with relative ease, CO_2 is more uncertain due to the anthropogenic rise. Furthermore, the CO_2 concentration profile with depth is often an input parameter to tune the model, thus, CO_2 is not a free parameter, which limits the interpretation.

2.1.8 Clathrate formation and disintegration

Although this process per se does not alter the gas composition within the ice, clathrate formation and afterwards its gradual disintegration after drilling strongly influences the mixing

---

[9] 1 Å (Angstrom) = 0.1 nm

[10] owing to diffusive loss of gases during storage, it is common practice for gas analysis to remove the at least 5 mm of the outer layer of an ice sample prior extraction.

ratios of the gas phase. This is crucial since conventional extraction techniques for $\delta^{13}C$ in ice cores are only capable to extract the gas in bubbles. The new sublimation approach described in this thesis allows to quantitatively extract not only the gas phase, but also the air enclosed in clathrates. Nevertheless, as changes in the mixing ratio of CO_2 are involved with the clathrate disintegration, an isotopic fractionation related to a diffusion processes must be considered.

Figure 2-4 gives an impression of the proportions of bubble ice and clathrate ice for a deep ice core, exemplified for the EDML core. It is striking that the zone with pure bubble ice, for which conventional mechanical extraction techniques are aimed for, comprises only the top 500 m or around 15% of the core length. In terms of age, the proportion of bubble ice is even marginal due to the thinning of the layer thickness with depth. For the EDML core, only the Holocene is covered within the bubble ice region and >95% of the climate history lies within the clathrate ice or in the transition zone.

Ordinary ice, I_h, has a hexagonal structure with the density (0.917 g cm^{-3}) considerably lower than the liquid phase water (1.00 g cm^{-3})[11]. This relatively loose packing of the ice crystal

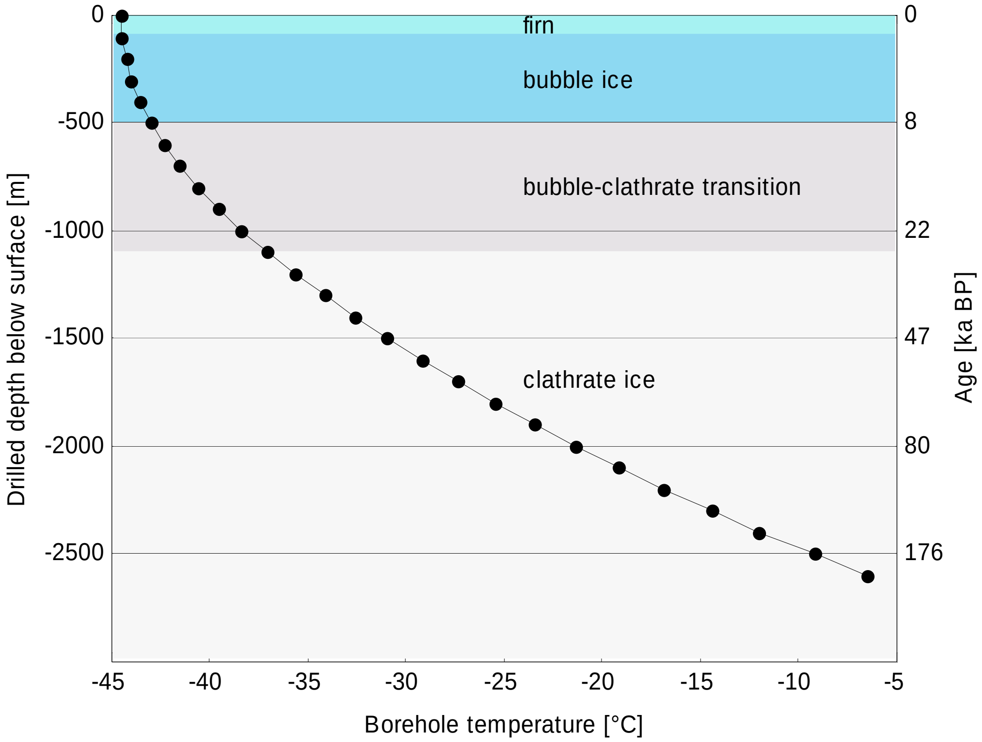

Figure 2-4 Schematic sketch of the EDML ice core with respect to the relative proportions of bubble and clathrate ice. The figure further shows the gradual temperature increase with depth as a consequence of the thermal heat flux from the bedrock. The temperature profile was derived from direct borehole measurements in the field (F. Wilhelms, unpublished data) For comparison, the ice age for the corresponding depth intervals are shown.

---

[11] both values for atmospheric pressure and 0 °C

allows to form voids or cages. Clathrates or air-hydrates form, when these cages are occupied by one or two guest molecules as shown in Figure 2-5. *Kuhs et al.* (1997) found that these cages occur in two different sizes, which are occupied by guest molecules of contrasting diameters depending on pressure and temperature. In case of the clathrates found in deep glacier ice, the guest molecules originate from the enclosed air, therefore, these special clathrates are often specified as air-hydrates. Nevertheless, the broader term clathrate and clathrate ice is widely used in the ice core literature.

Air-hydrates have a cubic crystal symmetry and are translucent. This property makes pure clathrate ice completely transparent in contrast to bubbly ice. To be stable, a set of thermodynamic conditions have to be fulfilled, i.e. temperature, partial pressure of a gas species have to exceed certain thresholds. For each gas and temperature a special dissociation pressure has to be reached until clathrates become the stable phase (*Ikeda-Fukazawa et al.,* 2001). The pressure within a bubble gradually increases with depth, with the bubble volume decreasing. When the dissociation pressure of the clathrate is exceeded, the bubbles gradually disappear as more and more gas diffuses into the ice matrix to form clathrates. This zone where both bubbles and clathrates coexist is generally several hundreds meters wide, for EDML approximately from ~500 m to ~1000 m depth and called transition zone[12]. Owing to the different

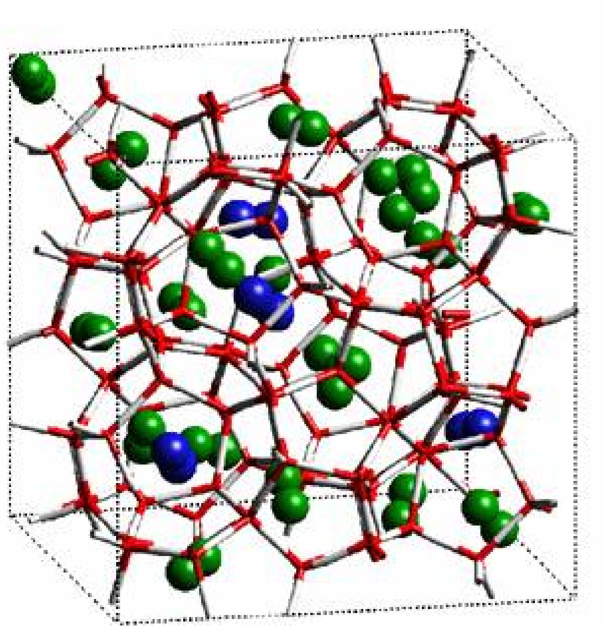

Figure 2-5 The crystal structure of air-hydrate. The red-white frame shows the water host lattice forming two types of cages in which the oxygen (blue) and nitrogen (green) atoms are located. The resulting structure has cubic symmetry and belongs to von Stackelberg's type II (unpublished, with permission of W. Kuhs from http://kristall.uni-mki.gwdg.de/).

---

[12] note, due to the high pressure within the bubbles the ice core is brittle around the depth of 500 m and the ice is of poor quality and highly cracked. Clathrate formation prevents further pressure built-up and results in good core quality of the transparent clathrate ice

dissociation pressures of the air components, the gas composition within a bubble is subject to changes. Moreover, the atmospheric gas components have different diffusion coefficients (*Salamatin et al.,* 2001; *Ikeda-Fukazawa et al.,* 2005). In case of the bulk components, O_2 and N_2, oxygen diffuses several times faster than nitrogen, hence, the latter becomes progressively enriched within the bubble. As a result of these effects, large anomalies in the mixing ratios of several gas components were reported for O_2/N_2 (*Ikeda et al.,* 1999) as well as for the CO_2 concentration within the bubble-clathrate transition zone (*Eyer,* 2004).

For the gas analysis of ice cores both the bubble-clathrate transition zone and the clathrate zone pose analytical challenges. Clathrates are metastable and slowly disintegrate due to pressure release after drilling on time scales of years to reform bubbles. Thus, once the gas is trapped within the clathrate cages, a quantitative extraction with mechanical means is hardly possible. During the disintegration of clathrates, the mixing ratios of the gases are distorted again due to kinetics and the gas specific dissociation pressures involved (*Ikeda-Fukazawa et al.,* 2005).

In contrast to the mixing ratios of gas species, which are largely effected by clathrate formation and disintegration, isotope effects have not yet been reported. This is due to the fact that the process of filling the clathrate cages is a matter of the geometry of the molecule related to the available cage size. Consequently, the filling-up of the cages is sensitive to the molecule's volume and not to its mass. Though the binding energy of the ^{13}C-^{16}O bond is slightly higher than for ^{12}C-^{16}O, thus its bond length is shorter, this difference is too small to induce a steric isotope effect (*Mook,* 2000). Nevertheless, low extraction efficiencies with mechanical techniques and diffusion effects during the disintegration of clathrates, which are known to cause isotopic fractionation, call for a quantitative extraction for $\delta^{13}C$ (*Eyer,* 2004).

2.2 Chemical reactions and a possible in-situ production of CO_2

In the following, chemical reactions of impurities found in polar ice cores are evaluated for their relevance for CO_2 and $\delta^{13}C$ ice core records.[13] Whereas the physical processes reviewed above strongly depend on climatic parameters of the site (e.g. temperature, accumulation rate), the chemistry of the ice is primarily influenced by source and transport processes of the impurities. Accordingly, the geographic position of an ice core drill site with respect to continental source regions and also atmospheric chemistry plays a major role. Chemical reactions and the issue of in-situ production of CO_2 within the ice have been known for a long time (*Delmas,* 1993; *Anklin et al.,* 1995; *Smith et al.,* 1997a). Similarly, for the greenhouse gas

---

[13] Organic compounds like acetaldehyde are critical for the mass spectrometric measurement of $\delta^{13}C$ on CO_2 as well. Acetaldehyde has a molecular mass of 44 g mol^{-1}, thus it might interfere with the identical masses of CO_2 if it enters the ion source of the mass spectrometer.

N_2O, artifacts were reported as well, especially from core sections with high dust concentrations (*Flückiger et al.,* 2004; *Spahni et al.,* 2005) and additionally for carbon monoxide, CO, measured in Greenland ice (*Haan and Raynaud,* 1998).

In addition to atmospheric CO_2, ice cores can contain other carbon sources. First, inorganic carbon, mainly in the form of $CaCO_3$ as a component of terrestrial dust. Secondly, a large suite of volatile and particulate organic compounds. They originate either from the oxidation of atmospheric trace gases (like formaldehyde from CH_4), are emitted during fire events (organic acids) or transported together within the continental dust particles (eroded soil material). In total, for Greenland ice these impurities can potentially contribute to an in-situ CO_2 production ranging from 140 ppmv within the Holocene to 700 ppmv during the glacial period, assuming these compounds were completely transformed to CO_2. Impurity concentrations for Antarctica are generally lower and the CO_2 equivalents amount to 80 ppmv in the Holocene, while for the glacial period the relevant impurities are more abundant (*Tschumi and Stauffer,* 2000). Note that for this worst case scenario of the in-situ production *Tschumi and Stauffer* (2000) assumed that the carbon containing impurities are stoichiometrically transformed to CO_2. However, an unequivocal contamination of CO_2 ice core records was so far shown only for Greenland, while Antarctic ice is assumed to be unproblematic in this respect.

Beginning with the discrepancies of early CO_2 concentration measurements on Greenland ice cores, the first paragraph reviews the status of in-situ CO_2 and its relation to possible chemical reactions. With the aid of a mass balance approach, the issue of the isotopic composition of a possible in-situ contaminant is highlighted. The following paragraphs summarize the basic information concerning possible sources and reactions of organic and inorganic compounds, which are related to a possible in-situ production. Where available, information about the stable carbon isotopic composition of these compounds is provided to assess their potential effect on the atmospheric $\delta^{13}C$ values trapped in the ice core.

2.2.1 Indications for CO_2 in-situ production from Greenland ice cores

As shown in the physical section above, molecular diffusion within the firn column smoothes out any seasonal and short term atmospheric CO_2 fluctuations. Nevertheless, CO_2 measurements on Greenland ice cores (GISP2, GRIP) conducted with a precision of ca. 3 ppmv revealed variations of 15-50 ppmv within an annual ice layer (*Anklin et al.,* 1995; *Tschumi and Stauffer,* 2000). Consequently, the observed CO_2 fluctuations cannot be explained with analytical uncertainties, which is confirmed by the analysis of corresponding Antarctic ice cores showing a scatter one order of magnitude lower (*Barnola,* 1999; *Stauffer et al.,* 2002; *Stauffer et al.,* 2003; *Siegenthaler et al.,* 2005a).

A second argument strongly pointing to a non-atmospheric contribution of CO_2 in ice cores is that also the mean CO_2 values from Greenland and Antarctic ice cores do considerably deviate (see Fig. 2-6). *Anklin et al.* (1995) compared CO_2 measurements throughout the younger Holocene among Greenland and Antarctic ice cores. To rule out systematic effects, the cores were measured at two different institutes using different measurement techniques. CO_2 values from Greenland cores were found to be considerably higher than the Antarctic values, i.e. Greenland cores contain so called excess CO_2. This difference increased with time leading to the assumption that the in-situ production is a function of time. *Smith et al.* (1997a) found even higher differences in certain parts of the glacial periods (Dansgaard Oeschger events). The direct comparison of CO_2 records from both hemispheres became more precise since dating between different cores was improved after CH_4 synchronization of these cores was established (*Blunier et al.,* 1998). It became evident that an interhemispheric CO_2 gradient of up to 20 ppmv is in contradiction with the rate of interhemispheric air mass exchange and regional distribution of CO_2 sources and sinks. Currently, the interhemispheric CO_2 gradient is ~2 ppmv and mainly the consequence of large emissions in the Northern Hemisphere (*Dargaville et al.,* 2003). As a consequence, Greenland ice cores must be contaminated in some way.

Large analytical efforts have been made in the following years at the Physics Institute of Bern to identify the cause of this excess CO_2 in Greenland ice (e.g. *Tschumi and Stauffer,* 2000). On core sections from different depth intervals highly resolved CO_2 records were measured

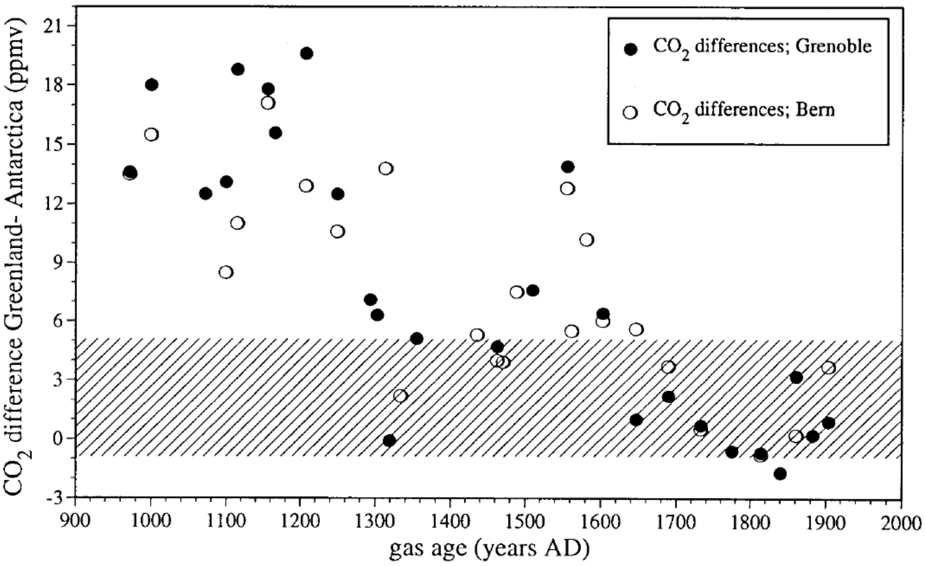

Figure 2-6 Comparison of CO_2 measurements between a Greenland (GRIP) and an Antarctic ice core (South Pole). The difference between the two records approaches up to 20 ppmv for gas ages of around 1000 years, but is small for younger ages. This feature could be reproduced from two individual laboratories using different extraction methods. The hatched area indicates the range, which can be explained by an interhemispheric CO_2 gradient. Figure from *Anklin et al.* (1995).

and compared with a suite of chemical components analyzed on the same section. These profiles were analyzed with a depth resolution of only a few centimeters. For Greenland ice from upper core sections this translates to a sub-annual time resolution (Fig. 2-7).

Tschumi and Stauffer (2000) found similarities of the CO_2 excess profile with the following chemical components or parameters: soluble calcium (Ca^{2+}), insoluble dust, hydrogen perox-

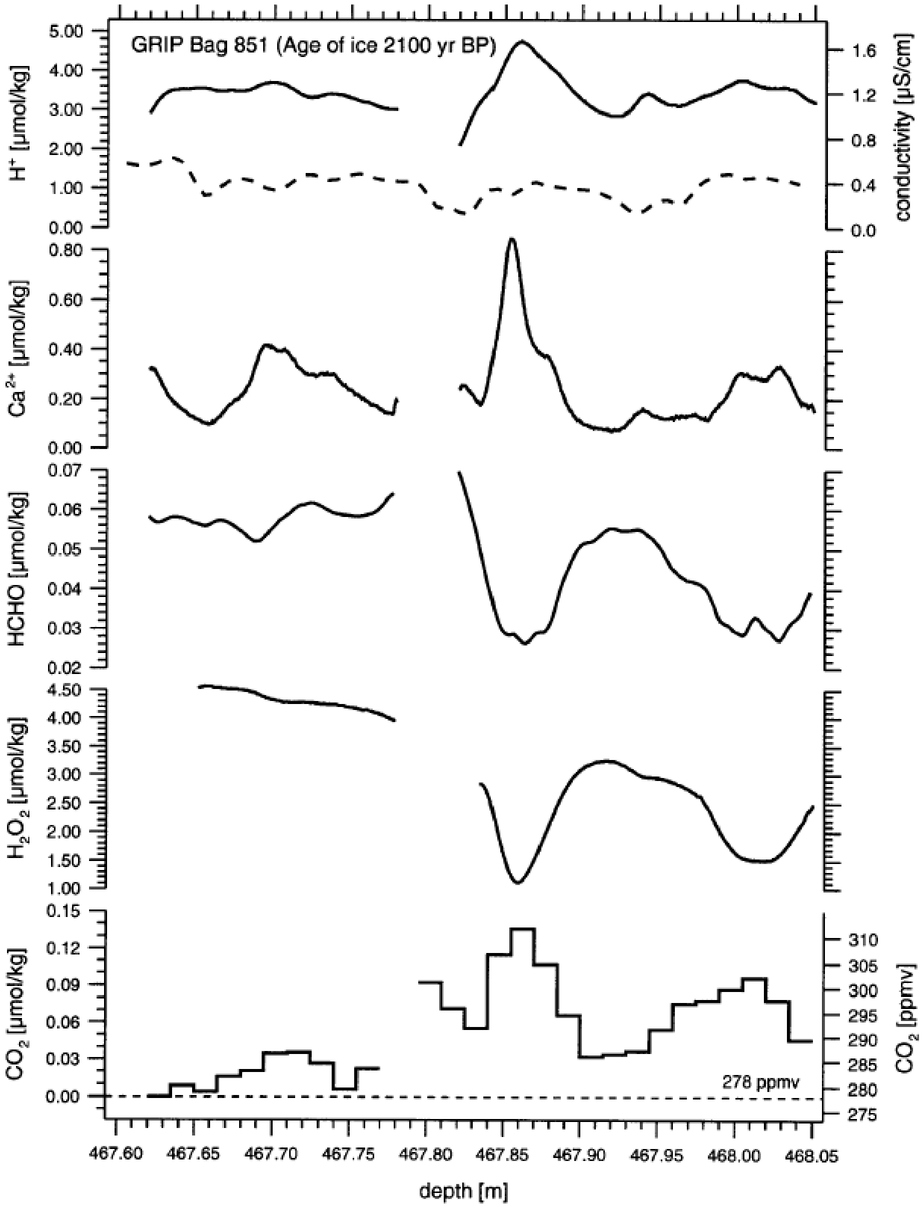

Figure 2-7 Highly resolved concentration of CO_2 from a Holocene section of the GRIP ice core compared with continuous records of H_2O_2, HCHO, Ca^{2+}, and H^+ and electrical conductivity of the meltwater as possible sources of excess CO_2. The proton concentration (solid line) was derived from the in-situ dc conductivity of the ice, whereas the conductivity in μScm^{-1} was measured after melting the ice in the meltwater (dashed line, left scale). Concentrations for the chemical compounds and the excess CO_2 are given as $\mu mol\ kg^{-1}$ ice. The total CO_2 concentration is reported as ppmv. The core section was dated to 2100 years BP (ice age) and comprises around three annual layers. The missing part is due to a break in the core; after *Tschumi and Stauffer* (2000). Note that these strong relations of excess CO_2 and chemical impurities were not found in all measured core sections.

ide (H_2O_2), formaldehyde (HCHO), electric conductivity of the meltwater, and the direct-current conductivity measurement (ECM) of the ice. From the ECM the concentration of protons (H^+)[14] can be derived as a measure of acidity since the ECM signal is predominantly controlled by the highly mobile H^+ ion (*Wolff et al.,* 1997).

With statistical analysis of the profiles, *Tschumi and Stauffer* (2000) found positive correlations of CO_2 excess and chemistry profiles for conductivity of the meltwater (r = +0.6) and Ca^{2+} concentration (r = +0.5). In contrast, negative correlations were found for CO_2 excess and the concentration profiles of H_2O_2 (r = -0.5 to -0.9) and HCHO (r = -0.3 to -0.9). These findings led to the assumption that the excess CO_2 found in these core sections was due to chemical reactions; either an acid-carbonate reaction or oxidation of organic compounds, or both at the same time.

Further evidence that the excess CO_2 may not be of atmospheric origin came from a few isotopic measurements conducted on suspicious core sections. The $\delta^{13}C$ values measured on extracted CO_2 samples considerably deviated from the expected atmospheric composition (around -6.3±0.5‰). On the GISP2 ice core*, Smith et al.* (1997a) analyzed $\delta^{13}C$ on CO_2 from both a LGM section (~17 ka BP) and from the Holocene (~2.5 ka BP). The LGM values were -4.45‰ and -3.70‰, thus, the isotopic composition of the added carbon source should be isotopically enriched with respect to the atmosphere. This would corroborate the idea that Greenland ice is contaminated by an acid-carbonate reaction, at least for the dust rich sections during the glacial period. For the Holocene, however, the $\delta^{13}C$ values were -7.23‰ and -7.43‰. In the light of the $\delta^{13}C$ data now available from Antarctica (Taylor Dome from *Smith et al.* (1999) and Law Dome from *Francey et al.* (1999)), and assuming no sudden $\delta^{13}C$ shifts during the last 3000 years, these data are surprisingly too negative. Assuming these Holocene data are not compromised by an analytical artifact like drill fluid contamination (*Leuenberger et al.,* 1992; *Smith et al.,* 1999), then the excess CO_2 should originate from an isotopically lighter source compared to the LGM. This could be explained by an in-situ contribution from an isotopically depleted organic compound.

To illustrate the effect of a contamination with different $\delta^{13}C$ values, a mass balance calculation was made (Fig. 2-8). To an uncontaminated atmospheric sample with $\delta^{13}C$ = -6.50‰ and 280 ppmv an increasing amount of 'foreign' CO_2 with an individual $\delta^{13}C$ value is added. Lines represent mixing of the two end members. The isotopic mass balance was calculated for the following $\delta^{13}C$ values: 0‰, -11‰, -28‰ and -55‰. These values were chosen to cover the full isotopic range of possible in-situ reactions from contrasting carbon sources. In this simple calculation it is assumed that the isotopic composition of the added CO_2 from each source remains constant and does not vary with the added amount. This might happen, when

---

[14] note, in ice core science the terms acidity and proton concentration are often used interchangeably to represent a measure of the acid content.

isotopic fractionation during the chemical reaction within a closed system is involved as discussed later (Rayleigh approach). From the mass balance mixing shown in Figure 2-8, it is clearly visible that already a small amount of added CO_2 might alter the atmospheric signal. The larger the difference between the atmospheric δ^{13}C value and an assumed δ^{13}C value of the added in-situ CO_2, the larger its effect on the mixed signal. As the measurement precision for the concentration of CO_2 with the state of the art ice core methods is in the order of 2 ppmv, small excess CO_2 contributions are hardly detectable. In case of a highly depleted contaminant this would only be visible in the δ^{13}C record.

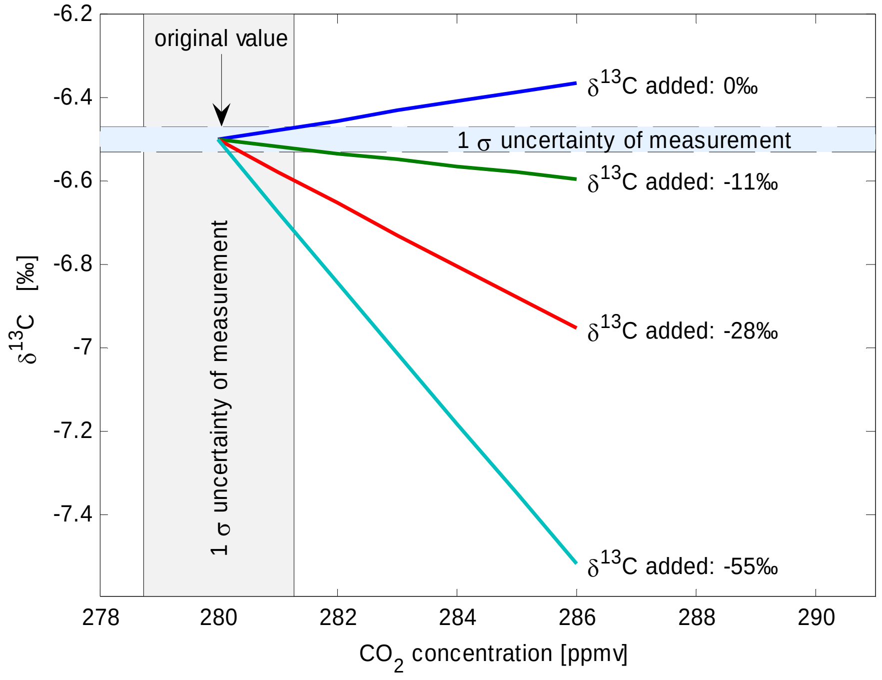

Figure 2-8 Mass balance calculation to simulate the contamination of different carbon sources on the original values (280 ppmv and -6.5‰). To this composition foreign carbon was added from 0 to 6 ppmv with contrasting isotopic signatures representing different carbon sources. From top to bottom: 0‰ for carbon originating from inorganic carbonates, -11‰ for plant or soil carbon from photosynthesis using the C_4 pathway, -28‰ for plant or soil carbon from C_3 pathway, and -55‰ for the assumed isotopic value of formaldehyde as a product from methane oxidation. Additionally shown is the 1 σ measurement precision with 2.5 ppmv for CO_2 concentration and 0.06‰ for the isotopic ratio.

2.2.2 In-situ reactions of organic compounds

From the chemicals usually found in the atmosphere only a few groups are actually relevant in our context and can be sorted out using two criteria. The first criterion is, if the atmospheric trace compound combines a certain set of physico-chemical properties to be adsorbed on or deposited with the snow and if the compound is then relatively inert to survive the oxidative degradation within the surface snow. The second criterion is, whether a compound that made its way from the atmosphere into ice has additionally the chemical potential to react to CO_2.

Two main groups, or homologous series, were identified in the past and measured in snow and ice: aldehyds (R-CHO), and mono- and dicarboxylic acids (R-COOH and HOOC-R-COOH)[15]. Prominent examples of these homologous series are formaldehyde and acetaldehyde and formic acid, acetic acid and oxalic acid, which were found in snow and ice (*Kawamura et al.,* 2001; *Guimbaud et al.,* 2002; *Houdier et al.,* 2002; *Narukawa et al.,* 2002; *Perrier et al.,* 2002).

2.2.2.1 Precursors and sources of organic compounds in ice cores

Characteristic for organic compounds found in snow and ice cores is that only a small amount is directly emitted, e.g. during fire events (*Kawamura et al.,* 2001), but the main share originates from oxidation of volatile organic precursors within the atmosphere or snow. Terrestrial and marine ecosystems produce large amounts of volatile organic compounds. To name a few, methane is predominantly emitted from wetlands and ruminants. Trees emit terpens and marine algae release organic compounds like DMS and alkyl halides (e.g. CH_3Cl, CH_3Br).
This organic mixture is subject to a suite of photochemical reactions within the troposphere and stratosphere. The reaction with the hydroxyl radical, *OH, is the most prominent one. As the reaction from methane to formaldehyde comprises several steps and involves also nitrogen oxides and O_2, Eqn. 2-7 is not stoichiometric.

$$CH_4 + {}^*OH \xrightarrow{h\nu,\, O_2,\, NO} HCHO + HO_2 \qquad (2-7)$$

Major side products of these photochemical reactions are peroxides, e.g. hydrogen peroxide and methylhydroperoxide. Note that formaldehyde itself is only an intermediate and reacts to CO and CO_2 (*Perrier et al.,* 2002). In similar reactions also organic acids and many other compounds are produced and deposited with the snow (*Chebbi and Carlier,* 1996).

2.2.2.2 Isotopic composition of organic compounds

Only little information is available about the carbon isotopic composition of organic compounds in the polar atmosphere and in snow. *Goldstein and Shaw* (2003) review the available information about the carbon isotopic composition of a wide range of organic trace compounds within the atmosphere. To get an overview, it is worthwhile to look into the general pattern of the isotopic composition of organic compounds. Variability in the $\delta^{13}C$ signature of organic carbon can be found on several levels:

---

[15] note that in organic chemistry R stands for the rest behind the functional group (R may be a carbon chain or only a H atom in case of the first element of a homologous series)

- among major functional plant types in terms of their bulk composition, e.g. plants using the C_3 pathway have mean $\delta^{13}C$ values of -28‰, whereas C_4 plants values of around -11‰ (*O'Leary,* 1981)
- among the main chemical groups, e.g. lipids are ~10‰ lighter than the bulk organic matter of plants, see reviews by *Lichtfouse* (2000) and *Hobbie et. al.,* (2004)
- among the carbon atoms of a single molecule (e.g. the methyl groups of molecules are generally up to 40‰ isotopically depleted compared to the mean value of the molecule (*Keppler et al.,* 2004))

Several conclusions can be drawn from above:
First, for a given compound its primary source determines its mean isotopic composition. Secondly, when a compound was identified to react within the ice and whereby producing in-situ CO_2, not its mean $\delta^{13}C$ value is decisive, but the $\delta^{13}C$ value of the carbon atom(s) transferred to CO_2 is relevant. This is due the fact that often not the whole molecule is involved in a reaction, but rather the carbon atom of the most labile group.
An additional effect has to be considered in this context. As most chemical reactions induce either a kinetic or an equilibrium fractionation, the isotopic composition of the educt and the product deviate and do not remain constant over time, but change in a predictable way. Generally, the product is isotopically depleted with the heavier isotope and the remaining educt becomes progressively enriched with the heavy isotope. This is due to the fact that molecules containing the lighter isotope react slightly faster and binding bonds of the molecules are stronger for the molecule with the heavier isotope.
A simple approach to illustrate this effect is applying a Rayleigh model to a reaction. For the situation within an ice sample with a known amount of a reactive compound, an approach with a given reservoir and one sink or loss process is most applicable (Eqn. 2-8 and 2-9).

$$\delta \quad = \quad \left(1+\delta_0\right)\cdot\left(\frac{N}{N_0}\right)^{\varepsilon} - 1 \qquad [‰] \qquad (2-8)$$

Derived from a mass balance approach (*Mook,* 2000), where δ_o denotes the original isotopic composition of the reservoir prior the reaction, δ the isotopic composition of the remaining reservoir after the reaction consumed a fraction of it. N_0 represents the reservoir size of the educt prior to the start of the reaction. N/N_0 is then the remaining fraction of the reservoir left after the reaction consumed some educt with a fractionation factor ε. As illustrated in Figure 2-9, the isotopic composition of the remaining fraction becomes successively enriched in the heavier isotope, hence, the δ values increase (black curve). In turn, the cumulative product gets depleted accordingly:

$$\delta_{cum} = \left(1+\delta_0\right) \frac{1-\left(\frac{N}{N_0}\right)^{1-\varepsilon}}{1-\frac{N}{N_0}} -1 \qquad [‰] \qquad (2-9)$$

with δ_{cum} the average isotopic composition of the reaction product after a certain fraction of the educt was consumed. In our example, with ε set to 10‰, the relative difference of the instantaneous product (blue curve) to the remaining product is always 10‰. But as the isotopic composition of the remaining educt (δ) steadily increases, the absolute value of the product increases as well. At the end of the reaction, when the educt quantitatively reacted to the product, δ_{cum} approaches the initial value of the educt (δ_0).

Consequently, to assess the impact of in-situ produced CO_2 on the δ^{13}C value of an ice core sample, the 'history' of a reaction is decisive. In other words, if a chemical reaction produces CO_2 from an educt, the remaining fraction of this educt has to be known. If the in-situ reaction

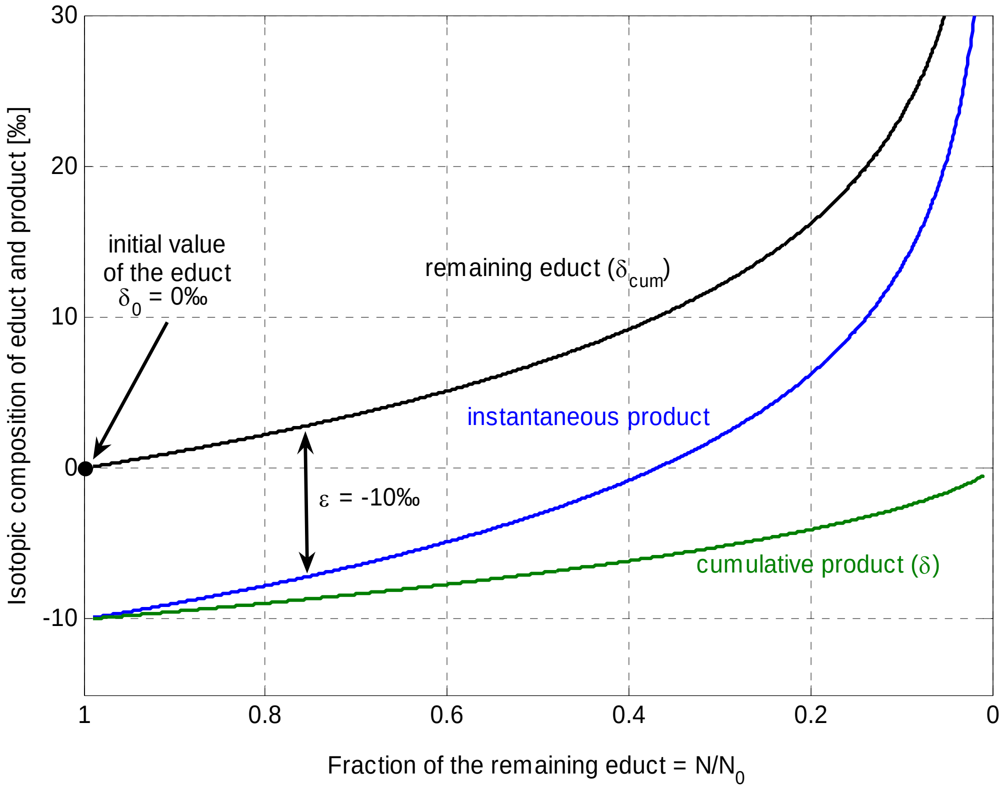

Figure 2-9 Rayleigh model describing the isotopic fractionation of educt and product during a reaction proceeding from left (fraction of remaining educt = 1) to right (fraction of educt = 0). In case of an in-situ reaction the educt is an organic compound and the product the excess CO_2. The isotopic composition of the educt at the beginning of the reaction, δ_0, was set to 0‰. A fractionation factor ε of 10‰ was chosen as the isotopic difference between the educt and the instantaneous product. The black line shows the gradual isotopic enrichment of the remaining educt as a function of the fraction already removed from a reservoir. The green line describes, δ_{cum}, the cumulative isotopic composition of the reaction product removed from the reservoir; figure adapted after Mook (2000).

has already consumed a large fraction of the educt, and this was accompanied with a large isotopic fractionation, then the measured $\delta^{13}C$ of the remaining educt would be relatively enriched. Consequently, not only the fractionation factor ε and the $\delta^{13}C$ of the educt has to be known, but also its remaining fraction N/N_o.

2.2.2.3 Formaldehyde as an example for in-situ reactions

To asses the extent of a possible impact of in-situ reactions on the $\delta^{13}C$ value extracted from ice cores, knowledge about the isotopic composition of the precursor is helpful. In the following paragraph it is exemplified, how different precursors can have a decisive effect on the carbon isotopic signature of an in-situ compound.

Formaldehyde as an example for organic compounds was selected since its concentration in ice cores is relatively high and it may be oxidized to CO_2, thus, may contribute to excess CO_2 in ice cores. Formaldehyde is a major intermediate oxidation product of methane, but other hydrocarbons may also react to formaldehyde (*Riedel et al.,* 2005). Atmospheric methane represents an isotopically highly depleted compound with a pre-industrial $\delta^{13}C$ value of around -50‰ (*Sowers et al.,* 2005). During the reaction with OH radicals, a fractionation of ~5‰ occurs, thus, the reaction product formaldehyde should approach a $\delta^{13}C$ value of around -55‰, if methane were its main source (*Brenninkmeijer et al.,* 2003). When formaldehyde is oxidized within the ice by H_2O_2 (Eqn. 2-10), the formed CO_2 is likely to be isotopically depleted as well. This in-situ CO_2 increases not only the CO_2 concentration, yet the effect is even worse when considering its impact on the isotopic composition of the atmospheric CO_2 in the ice. Note that neither the pathway nor the potential location of this chemical reaction within the ice were already identified. Interestingly, for some chemical compounds it was found that concentrations are not equally distributed within the ice, but enriched at the grain boundaries and especially in triple junctions[16], as revealed from microanalysis (*Barnes et al.,* 2003; *Ohno et al.,* 2005). It was speculated that even at temperatures as cold as -20 °C a quasi liquid layer might exist due to the lowering of the melting point caused by a local enrichment of chemical impurities. As a consequence, this layer may provide a liquid compartment for chemical reactions (*Weller et al.,* 2004; *Ohno et al.,* 2005).

$$2H_2O_2 + HCHO \quad \rightarrow \quad 3H_2O + CO_2 \qquad (2-10)$$

The partner of formaldehyde, H_2O_2, is mainly generated during photochemical reactions when organic compounds react with OH radicals (*Frey et al.,* 2005) and several studies report H_2O_2 measured in Antarctic snow and firn samples (*Gillett et al.,* 2000; *Hutterli et al.,* 2003).

---

[16] triple junctions or veins are located where three crystal boundaries meet

Recent studies modeling formaldehyde concentrations within the Antarctic firn and in the troposphere showed that other sources in addition to methane are needed to explain the measured formaldehyde concentration (*Riedel et al.,* 2005). Other volatile precursors like ethane and dimethylsulfide may contribute to the formaldehyde budged. The few existing $\delta^{13}C$ measurements on atmospheric formaldehyde are less depleted than one would assume if methane is its major source. *Goldstein and Shaw* (2003) report $\delta^{13}C$ values for formaldehyde in remote areas from -17 to -23‰. Similar high values are given in *Brenninkmeijer et al.* (2003), but they interpreted the unexpectedly high $\delta^{13}C$ values of formaldehyde as a result of a large kinetic fractionation occurring during a loss process of formaldehyde.

2.2.3 In-situ reactions of inorganic carbonate

Compared to the in-situ issue caused by organic compounds, where many species are potentially involved and reactions are unclear, the acid-carbonate reaction is straight forward. It is in principle one single carbon species, carbonate CO_3^{2-}, which reacts with protons[17] to form CO_2 in a two stage acid-base reaction. Carbonate occurring in dust particles is most likely associated with calcium or magnesium and nearly insoluble in pure water. Hence, its dissolved concentration is low compared to the solid phase.

$$CO_3^{2-} + H^+ \leftrightarrow HCO_3^- \qquad (2-11a)$$

$$HCO_3^- + H^+ \leftrightarrow CO_2 + H_2O \qquad (2-11b)$$

As shown in the reaction Equations 2-11a and b, in total two moles of protons are consumed to produce one mole CO_2. Further, both reactions are fully reversible and proceed until an equilibrium state is reached. Hence, high CO_3^{2-} and HCO_3^- levels can actually shift the equilibrium, then CO_2 is ‘consumed’ from the gas phase and solid phase carbonate being dissolved similar to the weathering process of limestone. This might be the case for carbonate-rich sections of Greenland ice cores. Here, partly lower CO_2 values than expected were occasionally measured (*Smith et al.,* 1997b). The possibility to reach a chemical equilibrium is in contrast to the oxidation reactions of the organic compounds discussed before, which have higher activation energies, thus, the back reaction is hardly possible.

Similar to the reaction of organic compounds, a local liquid phase along the grain boundaries and triple junctions is assumed as a reaction medium at the temperatures prevailing in polar ice sheets. Especially the acidic compounds sulfuric acid and methanesulfonate are preferentially located along the crystal boundaries (*Barnes et al.,* 2003). Further, different types of salt inclusions were found in Antarctic ice cores, which might indicate that carbonate particles

---

[17] for simplicity H^+ is used here instead of H_3O^+ used in formal aqueous chemistry

were already neutralized during the atmospheric transport by the acid-carbonate reaction (*Ohno et al.,* 2006). The authors found undissolved $CaSO_4$ particles in ice samples of the glacial period, which contains higher proportions of continental dust than during the Holocene. $CaSO_4$ is produced when $CaCO_3$ reacts with sulfuric acid, whereby CO_2 is liberated. Yet, it is not fully certain from these findings when the reaction of carbonate with the acid occurred, either during transport, during the snow and firn metamorphosis prior to the bubble close-off, or after bubble close-off. Only in the last case, CO_2 is trapped within the ice and can contaminate the atmospheric CO_2 composition.

2.2.3.1 Sources of carbonate in ice cores and isotopic composition

The main geographic sources of carbonate particles transported to the ice sheets are the dry regions of the continents. Only a negligible fraction stems from marine sea spray aerosols emitted from the open ocean due to wind action. With respect to their formation and composition, carbonate particles can be separated into three groups: First, from mechanical crumbling of rocks due to the action of glaciers. Often marine limestone was ground to fine particles blown out from the glacial foreland and river banks. This type is classic for the European loess deposits during the ice ages. $\delta^{13}C$ values of marine carbonates are close to the mean isotopic composition of the ocean (around 0‰). Secondly, limnic carbonates are formed by chemical weathering of soil and rocks and the subsequent transport of these solutes to lake basins. Dissolved inorganic carbon in rivers and carbonates from lake deposits have a higher variability in $\delta^{13}C$ and are sometimes isotopically lighter compared to marine carbonates (*Mook,* 2000; *Brunet et al.,* 2005). Lakes may dry out in phases of reduced precipitation and/or evaporation and lake sediments may be exposed and the be blown out. A special case are the dry regions of Taklimakan Desert, China, which is assumed to have provided the high dust and carbonate levels in the glacial ice of Greenland. Here, $\delta^{13}C$ values of around 0‰ were measured in surface carbonates, which was explained that these carbonates are mainly of marine origin with its isotopic composition nearly unaltered (*Wang et al.,* 2005). Thirdly, pedogenic carbonates mainly originate in semiarid soils and can be blown out after surface erosion by wind action. The $\delta^{13}C$ values of pedogenic carbonates are influenced from the vegetation type and other parameters, but are generally within the range from -10 to 0‰ (*Cerling et al.,* 1989; *Ding and Yang,* 2000; *Stevenson et al.,* 2005). Owing to the different genesis and geographic origin of carbonate aerosols, the ratio of $CaCO_3$ on the total mineral dust may considerably vary as well its carbon isotopic composition. According to Equations 2-11a and b, the liberation of CO_2 from carbonate particles is dependent on the availability of acidic compounds within the ice. The mere presence of carbonate in ice does not result in any CO_2 in-situ production. *Smith et al.* (1997a) reported that the highest in-situ production was found in ice samples originating from the warmer interstadials, where dust levels and hence the carbonate input was reduced, yet the acidic compounds were higher. In these core sections carbonate and acidic aerosols occurred simultaneously without reacting prior to the bubble close-off. The CO_2 concentration of the cold stadials characterized by the highest dust and calcium levels shows only little off-sets to the Antarctic values. As the acidity concentration derived from the ECM is zero, the conclusion can be drawn that this was already the case during the deposition of the snow.

2.3 Conclusions and requirements for the $\delta^{13}C$ analysis of ice cores

From the considerations about physical and chemical processes discussed above, the general conclusion can be drawn that ice core $\delta^{13}C$ values can considerably deviate from the original atmospheric value. Both physical and chemical processes were found to complicate and challenge the ultimate goal of $\delta^{13}C$ analysis of ice cores, i.e. to provide reliable data to reconstruct the global carbon cycle of the past. However, for the dominant fractionation process, the gravitative settling in the firn column, a sound physical theory can describe this phenomenon, and with the $\delta^{15}N$ value a measurable parameter is available to correct for this effect.

The other effects are still less understood and have to be critically evaluated, if and under which circumstances they actually disturb the atmospheric signal trapped within the ice. Especially for the chemical in-situ production of excess CO_2 only little is known which organic precursors are oxidized to CO_2 and how this happens. Most studies about chemical in-situ reactions were conducted on Greenland ice cores, which are now considered inadequate for accurate CO_2 and $\delta^{13}C$ measurements. Generally, Antarctic ice cores contain considerably less impurities and the mean annual temperatures are lower, thus, reaction rates are substantially reduced. Consequently, the small effects, which might also occur for Antarctic ice, are more difficult to detect with the current detection limits of the used analytic methods. Analyses on Antarctic ice cores, so far, gave no clear hint that they do not accurately represent the original atmospheric CO_2 concentration. However, highly resolved CO_2 concentration measurements on the two EPICA ice cores (EDML and EDC) revealed an unexplained scatter especially in young Holocene ice of EDML, which is beyond the analytical precision (*Stauffer et al.,* 2003; *Siegenthaler et al.,* 2005a). But, the authors state that the scatter of the samples is only slightly higher than the scatter for standards and analytical off-sets cannot be ruled out.

New analytic developments are underway at the Physics Institute of Bern (Dissertation U. Federer) to measure the total amount of organic compounds at a high depth resolution. Until then, the most pragmatic approach followed in this study for $\delta^{13}C$ analysis is first to carefully analyze ice core sections on the respective scale where a suspicious process might induce a $\delta^{13}C$ variability to be detected.

2.3.1 δ^{13}C artifacts as a matter of scale

The scale of those processes able to induce an off-set in the gas composition between ice cores and the atmospheric value, can vary from a few centimeters to several hundred meters. In terms of time this translates to time scales from sub-annual to centuries/millennia for typical conditions occurring in low accumulation regimes. In the following, the physical and chemical processes are divided according to the scale they affect. Not all listed effects have a direct impact on CO_2 or δ^{13}C, but in case of the Δ–age difference of gas to ice, the effect might be relevant for comparing and dating different ice cores. The principal aim is to illustrate at which scale these effects might add unexplained variability, to decide at which scale the analytic has to look at.

effects on the cm-scale may result from:

- chemical in-situ reactions since concentration profiles of impurities strongly vary among deposition events and especially on seasonal time scales
- size dependent fractionation during the process of bubble close-off as found for major atmospheric constituents (*Huber et al.,* 2006; *Severinghaus and Battle,* 2006)
- post coring diffusion processes during the years of storage induce gas fractionation in the outermost mm to cm of the ice samples (*Craig et al.,* 1988; *Bender et al.,* 1995; *Ikeda-Fukazawa et al.,* 2005)
- inhomogeneous clathrate formation/destruction within the bubble-clathrate transition zone influences the mixing ratio of gases and causes varying extraction efficiencies with mechanical techniques

effects on scales of up to several 100 m may result from:

- altered thickness of the firn's diffusive column height and rapid temperature fluctuations induce changes both in the extent of the fractionation processes, e.g. gravitative settling, but also for parameters like Δ–age and the age distribution
- chemical in-situ reactions I: due to principal changes in the mean concentration of impurities caused by major climatic changes (glacial-interglacial)
- chemical in-situ reactions II: due to the time dependent reaction rate the in-situ effect might gradually increase with time and depth as found in the growing difference between Greenland and Antarctic ice cores for older core sections (*Anklin et al.,* 1995)
- chemical in-situ reactions III: due to increased reaction rate with increasing temperature when ice becomes warmer owing to the geothermal heat flux from the bedrock

2.3.2 Analytical requirements

The analytical procedure must be capable to precisely analyze $\delta^{13}C$ and CO_2 on the respective scale and should meet the following analytical criteria for:

(1) sample size

The sample size should be small enough to detect an artifact on the respective scale, i.e. a few cm for chemical variations. Further, as ice is generally limited, the method should allow to make replicates and highly resolved profiles on a single core section.

(2) physical state of the trapped gas

The method should work indiscriminately for bubble and clathrate ice, i.e. the efficiency of the extraction must not depend on properties of the ice itself. This was not possible until now with the mechanical extraction devices, which extract trapped air only to 40-80% depending on the type of ice and storage history. Sublimation under vacuum allows an extraction efficiency of 100% and this technique was already used to measure CO_2 concentration on ice cores, but not for $\delta^{13}C$.

(3) isobaric interferences during the measurement

The mass spectrometric measurement of $\delta^{13}C$ should not be compromised by isobaric interferences. Several organic compounds, like chloro-fluoro carbons used as densifier for deep drilling, produce mass fragments during the ionization in the mass spectrometer, which are identical to CO_2. The state of the art analytical systems for $\delta^{13}C$ ice core measurements were not able to separate these compounds from CO_2.

(4) precision

The analytical error of the method should allow to detect possible artifacts in $\delta^{13}C$ in the order of 0.05‰. This precision is necessary as the entire variability of atmospheric $\delta^{13}C$ on glacial/interglacial time scales does not exceed the range of 0.5-1‰.

3 Methods and instruments for $\delta^{13}C$ and CO_2 analysis on ice cores

3.1 Introduction

The challenge to explain the glacial/interglacial variations in atmospheric CO_2 has been a task of outstanding importance for the paleoclimate community during the last decades and still is (*Indermühle et al.,* 1999; *Brovkin et al.,* 2002; *Broecker and Clark,* 2003; *Köhler and Fischer,* 2004). Although CO_2 data are now available for up to six glacial cycles with different resolution (*Fischer et al.,* 1999; *Petit et al.,* 1999; *Monnin et al.,* 2001; *Siegenthaler et al.,* 2005b), a long, highly resolved and trustworthy record of $\delta^{13}C$ is still awaited.

Chapter 3.2 summarizes the technical approaches developed during the last 25 years to analyze $\delta^{13}C$ on ice cores. A technical evaluation of the sublimation methods previously used for CO_2 extraction provides Chapter 3.3. The focus is put on the limitations and methodological shortcomings encountered during their usage to derive the essential requirements to improve these techniques. The general layout and concept of the newly developed methods in this work is presented in Chapter 3.4. In Chapter 3.5 and 3.6 the technical details of the sublimation extraction system followed by the tube cracker system are presented. The actual sample preparation and measurement protocol is described in Chapter 3.7. The data processing and the procedure verification with blanks and reference gas standards and the necessary corrections are discussed in Chapter 3.8 and 3.9.

3.2 Previous approaches for $\delta^{13}C$ on ice cores using mechanical devices

Starting in the early 1980s, first analytical attempts were initiated to extract CO_2 from ice cores to measure its isotopic composition (Tab. 3-1). Generally, the entire procedure comprises three steps: (1) release of the gases occluded in the ice, i.e. separation of the gas phase from the ice matrix, (2) followed by a sample clean-up to remove traces of water and to separate CO_2 from the bulk air[18] constituents, (3) finally the measurement of the isotopic composition in an isotope ratio mass spectrometer (IRMS) using two different inlet techniques: (1) dual-inlet micro volume and (2) continuous flow (CF). For an overview of the presently used IRMS approaches see review from *Ghosh and Brand* (2003).

Although the size of the sample needed per analysis greatly varied between ~5 g and 1 kg, all extraction techniques were mechanical, only differing in the way the ice was crushed. Typically, an ice sample was loaded into a stainless steel vessel, atmospheric air was pumped off using vacuum, and then the ice was crushed using either a needle cracker, milling device, or a

---

[18] N_2, O_2, Ar and other atmospheric compounds which are not condensable at liquid nitrogen temperature (-196 °C); in any cryogenic application CO_2 and N_2O are trapped together due to nearly identical physical properties.

cheese-grater. The sample clean-up and transfer, however, considerably varied according to the applied inlet coupling for the IRMS (Tab. 3-1).

(1) For the dual-inlet micro volume technique, the extracted air was purified in large diameter vacuum lines whereby either all air constituents were condensed together on a cold head at 15 K and CO_2 is separated afterwards from the air (*Friedli et al.,* 1984; *Friedli et al.,* 1986; *Siegenthaler et al.,* 1988). Or, CO_2 was immediately frozen out in cold traps held at liquid nitrogen temperature (LN at -196 °C), with the remnant air then collected on a cold head (*Leuenberger et al.,* 1992). A similar approach was used by *Smith et al.* (1997a), *Indermühle et al.* (1999) and *Fischer et al.* (2003), with the difference that CO_2 was separated from H_2O in two consecutive steps. Afterwards, CO_2 was transferred in a glass tube and stored for the later IRMS measurement. The most elaborate set-up was used by *Francey et al.* (1999), who condensed the whole extracted air first on a cold head, and in a

Table 3-1 Compilation of methods for $\delta^{13}C$ analysis on ice cores developed from several groups. The applied approaches differ widely in (1) required amount of ice per sample, (2) the extraction technique to liberate the gases from the ice and (3) the attained extraction efficiency, (4) the sample clean-up and the preparation of the gas sample prior to its measurement and (5) the type of inlet linking the mass spectrometer. The sample size has been dramatically reduced since the advance of a new inlet coupling, i.e. from dual-inlet micro volume (DI) to continuous flow (CF) isotope-ratio mass spectrometry (IRMS). Extraction efficiencies for bubble ice were reported to be ~80%, but lower for clathrate ice (values in brackets). * denotes interferences with drill fluid; ** denotes interferences with organic solvents (ethanol and isopropanol)

authors	sample size [g]	crushing device	recovery [%]	clean-up and transfer to IRMS	inlet
Friedli et al., 1984 *Friedli et al.,* 1986 *Siegenthaler et al.,* 1988	~700	milling cutter	80-90	complete trapping of released air and CO_2 on cold head (14 K), then cryogenic separation of CO_2 and air (offline)	DI
Leuenberger et al. 1992	~500	milling cutter	75-85	cryogenic CO_2 trapping prior the air is condensed on cold head (20 K), *	DI
Francey et al. 1999	1000	'cheese grater'	N/A	complete trapping on cold head (15K), then CO_2 extraction under controlled pressure for viscous flow (offline), **	DI
Smith et al., 1997a *Indermühle et al*., 1999 *Fischer et al.,* 2003	200	rotary crusher	N/A	cryogenic separation of CO_2 from air, flame-sealed glass ampoules (off-line), *	DI
Leuenberger et al., 2003 *Eyer* 2004	5-10	needle cracker	75 (50)	dried air expanded in large volume, separation of CO_2 from air in a continuous He flow at 3 bar using the Precon system (online), *, **	CF

second step they trapped CO_2 off the gas stream using a pressure control unit. Using this technique, viscous flow conditions within the LN traps of the vacuum line were maintained during the entire trapping procedure. Nevertheless, vacuum lines used for the sample clean-up prior to dual-inlet IRMS measurement are not suitable for more advanced sample clean-up techniques like gas chromatography (GC). Most studies reported problems during the IRMS measurement caused by isobaric interferences from organic impurities and N_2O. The organic impurities either originate from drill fluid contamination or were introduced during the sample preparation within the laboratory (organic solvents used in cold traps and cooling systems). Additionally, ice cores naturally contain traces of organic compounds like acetaldehyde, which may cause isobaric interferences during the IRMS measurement. The dual-inlet technique has the additional drawback that large sample amounts were needed (up to 1 kg) since only a small fraction (<1%) of the sample actually enters the ion source of the IRMS. However, the attainable precision of the dual-inlet technique is unrivaled and can be as low as 0.01‰ for atmospheric measurements on flasks samples (*Ciais et al.,* 1995; *Werner et al.,* 2001). Yet, the outstanding measurement performance of dual-inlet cannot be exploited as the overall precision of the whole procedure is determined and deteriorated by the sample preparation and from artifacts.

(2) In contrast, the continuous flow (CF) technique, which became available during the 1990s, principally allows to separate CO_2 from interferences using a GC, since the extracted gases are introduced into a continuous He flow. In a typical CF application, CO_2 is transferred and purified within small diameter capillaries using a pressurized He carrier. The sample is then transferred to the ion source of the IRMS using a so called open split device. Contrary to dual-inlet applications, here typically 30% of the sample enters the IRMS. Consequently, CF applications reduced the sample size for the analysis of up to two orders of magnitude. *Leuenberger et al.* (2003) were the first employing this elegant sample preparation technique for $\delta^{13}C$ analysis on ice cores by connecting the established needle cracker (*Monnin et al.,* 2001) to a new developed CF preparation system. Here, the released air from the extraction device expanded into a large expansion volume. Introduced in a He flow, CO_2 was then transferred to the CF system, where CO_2 was cryofocused and then admitted to the IRMS. Although principally possible with this CF system, *Leuenberger et al.* (2003) did not implement a GC separation. With this approach they dramatically reduced the sample size down to 5-10 g ice, which allowed highly resolved $\delta^{13}C$ measurements for the first time.

This CF approach was applied in the work of *Eyer* (2004), who measured $\delta^{13}C$ at high resolution on both EPICA ice cores (EDML and EDC). Though the same age intervals for both cores were measured under the identical preparation protocol, the $\delta^{13}C$ values between the two cores differed substantially and showed a large scatter (*Eyer,* 2004). This unexpectedly large scatter cannot be explained by an atmospheric signal as the variance was found on a sub-annual scale, which should be smoothed out in ice cores due to the slow bubble enclosure process. As the δ^{13}C results depended on the measured ice core and the precision of the reference gas measurements was 0.12‰, *Eyer* (2004)speculated that the scatter in EDML might be due to a process connected with the ice. Suggested candidates were fractionation during the bubble close-off and in-situ reactions, which are both relevant at the scale of a few cm. Since the sample size used in former studies was large (up to 1 kg, see Tab. 3-1), thus, small scale effects might have been unresolved, the results of *Eyer* (2004) challenged the δ^{13}C approach.

On the other hand, inherent limitations and problems with the ice core analysis itself might explain the large scatter as well. *Eyer* (2004) reported sporadic outliers with unusual negative δ^{13}C values, which he attributed to drill fluid contamination. These isobaric interferences during the IRMS measurement were reported in earlier studies as well (see references in Tab. 3-1). It can be concluded that an effective sample clean-up using a GC helps eliminate this issue. Chapter 3.6 describes the CF-IRMS system developed in this study, where a GC sample clean-up is applied for the first time for the δ^{13}C analysis on ice cores.

A second critical issue reported by *Eyer* (2004) was associated with the analysis of clathrate ice and confirmed also by *Siegenthaler* (2006), who found out that the extraction efficiency for clathrate ice (1) is considerably lower than for bubble ice and (2) both the efficiency and the CO_2 mixing ratio was strongly dependent on extraction time. Both studies came to the conclusion that the nonquantitative extraction of clathrate ice using mechanical devices fractionates at least the gas species (elemental fractionation). *Eyer* (2004) additionally found also strong effects on the carbon isotopic composition with more negative δ^{13}C values for deeper ice with higher clathrate content. Chapter 3.5 describes the developed sublimation system, which allows a quantitative sample extraction both for bubble and clathrate ice. Until now, sublimation of ice was only applied for concentration measurements and is used here for the first time for δ^{13}C on ice cores.

3.3 Quantitative extraction techniques for ice cores – sublimation in vacuum

Having in mind the low efficiency of mechanical extraction devices for clathrate ice together with elemental and isotope effects reported by *Eyer* (2004), the urgent need for a quantitative gas extraction for the analysis of δ^{13}C on clathrate ice is apparent. Note that pure bubble ice comprises only ~20% of the total length of a deep ice core from Antarctica, in terms of climate history the fraction is even smaller. The overwhelming part of the atmosphere's climate history is found in clathrate ice as pointed out in Chapter 2.1.

For the measurement of the concentration and isotopic ratios of most gases from ice cores (e.g. N_2, N_2O and $\delta^{15}N(N_2O)$, CH_4 and $\delta^{13}C(CH_4)$) a melt extraction is used (*Chappellaz et al.,* 1997; *Flückiger et al.,* 1999; *Sowers et al.,* 2005; *Bernard et al.,* 2006). With restrictions, also the CO_2 concentration can be analyzed using a wet extraction for Antarctic cores with low impurity concentrations, but results deviated from conventional data in certain core sections (*Kawamura et al.,* 2003). A $\delta^{13}C$ analysis using a wet extraction technique is probably not possible. This is primarily due to chemistry as a liquid phase provides favorable reaction conditions for the impurities (acid-carbonate, organic compounds and H_2O_2) as discussed also for the in-situ effects (*Tschumi and Stauffer,* 2000; *Kawamura et al.,* 2003). Since the $\delta^{13}C$ of calcite or organics substantially deviates from the atmospheric value, as shown in the Chapter 2.2, already a 1% contamination (e.g. 2 ppmv to 200 ppmv CO_2) could shift the $\delta^{13}C$ up to 0.2‰. A second difficulty is the high solubility of CO_2 connected with its isotopic fractionation during gas-liquid transfer from the aqueous HCO_3^-/H_2CO_3 system (*Anklin et al.,* 1995; *Zhang et al.,* 1995).

Thus, the only extraction technique which destroys the ice matrix and enables 100% extraction efficiency and avoids the above mentioned complications is sublimation under vacuum. Several sublimation techniques to quantitatively liberate air from polar ice cores were developed during the last 15 years (Tab. 3-2). First attempts to sublimate ice in vacuum were conducted by *Wilson and Donahue* (1990; 1992) with the aim to measure ^{14}C on ice samples to establish a means for absolute dating of ice cores. Sample sizes as large as several kg were processed in vacuum lines. The ice was sublimated in a glass vessel using infra red (IR) lamps, water vapor was removed in large external water traps cooled with organic solvents at -80 °C, and CO_2 was separated from air in LN traps. Interestingly, the authors used a molesieve to collect the air content, mainly to be independent from external vacuum during almost 18 h of sublimation. As the aim was to carbon-date the extracted CO_2, it was essential to assure that during the sublimation no 'dead carbon' from the $CaCO_3$ rich Greenland ice would

Table 3-2 Compilation of sublimation methods for quantitative extraction of CO_2 from ice cores. Note that all approaches used organic solvents for the H_2O cold traps (typically ethanol at -90 °C).

author	sample size [g]	sublimation temperature [°C]	energy source	collection of CO_2 and air
Wilson and Donahue, 1990 *Wilson and Donahue,* 1992 *Wilson and Long*, 1997	3000	-10	infra red lamps	LN cold trap and molesieve at LN
Güllük et al., 1998	20-50	-36 to -27	infra red lamps	cold head (18 K)
Siegenthaler 2002	15	-36	CO_2 laser	cold head (18 K)

release CO_2 due to an acid-carbonate reaction. Consequently, to rule out surface melting, the sublimation temperature was held below -10 °C and controlled by the resulting vapor pressure over ice (~2.5 mbar). In a later version (*Wilson and Long,* 1997), the sublimation apparatus was coupled on-line to the dual-inlet of a IRMS to allow also measuring δ^{13}C on ice core samples, however, without having success.

Güllük et al. (1998) built a new sublimation apparatus for the simultaneous concentration measurement of several greenhouse gases (CO_2, N_2O, CH_4) on polar ice cores. This set-up was considerably smaller and designed for a maximum sample size of 50 g ice. In contrast to the approaches of *Wilson and coworkers,* who had no possibility to admit reference gas to the apparatus, *Güllük's* approach allowed to manually introduce air standards to the sublimation vessel to check for artifacts and blanks. Instead of using LN cold traps and a molesieve to separate CO_2 from air, a cold head at 15 K was used to condense the entire air sample. As the intention of this set-up was to measure the CO_2 concentration with infra red laser spectrometry, separation of CO_2 from the air was not necessary. Unfortunately, the system suffered from large blank values, attributed to outgassing from the internal surface of the large water traps and tubing of the all-glass vacuum line. For CO_2, blank values were as high as 3-10% of the sample concentration, i.e. 10-25 ppmv. The authors found a second effect, which runs contrary to outgassing. When an air standard with known concentration was admitted to the dry sublimation vessel, meaning without adding ice, large loss effects of up to one third of the original concentration were observed. This interplay of adsorption on and desorption from the surfaces of the apparatus was related to the partial pressure of water (pH_2O) as well specific to the material as already reported by *Zumbrunn et al.* (1982). Further, outgassing of CO_2 increased when surfaces were unintentionally heated due to reflections of the IR-lamps used for sublimation. Problematic was also the extensive usage of Viton gaskets joining the sublimation vessel and the water trap.

To improve on the shortcomings of this approach, *Monnin* (2000) and *Siegenthaler* (2002) modified this system: First an IR laser replaced the IR lamps to prevent unintentional heating of the glass apparatus. A special optical window was inserted to transmit the laser radiation (~10 µm) to the ice. With the laser set-up, only a part of the ice cube can be sublimated due to the geometry of the optical window and lenses. Hence, the ratio of sample CO_2 to the surface area of the apparatus decreased. Secondly, the system's internal volume and area was reduced using smaller cold traps, but still high blank values persisted and the observed scatter in the ice core results was higher than for the mechanical extraction (*Siegenthaler et al.,* 2005a).

The two main general problems of this approach, the large surface area of the all-glass apparatus and the extensive usage of polymer material for seals and gaskets could not be reduced further within this technical set-up.

All approaches described above used organic solvents for the cooling traps. For the analysis of CO_2 concentrations this causes no problems. However, several studies measuring δ^{13}C on ice cores reported that minute amounts of organics caused isobaric interference during the IRMS measurement (see references in Tab. 3-1). These authors recommended to eliminate volatile organic solvents during the sample preparation, but also to keep the air in the laboratory of the mass spectrometer free from solvents.

To overcome the technical limitations of the previous sublimation approaches and to meet also the additional requirements for the δ^{13}C measurement, a new sublimation apparatus was designed. The approach of this work profits from three technical novelties.

- The system was constructed to minimize the surface effects. The sublimation vessel and the water trap are merged into one compact vessel, thus, large cross section tubing and seals to connect these devices are unnecessary. Only all-metal seals and valves are used and diameters of the metal tubing for the LN cold traps are kept as small as possible. Thus, the surface area of the apparatus was considerably reduced compared to previous approaches. This system is described in Chapter 3.5.4.
- Volatile solvents are excluded from any analytical step. To achieve this, a cooling system for the combined watertrap-sublimation vessel based on cold air replaced the solvents in the cooling baths of the previous studies. Further, a special water trap cooled with liquid nitrogen has been developed. These systems are described in Chapter 3.5.3 and 3.5.5.
- A reference inlet was constructed to introduce whole air standard to the sublimation vessel at viscous flow conditions. This device mimics the continuous release of air during the sublimation and aims at an identical treatment of sample and standard; the reference system is described in Chapter 3.5.8.

3.4 General layout of the entire method

This paragraph introduces the general strategy and set-up of the developed analytical method. Similar to the previous systems constructed to analyze ice cores for δ^{13}C, the entire analysis consists of three principal steps:

1. liberation of the trapped air from the ice
2. separation and purification of CO_2
3. measurement of the pure CO_2 in the IRMS

These three steps can be either coupled on-line, whereby the sample follows the whole chain of the analytical processes without interruption until the measurement is completed; or alternatively, using an off-line coupling, for which the chain of processes is interrupted at a certain step and the follow-up steps are decoupled from the first steps. In the field of stable isotope analysis, off-line coupling can be advantageous where one step is especially time consuming, whereas the other steps can be processed more quickly. Since the gas extraction from the ice is by far more time consuming than the actual IRMS measurement, off-line coupling was chosen and the entire process was split into two separated preparation lines. The two lines fulfill the following tasks:

- The first line liberates the trapped air from the ice sample and separates CO_2 from the air in a vacuum line. At the end, CO_2 is transferred into a tiny glass tube for storage.
- The second line purifies CO_2 from N_2O and other isobaric impurities in a continuous flow system leading to the IRMS measurement device (CF-IRMS).

This approach enables to measure a large number of extracted ice samples with the CF-IRMS system within a short time span and, thus, takes benefit from identical measurement conditions with the IRMS for a large set of samples. This is crucial as changes both in the performance of the IRMS, but also in the CF system are well known problems. Following this technical partition, first the setup of the ‘sublimation extraction’ is presented and then the CF system called ‘tube cracker-GC’ system leading to the IRMS (Fig. 3-1 and 3-2). With the sublimation extraction (Fig. 3-1), an ice sample is continuously sublimated and CO_2 is cryogenically separated from water vapor and the bulk air components. From one ice cube, weighing ~30 g, five discrete sub-samples are collected from the continuously released gas stream and separately stored in small glass tubes. During the ongoing sublimation the ice cube shrinks nearly symmetrically, which is illustrated in Figure 3-3. In parallel, the corresponding total air content of these sub-samples is determined manometrically. From this, the CO_2 mixing ratio is calculated using the m/z 44 signal from the mass spectrometric measurement. Off-line coupled to the sublimation extraction is the CF-IRMS system, where the stored tubes with the CO_2 are opened (‘cracked’) within a miniature tube-cracker and the CO_2 sample is transferred in a He carrier (Fig. 3-2). The He stream is first dried and with a cryofocus capillary a sharp peak is shaped, which is transferred to a GC column. The separated CO_2 peak is admitted to the IRMS via an open split. Both systems are equipped with reference devices to either introduce whole air standards or pure CO_2, and thus to mimic the sample’s way through the various analytic steps.

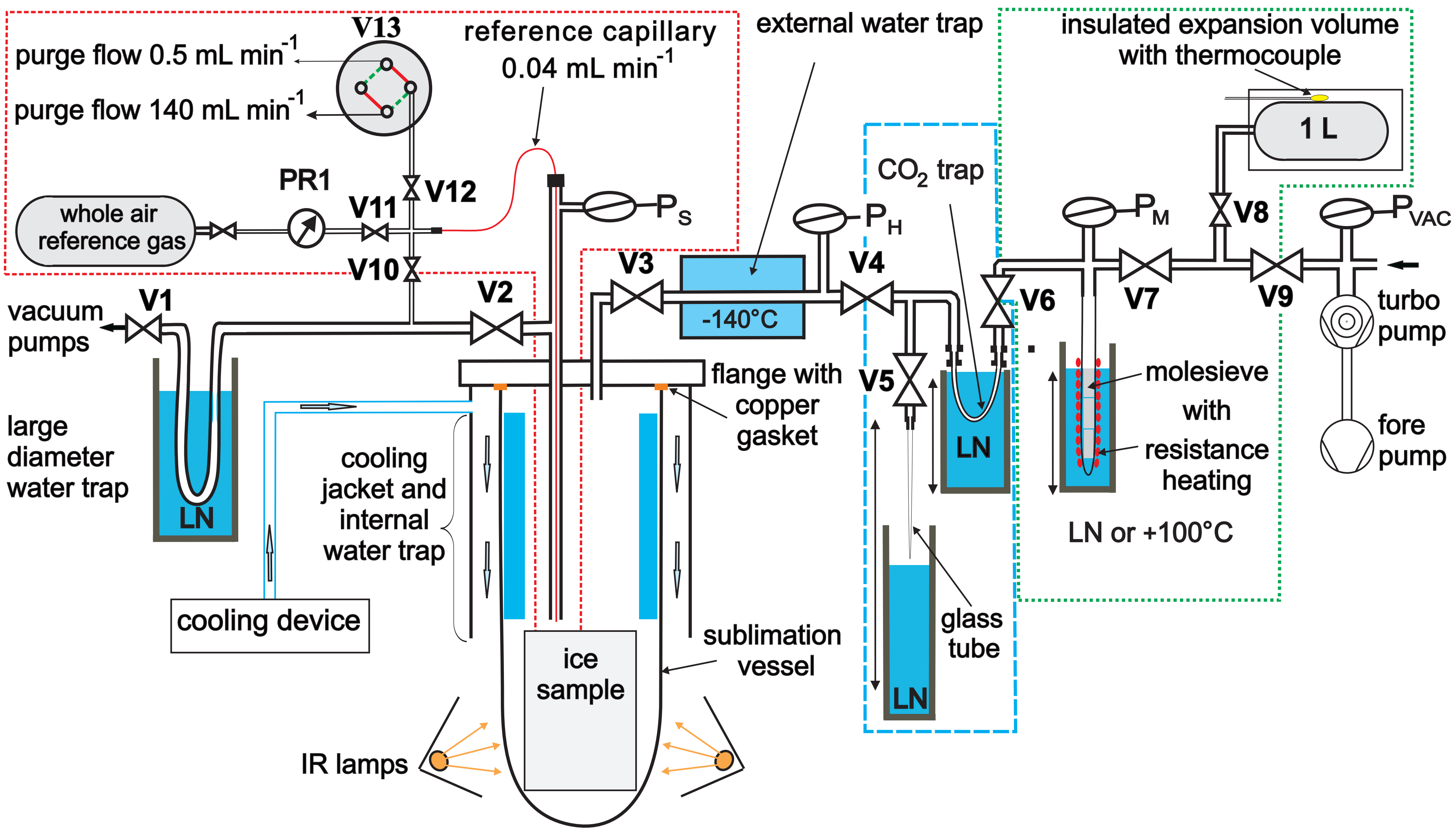

Figure 3-1 Schematic view of the sublimations extraction apparatus. The sublimation vessel with the ice sample is cooled by cold air supplied from a cooling device. The released air is dried in the external water trap and CO_2 is condensed in the CO_2 trap held at liquid nitrogen temperature (within blue dashed line) and transferred into a glass tube for further purification and analysis in the CF-IRMS system. The non-condensable gases like O_2 and N_2 are collected on the molesieve trap (within green dotted line) to determine the corresponding air volume. Air standards can be introduced into the sublimation vessel via the reference gas unit (within red dotted line) to provide identical treatment of samples and standards.

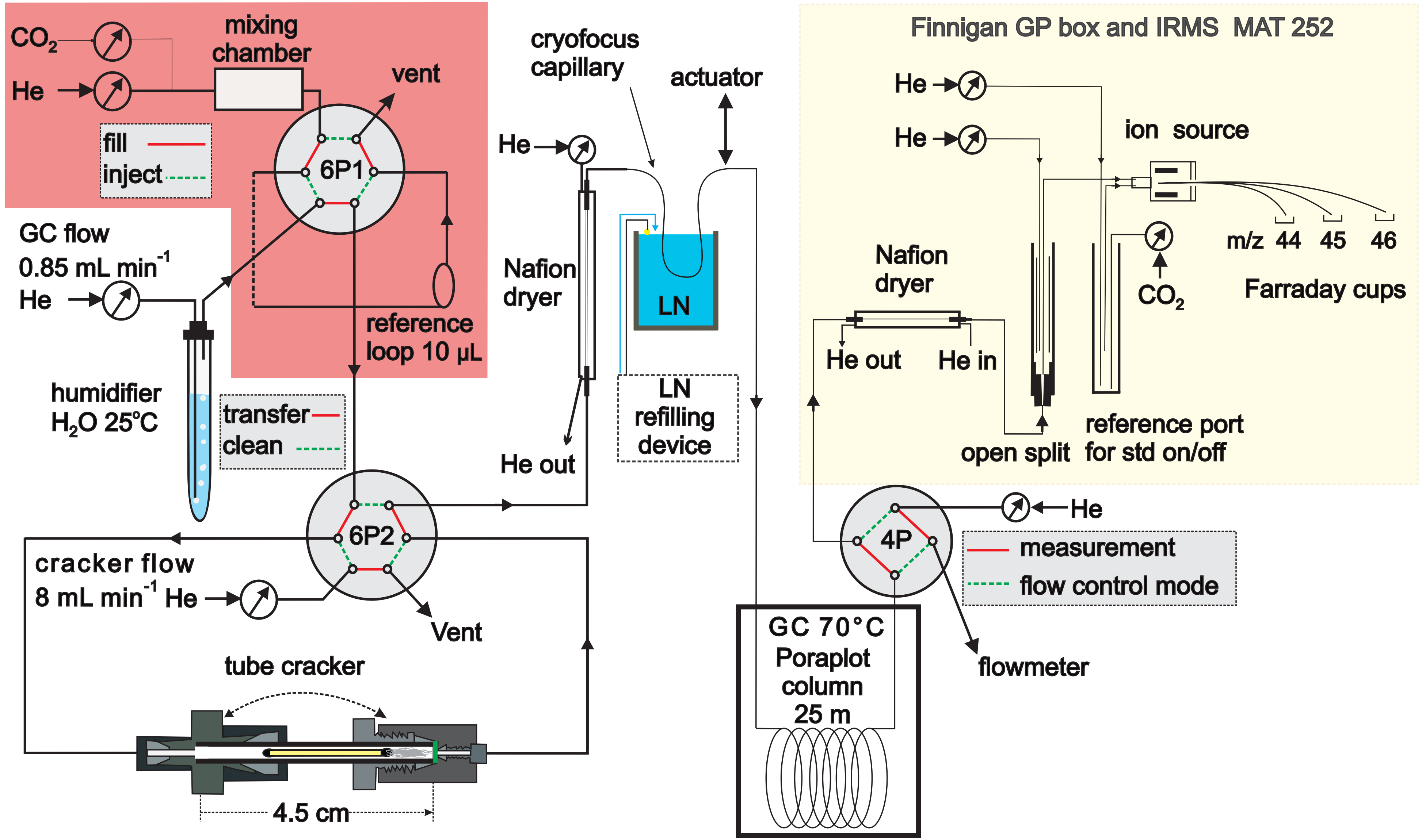

Figure 3-2 Flow scheme of the continuous flow tube cracker-GC-IRMS line. It consists of a CO_2 reference gas system (red area) to introduce CO_2 pulses onto the tube cracker, followed by a Nafion dryer, cryofocus capillary, GC, where CO_2 is chromatographically separated from N_2O and organic impurities. Via the Valco valve '4P' the system is linked to a commercial Finnigan GP box and MAT 252 (yellow area). The GP box houses the open split and the reference port for standard on/off. The open split capillary directs a fraction of the helium carrier to the ion source of the isotope ratio mass spectrometer (IRMS), where the ion currents of mass 44, 45, and 46 are measured and after integration the $\delta^{13}C$ values are computed.

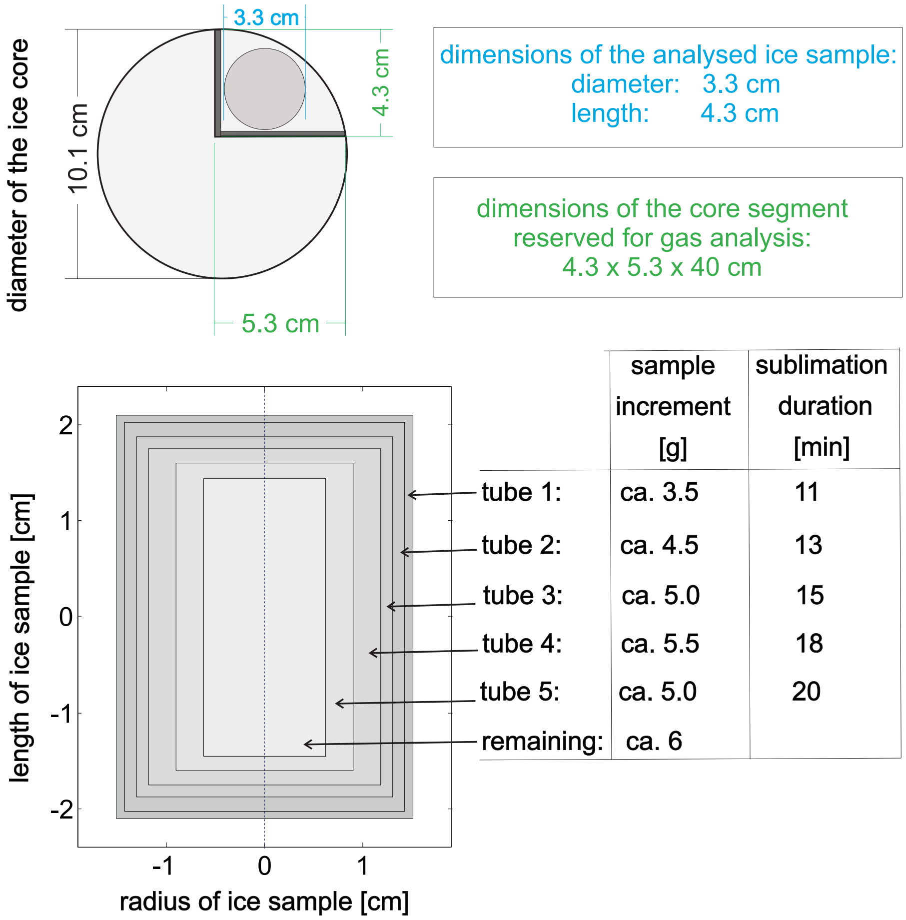

	sample increment [g]	sublimation duration [min]
tube 1:	ca. 3.5	11
tube 2:	ca. 4.5	13
tube 3:	ca. 5.0	15
tube 4:	ca. 5.5	18
tube 5:	ca. 5.0	20
remaining:	ca. 6	

Figure 3-3 The top of the figure shows the dimensions of the available ice core segment and the actual size of the ice cube used for the sublimation. The bottom of the figure illustrates the continuous shrinking of the ice cube with ongoing sublimation. Note that during the sublimation the ice cube retains its natural orientation, i.e. annual layers would be horizontal in this figure and orthogonal to the sublimation front. As the outer parts are gradually removed, the five sub-samples, or tube No. 1-5, originate from increasing ‘depth’ of the ice cube. Each tube contains on average the gas content of ~5 g ice, which corresponds to ~0.5 mL STP. A small amount of ice is left over, since the rate of the gas release decreases as the irradiated cross section of the small piece absorbs less energy.

3.5 The sublimation extraction system

3.5.1 Overall idea behind the sample trapping

The following paragraphs describe the technical details of the sublimation apparatus and its periphery. First, the procedure of repeated collection cycles is explained. As already mentioned above, one important feature of the presented sublimation apparatus is to process a single ice sample in a way to yield several sub-samples for the isotopic measurement. To do this, ice is sublimated continuously and from the liberated gas stream several discrete sub-samples are consecutively prepared for the off-line IRMS measurement until the sample is consumed. The reason for this approach is twofold:

- to yield better statistics of sample replicates from the IRMS analysis without opening the sublimation vessel to the atmosphere to load the next sample. Opening the vacuum system and the subsequent pumping to remove atmospheric CO_2 adsorbed on the surfaces is the most critical step in all applications for CO_2 and $\delta^{13}C$ analysis.
- to be able to detect side effects at the beginning and at the end of the sublimation phase. At the beginning the sublimation system needs some time and sample gas to equilibrate until stable conditions within the apparatus are reached. The conditions change again as the rate with which the gas is released from the ice decreases with sublimation time.

Depending both on the applied strategy for the trapping procedure and also on technical details of the equipment, more or less sub-samples can be obtained from one ice cube. Particularly crucial is, how fast one cycle can be completed to get the system ready for the next cycle. Figure 3-4 describes two collection schemes for the sublimation extraction: an earlier version, and the final version, which is presented in this work. In both cases trapping of CO_2 and air from the gas stream has to be interrupted in order to transfer the collected gases from the traps (light blue and yellow bars in Fig. 3-4). In the early version of the apparatus, the sample gas liberated during this time interval was diverted to vacuum until the cold traps were ready for the next collection cycle. Due to this partial sample loss, only three sub-samples could be collected from one ice cube. Unfortunately, the $\delta^{13}C$ values of the three sub-sample tubes slightly deviated from each other, which is most likely due to the non-quantitative collection approach (around 30 to 40% of the released gas was directed to vacuum). As isotopic fractionation between the sublimation vessel and the cold trap under the prevailing vacuum conditions seemed likely, the system was modified to a achieve quantitative sample recovery. The final design of the trapping devices allowed to shorten the time interval between two trapping cycles from six to three minutes. Further, this version improved the volumetric measurement of the air content from which the CO_2 mixing ratio is calculated together with the peak intensity of the IRMS signal. In the final version the sample gas is buffered for a short time interval (3 min) within the sublimation vessel until the traps are ready for the next cycle. Due to the accumulation of the liberated gas during the sublimation, the pressure within the vessel increases until the flow is re-directed to the cold traps (details concerning the precise timing of this procedure are presented in Chapter 3.7). This allowed a nearly quantitative sample collection. A small gas loss both at the very beginning of the sublimation and at the end, when the sample is almost consumed, is inherent to a continuous approach and not avoidable (red bars in Fig. 3-4). In total, more sample gas is collected this way, therefore five instead of three tubes can be collected. In the following description of the developed system only the final version is being presented.

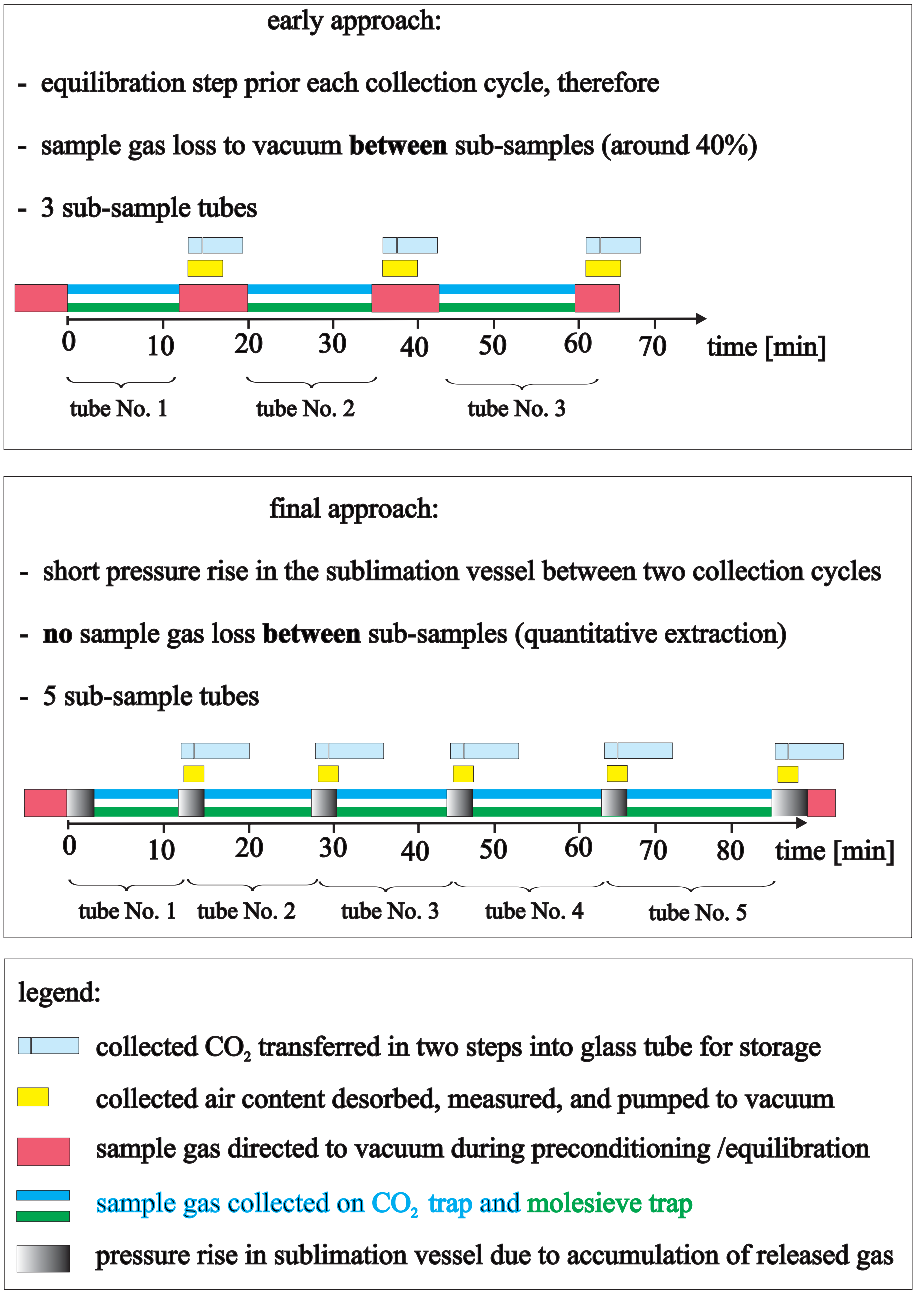

Figure 3-4 Comparison of collection schemes for the liberated air during the sublimation (top: early version; middle: final approach; bottom: legend). In the early version the entire procedure comprised three collection cycles, while five cycles in the final version. In both cases, the sublimation of ice samples is a continuous process, releasing a steady gas flow, which is then directed through the two cold traps (blue and green bars), where CO_2 and the air content are trapped separately. At the end of each cycle, the trapping process is interrupted for gas transfer and to prepare the traps for the next cycle. CO_2 is transferred from the trap to the glass tube (light blue bars), while the air content is desorbed from the molesieve, its pressure measured and the pumped to vacuum (yellow bars). The technical set-up and collection scheme for the early version of the sublimation system allowed only three sub-samples to be collected, while a large proportion of the sample gas was directed to vacuum between the trapping cycles (red bars). In the final set-up, the sample loss during the interruption for the gas transfer was solved as the released air during the sublimation is buffered within the sublimation vessel for 3 min (grey bars). This allowed five sub-samples to be collected and prevented sample loss in between.

3.5.2 Vacuum system and water removal

The vacuum within the sublimation apparatus (Fig. 3-1) is provided by a turbo molecular pump backed by a rotary vane (both Leybold Vacuum, Germany). Under conditions where no sample gas is directed to the vacuum line a minimum pressure of typically 2 x 10^{-7} mbar is reached at the 'P_{VAK}' pressure gauge. A ½'' o.d. water trap was inserted between the sublimation vessel and the turbo molecular pump to prevent H_2O from entering the high vacuum side via route V2 and V1 (Fig. 3-1). This would be the case, (1) while pumping off the moist atmospheric air after the sublimation vessel was opened to insert the sample, (2) and afterwards, during a 2-hour cleaning step to remove some mm ice from the outer part of the sample. H_2O strongly adsorbs on the stainless steel tubing and large diameter flexible hoses joining the vacuum line with the turbo pump, thus, it would take hours to remove all adsorbed H_2O from the surfaces and reach low baseline vacuum levels. Low baseline vacuum levels are crucial to detect leaks within the sublimation line.

3.5.3 Cooling system for compressed air

As stated above, one crucial feature of the newly developed sublimation line is its compact design that drastically reduces the surface area of the apparatus. This goal was achieved by combining the two main processes, sublimation and condensation of the ice, into one single glass vessel (see Fig. 3-1 and Chapter 3.5.4). To hold the internal water trap, i.e. the upper part of the glass vessel, at cold temperatures, an air stream from the cooling system is passed through a cooling jacket (details Fig. 3-1). For this, an insulated PCV tube of 8 cm with an inner diameter of ~5 mm wider than the glass vessel is used. The small slit between the jacket and the glass maintains a high and turbulent velocity of the coolant for better heat transfer to the glass vessel. The cooling jacket is attached and sealed to the flange with an O-ring. The still cold air stream passing the cooling jacket then cools the lower part of the vessel, which absorbs energy from the long wave part of the IR lamps.

However, a special cooling mechanism was required to cool the upper part of the glass vessel, while the lower part is irradiated with IR to sublimate the ice sample shown in Figure 3-1. No commercially available cooling device was found to suffice these technical demands.

A cooling system was developed that uses compressed air as the coolant medium. The system was constructed to fulfill the following requirements:

- to produce ~50 L $\min^{-1}$ cold air at -120 °C, equivalent to ~100 W (assumed ΔT of coolant and glass vessel ~100 °C)
- automatic adjustment to the selected temperature set-point of the coolant

- to manually adjust the temperature set-point and flow rate during the operation to meet the changing cooling demand for the sublimation vessel to remove latent heat flux and cooling of the lower glass section
- reliable performance during a 3-hour operation period
- technically adaptable for changed cooling demands during the development of the sublimation apparatus

Figure 3-5 shows the technical components of the cooling system. Briefly, compressed air is passed through a coiled heat exchanger unit made of copper tubing, which resides within a Dewar vessel. With a ‘pump’ a stream of liquid nitrogen droplets (LN) is automatically transferred from a reservoir into the heat exchange Dewar until the given temperature set-point is reached. Thermocouple 1 (TC1) measures the temperature of the cold air stream that is directed to the cooling jacket of the internal water trap of the sublimation vessel. A PID temperature controller (series 2300, West, UK) compares this temperature with the set-point and either opens or closes the relay for the electric current of the ‘pump’.

The physical principle behind this simple ‘pump’ is the so called Leidenfrost phenomenon. If

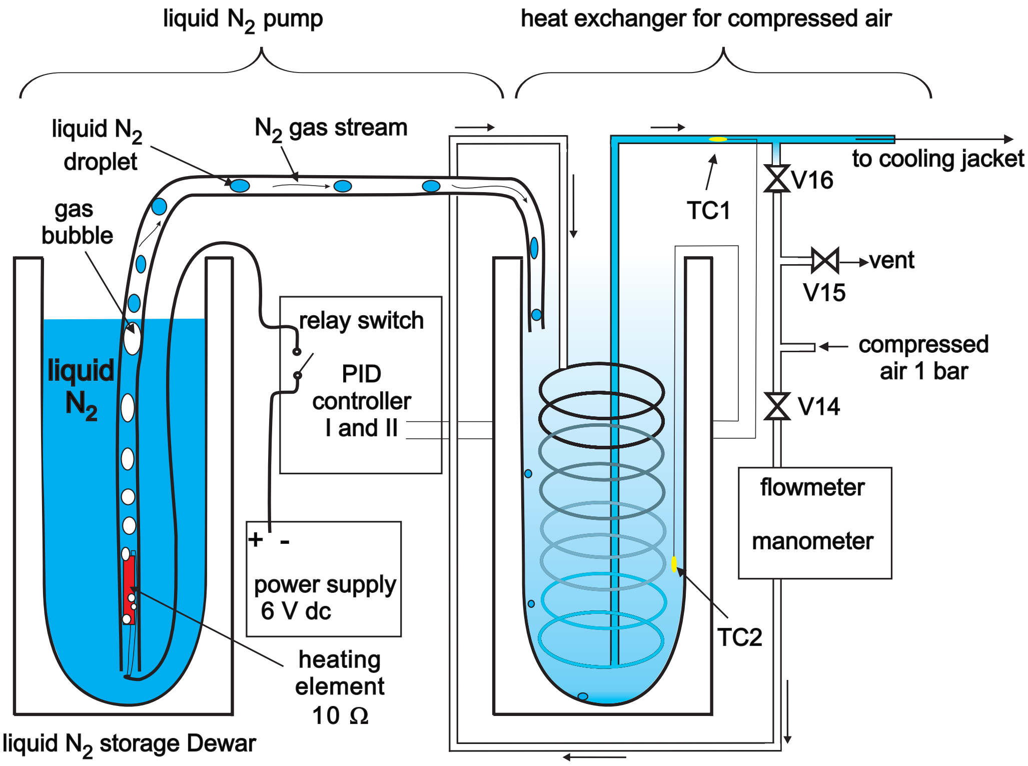

Figure 3-5 Schematic of the cooling apparatus for the sublimation vessel. The system consists of a pumping device transferring liquid nitrogen (LN) droplets from the 5 L storage Dewar to the heat exchanger unit. Within the heat exchanger the LN droplets vaporize and cool the copper coil in which the compressed air flows. With the PID I controller and thermocouple 1 (TC1) the set-point of the produced cold air stream can be adjusted. For the sublimation of ice samples usually a set-point of -120 °C is used with a volume flow of ~30-50 L min^{-1} at a pressure of 0.3-0.7 bar. Pressure and flow of the compressed air are manually adjusted using the flowmeter.

LN gets in contact with a warm surface (ΔT between LN and the object >100 °C) the cold liquid is quickly rejected from the surface and moves on its own vapor cushion, see *Linke et al.* (2006) for details. Hence, the heat transfer from the object to the LN droplet is largely inhibited if the temperature difference remains above a certain limit (Leidenfrost point). The small heating element at the bottom of the Dewar produces a gentle stream of nitrogen gas, which transfers the LN droplets through the tubing (see Fig. 3-5). This principle allows to pump LN droplets at -196 °C through a silicon tubing at near ambient temperature without vaporizing the LN within the tubing. Within the heat exchanger the LN droplets then vaporize and produce a large temperature gradient within the Dewar of the heat exchanger. To prevent overshooting of the cold air device, a second PID controller with TC2 stops the pump when the threshold is reached. The resulting temperature of the coolant gas measured at TC1 is fairly constant over time with changes being <2 °C. Although the principle of this simple LN pump was already used by *Brenninkmeijer* (1982), yet no application made use of actually pumping LN through longer tubing to link a LN reservoir with a second external device allowing more versatile applications.

Note that a similar LN pump is also used to transfer LN to the external water trap (Chapter 3.5.6) and to automatically refill the cryofocus trap in the cracker-GC system (Chapter 3.6.6).

To warm up the sublimation vessel after a sample is completed, the cold air stream is interrupted by closing V14 and opening V16 (see Fig. 3-5). Then the compressed air bypasses the heat exchanger and directly flows to the sublimation vessel to melt the condensed ice. With this bypass mode, the ice in the sublimation vessel is melted in ~20 min and the water can be removed to begin the next sample procedure.

3.5.4 Sublimation vessel, internal water trap, and IR lamps

As stated by *Güllük et al.* (1998) and *Siegenthaler* (2002), degassing and adsorption of CO_2 from glass and metal surfaces and polymer O-rings are critical issues and they reduce the overall precision of the methods. As pointed out above, the main advantage of our approach lies in the compact design combining the sublimation of the ice and the close-by removal of the bulk water vapor into one single glass vessel (shown above in Fig. 3-1). The vessel dimensions are: length 121 mm, outer diameter 33 mm and equipped with a DN40 CF flange to be mounted to a DN40 double feedthrough (Caburn, UK). On the head of the flange, a pressure transducer (‘P_S‘, 100 Torr max, Leybold Vacuum, Germany) is mounted to control the H_2O vapor pressure during the sublimation. Furthermore, an inlet capillary to continuously introduce a whole air standard is mounted on the feedtrough (see whole air reference inlet in Chapter 3.5.8).

The above mentioned dimensions of this glass vessel were chosen for an optimized use of the available segment of the ice core (see Fig. 3-3). Note that the EPICA cutting scheme for the gas piece does not allow for larger sample sizes as were available in the older studies, where large cross sections were used (*Fischer et al.,* 2003).

The total volume of this sublimation vessel with the associated joints and valves amounts to about 200 mL. For comparison, the devices used by the previous studies were considerably larger with 1700 mL reported by *Siegenthaler* (2002). Note that for convenience the volume of the devices is used here to roughly compare their areas. Since the sample size of *Siegenthaler* (2002) was comparable to the ~30 g used in this work, with this new approach a considerable reduction of the specific surface area of the apparatus was achieved (i.e. the surface area of the sublimation apparatus exposed to the sample). Without this considerable reduction of specific surface area the necessary precision for $\delta^{13}C$ and CO_2 mixing ratio would not be feasible.

This single vessel approach results in two benefits: First, the total surface area is reduced and the number of potentially leaky seals or connections is kept at its minimum. Secondly, it optimizes the flow conditions of the water vapor, i.e. short distances and a large flow cross-section. Consequently, the pressure and temperature differences between the heated ice sample and the condensed ice in the internal water trap is only small due to the high conductivity of the cross section. This is mandatory to achieve a high sublimation rate at a low temperature and pressure to keep the ice surface well below -20 °C. Above this temperature a quasi-liquid layer might form on the ice surface allowing chemical reactions to take place (*Güllük et al.,* 1998; *Barnes et al.,* 2003).

The glass bulb of the vessel is made of 7052 borosilicate glass that is transparent to visual and infrared light (λ 0.3 to ~3.5 µm). Infrared light from four halogen bulbs (12 cm length, 500 W maximum at 230V, Osram) provides the energy for sublimation. The current for the bulbs is regulated by a continuous power supply to adjust the output to 200-400 W. Compared to the IR laser source used by *Monnin* (2000) and *Siegenthaler* (2002), here the simpler approach with halogen bulbs already used by *Güllük et al.* (1998) and *Wilson and Long* (1997) was preferred, as this set-up avoids problems associated with the optical window, e.g. leak problems due to temperatures change and only a partial sample consumption due to the unidirectional irradiation by the laser.

3.5.5 External water trap

Although the internal water trap already removes 99% of the water vapor, a special external water trap was needed to achieve the requirements for extreme low pH_2O. Furthermore, a compact design to minimize the total surface area of the system was also aimed at. In most dual-inlet and continuous flow applications (*Werner et al.,* 2001; *Ribas-Carbo et al.,* 2002; *Leuenberger et al.,* 2003) the sample gas stream is sufficiently dried by immersing a capillary coil into a dry ice/ethanol bath of about -80 °C. Since in this work the trapped CO_2 and simultaneously traces of H_2O are ultimately transferred into a miniature glass tube with a volume of only 15 µL, an H_2O amount of just 0.1 µg is sufficient to form a liquid phase. A rough calculation assuming laminar flow reveals that this amount is already co-transported to the CO_2 trap at a trap temperature of -100 °C. Note that the released air amount of ~0.5 mL STP per sub-sample occupies a volume of ~5000 mL at the operating pressure of ~0.1 mbar within the traps. The actual H_2O flux is further increased if a diffusive flux by a Knudsen flow regime (mean free path at 0.2 mbar ~1 mm; CO_2 trap i.d. 2 mm) is assumed instead of a laminar flow. In cases the H_2O flux exceeded 0.1 µg, liquid H_2O formed within the tube after the transfer from the CO_2 trap to the glass capillary and warming to ambient temperature. Further, the presence of a liquid phase within the tube leads to an isotopic exchange of oxygen between CO_2 and H_2O. This shifts the $\delta^{18}O$ values to more depleted values of up to 10‰. Therefore, temperatures as cold as -140 °C in the water trap are needed to suppress the formation of a liquid phase in the tube. Since classical cooling systems, e.g. dry ice/pentane slush (*Leckrone and Hayes,* 1997) are not readily suitable for this temperature range and closed-cycle He coolers are too bulky, a special trap cooled with LN droplets and cold nitrogen gas was developed. A second reason for the usage of a LN cooled water trap is the exclusion of solvents within the laboratory as traces of organic contaminants interfere with the IRMS measurement (*Francey et al.,* 1999; *Leuenberger et al.,* 2003; *Eyer,* 2004).

Function and operation of the external water trap:

The technical details of the external water trap are illustrated in Figure 3-6. Similar to the cooling system for the compressed air, droplets of LN are automatically pumped from a large reservoir into the trap, where the LN droplets vaporize on an extensive sheet of copper wire. In this application the silicon tubing that connects the LN pump with the trap has to be heated with a heating jacket. This was necessary since here LN is pumped upwards (~30 cm) from the reservoir to the above water trap. As the heat transfer from the tubing to the LN droplets is more intense in this case, the temperature of the tubing falls below the threshold of the Leidenfrost point and the pump stops operating properly. The heating jacket around the silicon tubing prevents this and allows upward pumping of LN to the external water trap (the heating jacket consists of ~1 m resistance wire (10 $\Omega\ m^{-1}$) wrapped around the silicon tubing, marked red in Fig. 3-6).

The temperature of the trap (¼'' o.d., 0.53 cm i.d., 20 cm length) is automatically controlled via a thermocouple plugged into a PID controller, which regulates the operation of the pump similar to the air cooling system of the sublimation vessel. On the downstream side of the trap, a pressure transducer (P_H, 10^{-4} -1 Torr max) is installed to monitor the gas flow during the sublimation. Since the trap is operated only 20 °C above the CO_2 saturation pressure during sublimation conditions, cold spots in the trap are of special concern. To detect potential cold spots, the trap was filled with CO_2 at 0.001 mbar and the trap was held at -140 °C for 10 min to observe a potential pressure drop due to condensation or adsorption of CO_2 onto the surfaces. Within the range of precision of the pressure measurement no loss of CO_2 was observed, thus, there is no indication that the trap shows cold spots.

Note that an exchangeable joint in the silicon tubing of the pump allows alternatively to direct warm pressurized air through the external water trap (Fig. 3-6). This is necessary to rapidly warm up the water trap to remove the condensed ice within the trap after the sample is finished. As the external water trap is highly insulated with several layers of insulating foil heat conduction from the outside would be too low to warm up the trap in a reasonable time.

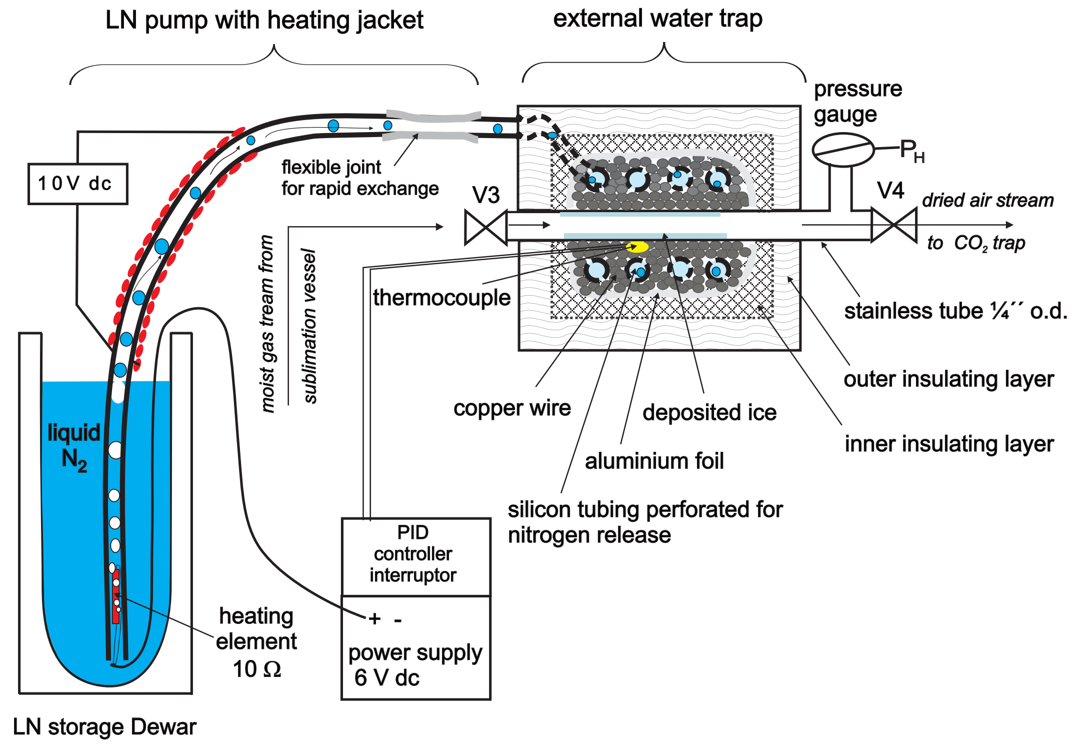

Figure 3-6 Schematic view of the external water trap with its associated pumping system and temperature controller. Liquid nitrogen is pumped from the storage Dewar to the watertrap using a heated silicon tubing. Within the external trap the LN droplets vaporize on layers of copper wire wrapped around the ¼'' tubing from the sublimation vessel. The large copper layers conduct the temperature to the inner part of the trap, where the temperature fluctuations become attenuated. Due to the large heat capacity of the copper layers the trap needs about one hour to establish isothermal conditions of -140 °C in the inner part (monitored by the thermocouple). The copper layers are covered with layers of aluminum foil to prevent condensation of atmospheric moisture that would quickly clog the trap. Several layers of insulating foil wrapped around the trap reduce heat conductance from outside. The flexible joint within the silicon tubing connecting the pump with the water trap enables a rapid warm up of the trap by flushing it with pressurized air at ambient temperature to remove the condensed ice after the operation.

3.5.6 CO_2 trap and glass capillaries for CO_2 storage

The dried gas stream (H_2O dewpoint -140 °C) which passed through the external water trap is directed to the U-shaped stainless steel tubing (⅛'' o.d., 0.085'' i.d., 10 cm length) immersed in LN (Fig. 3-7). Within this trap, CO_2 together with N_2O are efficiently condensed from the gas stream, which is then directed to the molesieve trap to remove the remaining gas components.

To achieve efficient trapping on the CO_2 trap, a ⅛'' tubing was used here instead of ¼'' tubing used for all other sections within the sublimation and trap system. Without this short ⅛'' section, the pressure of the gas flow within the CO_2 trap would be too low to condense CO_2 efficiently. The reason for this is that with decreasing total gas pressure the mean free path of molecules increases, i.e. molecules travel larger distances between collisions with other molecules or the cold surface of the trap. Further, also the partial pressure of CO_2 would then leave the region where CO_2 can be easily condensed at liquid nitrogen temperature. On the other hand, a too long ⅛'' tubing section would cause an undesirably large back pressure and long residence time of the released gas within the sublimation vessel and the external water trap. This situation has to be avoided for two reasons: First, loss processes, like adsorption of CO_2 on surfaces and co-deposition of CO_2 with H_2O in the water trap, increase with higher CO_2 partial pressure. Secondly, the amount of gas remaining in the sublimation vessel at equilib-

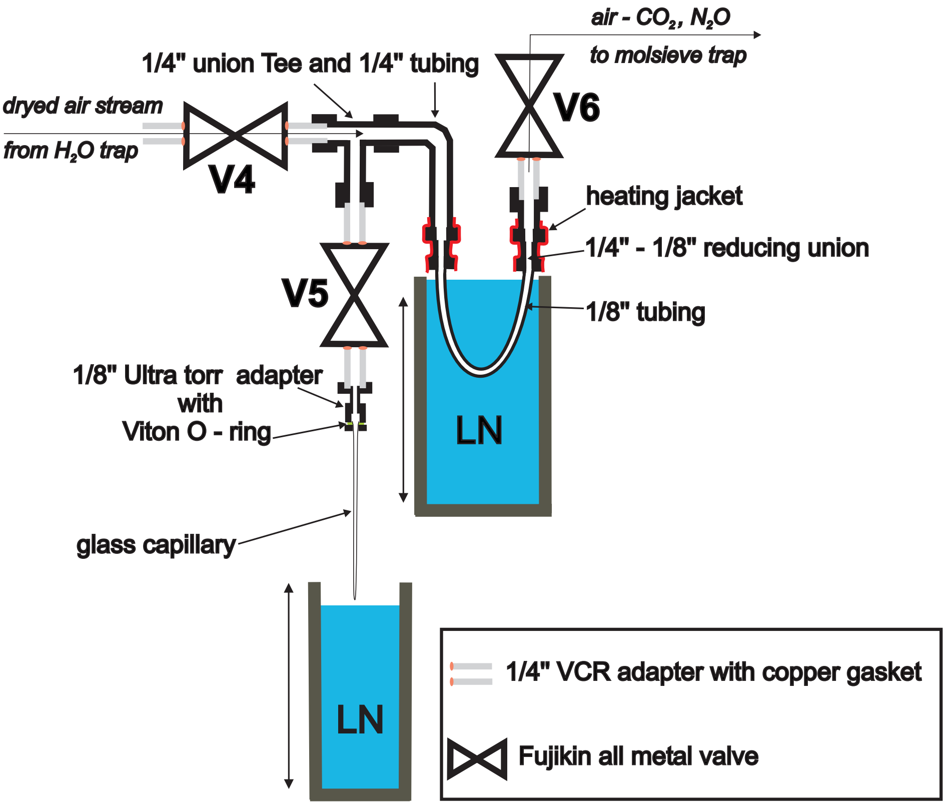

Figure 3-7 Scheme of the CO_2 trapping device. Shown are the positions of the Dewars for the situation during the trapping of released air with the CO_2 trap immersed in LN, while the glass capillary is not immersed.

rium flow conditions scales with back pressure thereby counteracting with the goal to achieve quantitative sample collection. Hence, length and shape of the ⅛'' tubing of the CO_2 trap was optimized to be as short as possible, while at the same time reach high efficiency and a suitable shape to be immersed in a LN Dewar. As the viscosity of gases roughly increases with the square root of temperature, the sections of the ⅛'' tubing that are not immersed in LN during trapping have to be minimized. The optimal solution was found using a U-shaped trap of ⅛'' tubing with 10 cm length, which can be immersed in LN just a few mm below the ⅛-¼'' reducing union fittings (Swagelok, stainless steel). With this design almost ~9 cm of the total length of 10 cm are actually immersed in LN to condense CO_2 off the gas stream while only ~1 cm of the ⅛'' tubing are above the LN level. A heating jacket keeps the two ⅛-¼'' reducing unions at ambient temperature while the ⅛'' tubing of the trap is immersed in LN (Fig. 3-7). If not heated, the unions would cool down to almost LN temperature while the trap is immersed in LN and due to their larger thermal inertia compared to the thin ⅛'' tubing, warming-up would be considerably retarded during the CO_2 transfer into the glass tube.

Attached to this trap is a long glass capillary, to which the trapped CO_2 is transferred and then a section of 2 cm of this capillary is flame-sealed and the closed tube is stored for the later steps (see Chapter 3.6). Hence, the glass capillary and the resulting tubes act as the link in this off-line coupling.

As tube material standard Pasteur pipettes are used (length of the capillary 12 cm, o.d. 2 mm). Prior to usage the glass capillaries are cleaned in an ultrasonic bath with diluted HCl and thoroughly rinsed with deionized water to eliminate any organic and inorganic contaminants from the glass surface. The capillary's tip is flame-sealed and the outer diameter of the open end is adjusted to 3 mm and rounded with a hand torch to fit a ⅛'' o.d. Cajon-Ultratorr adapter. With this adapter the glass capillary is connected to the ¼'' tubing leading of the V5 valve, which links the CO_2 trap with the glass capillary (see Fig. 3-7).

3.5.7 Molesieve trap - air content measurement

Although the main purpose of the described analysis method of this work is the precise determination of $\delta^{13}C$, measuring the CO_2 mixing ratio on the same sample is very useful. First, it is a valuable tool to detect contamination or loss processes during the whole analysis. Secondly, for a quantitative interpretation of global atmospheric $\delta^{13}C$ changes, it is imperative to have the data of both the isotopic and the mixing ratio at the same time interval. Although highly resolved time series on CO_2 mixing ratio are available for the Holocene (*Monnin et al.,* 2001; *Siegenthaler et al.,* 2005a), temporal resolution is still poorer during MIS3 and older periods. Further, uncertainties with dating or a mismatch in the ice-age/gas-age difference of two cores deteriorate the precision necessary to entangle global carbon fluxes.

With the mass spectrometer providing the amount of CO_2 via the m/z 44 peak intensity, the corresponding amount of air is determined volumetrically with the molesieve trap. Briefly, a glass tube (¼''o.d, ⅛'' i.d.) is filled with 5 Å molesieve pellets. Before each use and for weekly regeneration, water is removed by heating the molesieve to ~200 °C for some hours. During the sublimation, the molesieve is immersed into LN and acts like a normal vacuum pump. At -196 °C the equilibrium pressure of a loaded molesieve (1 mL STP air) is <0.0020 mbar (P_M pressure transducer, 10^{-4} - 1 Torr max). It is therefore the molesieve 'pump' which drives the pressure gradient from the sublimation vessel through the water trap and the CO_2 trap to the molesieve trap. Typical values during the sublimation of an ice sample are ~0.4 mbar within the sublimation vessel, whereby the partial pressure of H_2O dominates while the partial pressure of the air constituents account for only ~0.02 mbar. However, after the external water trap, pressure reading at the P_H transducer, the total pressure of ~0.09 mbar is entirely established from the air constituents as H_2O is removed from the gas stream. A pressure of only ~0.02 mbar is measured in the molesieve trap with the P_M transducer.

The quantitative release of the adsorbed air is accomplished by quickly heating the molesieve to 100 °C using an automatically controlled heating jacket. This device allows heating the molesieve from -196 °C to +100 °C within 40 s using a resistance wire (length 50 cm and 10 $\Omega\ m^{-1}$ operated with 7 V). After the heating jacket is switched on, the temperature is rapidly rising until the set-point is reached at the thermocouple and the PID controller interrupts the current and adjusts the temperature at +100 °C; i.e. a technical set-up similar to the external water trap. Note that the quick desorption of the air from the molesieve trap is of special importance since this step determines the time the trapping is interrupted and the released air from the sublimation buffered within the vessel. The desorbed air from the molesieve expands into an insulated 1L stainless steel cylinder (referred further on as expansion volume) and the temperature of the expansion volume is read out using a thermocouple (see Fig. 3-1). Insulation of the expansion volume and monitoring its actual temperature is essential since temperature fluctuations would otherwise bias the pressure at the P_M transducer, thus, the calculated CO_2 concentration. After the desorption from the molesieve, the air occupies the entire volume between the valves V6 and V9, framed by the green rectangle in Figure 3-1. However, only the temperature of the insulated expansion volume is sufficiently stable and is measured for the temperature correction of the pressure. Especially the temperature of the tubing section between V6 and V7 cannot be stabilized fast enough. However, the enclosed volume of this section is only ~20 mL, thus, small compared to the 1000 mL of the temperature controlled expansion volume and negligible within the measurement precision of temperature and pressure.

A typical ice sample (~6 g per sub-sample) with a gas content of about 0.5 mL STP results in a pressure of 0.5 mbar within the expansion volume. After the molsieve trap reached the set-point of +100 °C at ~40 s, the desorption is quantitative and the pressure becomes stable (trend <0.0005 mbar min^{-1}) at the time of read out at 60 s. This design allows a precision of the total air content measurement of <0.5%, which corresponds to <1 ppmv for the CO_2 mixing ratio.

3.5.8 Whole air reference inlet to introduce whole air standards

The prerequisite of accurate measurements for isotope analysis is the so called 'principle of identical treatment', coined by *Werner and Brand* (2001). To fulfill this requirement, one would need at best artificial ice with ~10% air inclusions of known composition.

This reference material is not available as this would imply to reproduce the sintering conditions of snow to bubbly glacier ice in the laboratory. At low temperatures this close-off process takes at least decades to proceed (see Chapter 2.1). Speeding up this process about several orders of magnitude would either imply increasing the temperature near to melting point and working with a high pressure apparatus. As an isotopic fractionation of the enclosing air is very likely to occur under these conditions, a thus produced reference material would not be trustworthy enough for the aimed high precision measurements.

The next best referencing strategy is a whole air standard introduced during the sublimation of a blank ice cube. This treatment mimics the air release from the sample during the sublimation as closely as possible. Except for the actual gas release off the ice surface, all subsequent steps are identical for reference and sample.

For the calibration of the system a high pressure cylinder with synthetic air (Air Liquid, Germany) is used as the whole air working standard (referred as 'air standard'). Its precise gas concentrations and the isotopic composition of CO_2 have been measured at the Institute for Environmental Physics at the University of Heidelberg by I. Levin (CO_2 = 277.7 ppmv; $\delta^{13}C$ = -2.75‰; $\delta^{18}O$ = -14.72‰; N_2O = 233 ppbv).

Since the release of the trapped air during sublimation is a slow and continuous process, a reference inlet was needed to introduce a constant flow of compressed air into vacuum conditions without fractionation. Admitting air into vacuum without isotopic fractionation is not trivial. Generally, during the expansion from the high pressure region to vacuum conditions the physical principles of gas flow change dramatically. With decreasing pressure three flow regimes are distinguishable: (1) viscous flow, (2) Knudsen flow, and (3) molecular flow. The prevailing regime at a given point can be classified by the ratio of the molecules' mean free path to the cross section diameter of the tubing. Pure viscous flow occurs below a ratio of 0.1, and pure molecular flow above a ratio of 10, with Knudsen flow in between. Both Knudsen flow and molecular flow cause large a fractionation (up to 4.4‰ for diffusion of CO_2 in air) of the gas species and their isotopes since diffusion of the molecules is mass dependent. This produces elemental and isotopic gradients within the tubing, which was already noticed in the early days of mass spectrometry (*Honig,* 1945; *Halsted and Nier,* 1950).

Consequently, the device to transfer gas from a high pressure reservoir to a vacuum apparatus must avoid net fractionation between the reservoir and the admitted gas. This can be achieved when the flow velocity within the tube is high enough to overcome any back diffusion to the reservoir. The developed reference gas inlet system consists mainly of four components (see section enclosed by red rectangle in Figure 3.1):

(1) reservoir with the compressed air standard
(2) pressure regulator
(3) inlet capillary
(4) purge port with two vent capillaries

(1) The working standard is stored in a 1000 mL stainless steel container at 500 kPa and is filled from the high pressure cylinder. (2) With a pressure regulator (PR1; Porter 8286-SMVS-30, USA), the air pressure and thus the flow through the capillary can be adjusted from 100 to 350 kPa to cover the rates of air release during the sublimation of ice samples (0.02-0.06 mL STP min^{-1}). (3) The inlet capillary has an i.d. of 0.05 mm, thus, the same i.d. as the CO_2 reference gas capillary of the MAT 252 and provides a viscous flow regime at this pressure range. The length of the capillary is adjusted to 2.5 m to attain flow rates of 0.02-0.08 mL STP min^{-1} at corresponding pressures of 100 to 350 kPa. Usually, an air pressure of 250 kPa is set at the pressure regulator (PR1) leading to a flow rate of 0.04 mL STP min^{-1}. This rate is comparable to the rate with which air is released during the sublimation of ice core samples. The exit of this capillary within the sublimation vessel is only a few mm above the ice cube to release the air standard in a position similar to the sample. (4) The volumetric flow through this inlet capillary is too low to flush the reference system efficiently. Note the internal volume of the entire reference device amounts to ~ 7 mL, which is largely due to the dead volume within the pressure regulator. Therefore, the reference system is equipped with a purge port continuously directing air to the vent capillaries. Via a 4-port valve (V13,Valco, SS2H) the air standard can be either directed to a wide bore capillary (fused silica, 0.23 mm i.d., 1 m) for a rapid high volume flushing allowing for approx. 140 mL STP min^{-1} at 200 kPa. Or alternatively, to a narrow bore capillary (fused silica, 0.05 mm i.d., 15 cm) with which the system can be continuously flushed during preparation of air standard tubes. This flow is ~0.5 mL STP min^{-1} at 200 kPa. Permanently flushing the inlet system is a prerequisite for stable results, otherwise long lasting drift phenomena for ^{13}C and CO_2 and bad precision would result.

The inlet system is connected to the vacuum system via V10. This valve is kept closed when the reference inlet is operating and air standard being introduced to the sublimation vessel via the inlet capillary. Contrary, when an ice core sample is sublimated within the vessel, V10 is open to the vacuum side to evacuate the inlet system, with V11 and V12 being closed. The outer diameter of the union cross of the inlet system and the tubing between the ⅛'' valves V10, V11, and V12 (Swagelok SS-2H) is ⅛'' and connections are kept as short as possible, typically 3 cm. This helps to minimize the internal volume of the inlet and reduces the residence time of the gas within the reference system.

Considerations for the preparation of air standards:
With this reference inlet an air standard can be introduced during the sublimation of bubble free blank ice, thus, identical treatment of sample and reference is possible. However, at best two blank ice samples a day can be processed this way, resulting in ten single tubes. This is due to the fact that the sublimation of one blank ice sample results in five air standard tubes and a cycle of opening/closing the sublimation vessel followed by long pumping takes about 3 hours.

To overcome this inherent drawback, additionally a more rapid procedure is used to provide air standard tubes. This was useful to test the performance of the system at different temperature, pressure, or flow conditions during the development of the apparatus. Instead of admitting air while the blank ice is actually sublimating using the IR lamps, ice is held at the same temperature and pH_2O conditions as during the actual sublimation, i.e. -27 °C corresponding to a H_2O partial pressure of ~0.5 mbar. However, the blank ice is not 'consumed' since the sublimation vessel is held isothermal without temperature differences between blank ice and cold air steam. Hence, using this procedure termed 'static', the time consuming replacement of the ice is not necessary. With this procedure, pressure and flow within the traps are identical to the conditions during sublimation, yet the H_2O pressure gradient and the H_2O flux within the sublimation vessel is lacking. Further, the glass vessel is not irradiated during this procedure (see Chapter 3.7.2 for a detailed description of air standards). Both approaches were used during the development of the analysis as well along with the processing of ice core samples (see Chapter 3.9 for the results of air standard measurements).

3.6 The tube cracker-GC-IRMS system (CF-IRMS)

The following paragraphs deal with the development and functionality of the tube cracker-GC system (Fig. 3-2). First, the reasoning for a gaschromatographic purification of the extracted gas sample prior to the IRMS analysis is stressed, followed by the general idea of the measurement scheme. Finally, the technical components necessary to realize this scheme are described.

Briefly, the tubes with the extracted gas sample, consisting mainly of CO_2 and N_2O, are opened ('cracked') using a tube-cracker device and the sample is entrained in a He carrier. The gas stream is dried, cryofocused, and CO_2 is separated from N_2O and other impurities using gas chromatography. The purified CO_2 peak is then introduced to the ion source of the IRMS, where the ion currents of mass 44, 45, and 46 are measured.

3.6.1 Reasoning for a GC separation of the extracted gas sample

As outlined above, the entire analysis method for measuring δ^{13}C on ice core samples was split into two separate lines, thus, off-line coupled. Within the vacuum line of the sublimation apparatus, CO_2 and N_2O are separated from the bulk air components (N_2/O_2/Ar) using cryogenic traps. Afterwards, gas chromatography is used to separate CO_2 from N_2O and organic contaminants.

N_2O is isobaric to CO_2, i.e. within the ion source of the IRMS it produces ions with masses 44, 45 and 46 like CO_2 does, but at different isotope ratios. A typical mixing ratio of CO_2/N_2O in air of ~1000 causes a depleting of the δ^{13}C of CO_2 by about 0.3‰. For dual-inlet measurements this effect can be corrected mathematically when the ionization efficiency of CO_2 vs. N_2O is empirically determined and the CO_2/N_2O mixing ratio is well know as it is the case for modern atmospheric air samples (*Ghosh and Brand,* 2004). For ice core samples, however, this correction is not easily possible. First, due to the sparse N_2O data at glacial times, and secondly, due N_2O in-situ production in dust-rich glacial ice samples (*Spahni et al.,* 2005). While GC separation of CO_2 and N_2O was already used for measuring δ^{13}C on atmospheric air samples (*Ferretti et al.,* 2000; *Ribas-Carbo et al.,* 2002), for ice core samples this technique is applied here for the first time (see Chapter 3.6.5).

As discussed in Chapter 3.2, nearly all authors who analyzed δ^{13}C on deep ice cores reported problems during the mass spectrometric analysis caused by drill fluid contamination[19]. Since some components of the drill fluid behave physicochemically similar to CO_2 during the extraction process, minute traces can simultaneously reach the ion source together with CO_2. During the course of the early development for this work, ice core samples were measured without GC separation resulting in excessively high m/z 45 and 46 traces yielding highly enriched δ^{13}C ratios. As an example, Figure 3-8 shows the measurement of a contaminated ice core sample. A δ^{13}C value of +1420‰ was calculated for this sample illustrating the high sensitivity of even small amounts of contaminants in ice core samples. Recently, *Eyer* (2004) demonstrated that probably the halogenated compound $C_2H_3Cl_2F$, or Freon141b, used as den-

---

[19] note, the use of drill fluid is compulsory during the operation of deep ice core drilling as otherwise the open drill hole would rapidly close due to ice flow. Contrary, shallow cores can be drilled 'dry'.

sifier in the drill liquid is producing these m/z 45 and 46 fragments during its disintegration in the ion source. Although a severe contamination can be easily detected by unusual positive $\delta^{13}C$ values and excluded from the data set, minor contaminations are harder to detect and require many replicates or a comparison of different cores. As a conclusion, gas chromatographic separation of CO_2 from N_2O and organic impurities from the extracted gas sample is indispensable.

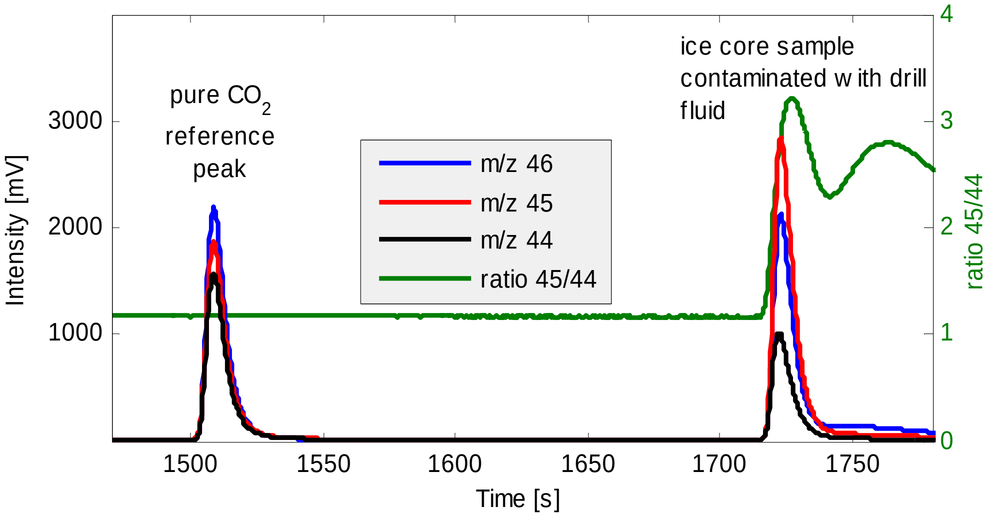

Figure 3-8 Example of a contaminated ice core sample (right) with a reference peak of pure CO_2 (left). The heights of the three mass traces of 44, 45 and 46 of the pure CO_2 peak reflect the natural abundance of CO_2 level with a ratio of 45/44 around 1.1 (right axis). In contrast, the contaminated sample shows highly elevated intensities of the mass traces 45 and 46 relative to 44, which produce the odd 45/44 ratio on the right axis. Note that the plotted voltage intensities for the mass traces 44, 45, 46 do not reflect the true abundance of these ion fragments. For convenience, the measured ion currents were converted to voltages using different resistors to produce signal ratios near unity (see Chapter 3.6.7).

3.6.2 General layout of the measurement sequence for the CF-IRMS system

The central principle of any stable isotope analysis is to compare the signal of a sample with that of a reference standard and to report the relative difference to this standard. The reason for this is that isotope ratio mass spectrometers are especially designed to compare signal ratios at an utmost precision, but not to precisely measure their absolute intensities (*Brand,* 1996). The key is to treat sample and standard in the course of the analysis in exactly the same way. This principle of identical treatment is applied during the classic dual-inlet measurement, commonly used for larger sample sizes. In an alternating sequence, the introduction of samples and standards to the ion source is rapidly switched many times, whereby their signal intensities are adjusted. While this rapid switching minimizes the temporal drift of the mass spectrometer, the adjustment of the signal intensities minimizes the dependence of the δ^{13}C value on the signal intensity (‘linearity’).

In contrast, accuracy and precision of CF applications are often diminished by the drift and a ‘linearity’ of the mass spectrometer or the periphery since the dual-inlet principle can only be roughly mimicked. The reason is that in CF applications short sample peaks arrive with the carrier gas flow at the ion source of the IRMS, instead of a continuous plateau in case of the dual-inlet. An active adjustment of signal intensities of standard and sample is not possible. To mimic the dual-inlet measurement principle for the CF approach developed in this work the following requisites have to be met:

(1) introduce reference peaks onto the cracker and treat them identically to a sample

(2) generate reference peaks with different intensities to cover the range of samples to correct for linearity

(3) make a single sequence of standard and sample as short as possible to minimize drift and allow measuring a large number of samples in a single session to profit from identical measurement conditions

(4) allow standards to be measured in a fully automated procedure to improve reproducibility with statistics and reduce personal attendance to the system

Based on these requirements, the tube cracker GC-IRMS system (shown in Fig. 3-2) was built and a measurement protocol for alternating standards and samples was developed (Fig. 3-9). To meet requirement (1) and (2), three different sizes of CO_2 pulses can be injected to the tube cracker via the reference loop (‘linearity loops’ L1, L2, and L3 in Fig. 3-9) to correct for the sample size effect (see Chapter 3.8). With the He carrier the CO_2 sample is then transferred to the cryofocus and to the GC, from which a purified CO_2 peak is directed to the ion source of the IRMS, where the $\delta^{13}CO_2$ value is measured. In between, the cracker is cleaned and prepared for the next sample or reference standard. A pair of one reference peak (EQ, see Fig. 3-9) and one sample (SA) takes less than 10 min to be completed allowing the repeated measurement of a large number of reference and sample pairs within a measurement session, requirement (3). Except for one step, the cracking of the sample tube, the entire analysis with the tube cracker-GC-IRMS system has been fully automated using pneumatic valves and actuators operated with a script embedded into the IRMS software, requirement (4).

The aim of preceding each linearity or sample peak with an equilibration peak (EQ) is to provide identical measurement conditions by equilibrating both the cracker-GC system and the ion source. Equilibrating the system always to the same CO_2 level is especially mandatory to achieve a reproducible signal intensity of mass 44 used to calculate the CO_2 mixing ratios. The peak area of a sample peak would otherwise be slightly influenced by the intensity of the preceding peak, i.e. affected by an memory effect. Further, the time series of all EQ peaks are used to calculate the $\delta^{13}C$ drift with time (see Chapter 3.8 for data processing).

As can be seen in Figure 3-9, in addition to reference and sample peaks, another type of CO_2 peak is admitted to the ion source at the very beginning and at the end of the measurement run. These std on/off pulses are fundamentally different to the other peaks as they are directly introduced to the ion source of the IRMS with a separate reference port and a second inlet capillary (see yellow box with Finnigan GP box and IRMS in Fig. 3-2). These std on/off pulses do not reflect the conditions within tube cracker-GC system, but only those of the pure IRMS measurement. Consequently, its principal use is to check the performance of the IRMS and together with the reference peaks admitted to the tube cracker system they allow to differentiate which part actually causes an observed $\delta^{13}C$ drift (see Chapter 3.8).

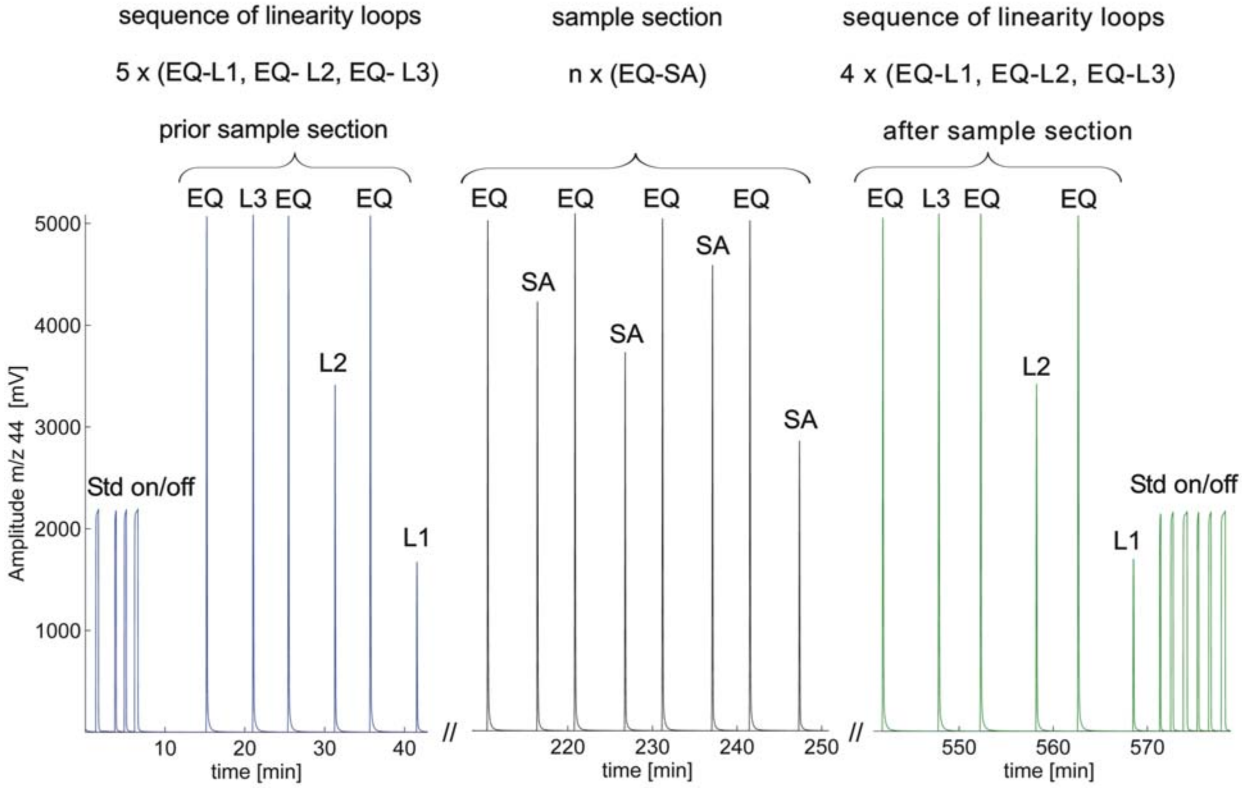

Figure 3-9 Measurement scheme for the tube cracker-GC-IRMS system. With std on/off reference pulses the performance of the sole IRMS machine without the tube cracker periphery is monitored before and after the actual tube cracker measurements. The performance (drift, linearity and reproducibility) of the tube cracker system itself is checked before (blue section) and after (green section) the sample tube measurements in a repeating sequence of reference peaks with different peak heights (linearity loops L3, L2, L1) to allow correction of linearity effects. Bracketed between these two linearity sections is the sample section, where the glass tubes with the extracted CO_2 from the ice core samples are processed. Each sample tube (SA) is preceded by a reference gas peak (EQ) to equilibrate the system identically for all tubes measured within a measurement session. Note that the SA tubes include both ice core samples (SA_{ice}) and air standards (SA_{air}) and tubes were randomized prior to the measurement to cancel out any bias during the measurement run. Typically around 20-30 tubes were measured together resulting in a total length of the IRMS run of up to 10 hours.

3.6.3 The tube cracker

The tube cracker device is the link between the sublimation extraction at vacuum and the CF-system at pressurized He. Within the tube cracker, the glass tube with the extracted gas is opened by bending it and its content is entrained into a continuous He carrier (Fig. 3-10). Until now, tube crackers were only applied in conjunction with dual-inlet or micro volume IRMS applications. The traditional design of tube crackers is a dead-end construction of two Ultra-Torr fittings with a flexible, corrugated steel tubing in between (*Des Marais and Hayes,* 1976; *Coleman,* 1981; *Norton,* 2005). Tube outer diameter dimensions normally used were ¼’’ or ⅜’’, and after breaking the tube at vacuum the gas was expanded into a bellow or condensed into a cold finger (*Kennedy and Kennedy,* 1994). As the latter techniques require rather large sample sizes (~10 to 100 times more than for CF approaches), use Ultra-Torr fittings with Viton O-rings, and operate at vacuum conditions, the traditional tube cracker design had to be adapted to meet the needs of this CF application:

- a flow through design and a small internal volume to permit rapid and quantitative transfer at a low flow rate
- a all-metal stainless steel construction and exclusion of polymer materials to minimize memory and surface effects

The tube cracker developed in this work is composed of a Swagelock reducing union, a 4.5

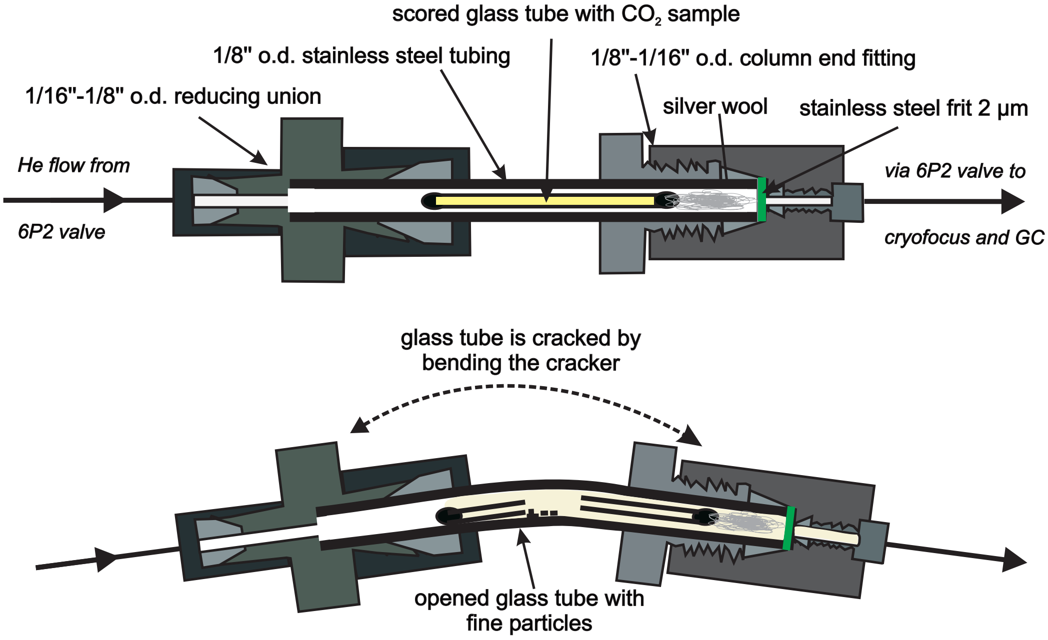

Figure 3-10 Schematic of the tube cracker device constructed to open small glass tubes in a continuous Helium flow. The top shows the cracker with an intact glass tube containing the CO_2 sample (yellow). Below, the cracker is shown after bending it a few degrees. The glass tube is opened and the released CO_2 being flushed out of the cracker. For comparison, the length of the glass tube is ~25 mm with an outer diameter of ~1 mm.

cm long stainless steel tubing, which is the flexible part and houses the glass tube, and a Valco column end fitting (Fig. 3-10 for technical details). To prevent glass particles from entering the down stream valves, the Valco column end fitting is equipped with a 2-µm stainless steel frit. A clew of silver wool fixes the glass tube within the cracker and facilitates the cracking of the tube. The tube is cracked while the cracker is manually bended using two pliers. The total internal volume of the cracker is only 160 µL, thus, only a single supply of He at a low flow rate (0.85 mL min^{-1}) is required to flush the sample to the cryofocus capillary. With two stainless steel capillaries the cracker is connected to the Valco 6P2 valve to allow for flexible handling during the cracking.

3.6.4 Device to introduce CO_2 reference gas to the tube cracker

To allow the identical treatment of samples and reference gas standards within the cracker-GC-IRMS system, pulses of CO_2 in He can be injected into the cracker. The reference gas assembly consists of three parts (red area in Fig. 3-2):

- mixing device to dilute CO_2 with He
- stainless steel reference loop (10 µL)
- Valco 6-port valve to either fill or inject the reference loop

With two pressure regulators (Porter 8286-SMVS-30, USA) the flow rate is set to ~0.1 mL min^{-1} for CO_2, and ~15 mL min^{-1} for He. Prior to their use, the two gases are homogenously mixed within a mixing chamber (15 mL stainless steel cylinder). By changing the flow rates of the two gases, the CO_2 concentration of the He/CO_2 mixture can be adjusted to a convenient value of ~1% CO_2, or ~2 nmol per 10 µL. This mixing device allows an adjustment of the signal height of the reference peaks without the need to switch between different loop sizes. To introduce a CO_2 pulse to the tube cracker, the Valco 6P1 valve is switched from the ‘fill position’ to the ‘inject position’ and the GC flow (0.85 mL min^{-1}) flushes the CO_2 from the reference loop via the 6P2 valve (in ‘transfer mode’) to the cracker device (Fig.3-2). The CO_2 reference gas used in this device originates from the same high pressure cylinder as for the reference port to introduce std on/off CO_2 pulses (see Chapter 3.6.7). Its δ^{13}C value is -6.97‰ vs. VPDB, thus close to the composition of the preindustrial atmospheric CO_2 value. Note that during the IRMS measurement and during the data processing the raw δ^{13}C values of the tube samples are referenced onto this CO_2 standard. However, during the final calculation the δ^{13}C values of the ice core samples were referenced onto the whole air standard (see Chapter 3.8).

3.6.5 Humidifier for the He carrier (GC flow)

High precision $\delta^{13}C$ measurements on CO_2 require low and constant water levels within the ion source of the mass spectrometer. During the ionization, H_2O and CO_2 form HCO_2^+ ions that are isobaric to $^{13}CO_2$ and cause an apparent sample enrichment (*Leckrone and Hayes,* 1998; *Meier-Augenstein,* 1999; *Rice et al.,* 2001). Therefore, the water vapor level of He carrier in CF-IRMS applications are generally kept as low as possible. Contrary to this common notion, a special humidifier device that saturates the carrier gas with H_2O had to be inserted upstream to the tube cracker. Note that the water vapor is removed from the carrier via a Nafion dryer after the carrier passed the cracker (see Fig. 3-2). During an early development stage of this method, CO_2 pulses admitted to the cracker via the reference loop resulted in reproducible $\delta^{13}C$ values, unfortunately, similar measurements of CO_2 prepared in glass tubes revealed a serious fractionation with poor precision (>1‰). The cause of this problem was identified as a strong isotopic fractionation occurring on the fresh glass surfaces after breaking the tubes in the cracker.

To do this, empty tubes were prepared and sealed off at high vacuum. These tubes were then inserted into the cracker and a first measurement was conducted, whereby a first CO_2 pulse from the reference loop passed the cracker flowing around the intact glass tube. Then, a second CO_2 pulse was admitted to the cracker while the empty tube was broken some seconds prior to the arrival of the CO_2 pulse at the crushed glass particles. Whereas no effect was visible in case of the intact tube, two effects were visible for the crushed tube. First, the area of the CO_2 peak was considerably reduced by up to 15%, depending on the breaking conditions, e.g. with more or less particles produced during the cracking. Secondly, and more severe for the isotopes, the $\delta^{13}C$ and $\delta^{18}O$ values were shifted by around +1‰ for $\delta^{13}C$ and around +2‰ for $\delta^{18}O$. This experiment indicated that an adsorption process with kinetic fractionation happened at the fresh glass surfaces. Although the tube cracker technique has been used for many decades, until now it was only used for dual-inlet Multiport measurements with CO_2 amounts a factor of 100 larger than in this study. Interestingly, isotopic fractionation connected with the adsorption of CO_2 on fine glass particles were already reported for a dual-inlet application (*Coleman,* 1996). Although the amount of glass particles produced from the cracking can be reduced by scoring the tube, however, due to the tiny dimensions of the tube (1 mm o.d.) this is not reliably enough. Consequently, the other option is to inhibit the CO_2 adsorption. This was accomplished by providing a strong adsorbent in excess to the He carrier: water vapor. The He of the GC carrier gas flow is bubbled through deionized water within a ¼’’ o.d. glass tube, similar to the humidifier used by *Leckrone and Hayes* (1997). The excess of H_2O compared to CO_2 (molar ratio H_2O/CO_2 ~20 within the cracker) then prevents CO_2 from adsorbing at the glass surfaces, accordingly, the fractionation phenomenon disappeared after the humidifier was installed. At room temperature, the humidifier causes a saturated H_2O partial pressure within the He carrier of 26 mbar.

As a consequence, an extra long Nafion dryer is needed to remove this unusually high load of water vapor from the He carrier before the stream enters the cryofocus capillary. The Nafion membrane (0.03'' o.d. and 50 cm length, Ansyco, Germany) houses in a ⅛'' o.d. glass tube and a countercurrent He stream of 5 mL min^{-1} dries the GC flow (Fig. 3-2).

3.6.6 Cryofocus and gas chromatographic separation of CO_2 and N_2O

To allow a gas chromatographic separation (Fig. 3-11) of the sample gases, a sharp peak has to be injected onto the GC column. For this, the CO_2/N_2O mixture flushed out of the tube cracker is cryogenically condensed on a cryofocus capillary. A short loop of deactivated fused silica (0.32 mm i.d., 20 cm length) is used for this purpose, which can be immersed in a LN Dewar using a pneumatic actuator controlled by the ISODAT software (see Fig. 3-2). The LN level of the Dewar is maintained constant during the ~10 hour measurement session. To achieve this, a LN refilling device was built based on the principle used for the cooling systems described in Chapter 3.5.3 and 3.5.5. The LN level within the Dewar is monitored using a thermocouple (Fig. 3-2). The automatic refilling of the LN Dewar is deactivated for the time

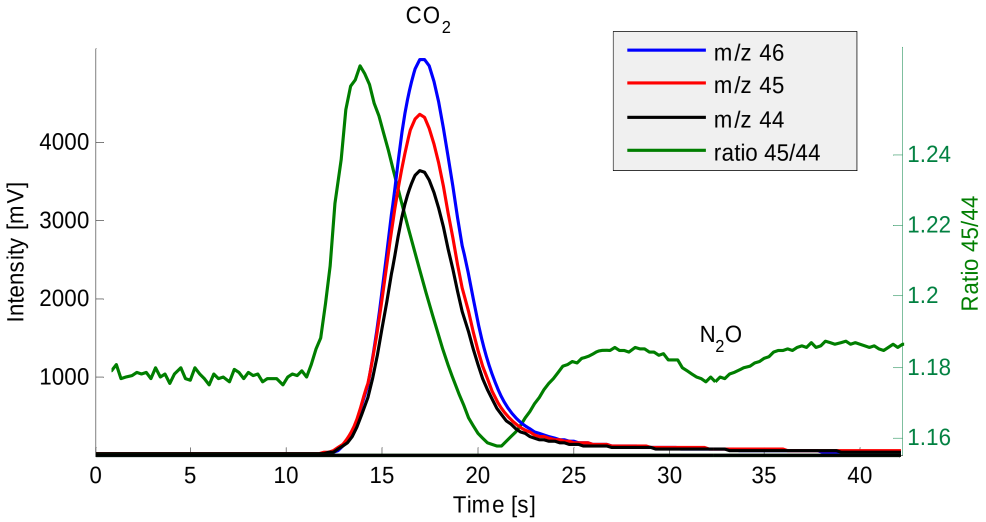

Figure 3-11 Chromatogram showing the separation of CO_2 from N_2O at a GC temperature of 70 °C. Due to the high mixing ratio of CO_2/N_2O of ~1000, the separated N_2O peak is not visible in the intensity plot (left axis), but it is visible as a bump between 28 and 37 s in the mass ratio 45/44 (right axis) as the isotopic ratio of N_2O is considerably lighter than CO_2. The characteristic up-and down swing of the isotopic ratio 45/44 is due to the chromatographic effect separating not only gas species, but also their isotopes whereby the heavier $^{13}CO_2$ molecules elute earlier from the GC column than the lighter $^{12}CO_2$. For the automatic integration of the separated CO_2 peak using the Finnigan software package ISODAT, start end endslope values of the mass trace 44 are defined. At this example, the peak integration starts at 11 s and ends at 26 s on this arbitrary time axis. Note that prior to the calculation of the 45/44 ratio, a constant off-set (50 mV for mass 44 and 59 mV for mass 45) was added to the ion beams to gain a smooth ratio at the edges of the peak when intensities are low.

the cryofocus is immersed in LN to avoid interference. This is accomplished using a relay switch controlled by the ISODAT software (detailed description in Chapter 3.7.3).

The sharp sample pulse from the cryofocus is directed to the GC, where CO_2 is separated from N_2O and drilling contaminants using a Porabond column (25 m length; 0.32 mm i.d.; 5 µm film thickness; Varian) isothermally at 70 °C (see sample gas chromatogram in Fig. 3-11). Contrary to the preferred GC temperature of 40 °C, used e.g. by *Ferretti et al.* (2000), 70 °C was used for this application. At higher temperatures the GC conditions were found more stable during the long measurement sessions spanning ~10 hours. At lower temperatures the $\delta^{13}C$ values of the reference gas peaks often drifted with time and showed a larger dependency on the peak intensity ('linearity' of the CF periphery). Although peak separation of CO_2 and N_2O is reduced at higher temperatures (for comparison: distance of peak maxima for CO_2-N_2O is 25 s for 40 °C, but only 13 s at 70 °C), operation at 70 °C was chosen due to more stable measurement conditions. The isotopic separation of CO_2 strongly depends on the temperature at which the GC was operated (Fig. 3-12). At 40 °C the chromatographic isotope effect leads to a fractionation of the CO_2 peak ranging from -100‰ to +100‰, which is large compared to the attained measurement precision of 0.05‰ after peak integration. As visible in Figure 3-11, the CO_2 peak shows a tailing due to adsorption effects of CO_2 in the GC system

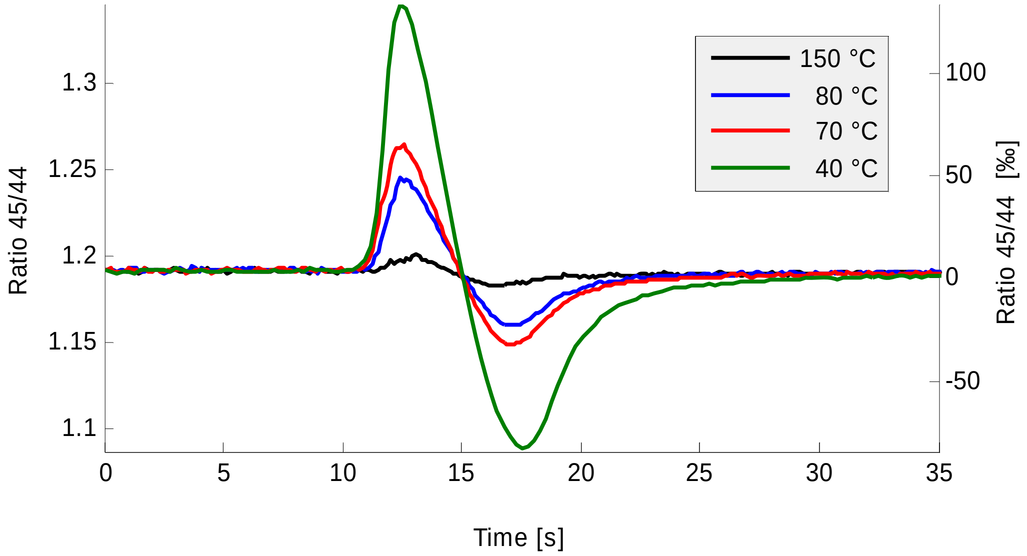

Figure 3-12 Comparison of the isotopic separation of CO_2 reference gas peaks due to the gas chromatography. The maximum peak intensity of mass 44 was ~5 V for all experiments at ~16 s on the arbitrary time scale of the x-axis. For higher temperatures the chromatographic isotope effect during the passage of CO_2 through the GC becomes smaller as the interaction of CO_2 with the column becomes smaller as well. The left y-axis shows the ion beam ratio of mass 45 and mass 44 (note, mass 45 beam is multiplied with 100 due to different resistors of the Faraday cups). On the right y-axis the 45/44 ratio was transformed to ‰ to visualize the strong chromatographic effect on CO_2 (45/44 / mean(45/44) -1) x 1000). Prior to the calculation of the 45/44 ratio, a constant off-set (50 mV for mass 44 and 59 mV for mass 45) was added to the ion beams to gain a smooth ratio at the edges of the peak when intensities are low.

as well in the ion source. Due to the peak tailing, the integrated peak area is ~97% and induces a small bias in the δ^{13}C value depending on the selected integration boundaries. With different peak intensities the integrated fraction varies according to the integration parameter, i.e. choosing a fixed end slope value results in a slightly earlier cut-off of the peak's tail, thus, a slightly smaller percentage of the integrated peak area. Due to this dependency of the peak integration on the peak intensity, usually a dependence of the δ^{13}C on the peak intensity is observed ('linearity'), which has to be corrected for (Chapter 3.8).

Since the isotopic fractionation is largest at 40 °C, adsorption effects should have a higher impact on the long term measurement stability, which might be responsible for the observed less reproducible conditions at 40 °C. On can speculate that at a higher GC temperature the memory effect decreases, i.e. the equilibration of the column is quicker and it saturates at a lower level. The shape and extent of the linearity effect is slightly changing from one measurement session to the other. Therefore, the system's behavior has to be determined for each session to account for altered measurement conditions. The effect of linearity or amount dependency of the δ^{13}C value is a common phenomenon with GC-IRMS applications (*Meier-Augenstein et al.,* 1996; *Hall et al.,* 1999; *Schmitt et al.,* 2003).

While the successful GC separation of CO_2 from N_2O can be visualized in the chromatogram as a small N_2O bump eluting after the large CO_2 peak (Fig. 3-11), unfortunately this is not possible in case of the drill fluid impurities. Since the Porabond GC column was introduced, no sudden distortion of the 45/44 ratio was observed any longer for ice core samples. As it is unlikely that all measured samples were free of this contamination, it must be assumed that these substances do not elute from the column at 70 °C, but are retained on the column. Possibly, these substances are flushed from the column in the 'stand by mode' when the GC temperature is set to 200 °C to remove water traces accumulated during the operation at 70 °C.

3.6.7 Open split and IRMS measurement

The open split acts as the interface coupling the pressurized He flow system with the high vacuum side of the ion source of the mass spectrometer. The GC carrier gas flow enters the open split of the GP-Interface (Finnigan, Bremen, Germany) and only a fraction actually enters the ion source of the IRMS (see Fig. 3-2 for details). As the open split operates at atmospheric pressure, a fixed flow rate of 0.3 mL min^{-1} is directed to the ion source, regardless of pressure and flow rate of the GC carrier. The remainder of the carrier flow is discarded to the atmosphere, i.e. is lost for the analysis. The split ratio is defined as the ratio of the total carrier gas flow to the flow directed to the ion source. This ratio usually ranges between 5 and 10 depending on the application's carrier flow. Applications developed for the δ^{13}C analysis of large atmospheric samples operate at a high carrier flow, hence, a high sample loss due to elevated split ratios, e.g. *Ferretti et al.* (2000) used 3 mL min^{-1} and *Ribas-Carbo et al*. (2002) 1.5 mL min^{-1}. For small ice core samples, a large sample loss at the open split has to be prevented to achieve the required precision of <0.05‰. *Leuenberger et al.* (2003) used 1.0 mL min^{-1} and in this work the flow rate was further reduced to 0.85 mL min^{-1}, resulting in a split rate of 2.8. This value is at the lower boundary of the proper working range of an open split. To prevent inward diffusion from the atmosphere, the open split is purged with 1.4 bar He with the standard setup of the Finnigan GP-Interface.

A Finnigan MAT 252 in continuous flow mode equipped with a universal triple collector having three Faraday cups tuned for the masses 44, 45, 46, is used for the measurement of the isotopic ratios δ^{13}C and δ^{18}O. The continuous ion currents from the three Faraday cups are converted to voltages using resistors with $3 \times 10^{8}\ \Omega$ for mass 44, $3 \times 10^{10}\ \Omega$ for mass 45, and $1 \times 10^{11}\ \Omega$ for mass 46. An integration time of 0.25 s was selected as sampling rate for the three mass traces.

3.7 Description on of the analysis procedure

The following section describes the entire analysis procedure in the laboratory for the ice core samples and the whole air standards. First the sublimation system, in which the air is extracted from the ice sample mostly by manual handling of the valves and the cryogenic traps. Secondly, the tube cracker-IRMS system, with which the stored sample tubes are transferred in a Helium flow, cryofocused, purified and finally measured. The latter system is highly automated, except the tube cracker, using pneumatic valves, which are operated by the Finnigan software ISODAT.

3.7.1 Sublimation extraction for ice core samples

Initialization and sample preparation

The first step of the sublimation extraction procedure is mounting a cleaned glass tube to the Ultra Torr fitting (see Fig. 3-7). Then V5 is opened and the air pumped to vacuum. To remove any impurities or water adsorbed on the glass surface, the tube is heated with a small torch. Prior to the next sample is loaded, the cooling system is started to cool down the sublimation vessel at temperatures of around -5 °C. To provide a clean surface, each ice cube has to be prepared separately in the cold lab in the following way: The ice cube is cut with a band saw to the dimensions 3.3 cm x 3.3 cm x 4.8 cm length. To fit this cube into the sublimation vessel with an internal diameter of 3.3 cm, the edges are rounded and trimmed with a stainless steel knife to a cylinder of ~3.2 cm diameter and weighing around 33 g.

Evacuation and cleaning of ice and vessel

The ice is inserted in the precooled sublimation vessel and the vessel then mounted to the flange via a copper gasket. With the cooling system a temperature of ~-23 °C is adjusted within the vessel. The air is pumped out of the vessel until a constant pressure reading is reached corresponding to the vapor pressure of the ice (pH_2O of ~0.7 mbar). The air is pumped off via V2 and V1 passing the large diameter LN water trap to freeze out any water vapor (Fig. 3-1). The removal of the water is essential to check the entire system for leaks. If water were not removed, the pH_2O would dominate the total pressure within the vacuum system and small leaks, e.g. at the flange, could not be detected. A two-hour pumping step at a pH_2O of ~0.7 mbar is followed since CO_2 sorption effects of the vessel surfaces is a critical issue and desorption from surfaces is most effective at high pH_2O pressures (*Zumbrunn et al.,* 1982; *Güllük et al.,* 1998). In parallel, a few mm ice sublimates from the sample surface and further cleans the ice core sample. After around 30 min pumping, the pressure of the high vacuum system (P_{VAC}) approaches $<2 \times 10^{-6}$ mbar as the temperature of the ice and the cooled glass vessel are in thermal equilibrium, hence, the sublimation is gradually declining. After one hour and provided the system is leak free, a final pressure of $<3 \times 10^{-7}$ mbar is achieved in case of bubble free ice, and $\sim 5 \times 10^{-7}$ for clathrate ice due to slow decomposition of the clathrates continuously releasing some air. After two hours, a few millimeters of ice have been removed and the surfaces of the vessel and traps are cleaned.

In between, the cooling device of the external water is started 60 min prior to its actual usage for the sublimation of the ice sample to reach the set-point of -140 °C±2 °C and allow temperature equilibration within the trap.

Preconditioning sublimation

The sublimation of the ice sample is started by (1) slowly rising the current of the halogen bulbs, thus providing energy for the sublimation of the ice sample, (2) simultaneously decreasing the temperature of the cold air stream to -120 °C and (3) increasing its flow rate, using the regulator for compressed air and V14 + V15, that a pH_2O of ~0.5 mbar results. This corresponds to an ice temperature of -28 °C being well below where a quasi liquid layer might form at the ice's surface. The gas stream liberated from the ice is now directed to the trapping system by closing V2 and directing the gas flow through the traps (V3-V9 being opened, V8 closed). In order to achieve pressure equilibrium within the system and a saturation of the surfaces with sample CO_2, sublimation is run for ~3 min without collecting the trapped air for further measurement. This step is called preconditioning. A detailed time table showing the manual sequence of switching of the valves and cooling and heating of the traps is given in the Appendix (Fig. 5-1).

Main sublimation

During the main sublimation the gas release from the ice sample is continuously operating and in total 5 sub-sample tubes are being collected in a repeated sequence. The details for this procedure are summarized in Figure 5-2 in the Appendix. Briefly, the released sample gases are collected for 11-20 min onto the CO_2 trap and the molesieve trap, which are both immersed in LN. The respective times for each sub-sample number (corresponding to tube No. 1-5), are listed in Table 3-3. When the trapping duration is terminated, trapping is interrupted and V3 closed for around 3 min. During this time interval the condensed CO_2 is vaporized from the CO_2 trap and finally transferred to the glass tube. This CO_2 transfer requires two stages to achieve 100% recovery: First, from the CO_2 trap to the top of the capillary and in the second step to the tip of the capillary. The second step takes rather long (6 min) to accomplish a quantitative transfer into the small diameter capillary. In parallel, the molesieve trap is automatically heated to 100 °C and the air is released to the insulated expansion volume. After pressure equilibrium, the pressure is read out at the P_M transducer and the temperature of the expansion volume is noted to allow a temperature correction. Both traps are then evacuated and again immersed in LN to cool them down to -196 °C, V3 and V4 are opened and the accumulated gas in the sublimation vessel is passed through the cold traps to begin the next collection cycle. Note that at this time, the second step of the CO_2 transfer within the tube has not yet been finished. After 6 min, the tube is closed at 2 cm length with a small gas torch. The whole sequence is repeated 5 times until the ice is almost consumed.

Table 3-3 Shown are the applied process parameters for the five sub-samples or tube numbers. As the ice sample continuously shrinks during sublimation, the time for sample collection has to be increased to achieve similar amounts of released air per tube. To prevent excessive sublimation durations, IR emission is successively increased and the cooling capacity adjusted accordingly to operate the sublimation at constant temperature.

sub-sample/ tube [No.]	trapping duration [min]	IR lamp power [W]	amount of air released [mL STP]	pressure of cooling system [bar]
1	11	200-240	~0.4	0.5
2	13	240	~0.45	0.5-0.55
3	15	240-280	~0.5	0.55
4	18	280-330	~0.55	0.55-0.6
5	20	330-400	~0.5	0.6

Regeneration of the system for the next ice sample

The following routine was applied to reinitialize the sublimation system for the next ice sample. Basically, the sublimation vessel and the external water trap are rapidly warmed up using compressed air at ambient temperature to melt the ice for removal.

- the automatic LN refilling for the cold air system and the external water trap are switched off
- an compressed air stream is directed through the external water trap (see Fig. 3-6), after thawing of the ice (~100 mg) condensed within the external water trap, V3 is opened and the water transferred to the sublimation vessel
- compressed air is directed through the cooling jacket of the sublimation vessel (V14 is closed, while V16 is opened; see Fig. 3-5 for details) thereby the condensed ice is melted and after opening the flange the meltwater is removed and the vessel dried
- the molesieve trap is constantly heated to 140 °C for 1 h to remove water traces

3.7.2 Procedure to verify the analysis with air standards

In the following, the preparation of air standards using the reference inlet is described. The aim is to introduce the air standard into the sublimation vessel and process this air identically to the air released from an ice core sample. Thus, with these air standards the analysis of ice core samples is simulated as closely as possible to verify the procedure and to calculate the total off-set of the analysis. As already stated in Chapter 3.5.8 two different methods were applied:

a) introduction of air standards *with* sublimation of blank ice

Generally, this procedure closely follows that for ice core samples described in Chapter 3.7.1 with the two following modifications.

- Instead of an ice core sample, bubble free ice is inserted into the sublimation vessel, which is cut and prepared identically to a sample. It was kindly provided by the University of Bern and was produced by degassing distilled water using a zone melting - refreezing approach (M. Eyer, personal communication 2005). This blank ice (‘Bern blank ice’) is free of visible air inclusions and expected to be free of CO_2.
- The reference inlet (see Fig. 3-2 for details) has to be preconditioned already 90 min prior to the start of the sublimation to remove stagnant gas and to equilibrate the surfaces. To do this, V10 is closed while V11 and V12 are opened. The inlet is flushed five times within 30 min by switching V13 for 10 s from the low purge to the high purge capillary with a

flow rate of ~140 mL min^{-1}. After repeatedly flushing the inlet at a high flow rate, V13 is set to the low purge flow to purge the inlet for 60 min at a flow rate of 0.5 mL min^{-1}.

The blank ice is then sublimated and the continuously introduced air standard processed to tubes as described above in Chapter 3.7.1.

b) introduction of air standard *without* sublimation of blank ice – 'static' conditions

In this alternative version, air standard tubes are processed under 'static' conditions, i.e. the ice in the sublimation vessel is not sublimating, but the ice is held isothermally at the same temperature and pH_2O conditions like during the sublimation. To do this, the description for version a) is followed, but instead of starting the sublimation, the temperature and the flow rate of the cold air stream are adjusted to -30 °C and 6 L min^{-1} to yield a pH_2O of ~0.4 mbar within the sublimation vessel.

Note that bubble free blank ice can be produced also 'in-situ' within the sublimation vessel by refreezing meltwater. If this is done carefully, the water slowly freezes from the bottom to the top and the freezing front expels any dissolved gases during crystallization without breaking the glass vessel. Blank ice produced with this refreezing method, combined with the 'static' conditions was the preferred procedure to process air standards. In a couple of experiments 'Bern blank ice' was used instead, and these air standards will be referred accordingly 'Bern blank ice' air standard.

3.7.3 Tube cracker-GC-IRMS measurement scheme

According to Figure 3-9, a measurement session is started with std on/off pulses generated with the GP-box reference port (see Fig. 3-2). The proper measurement with the cracker-GC system begins with a 'linearity section' followed by the randomized measurement of the sample tubes to prevent a bias resulting from the measurement order. After the measurement of sample tubes is completed, a second 'linearity section' and std on/off pulses terminate the session. The detailed time scheme describing the operation of the valves and the movement of the cryofocus actuator is provided in the Appendix (Fig. 5-3). Briefly a measurement cycle for a sample tube (EQ-SA) is executed as follows:

The LN Dewar of the cryofocus is automatically refilled until the set-point level is reached. The tube cracker is first flushed with the high cracker flow. After switching the Valco (6P2) valve to the 'transfer mode', the GC carrier flows through the cracker. The CO_2 pulses are admitted to the cracker by switching the Valco 1 (6P1) from 'fill' to 'inject' and reverse. Each time 10 µL with ~3 nmol CO_2 are transferred from the reference loop to the GC carrier and pass the tube cracker. For 90 s, the cryofocus capillary is immersed into LN, CO_2 is trapped, and after lifting the capillary from LN a sharp peak of CO_2 enters the GC column. After 30 s delay, Valco 2 is switched to the clean mode and the GC carrier bypasses the cracker. To load the cracker with a new tube, the cracker is opened, the glass shards of the last tube are removed and the next tube is carefully inserted. After closing it, the cracker flow sweeps the atmospheric air to the vent. Flushing the cracker in this 'clean-mode' takes 60 s. Valco 2 is then switched back to the 'transfer mode' and the GC carrier passes the cracker again. Through bending the cracker, the scored tube is broken into two pieces and the sample gas transferred to the cryofocus capillary immersed in LN. After cryofocusing the sample for 90 s, the capillary is automatically lifted and after a delay of 30 s the cycle begins again for the next EQ reference gas peak.

From this follows that the previous sample peak is still on the GC column, while the cracker is prepared for the following reference peak (or vice versa). The automatic procedure for the linearity section (EQ-L1, L2, and L3) is identical to the procedure described above, with the exception that CO$_2$ pulses are admitted to the cracker instead of cracking a tube. Moreover, the cracker is not opened in between. The injection of CO$_2$ to the carrier is executed at the precise time the tube would be cracked in case of the sample procedure. To produce reference peaks with different peak sizes (L1, L2, L3), the reference loop is filled and flushed several times accordingly. Note that due to the cryofocus the general peak shape for different peak sizes is identical for tube samples and reference peaks, which is a prerequisite for applying the identical treatment principle.

Following this alternating EQ-SA scheme, all sample tubes are measured. A final 'linearity section', to check whether the system's linearity changed during the analysis, completes the IRMS run. A measurement session is ended with a series of std on/off peaks to check the performance of the IRMS. Having both the information from std on/off and the linearity peaks admitted to the cracker system one can distinguish whether an observed drift phenomena is caused by the mass spectrometer or from the cracker system.

3.8 Raw data processing and performance of the CF-IRMS analysis

The following paragraph describes calculations applied on the raw data of the IRMS results to correct the measured tubes of ice core samples (SA$_{ice}$) and air standards (SA$_{air}$) for instrument drift and linearity effects. As stated above, a set of 20-30 tubes with extracted ice samples and air standards was analyzed within a single session (see Fig. 3-9). The calculated correction functions for drift and the linearity effect may slightly change from one session to another. Note that additional corrections for ice core samples (air standard off-set and correction for gravitational settling) are described in Chapter 3.9 and 4.4. The entire step by step correction scheme for ice core samples is given in Figure 5-4 in the Appendix.

3.8.1 $\delta^{13}C$

3.8.1.1 Corrections by the IRMS software

To derive internationally referenced $\delta^{13}C$ values from the three ion current signals m44, m45 and m46, four basic steps are necessary:

- definition of the integration boundaries (start and end slope of the peak)
- background correction of the ion currents
- $\delta^{17}O$ correction
- shift of the working standard to the VPDB scale

These steps were performed using the Finnigan software package ISODAT NT, with which the CF-IRMS system was operated. As shown above (Fig. 3-11), the CO_2 peak entering the ion source is almost of Gaussian shape and N_2O resides on the tail of the much larger CO_2 peak. The side effect of the GC separation is that the isotopic composition within the CO_2 peak is highly fractionated (Fig. 3-12). While the front is enriched with the heavier isotopologues, the tail is isotopically depleted. Consequently, the maxima of the three mass traces are shifted on the order of 0.2 s. Usually, a so called time-shift correction is made to align the maxima of the three traces prior to integration. Unfortunately, the time-shift correction embedded in the ISODAT software produced noisy results for the selected integration time of 0.25 s, which might be due to the coincidence that the time shift and the integration time have quite similar numbers. A shorter integration time, whereby increasing the number of data points, cannot be applied for long measurement sessions due to the software's limited storage capacity. Therefore, the time-shift correction was disabled. However, this can be justified by the fact that the off-set is rather small, and as reference gas peaks and sample peaks were treated identically, the off-set cancels out.

To define the integration boundaries for each peak, a threshold for the start slope of 1 mV s^{-1}, and 20 mV s^{-1} for the end slope was found to gain most reproducible results. A background signal of mass 44 of 2-3 mV was subtracted using the 'individual background' setting. Before $\delta^{13}C$ values are calculated from the integrated ion currents, the contribution of the oxygen isotope ^{17}O to the mass 45 has to be quantified, the so called 'Craig correction', (*Craig,* 1957). This correction is necessary since not only $^{13}CO_2$ contributes to mass 45, but also the rarest of three oxygen isotopes, ^{17}O. For this, the detection of three masses (44, 45, 46) is required to determine the $^{13}C/^{12}C$ ratio of CO_2. Prior to the calculation of the $\delta^{13}C$ value, the contribution of ^{17}O to mass 45 is calculated from $\delta^{18}O$ using mass 46 and the natural abundance ratio between $\delta^{17}O$ and $\delta^{18}O$ of 0.5146; for details see review by *Santrock et al.* (1985). These $\delta^{13}C$ values are initially measured against the isotopic composition of an internal reference gas or working standard. To report these values relative to the international VPDB scale the following equation was used:

$$\delta_{(SA\text{-}VPDB)} = \delta_{(SA\text{-}Ref)} + \delta_{(Ref\text{-}VPDB)} + \frac{\delta_{(SA\text{-}Ref)} \cdot \delta_{(Ref\text{-}VPDB)}}{1000} \qquad (3-1)$$

where $\delta_{(SA\text{-}VPDB)}$ denotes the δ value of the sample *(SA)* relative to the VPDB standard, $\delta_{(SA\text{-}Ref)}$ the δ value of the sample to the internal reference *(Ref)* ,and $\delta_{(Ref\text{-}VPDB)}$ the δ value of the internal reference gas against the VPDB standard. After these basic corrections, the data was exported to MATLAB where the data set of each measurement session was further processed.

3.8.1.2 Drift with time

A frequently observed feature during IRMS measurements is that the isotopic ratio is not stable, but rather drifts with time. To correct for this drift and identify its origin during the measurement, CO$_2$ reference gas of known isotopic composition was directed to the IRMS. During a measurement session two different types of standards were used: First, std on/off pulses, which do not pass the tube cracker system, but are directly introduced to the ion source. Secondly, reference peaks, which pass the entire tube cracker system (EQ peaks and linearity peaks L1, L2, and L3 with different intensities, shown in Fig. 3-9). While the std on/off pulses provide information only at two points (start and end of the measurement), a continuous time series spanning the 10 h measurement is available in case of the EQ peaks (Fig. 3-13). From this time series a slope is calculated to detrend the δ^{13}C values for the entire measurement. Although less robust due to only two tie points, a statistically identical slope is calculated

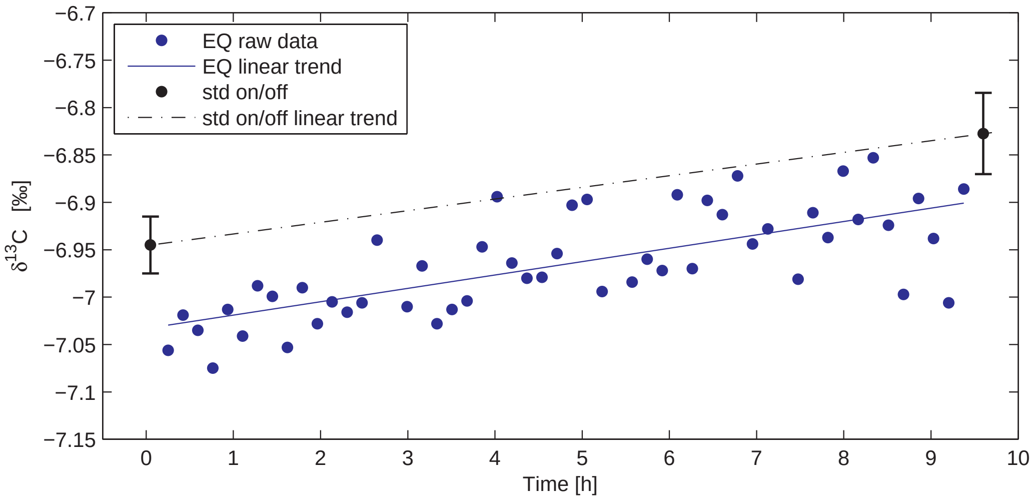

Figure 3-13 Comparison of the δ^{13}C drift observed during a measurement session of 10 hours. In this example the δ^{13}C values of EQ reference pulses (blue dots) linearly increase with time with a slope of 0.012‰ h^{-1} (blue line). The std on/off pulses directly introduced into the ion source of the IRMS at the start and the end of the measurement session show almost the same slope 0.014‰ h^{-1} (black dotted line). After the δ^{13}C values were detrended the standard deviation of the EQ peaks is 0.04‰. The observed off-set between std on/off and EQ measurements of ~0.07‰ is rather small given the fact that the CO$_2$ reference gas is treated completely different prior to injection to the ion source.

from the std on/off measurements. As visible in Figure 3-13, for this measurement both slopes were almost identical indicating that the observed drift is not due to the tube cracker system, but caused by the IRMS instrument alone.

3.8.1.3 Amount dependence of $\delta^{13}C$ values – 'linearity'

A second feature encountered in IRMS applications is that the isotopic ratio slightly depends on the peak intensity, i.e. the amount of gas introduced into the ion source. Within the isotope community this behavior is generally termed 'linearity', though the relation between $\delta^{13}C$ and the peak intensity is rarely a linear function, but often exponential (*Hall et al.,* 1999). To correct for this effect, reference peaks with three different intensities ('linearity' peaks) were admitted to the tube cracker (L1, L2, L3). Note that std on/off peaks cannot be used for this purpose as the std on/off procedure generates roughly a rectangular peak shape, whereas peaks transmitted through the cracker system have a Gaussian shape. Further, the latter peaks have the characteristic up and down of the 45/44 mass ratio due to isotopic fractionation induced from the GC separation (see Fig. 3-11). As both the peak shape and the isotopic fractionation within the peak influence peak integration and the resulting $\delta^{13}C$ value, sample and reference peaks must be identically in this respect (*Meier-Augenstein et al.,* 1996).

The left plot in Figure 3-14 illustrates the linearity effect of a measurement session with the tube cracker-GC-IRMS system. As shown above (Fig. 3-9), a section of linearity peaks is measured before and after the sample tubes, in total 9 peaks per size class. Their amplitudes range from ~1.7 V for L1 to ~5.1 V for the L3 peak, with the $\delta^{13}C$ value nonlinearly decreasing with increasing amplitude (-6.82‰ for 1.7 V, - 6.90‰ for 3.4 V, and -6.93‰ for 5.1 V). The data is best described with a first order polynomial fit of the logarithm of the peak amplitude (intensity of mass 44 = *i44*) marked with a blue line in Figure 3-14.

The $\delta^{13}C$ values of reference peaks and tube peaks were corrected for this linearity effect with Eqn. 3-1 as described previously (*Hall et al.,* 1999; *Schmitt et al.,* 2003):

$$\delta^{13}C_{corr} = \delta^{13}C_{raw} - m \cdot \log(i44) + c \qquad (3-2)$$

with $\delta^{13}C_{corr}$ the corrected $\delta^{13}C$ values, $\delta^{13}C_{raw}$ the detrended $\delta^{13}C$ values, *m* and *c* the coefficients of the polynomial, and *i44* the peak intensity (maximum amplitude in mV).

The corrected $\delta^{13}C$ values of the linearity peaks are shown in Figure 3-14 on the right plot. The precision of the reference peaks admitted to the cracker system and measured with the IRMS is on average 0.05‰ for the small peaks, and 0.03-0.04‰ for the larger peaks. According to theoretical assumptions of the ion current measurement in the IRMS instrument, the attained precision with the whole CF-IRMS system is about 2 times the theoretical shot noise limit calculated after *Merritt and Hayes* (1994).

Note that the amplitudes of sample tubes generally fall within a narrow range from 3 to 5 V for Holocene ice. As the linearity effect for high amplitudes is only small, the absolute δ^{13}C correction is rather small too and amounts on average ~0.01-0.02‰. For ice with low CO_2 concentrations, like from the glacial period, the absolute correction is ~0.03‰ as the sample amplitudes fall in the steeper range of the linearity function. As the coefficient of determination of the linear regression line with Eqn. 3-1 is on average ~0.7, the error introduced by the linearity correction is <0.01‰ for all samples.

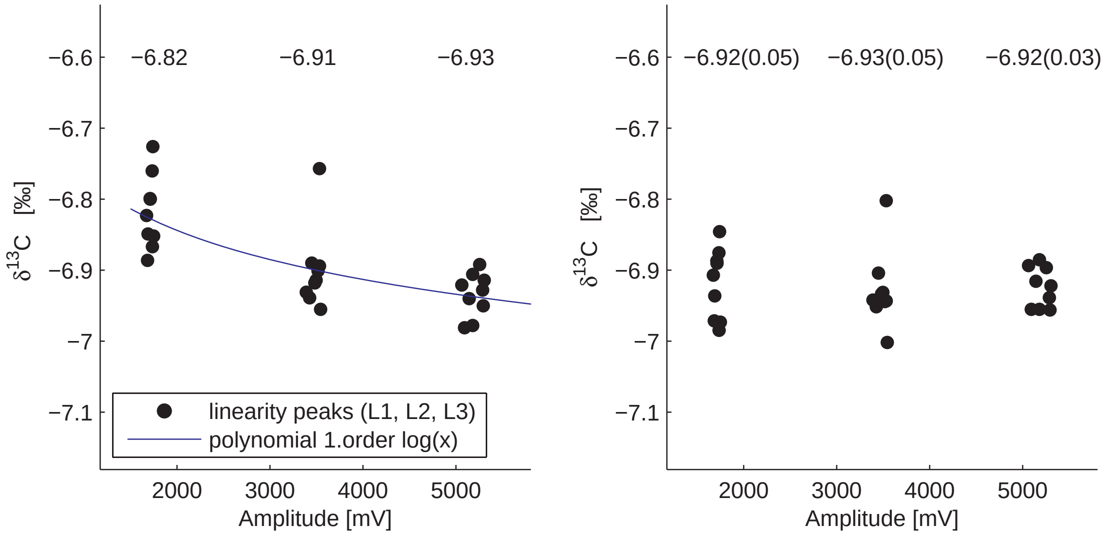

Figure 3-14 Left plot: dependence of the δ^{13}C value on the peak amplitude or signal intensity ('linearity effect'), numbers indicate the δ^{13}C means for the three peak classes (L1, L2, L3); the blue line illustrates the polynomial fit of the logarithm of the peak amplitude. Right plot: corrected δ^{13}C data with values for means and standard deviations (1σ) given on top.

3.8.2 CO_2 concentration

To calculate CO_2 concentrations for the extracted air of the ice samples, a similar approach as used by *Ribas-Carbo et al.* (2002) and *Eyer* (2004) was applied using the following equation:

$$CO_2(sample) = \frac{i_{sample} \cdot p_{air-std}}{p_{sample} \cdot i_{air-std}} \cdot CO_2(air-std) \qquad (3-3)$$

with *CO₂*(*sample*) and *CO₂*(*air-std*) denoting the respective CO_2 concentrations in ppmv for the ice core sample and the air standard, i_{sample} and $i_{air-std}$ the respective ion current intensities of mass 44 (peak maximum) for the sample and air standard; p_{sample} and $p_{air-std}$ the pressure reading of the expanded air measured with the pressure transducer P_M at the molesieve trap. Note that prior to the calculation, the raw pressure reading from the transducer was corrected with the temperature reading, T_{ex} (the thermocouple attached to the expansion volume in Fig. 3-1), for the influence of temperature variations using the ideal gas law.

For each measurement session 5-10 air standard tubes were prepared together with 15-20 ice sample tubes. To achieve a robust calibration, the $p_{air\text{-}std}/i_{air\text{-}std}$ ratio for each standard tube was calculated and after removing outliers the mean $p_{air\text{-}std}/i_{air\text{-}std}$ was then used in Eqn. 3-1 to calculate CO_2 concentrations for the samples.

Contrary to $\delta^{13}C$, where the systematic trend of the EQ peaks can be used to correct the raw $\delta^{13}C$ values of the sample tubes, the intensity of the EQ peaks cannot be used to correct the sample tubes in case of the CO_2 concentration. Although for some measurement sessions a trend was visible in the m44 intensity time series of the EQ peaks (see example in Fig. 3-15 left panel), no relation was found between the intensity of EQ peaks and the time series of the calculated CO_2 concentration of sample tubes. It can be reasoned that the scatter in the intensity of the EQ peaks does not reflect changes in the performance of the cracker-GC-IRMS system. Rather, the intensity changes of the EQ peaks probably reflect small CO_2/He mixing ratio fluctuations within the reference gas device (Fig. 3-2). Note that an observed trend in the m44 intensity does not necessarily correspond with $\delta^{13}C$ fluctuations also indicating two independent causes for both parameters (Fig. 3-15 right panel).

The relative standard deviation (standard deviation divided by its mean) for EQ peaks is ~0.4%, this translates to a standard deviation of ~1.1 ppmv assuming a sample with a CO_2 concentration of 280 ppmv. Since an additional factor independently contributes variability to the EQ intensity without adding variability to the sample measurement, the 1.1 ppmv standard deviation can be regarded as an upper estimation for the measurement error of the CO_2 concentration measurement. The second source of error for the CO_2 concentration (according to Eqn. 3-2) is due to the error introduced from the pressure reading (reading precision ±0.0001 mbar for an absolute value of ~0.5 mbar) including the uncertainty from the temperature

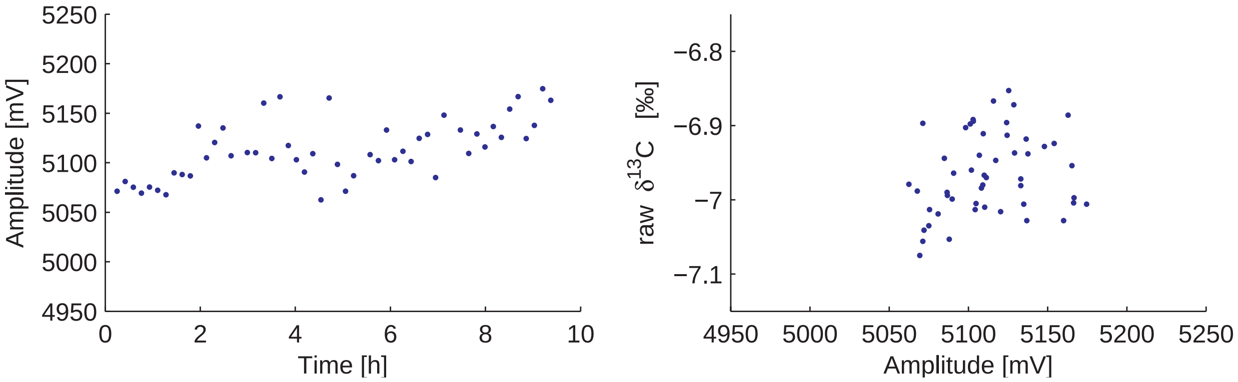

Figure 3-15 Left: time series of the m44 amplitude of the EQ peaks. The right panel shows the scatter of the $\delta^{13}C$ raw data with amplitude for the EQ peaks.

(reading precision ±0.1 K at 293 K). The uncertainty introduced from the reading precision is 0.1 ppmv for both parameters.

As the CO_2 concentration of the air standard is 277.7 ppmv, thus, close to average CO_2 concentration of the Holocene, this 1-point calibration approach of Eqn. 3-1 is justified to gain accurate values at least for the Holocene period. For the considerably lower glacial CO_2 concentrations a second air standard would be required to check whether the relation in Eqn. 3-1 still holds for low CO_2 concentrations. As the main focus of this study was δ^{13}C and its small scale variability, the accuracy of the absolute CO_2 concentration had second priority so far. However, more important are the relative differences among adjoining samples and among the five sub-samples collected during the sublimation extraction of one ice sample as those allow clues about small scale variability within the ice itself and help identify processes during the sublimation extraction.

3.9 Results from air standard and blank measurements

To characterize the performance of a newly developed analytical method usually three parameters are examined: (1) the reproducibility of repeated measurements of standards, (2) the absolute accuracy or deviation of the measured value from the expected 'true value', (3) the amount of analytical blank when no sample is processed. The following section summarizes the results of air standards admitted to the sublimation apparatus and discusses blank measurements. As pointed out above, air standards mimic the sample treatment as closely as possible and therefore serve as the reference on which the δ^{13}C values and CO_2 concentrations of ice core samples are based on. Air standards providing the reference base were prepared using the 'static' setting (Chapter 3.7.2) and were measured jointly with a set of samples. As these standards were processed and measured over a period of 4 months, this data set is used here (Chapter 3.9.1 and 3.9.2) to calculate the analysis reproducibility to which the reproducibility of the ice core measurements can be compared.

Besides these regular air standards, further experiments were conducted to investigate the influence of different settings during the admission of air standards (admission of air to 'blank ice' with and without sublimation and a variation of the flow rate). As illustrated in the left panel (Fig. 3-16) the rate with which air is released from ice core samples during the sublimation is not constant as it is for air standards. Therefore, to identify and estimate 'side effects' due to different air release rates between ice core samples and air standards a number of experiments were conducted. These results are discussed in Chapter 3.9.3.

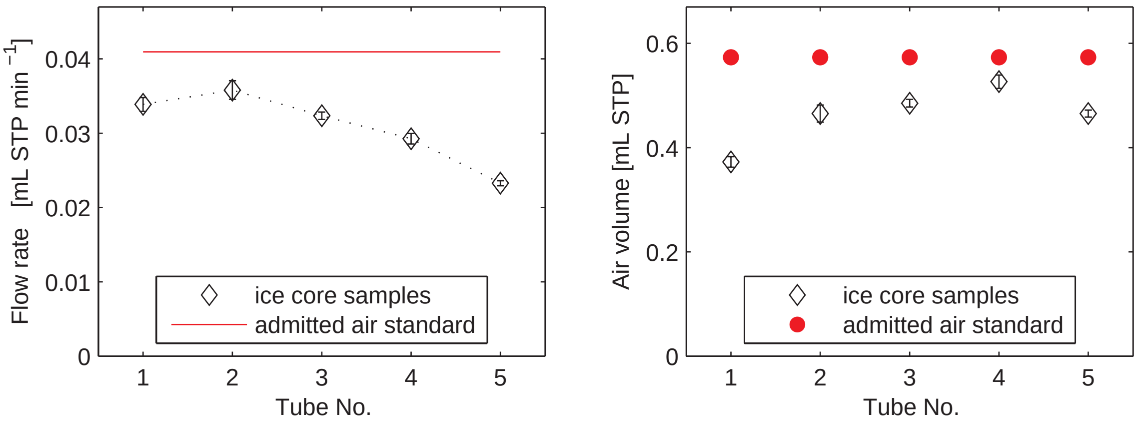

Figure 3-16 Comparison of procedural parameters between air standards (red) and ice core samples (diamonds, EDML 420 m). For the regular procedure to process air standards ('static' conditions), the flow rate was kept constant at ~0.04 mL min^{-1} (left panel). As the collection time for air standards was fixed at 14 min, a constant air volume of 0.57 mL STP results for all five tube numbers (right panel). This is slightly higher than the volume collected from Holocene ice core samples. As the ice sample is continuously shrinking during the ongoing sublimation the collection time is gradually increased (from 11 to 20 min) to compensate the reduced air release rate and gain comparable total air volumes (see Fig. 3-3).

3.9.1 Reproducibility of δ^{13}C and overall accuracy for air standards

Before the δ^{13}C data are analyzed for reproducibility and overall accuracy, a first step is to detect differences among the five tube numbers. To this end, the calculated off-set to the assigned δ^{13}C value of the air standard (Tab. 3-4) was subtracted from each data set to remove systematic differences among individual measurement sessions. Afterwards, the data sets were combined and the mean and standard deviation (1 σ) calculated for each tube number (Fig. 3-17, diamonds with error bars). If no differences were present among the five tube numbers, the means would be identical and the standard deviation zero. However, slight but

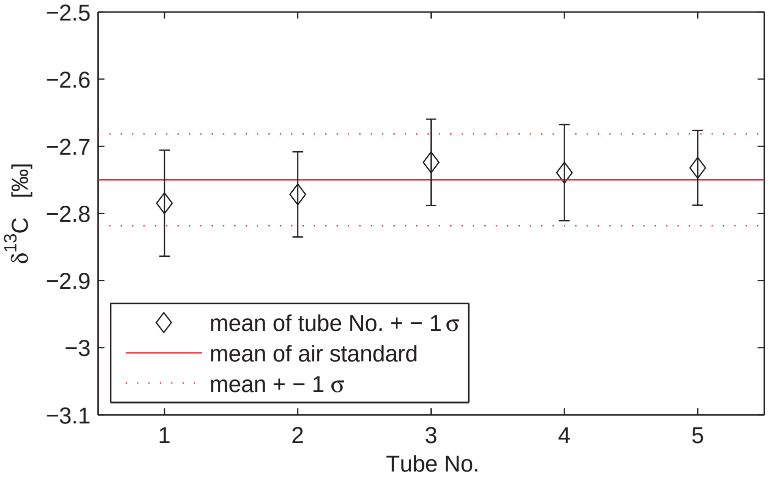

Figure 3-17 Compilation of δ^{13}C results of air standard measurements according to the tube number. The data was compiled from five measurement sessions (total n=33, after removing 2 outliers).

not significant differences can be observed in Figure 3-17. The red solid line marks the assigned $\delta^{13}C$ value to which the averaged standard deviation of the seven data sets for tube numbers 1-5 (average $\sigma \pm 0.07‰$ from Tab. 3-4) was added (dotted red lines). Though not a statistical outlier, tube number 1 is on average 0.05‰ more negative than the other four tubes. More pronounced is this anomaly for the corresponding CO_2 concentration as visible in Figure 3-18. As the CO_2 concentration is lower for tube number 1, a contamination can be readily excluded. More likely is a loss process associated with the transfer into the very tip of the glass capillary; for tube number 1, the glass capillary is longest, hence, diffusion into its tip takes longer to achieve 100% than the following tube numbers as the capillary is getting shorter. Another possibility for the deviation of tube number 1 would be an isotopic fractionation associated with a loss due to adsorption on unsaturated surfaces.

From this first data analysis it can be concluded that the five tubes do not show considerable differences among the tube numbers. For the second step, the means and standard deviations from each data set were calculated over all five tube numbers to yield a measure to describe the reproducibility and accuracy of the method. Note that for this calculation the off-set to the assigned value was not subtracted since this constitutes the overall accuracy of the analysis technique.

The results are summarized in Table 3-4. The standard deviation (1σ) ranged between 0.05 and 0.08‰ with an average of 0.07‰. When tube number 1 is removed, i.e. number 2-5 only, the standard deviation slightly improves (0.06‰). To characterize the performance of the sublimation extraction, one can compare the reproducibility of these air standards with the reproducibility of the CO_2 reference gas pulses of similar peak size. As shown earlier (Chapter 3.8.1), the measurement error of the cracker-GC-IRMS system alone was 0.04-0.05‰ for pure CO_2 peaks. Hence, only little variance was added from the additional steps associated with the introduction of the air standard to the sublimation extraction apparatus and separation

Table 3-4 Reproducibility of air standards processed with the 'static' procedure. For each session the standard deviation (1σ), the mean over all tube numbers (tube No. 1-5) and the off-set of the mean to the assigned value of the air standard (-2.75‰) was calculated. In two cases ('std only' and '1056') an outlier has been removed. * For the calculation of the 'total average' from the five standard deviations the pooled standard deviation (σ_{pooled}) was calculated according to Eqn. 3-4 (see explanation below).

measurement session: date:	'std only' 2.12.05	'276' 20.12.05	'253' 26.01.06	'420' 6.2.06	'1056' 21.2.06	**total average***
number of standards	9	5	10	4	5	
standard deviation [‰]	0.07	0.06	0.08	0.05	0.07	**0.07**
mean [‰]	-3.08	-3.06	-3.09	-3.02	-2.93	**-3.04**
off-set [‰]	-0.33	-0.31	-0.34	-0.27	-0.18	**-0.29**

of CO_2 from the bulk air components. The achieved performance for measuring $\delta^{13}C$ on air standards of 0.06‰ is undoubtedly inferior to the state of the art measurements on large atmospheric samples of typically 0.03‰. However, compared to the results from previous studies on small ice core samples (0.12‰ reported by *Eyer,* 2004), the performance is very good and precise enough to resolve the proposed natural variance (~0.5-1‰ on glacial/interglacial time scales).

Since the numbers of replicates for each measurement session ranges from four to ten, additionally the pooled standard deviation, σ_{pooled}, was calculated to exclude the bias from those measurements with only few replicates. With σ_{pooled} being the square root of summed squared deviations of replicates δ_i from their respective means divided by the degrees of freedom, i.e. the number of samples n minus the number of reported means m.

$$\sigma_{pooled} = \sqrt{\frac{\sum_{i,j=1}^{n,m} (\delta_i - \overline{\delta_j})^2}{n-m}} \qquad (3-4)$$

Concerning the overall accuracy of the method, the off-set of the measured $\delta^{13}C$ to the assigned value was ~0.3‰, except for the last measurement session ('1056') with an off-set of only 0.18‰. This smaller off-set might be due to an observed pressure drop near the end of the live time of the high pressure cylinder of the CO_2 reference gas of the IRMS system. Therefore, it is likely that not the $\delta^{13}C$ value of the air standard changed, but rather the reference basis. Similar shifts noticed *Eyer* (2004), who speculated that due to the pressure drop the liquid CO_2 phase, which is usually found in the cylinder disappears. With the phase change an isotopic fractionation is involved shifting the CO_2 reference gas. As the $\delta^{13}C$ values of the ice core measurements were finally referenced on the air standard, an absolute shift of the CO_2 reference gas is not critical for the ice core samples' absolute values.

3.9.2 Reproducibility of the CO_2 concentration for air standards

In analogy to the $\delta^{13}C$ data analysis presented above, first the differences among the five tube numbers are discussed. The calculations were identical with the exception that considering an off-set is dispensable as the value for the CO_2 concentration of the air standard was assigned to the calculated IRMS response (see Chapter 3.8.2). The results are shown in Figure 3-18 with the mean and standard deviation for each tube number class marked with diamonds and error bars (1 σ). Visible is the distinct deviation of tube number 1, with the mean CO_2 concentration being 2 ppmv lower than the overall average for all tubes (red solid line). As discussed above for $\delta^{13}C$, tube number 1 is probably subject to a systematic loss process, and therefore,

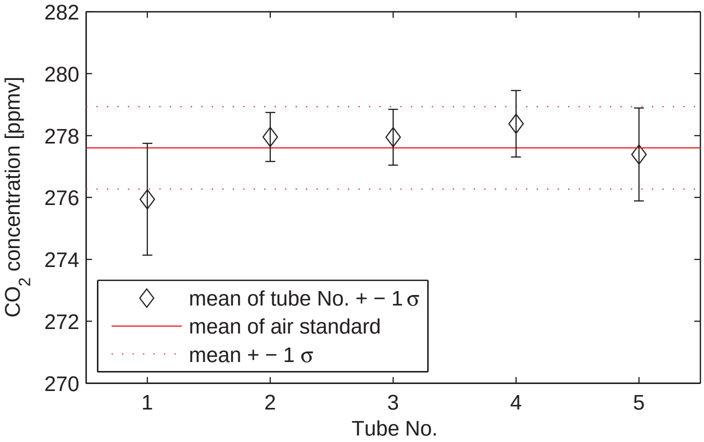

Figure 3-18 Compilation of the CO_2 concentration of whole air standards processed using the 'static' method. The data was compiled from five measurement sessions (total n=33, after removing two outliers). For each tube number the mean and standard deviation (1 σ) was calculated (diamonds with error bars). The red solid line is the assigned value of the CO_2 concentration of the air standard. The two red dotted lines represent the averaged standard deviation of the seven data sets for tube numbers 1-5 (average σ ± 1.5 ppmv). Except for tube No. 1 the means of tube No. 2-4 do not deviate significantly from each other.

treated with caution for the calculation and interpretation of the ice core data. However, as the missing 2 ppmv of tube number 1 is a stable feature at constant conditions, this data was not immediately discarded.

The reproducibility for CO_2 concentrations of air standards is summarized in Table 3-5. The pooled standard deviation over all tube numbers was 1.5 ppmv, and 1.4 ppmv for tube numbers 2-5. This performance is comparable to other studies measuring CO_2 concentrations on ice core samples (e.g. 1.7 ppmv reported by *Siegenthaler et al.,* 2005a). However, that the actual precision for samples is supposed to be lower as constant process parameters (flow rate, total air amount) were applied for these air standards. As will be shown below, a deviation from these constant settings introduces an additional uncertainty for the ice core results since the gas release rates during the sublimation of ice do slightly vary.

Table 3-5 Results for CO_2 concentration from five measurement sessions showing the reproducibility of air standards processed with the standard procedure ('static' method). For each session, the standard deviation (1σ) was first calculated including all data (tube numbers 1-5), and secondly after tube number 1 was discarded from the data since the first tube number deviated from the others (Fig. 3-18). The pooled standard deviation, or average reproducibility of the measurement is 1.5 ppmv including all data, and 1.4 ppmv for tube numbers 2-5.

measurement session:	'std only'	'276'	'253'	'420'	'1056'	σ_{pooled}
date:	2.12.05	20.12.05	26.01.06	6.2.06	21.2.06	
tube No. 1-5						
number of standards	9	4	10	4	5	
standard deviation [ppmv]	1.6	1.0	1.5	0.6	1.9	**1.5**
tube No. 2-5						
number of standards	8	4	8	3	4	
standard deviation [ppmv]	0.8	1.0	1.6	0.2	0.9	**1.4**

3.9.3 Estimation of 'side effects' from air standards

Besides the above discussed air standards processed under 'static' conditions, a couple of additional experiments were conducted at modified conditions. First, air standard was admitted during the sublimation of 'Bern blank ice' for a comparison with the 'static method' (see Chapter 3.7.2 for details). Secondly, the rate with which the air standard was admitted to the sublimation vessel was varied to evaluate its influence on $\delta^{13}C$ or the CO_2 concentration.

Comparison between air standards processed under 'static' and sublimation conditions

Results from three experiments comparing both methods showed that $\delta^{13}C$ values were slightly more negative for the experiments with sublimation of 'Bern blank ice'. On average, the latter values were 0.1-0.15‰ more negative and were less precise (1 σ ~0.08‰) than the 'static' ones. This discrepancy between both methods was already observed during the early development stage of the sublimation apparatus (see Chapter 3.5) and led to the conclusion that experiments conducted with sublimation of 'blank ice' were less conclusive than the 'static' version. As a result, most experiments further on were conducted using the more reliable 'static' method. The speculation is that the 'blank ice' might contain traces of atmospheric CO_2 that were not removed during the preparation. As the used air standard is relatively heavy ($\delta^{13}C$ = -2.75‰), a small amount of isotopically depleted CO_2 might be responsible for this shift. The precision of the early measurement set-up did not allow a detection of this small extra CO_2. With the final analysis set-up, a few experiments with sublimation of blank ice were repeated and resulted in ~3 ppmv higher CO_2 concentrations compared to the 'static' method without sublimation. Slightly higher CO_2 values together with ~0.1‰ more negative $\delta^{13}C$ values points to a contamination of the blank ice. Using an isotopic mass balance, a $\delta^{13}C$ value of -12‰ (conceivable for laboratory air) would match the 0.1‰ shift of the mixture and a 3 ppmv concentration increase. Though the admission of air standard during the sublimation of blank ice mimics the air release from ice samples more realistically, the $\delta^{13}C$ results from the 'static' procedure are regarded more accurate. Until truly CO_2-free blank ice is available, it is more conservative to correct the ice core samples with a system off-set from the 'static' procedure. Note that this ~0.1-0.15‰ off-set uncertainty in the absolute $\delta^{13}C$ correction value and ~3 ppmv for CO_2 does not compromise the outcome concerning the small-scale heterogeneity in the ice (Chapter 4.3) as the off-set is a constant factor. However, this off-set is a critical issue for the comparison with other ice core data (Chapter 4.4).

Influence of the admission rate

As shown above (Fig. 3-16), the admission rate of air for the preparation of air standards was slightly higher than the mean air release rate observed during the sublimation of Holocene ice core samples. Further, the release rate for ice core samples (Fig. 3-16 and 3-19) shows a systematic variation during the sublimation as the ice cube continuously shrinks in parallel to the increase in supplied infra red energy. However, due to technical constraints in the reference inlet, a simultaneous variation of the admission rate for air standards (i.e. the pressure within the reference inlet) during the experiment was not possible so far. This is mainly due to the large dead volume within the pressure regulator making a quick down-regulation of the pressure difficult. For this, the admission rate was reduced from 0.04 to 0.027 mL STP min^{-1} prior to the experiment and then held constant (Fig. 3-19). This reduced rate was chosen to account for the conditions (in terms of the CO_2 flow rate) of glacial ice core samples with low CO_2 concentrations. Considering only the flow rate of air (left panel, red line) and the total air volume (center, red dots) admitted with the high admission rate, the corresponding values for glacial samples (marked as diamonds) are well matched. However, in case of the amount of CO_2 (and also its flow rate) the low admission rate (right panel, blue dots) is probably more representative for ice core samples with low CO_2 concentrations.

Within the uncertainty of the measurement, the means in δ^{13}C for both rates did not differ (Fig. 3-20). Further, for the low rate even more negative values (~0.1‰) were found for tube number 1 compared to the high rate (Fig. 3-17). This confirms the notion that the first tube number has a systematic bias towards lower values. Note that for this experiment the collection time was identical for both admission rates. Consequently, less CO_2 was collected in case of the lower admission rate. This resembles roughly the conditions of the CO_2 flow rate for glacial ice and the experiment was aimed to look for a systematic bias between Holocene and glacial samples due to the contrasting CO_2 concentrations. Although this flow rate change experiments are suitable to simulate the variation of air release from ice core samples during

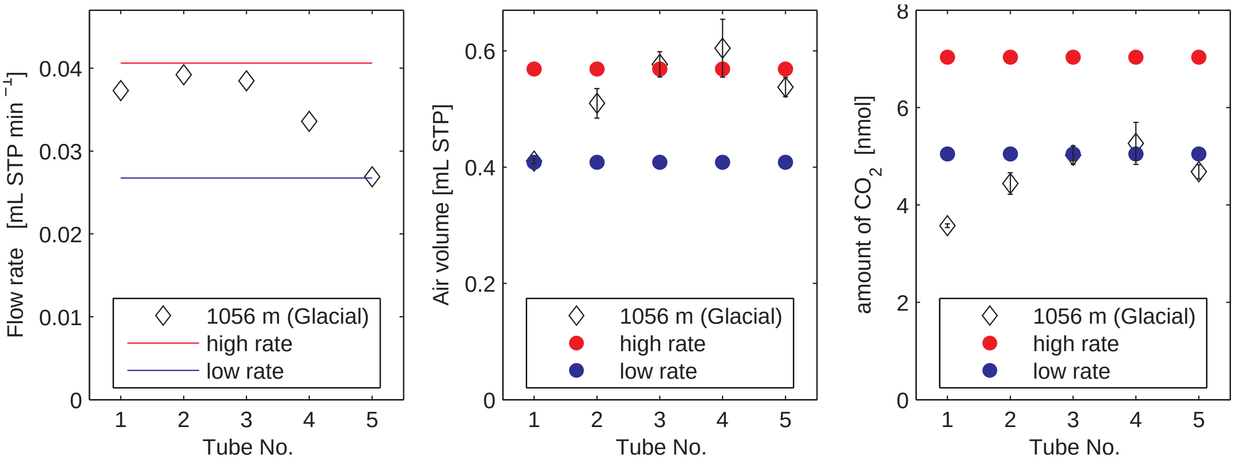

Figure 3-19 Comparison of process parameters for the sublimation apparatus between the admission of air standard at a high and at a lower rate, marked with red and blue in each panels, and the corresponding parameters for a ice core sample from the glacial period. Note that the air content of glacial ice is slightly higher so the collected air volume almost matches that of the standard (see Fig. 3-16 for comparison).

the sublimation, it is only an approximation to simulate the different CO_2 concentrations between Holocene and glacial periods. Nevertheless, the comparison showed that the flow rate does not influence the $\delta^{13}C$ values. To gain more confidence, air standards with contrasting CO_2 levels will be used in the future to better address this issue.

For the CO_2 concentration a difference was observed between both rates. For the low rate, the CO_2 concentrations were systematically lower by 5 ppmv (Fig. 3-20). Here as well, tube number 1 is shifted towards lower values by ~2 ppmv. The slightly lower values cannot be explained with an IRMS measurement linearity effect comparable to $\delta^{13}C$. A calculation of the specific IRMS response for the three linearity peaks, L1, L2, and L3, corresponding to CO_2 amounts of ~3, 5, and 7 nmol, respectively, did exclude the CF-IRMS measurement system to cause this deviation. The specific CF-IRMS response derived from linearity peaks rather suggests CO_2 values to be ~1 ppmv higher for the 5 nmol CO_2 level (L2) compared to 7 nmol (L3). The latter calculation assumes that the CO_2 amount admitted to the cracker by consecutively filling the reference loop once, twice, and three times precisely scales with the peak amplitude.

An initial explanation for the observed 5 ppmv difference might be that a constant CO_2 amount is lost within the sublimation apparatus itself or during the transfer into the glass capillary, which results in a relative loss for the concentration. A second explanation might be that the apparent loss in CO_2 is due to a non-linearity effect of the air volume measurement with the pressure transducer. Again, further experiments using air standards with different CO_2 concentrations will help to clarify this effect and reduce the uncertainty of the CO_2 concentration measurement.

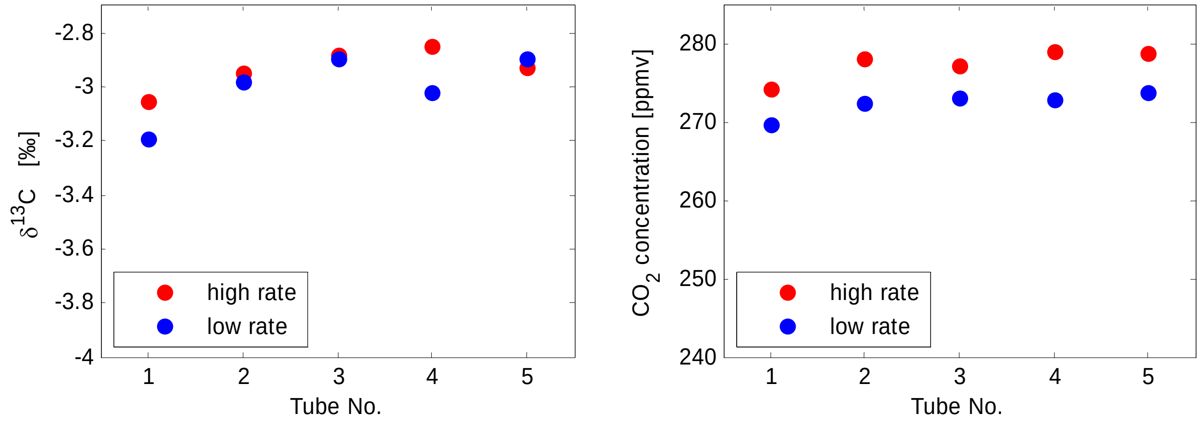

Figure 3-20 Experimental results showing the influence of the admission rate (high rate 0.04 mL STP min^{-1}, low rate 0.027 mL STP min^{-1}) on the $\delta^{13}C$ values (left panel) and the CO_2 concentration (right panel).

3.9.4 Procedural blanks

Blank experiments were conducted to estimate the proportion of CO_2 that either originates from an external contamination, or from a memory effect. Using an extended vacuum system like in this work, a steady inflow of air from the outside due to a leakage is the most conceivable way to produce blank values. Yet, air leakages within the vacuum apparatus can be detected from a pressure increase in the high vacuum system (P_{Vac} pressure sensor). As copper gaskets seals were used to connect the sublimation vessel with the vacuum line and the fittings were all-metal, the permeation of air into the vacuum apparatus was small. From the pressure reading of the vacuum sensor P_{Vac}, the leakage rate of air into the sublimation apparatus was <0.001 mL STP h^{-1}, corresponding to <1 ppmv blank assuming 6 nmol CO_2 as a typical sample amount, 400 ppmv CO_2 for the ambient air, and a collection time of 15 min. More critical than the contamination from outside is the desorption of CO_2 from the internal surfaces of the apparatus itself. In gas analytics, CO_2 is known as a 'sticky' gas species as it readily adsorbs on metal, glass, and polymer materials to desorb from these surfaces at a later time. This ad- and desorption behavior was already noticed since the beginning of ice core CO_2 analysis by *Zumbrunn et al.* (1982) and the problem was constantly confirmed later on (*Güllük et al.,* 1998; *Siegenthaler,* 2006). The actual desorption rate from a surface depends on the surface's initial CO_2 saturation when the surface was exposed to a certain CO_2 partial pressure, on the time constant of the desorption, and its temperature dependency. Further, the desorption rate depends on the concentration of competing molecules, like H_2O, which preferentially displaces CO_2 from a surface due to its strong dipole moment. Owing to this complex ad- and desorption processes, a couple of representative blank experiments were conducted to achieve first order estimations for the conditions relevant during the sample preparation and measurement.

Description of blank experiments

Five different blank experiments were conducted to estimate the cumulative contribution of non-sample CO_2 during the analysis process, termed blank contribution:

(1) 'He-blank' to estimate the contribution from the He carrier gas. The carrier passing the tube cracker was cryofocused for 90 s and any collected CO_2 afterwards transferred to the GC. To exclude a memory effect from the cracker, i.e. CO_2 desorption from its surfaces, no CO_2 reference gas pulse was admitted to the cracker for one hour prior to this experiment.

(2) 'cracker-blank' to estimate the CO_2 amount added during the normal operation of the tube cracker: similar to experiment (1), but preceded by a large CO_2 reference pulse (EQ peak). This procedure estimates the cracker's memory effect under typical measurement conditions.

(3) ‘empty tube blank’ to estimate the CO_2 release during the flame sealing of the glass tube. New glass capillaries were prepared identically to the sample procedure (Chapter 3.7.1). The CO_2 trap and the glass capillary were evacuated, V5 closed, and the tip of the capillary immersed in LN. Then the tube was flame-sealed.

(4) ‘CO_2 trap blank’ to estimate leakage or outgassing of the CO_2 trap. The CO_2 trap was held at LN temperature for 10 min with V4 and V6 being closed, then the trap was warmed up and the vaporized CO_2 transferred to the glass capillary and the tube flame sealed.

(5) ‘sublimation blank’ to estimate the effect during the sublimation of the blank ice. The experiment is identical to the procedure described for air standards (Chapter 3.7.2), but without admitting air to the sublimation vessel.

Results from blank experiments

With each analytical step, the blank progressively increases as shown in Table 3-6, with a total sum of 0.03 nmol CO_2 measured for the ‘sublimation blank’. The steps with the largest CO_2 contribution are the ‘cracker blank’ and the ‘sublimation blank’. The amount added to the ‘cracker blank’ is most likely due to surface desorption from the cracker device and its connection tubing to the valves. This can be derived from the ‘He blank’, which is only halve the size of the ‘cracker blank’ since the tube cracker had not ‘seen’ CO_2 for one hour, i.e. desorption from the surface declined. It is important to note that as the relative contribution from the cracker-GC-IRMS system is relatively large (45% from the total), and due to the additive character of the blanks, the smaller contributions from consecutive steps represent coarse es-

Table 3-6 Step by step contribution of blank CO_2 during the analysis starting (separated for the cracker-GC-IRMS system and the sublimation extraction apparatus). The first column lists five blank experiments described above in sequence of increasing components involved during the analysis (with number of measurements in brackets). Second column: absolute amount of CO_2 from each experiment. As the blanks are expected to be cumulative during the analysis, the right column shows the relative fraction of each blank experiment.

number of blank experiment	amount of CO_2 [nmol]	relative contribution to total blank [%]
cracker-GC-IRMS only:		
(1) ‘He-blank’ (n= 10)	0.004±0.005	~15
(2) ‘cracker-blank’ (n= 20)	0.015±0.005	~30
+ sublimation extraction:		
(3) ‘empty tube blank’ (n= 10)	0.02±0.005	~15
(4) ‘CO_2 trap blank’ (n= 5)	0.025±0.005	~20
(5) ‘sublimation blank’ (n= 10)	0.03±0.005	~20

timates. The total sublimation blank amounts to roughly 0.03 nmol CO_2 measured from the sublimation of ~5 g 'blank ice'. For comparison, the amount of CO_2 extracted from a Holocene ice core sample is ~6 nmol (~5 g ice with 10% volumetric air content and ~280 ppmv CO_2), thus, the contribution of the blank is 1-2 ppmv. The blank numbers 3-5 measured for the sublimation extraction do not necessarily imply that the amount of CO_2 for ice core samples is increased by this blank. It is more likely that during the preconditioning step of the sample preparation any 'outside CO_2' adsorbed onto surfaces is replaced by sample CO_2, which then gradually desorbs and exchanges during the sublimation of an ice sample. Likewise, the impact of the measured CO_2 blank on the $\delta^{13}C$ values of samples and standards can only be estimated since the small blank peaks are out of the range for which $\delta^{13}C$ values can be reliably calculated. For a first order estimation of the blank's influence on the $\delta^{13}C$ measurement using an isotopic mass balance calculation one can assume that the $\delta^{13}C$ value of the blank is range of ±5‰ of the sample value. The resulting $\delta^{13}C$ shift from 0.03 nmol blank on a typical sample would then account for ±0.04‰.

4 Results and discussion of ice core measurements

In the following Chapter first results from ice core measurements using the newly developed analysis technique will be presented. The key objective was to clarify, whether the measured small-scale $\delta^{13}C$ fluctuations, i.e. differences on a few centimeters or smaller than a year, reported by *Eyer* (2004) are a real feature or not. In the study by *Eyer* (2004) the average standard deviation of the measurement for the Holocene ice of the EDML ice core was 0.23‰. Surprisingly, results on the EDC core had a scatter that was only half the value of the EDML core. Furthermore, both $\delta^{13}C$ records deviated also with respect to their mean values, with EDML being ~0.2‰ more negative. Neither these high $\delta^{13}C$ fluctuations on a sub-annual scale, nor an absolute off-set between two ice cores on the same hemisphere are plausible for a well mixed atmospheric parameter with a life time of decades or longer. Consequently, *Eyer* (2004) speculated that an up to now not identified fractionation process during the bubble close-off might be responsible for this phenomenon. For other gas species, evidence from firn air measurements emerged, pointing to a size dependent fractionation (*Huber et al.,* 2006; *Severinghaus and Battle,* 2006). Yet, no indication was found that CO_2 or the isotopic composition of CO_2 might be affected by this physical fractionation process as well. Nevertheless, the disappointing findings from *Eyer* (2004) somehow questioned the integrity of ice core $\delta^{13}C$ information as representative for the paleoatmosphere.

This Chapter is organized in the following way: Chapter 4.1 provides a brief description of the measured ice core samples, followed by an overview of the main characteristics of the measured $\delta^{13}C$ and CO_2 concentration data showing the results of one sample depth (Chapter 4.2). Next, the following three main issues will be discussed. First, the performance of the newly developed analysis technique is evaluated on basis of real ice core samples and the results are compared with the performance of the air standard measurements (Chapter 4.3). Secondly, the ice core data are analyzed to address the question of the small-scale $\delta^{13}C$ variability. Here, the differences among the sample replicates are considered (Chapter 4.4). Thirdly, the absolute values for $\delta^{13}C$ and the CO_2 concentration are compared with existing records to assess the accuracy of this analysis technique (Chapter 4.5).

4.1 Ice core samples from the EDML ice core

Based on the findings of *Eyer* (2004), the first crucial application of this newly developed method was to shed light on this small-scale $\delta^{13}C$ scatter. To this end, sample replicates were analyzed on the EDML ice core, the core for which *Eyer* (2004) found the largest $\delta^{13}C$ scatter. Four depth intervals were selected for this study: 151 m, 253 m, 420 m, and 1056 m. While the first three depths are of Holocene age and the ice quality is pure bubble ice, the samples from the 1056 m depth interval correspond to the glacial period (Fig. 4-1). At this depth bubbles disappeared and most of the air content has already transformed to clathrates.

Figure 4-1 gives an impression of the time interval a single ice sample of 4.2 cm comprises in terms of age. For the Holocene samples, between 0.5 and 0.8 years of ice are covered within a single sample, for the glacial ice, the value is 1.5 years. However, these values correspond to a time interval for the ice matrix, thus, to the time scale of dissolved and particulate impurities in the ice. For the enclosed air the age difference between adjoining samples is virtually zero due to the bubble enclosure processes during firnification (see Chapter 2.1). As the age distribution at the bubble close-off depth at EDML is ~59 years (see Fig. 2-3), ice samples that are only centimeters to a few decimeters apart effectively contain identical air samples. From each depth interval, three, four in case of depth 253 m, vertically adjoining ice core samples were analyzed with the new method. As described above, each sample yields five sub-samples in separate glass tubes. To achieve optimal measurement conditions to detect differences among the three adjoining samples, all tubes of a depth interval were analyzed jointly within one IRMS measurement session. Applying this design, potential differences among individual IRMS runs, potentially introducing additional variance, were excluded.

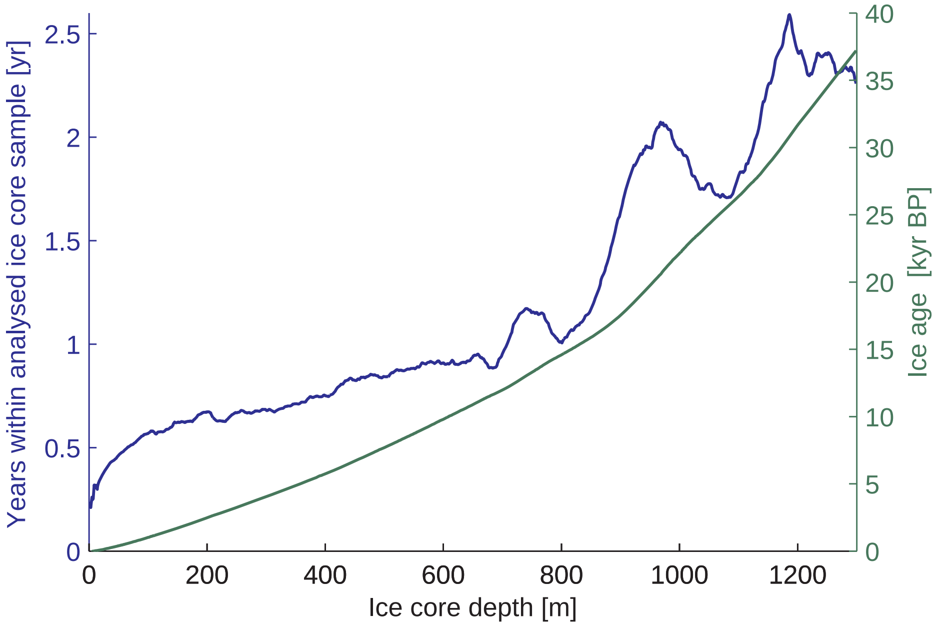

Figure 4-1 Basic stratigraphic properties of the EDML ice core and its relation to the sample size to assess the 'small-scale heterogeneity'. Left axis: number of years covered within the measured ice core sample of 4.2 cm as a function of ice core depth. Right axis: Age of the ice as a function of depth (U. Ruth, personal communication, 2006). The general trend of the blue curve towards more years covered within a single ice sample is due to the thinning rate with increasing depth and elapsed time. Superimposed on this trend is the shift in accumulation rate due to climate changes.

4.2 Main characteristics of the measured ice core data

Before the results of the measured ice samples are analyzed in detail, the data set of one depth interval (420 m) is shown to visualize the general measurement features (Fig. 4-2). Shown are the combined results for the $\delta^{13}C$ values (upper panel) and the CO_2 concentrations (lower panel) for three vertical replicates (sample 1, 2, 3). Three general features are readily visible: (1) Systematic differences among the three samples replicates are not observed. (2) Fairly good reproducibility within a tube number class. (3) Systematic differences among the five tube number classes are especially pronounced for $\delta^{13}C$ values.

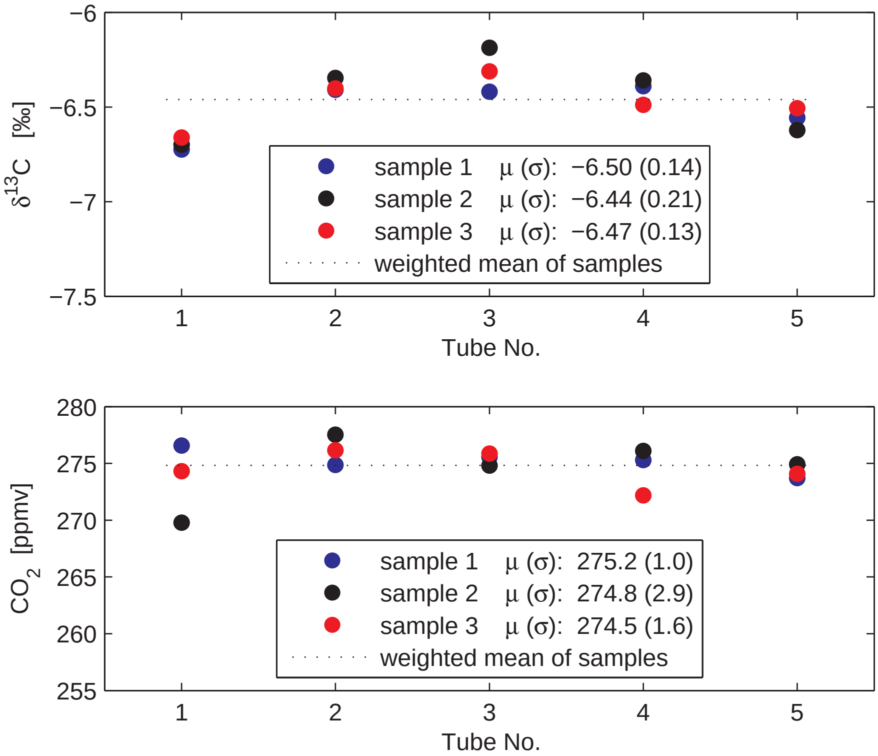

Figure 4-2 Example showing the measurement results of three ice core replicates from the depth interval '420 m'. Upper panel: $\delta^{13}C$ values grouped according to the tube number, i.e. the sequence of sub-samples collected during the sublimation of an ice sample. Visible is the marked deviation of the first tube number from the weighted mean[20] of all sample tubes (dotted line), while tube number 2, 3, and 4 have almost the same level. As a general feature, no systematic differences were observed among the three samples (weighted mean and standard deviation of tube 1-5 are given in the legend). Where means deviated among the three samples it was due to erratic 'outliers', which were not removed from the data set when no obvious reason during the analysis procedure could be identified. Bottom panel: In this example CO_2 concentration results show little dependence on the tube number, but a somewhat increased scatter for tube number 1.

---

[20] for averaging $\delta^{13}C$ values and CO_2 concentrations weighted means were calculated further on, since the corresponding air volume to which these values refer is not equal for all tubes (see Fig. 3-16 for details)

4.3 Systematic differences during the sublimation extraction

This paragraph focuses on potential processes to explain the observed differences among the five tube numbers. As shown above for the sample depth 420 m (Fig. 4-2), the $\delta^{13}C$ values of tube number 1 are systematically lighter compared to the other tubes. This observation is valid for all measurements. On average, the $\delta^{13}C$ values for tube number 1 are 0.25‰ isotopically lighter than the overall $\delta^{13}C$ mean as summarized in Table 4-1. Moreover, slightly lighter $\delta^{13}C$ values were found as well for tube number 5. Additionally, the CO_2 concentrations for tube number 5 are on average 3.5 ppmv lower than the mean over all five tube numbers (see Tab. 4-2). As the marked $\delta^{13}C$ anomaly for tube number 1 is not observable for air standard

Table 4-1 Compilation of the $\delta^{13}C$ results for the 'vertical replicates' of the four measured depths intervals. From each depth interval three vertically adjoining ice core samples (replicates) were analyzed and corrected as described in Chapter 3.8 except for the gravitation effect, which is not relevant at this stage. The standard deviation (1σ) and average for three replicates were calculated for each tube number class separately. To characterize the systematic difference among the five tube numbers, $\Delta_{average}$, the deviation of each tube number mean from the total average was calculated. The standard deviations of the five tube number classes for each depth interval were averaged to characterize the scatter between the three sample replicates. A total average was calculated for the standard deviations of each tube number to characterize the reproducibility for each tube number. Furthermore, for each depth interval an average is calculated for the standard deviations and means over tube numbers 1-5 (right column) to provide a measure for the scatter among the three replicate samples and to allow a first comparison of the samples' absolute values prior to the gravitation correction.

	tube number (sub-sample during the sublimation)					
ice core depth interval	1	2	3	4	5	**average**
151 m						
standard deviation [‰]	0.05	0.07	0.08	0.11	0.05	**0.07**
mean [‰]	-6.66	-6.34	-6.15	-6.23	-6.32	-6.34
$\Delta_{average}$ [‰]	-0.32	0.00	0.19	0.11	0.02	
253 m						
standard deviation [‰]	0.12	0.06	0.07	0.05	0.04	**0.07**
mean [‰]	-6.55	-6.21	-6.16	-6.20	-6.14	-6.25
$\Delta_{average}$ [‰]	-0.30	0.04	0.09	0.05	0.11	
420 m						
standard deviation [‰]	0.03	0.03	0.12	0.07	0.06	**0.06**
mean [‰]	-6.69	-6.39	-6.31	-6.41	-6.56	-6.47
$\Delta_{average}$ [‰]	-0.22	0.09	0.17	0.06	-0.09	
1056 m						
standard deviation [‰]	0.06	0.00	0.01	0.05	0.09	**0.04**
mean [‰]	-6.46	-6.23	-6.17	-6.27	-6.42	-6.31
$\Delta_{average}$ [‰]	-0.15	0.08	0.14	0.04	-0.11	
total averages						
standard deviation [‰]	**0.07**	**0.04**	**0.07**	**0.07**	**0.06**	**0.06**
$\Delta_{average}$ [‰]	-0.25	0.05	0.15	0.07	-0.02	

measurements, the cause must be either related to a property of the ice core sample itself. Or, the anomaly is caused by a process unique to the conditions occurring during the sublimation of an ice core sample; i.e. a process that is not properly simulated by the introduction of air standard to 'blank ice' with the reference gas inlet. However, a deviation for tube number 1 to slightly more negative $\delta^{13}C$ values was also detected for air standards, but this difference was well within the envelope of the 1 σ measurement reproducibility (Fig. 3-17).

The option that the systematic $\delta^{13}C$ differences among the tube numbers do reflect a primary signal within the ice itself, like the postulated small-scale $\delta^{13}C$ variability (*Eyer,* 2004), is unlikely. For a layered ice core, the preferred concentration gradients for chemical compounds as well as changes in physical properties (e.g. the total air content or crystal size) are

Table 4-2 Compilation for the CO_2 concentrations of the four measured depths intervals. The standard deviation (1σ) and average for the three replicates were calculated for each tube number class separately. To characterize the systematic difference among the five tube numbers, $\Delta_{average}$, the deviation of each tube number mean from the total average was calculated. The standard deviations of the five tube number classes for each depth interval were averaged to characterize the scatter between the three ice core replicates. A total average was calculated for the standard deviations of each tube number to characterize the reproducibility for each tube number. Furthermore, for each depth interval an average is calculated for the standard deviations and means over tube numbers 1-5 (right column) to provide a measure for the scatter between the three replicate samples, which allows a first comparison of the samples' absolute values prior to gravitation correction.

	tube number (sub-sample during the sublimation)					
ice core depth interval	1	2	3	4	5	**average**
151 m						
standard deviation [ppmv]	3.0	4.3	2.1	5.1	2.8	3.5
mean [ppmv]	286.1	281.2	280.8	281.4	277.0	281.3
$\Delta_{average}$ [ppmv]	4.8	-0.1	-0.5	0.1	-4.3	
253 m						
standard deviation [ppmv]	3.4	3.4	3.9	2.2	5.1	3.6
mean [ppmv]	278.4	277.7	277.4	278.1	271.7	276.7
$\Delta_{average}$ [ppmv]	1.7	1.0	0.8	1.5	-5.0	
420 m						
standard deviation [ppmv]	3.5	1.3	0.5	2.1	0.6	1.6
mean [ppmv]	273.6	276.2	275.4	274.5	274.2	274.8
$\Delta_{average}$ [ppmv]	-1.2	1.4	0.6	-0.3	-0.5	
1056 m						
standard deviation [ppmv]	0.6	2.4	1.1	1.5	6.5	2.4
mean [ppmv]	192.7	196.3	205.4	197.4	192.5	196.9
$\Delta_{average}$ [ppmv]	-4.1	-0.6	8.5	0.5	-4.3	
total averages						
standard deviation [ppmv]	2.6	2.9	1.9	2.7	3.7	2.8
$\Delta_{average}$ [ppmv]	0.3	0.4	2.4	0.5	-3.5	

perpendicular to the horizontal plane. Because the ice core samples retain their natural orientation during the sublimation (see Fig. 3-3), the sublimation proceeds almost circular and orthogonal to the layering. Thus, for any time step equal amounts of ice are removed from each horizontal layer. Therefore, an ordinary ice signal cannot explain the observed $\delta^{13}C$ deviations among the tubes.

More tricky are the next two scenarios, which assess whether the observed inter-tube $\delta^{13}C$ differences might reflect an apparent $\delta^{13}C$ signal from the ice core sample. In this scenario, the measured inter-tube $\delta^{13}C$ differences are not regarded to reflect a primary, or 'natural' signal, but rather a post coring storage effect, or the result of the sample preparation. The fact that the enclosed air in ice cores might partially be lost during the storage of ice cores was first noticed during the analysis of the N_2/O_2 ratio (*Bender et al.,* 1995). In case of the CO_2 concentration, it is generally assumed that this storage effect is minor, and by removing a few mm of ice prior to the analysis this problem is solved. Only recently *Siegenthaler* (2006) revisited this issue and modeled the effect of gas loss during the storage on the CO_2 concentration. To this end, *Siegenthaler* (2006) used revised permeation coefficients of gas species through ice, which are much higher than previously calculated (*Ikeda-Fukazawa et al.,* 2004). As shown in Figure 4-3, *Siegenthaler* (2006) found that CO_2 becomes increasingly enriched in the outer rim due to a preferential loss of gas species with higher permeabilities (mainly O_2 and N_2). So far, there is no evidence that also an isotopic fractionation might be connected

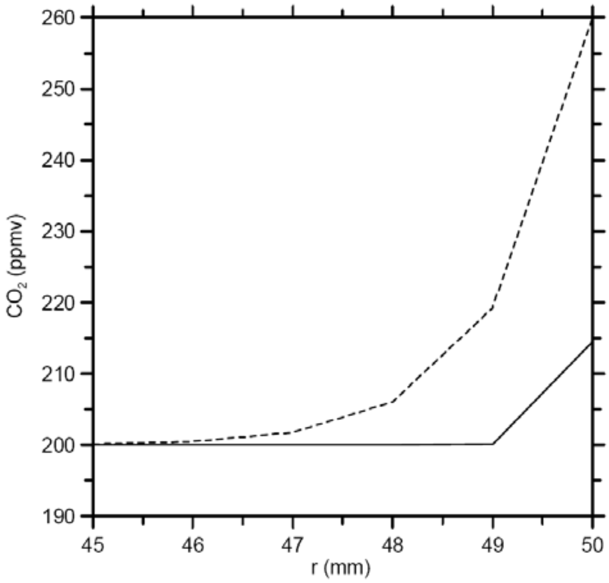

Figure 4-3 Modeling results conducted by *Siegenthaler* (2006) to estimate the effect of selective gas loss during the storage of ice cores on its CO_2 concentration. The two curves illustrate the relative CO_2 increase for two years for an ice cylinder with a diameter of 5 cm at -25 °C using two permeation coefficients (previous assumptions: solid line; new assumptions: dashed line; see details in *Siegenthaler* (2006)). Note that the calculated CO_2 increase for the outer part is not due to an inward diffusion from the ambient air as the absolute CO_2 pressure within the ice core is considerably higher than the outside pressure.

with this effect, i.e. whether $\delta^{13}C$ values might also be affected. Because for this study at least 4 mm of ice were removed from the outer part, this effect is unlikely to explain the observed $\delta^{13}C$ anomaly of the first tube number. Likewise, the CO_2 concentrations for the first tube number are not notably elevated, except for the depth interval 151 m (see Tab. 4-1). Therefore, this storage effect cannot explain the observed inter-tube differences. Nevertheless, the gas extraction technique used here, which successively penetrates from the outer part into the inner part of an ice sample, is certainly especially vulnerable for such an effect (see Fig. 3-3). In contrast, with mechanical extraction techniques the entire ice sample is extracted at once and then yields a single value ('mean of the ice piece'). In this case, the amount of air extracted from a possibly fractionated outer part will then be diluted by the bulk, thus, masking this effect.

The second scenario assumes that during the sample preparation (vacuum pumping for two hours) a selective gas loss occurs from the ice sample's outer sheath. *Craig et al*. (1988) observed a gas loss induced by pumping at vacuum conditions during the analysis of fractured ice samples with many visible micro cracks. As this fractionation effect involves molecular diffusion, besides an elemental fractionation, also an isotopic fractionation will occur. As a consequence, this causes an isotopic enrichment of the remaining gas while the escaped gas, in turn, becomes isotopically depleted. In fact, *Craig et al*. (1988) found enriched $\delta^{13}C(CH_4)$ values for fractured ice core samples and also *Schaefer* (2005) reported a higher scatter for $\delta^{13}C(CH_4)$ values associated with fractured ice core samples. However, the deviation for tube number 1 is in the opposite direction to this scenario, and the samples were inspected for visible cracks prior to the sample preparation and none of the analyzed samples had visible cracks.

However, such cracks might form during the sublimation process when the ice is irradiated with IR light, a phenomenon reported also by others (*Güllük et al.,* 1998). Depending on the light's wavelength, the IR energy penetrates several mm to cm into the ice sample until it is absorbed, whereby increasing the temperature. In contrast, energy can be removed from the ice sample only at the sublimating surface by the latent heat flux. After a while the incoming IR flux is balanced by the latent heat flux until a steady state is reached. In consequence, one can imagine that within the ice sample a temperature gradient will establish due to differential heat supply and removal. In accordance with this, at the method's early development stage, ice samples sometimes broke suddenly apart in several pieces during the ongoing sublimation. The disintegration of ice samples during the sublimation was also described by *Güllük et al.* (1998) as a common phenomenon at the beginning of the sublimation procedure when the ice sample had an inhomogeneous temperature distribution. However, for the applied sublimation settings used in this work, a sample break-up did not occur anymore, as the energy supply is smoothly increased during the sublimation (see Tab. 3-3 in Chapter 3-3). Yet, it is not clear, whether micro cracks might form within the IR absorbing outer part of the ice sample and if, whether this can induce a measurable effect on the released gas composition given the short time scales. Though possible effects from the latter scenario cannot be easily ruled out, the fact that the analytical reproducibility for tube number 1 is as good as for the other tubes does not concur with a cracking process (see Tab. 4-1 and 4-2). As a process like cracking of an ice sample should be erratic, one would assume that the measured data are more randomly scattered, i.e. should lead to a higher standard deviation.

While the above discussed processes focused on the ice sample, sorption processes within the sublimation apparatus will be examined in the following:

First the desorption of CO_2 from the surfaces of the apparatus is considered. CO_2 might desorb from surfaces at the beginning of the sublimation either due to a higher H_2O partial pressure by replacing CO_2 from adsorption sites. Or, due to a temperature increase of the glass vessel caused by the IR irradiation. Both effects were observed in previous studies and ascribed to measured CO_2 concentration off-sets (*Zumbrunn et al.,* 1982; *Güllük et al.,* 1998; *Siegenthaler,* 2002). When desorption or outgassing takes place, the CO_2 concentration would increase and, in turn, $\delta^{13}C$ is expected to decrease if one assumes desorption of 'outside' CO_2. Ambient air within the laboratory is usually isotopically lighter than the sample by about several permil. If this scenario were plausible, the $\delta^{13}C$ shift of on average 0.25‰ observed for the first tube number should be in line with an isotopic mass balance calculation. However, only the two uppermost sample depths (151 m and 253 m) show elevated CO_2 concentrations for the first tube number at all (see $\Delta_{average}$ values in Tab. 4-2), while in the other cases the CO_2 concentrations are lower than the overall average. Applying an isotopic mass balance for the 151 m depth interval, the 4.8 ppmv positive off-set connected with a negative $\delta^{13}C$ off-set of 0.31‰ would be in line with a $\delta^{13}C$ value of the added CO_2 of -25‰. For the depth interval 253 m, with $\Delta_{average}$ values of 1.7 ppmv and 0.30‰ (see Tab. 4-2), the $\delta^{13}C$ value of the added CO_2 would be -50‰. Such negative $\delta^{13}C$ values are unrealistic for the current atmospheric $\delta^{13}C$ level of -8.5‰ and considering the air exchange rate within rooms.

Secondly, the adsorption of CO_2 onto the surfaces of the apparatus is discussed. As CO_2 is preferentially lost by this process, the CO_2 concentration will decrease. If this adsorption process is connected either with a kinetic or an equilibrium fractionation, then also the $\delta^{13}C$ value of the remaining fraction becomes affected. Unfortunately, fractionation factors for carbon isotopes for adsorption processes of CO_2 are not available from the literature. Similar to the isotopic mass balance calculation from above, huge and unrealistic fractionation factors must be assumed to explain an 0.3‰ shift for a CO_2 loss of only a few ppmv.

Therefore, neither assuming desorption from surfaces nor adsorption onto surfaces can conclusively explain the observed $\delta^{13}C$ anomaly of tube number 1. The same is true for the less pronounced deviation observed for tube number 5. Likewise, $\delta^{13}C$ values are slightly more negative and CO_2 concentrations lower for the last tube number (Tab. 4-1 and 4-2). As described for air standard measurements in Chapter 3.8, small nonlinearities during the mass spectrometric detection and the consecutive calculation steps might affect the $\delta^{13}C$ and CO_2 concentration results. Further analytic efforts are needed to identify the physical reasons for the observed systematic differences among the five tube numbers. As a pragmatic step, both the first and the last tube number were excluded from the calculations for the absolute values. The three tubes collected in the middle of the continuous sublimation, numbers 2, 3 and 4, reproduce well. Therefore, the averages of these central sub-samples are used for the comparison with other ice core data (Chapter 4-5). Note that the chance to identify such a bias during the gas extraction process and afterwards to select the most trustworthy sub-samples is actually the strength of the approach developed in this work. Previous studies were dependent on one single value being representative for the entire procedure. Thus, critical side effects at the beginning or at the end of a procedure cannot be detected.

4.4 Small-scale variability – differences among replicates

One key question to be addressed by this first measurement campaign with three adjoining sample replicates from four depth intervals is the issue of a small-scale $\delta^{13}C$ variability. The basic idea behind is, whether $\delta^{13}C$ shows a variability on a temporal scale that is not of atmospheric origin. In other words, are there additional processes on the scale of centimeters within the ice which add variability to the atmospheric $\delta^{13}C$ signal? As described in Chapter 2, three physical processes are known to alter the atmosphere's original $\delta^{13}C$ value (gravitative settling, thermal diffusion, and diffusion along a concentration gradient). Though these processes affect the $\delta^{13}C$ values within the firn column and in the ice cores, none of these processes is able to produce a $\delta^{13}C$ variability on the centimeter scale.

The following calculation method is used to analyze the measured samples for a $\delta^{13}C$ variability on a few centimeters. This approach is equivalent to the calculation of the method's analytical reproducibility. However in its strict sense, the concept of analytical reproducibility cannot be applied for this ice core analysis since the homogeneity of the sample material with respect to $\delta^{13}C$ is a priori not known. First, for each tube number class the standard deviation (1σ) from the three sample replicates are calculated. This separate calculation for each tube number class is essential due to the systematic differences observed among the different tube numbers. This calculation is repeated for the four depth intervals. Secondly, the averaged standard deviation for each of the five tube number classes is calculated. These total averages range from 0.04‰ to 0.07‰, with an overall mean of 0.06‰ (see total averages at the bottom of Tab. 4-1). Similarly, an averaged standard deviation is calculated for each depth interval from the individual standard deviation of the five tube numbers. Here, the average standard deviations range from 0.04 to 0.07‰, with an overall average of 0.06‰ (see averages in the right column of Tab 4-1). Note that all five tube numbers were used for these calculations as there is no evidence that the variability of tube number 1 and 5 is significantly higher compared to tube numbers 2, 3, and 4. As pointed out above, the reason for the observed $\delta^{13}C$ offset for the first and the last tube number has not been identified. But irrespective of the nature of this influence, it is save to assume that the variability of the replicates would rather be increased than decreased by adding an additional effect.

In effect, the average $\delta^{13}C$ variability of 0.06‰ among three adjoining ice samples is not higher than the reproducibility of air standard measurements as shown in Chapter 3.9. In turn, this also implies that the ice core samples did not add to the overall measurement error derived from air standard measurements. Consequently, one can hypothesize for the EDML ice core that the true $\delta^{13}C$ variance along a few centimeters might in fact be lower than the measured variability ('analytical reproducibility') of 0.06‰.

Based on these replicate measurements from four selected depth intervals, there is no evidence to assume a small-scale $\delta^{13}C$ variability within the EDML core. Hence, the large $\delta^{13}C$ scatter of 0.23‰, reported by *Eyer* (2004) for EDML, cannot be confirmed with the analytical approach used in this work. However, besides numerous technical differences between the two methods one critical aspect is the sample size used for the analysis. *Eyer* (2004) measured on ice cubes with the dimensions of 2.5 cm x 2.5 cm x 1. 5 cm, whereby the shortest side with 1.5 cm was in direction of the vertical axis of the ice core. Hence, the vertical resolution was 1.5 cm, while in this study a sample comprises 4.2 cm of the ice core depth. *Eyer* (2004) argued that the large $\delta^{13}C$ scatter he found in the EDML record might be due to an ice-internal $\delta^{13}C$ variability of unknown origin, but somehow related to the annual layering of the ice core. Due to the small sample size of only 1.5 cm this signal was then resolved (*Eyer*, 2004). As the vertical depth increment for this work is almost three times that of *Eyer* (2004), it is conceivable that the smaller variability found in this study might be an effect of the larger sample size. If the assumed small scale $\delta^{13}C$ variability is a cyclical signal, then integrating over a larger depth increment might explain this observation. On the other hand, if it is a randomly distributed $\delta^{13}C$ variability, then the scatter should be invariant to the analyzed sample size. However, even the larger samples used in this study are shorter than the length of an annual layer in the Holocene. Furthermore, Holocene and LGM samples, which average over different time intervals, have the same reproducibility. From the experiences of this work, it is more likely that the large scatter found for the small sample size used in the work of *Eyer* (2004) is rather related to an unrecognized equilibration or 'side effect', similar to the anomaly measured for the first tube number in this study.

4.5 Data comparison of the absolute values

In this paragraph the measured data from the EDML ice core will be compared with existing $\delta^{13}C$ and CO_2 concentration time series from other ice cores. To compare and align the measured data with other ice core data two steps are crucial: First, correction for gravitational settling to account for fractionation in the firn column and secondly, the transfer of the data from the primary depth scale to the gas-age scale. Both steps require special attention as two different methods were applied in the literature for the gravitational settling, and further, precise dating of ice cores, especially the dating of the gas-age, is usually an ongoing effort. Besides this, note that in all previous studies the measured $\delta^{13}C$ values had been additionally corrected for the isobaric interference of N_2O during the mass spectrometric measurement, the called N_2O correction. As in this study CO_2 and N_2O were gas chromatographically separated prior to the measurement, this correction does not apply to the $\delta^{13}C$ data of this study, hence, no uncertainty is introduced from this additional correction.

4.5.1 Gravitational correction and ice core dating

The effect of gravitational settling within the firn column on both the isotopic composition and on mixing ratios of gas species can be either modeled with a firnification model, or determined empirically by measuring $\delta^{15}N$ on the ice core. Only recently, *Landais et al*. (2006) showed that although firnification models work fine for the Holocene conditions, they fail for glacial conditions at low accumulation sites of East Antarctica. For the EDML core the re-

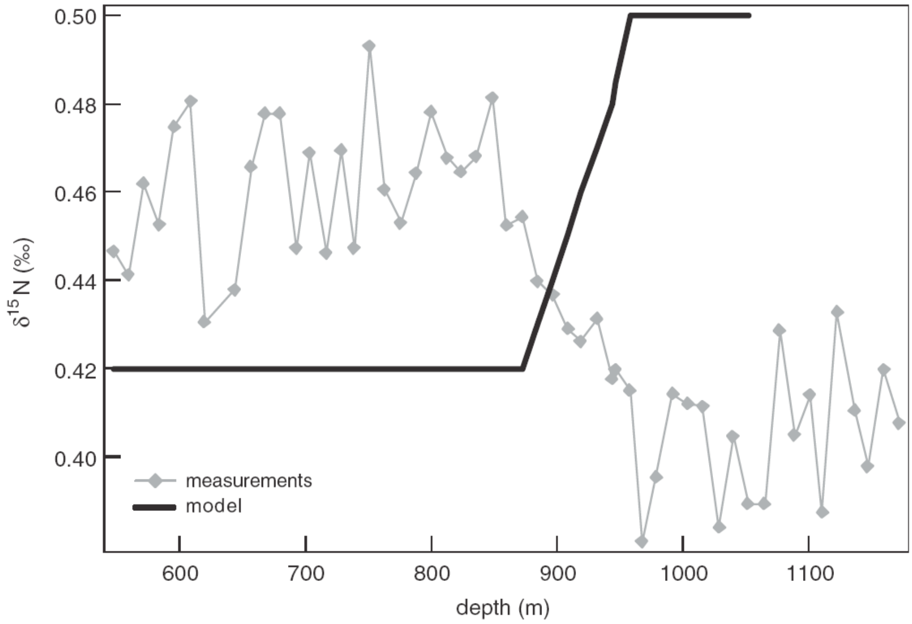

Figure 4-4 Comparison of measured $\delta^{15}N$ values from the EDML ice core (grey diamonds) with model results (black line) using a steady state approach calculating means for the Early Holocene and the Last Glacial Maximum (reproduced after *Landais et al.,* 2006).

ported mismatch between modeled and measured δ^{15}N values is ~0.1‰ for glacial conditions, and ~0.05‰ for the Holocene (Fig. 4-4). Except for rapid climate changes, δ^{15}N values can be readily used to correct δ^{13}C values as gravitational settling depends only on the absolute mass difference. If rapid climate changes produce a significant temperature gradient within the whole firn column, additionally thermal diffusion has to be taken into account (see Chapter 2.1). As rapid climate changes are not encountered in Antarctic ice (*Blunier et al.,* 1998; *EPICA community members,* 2006), gravitational correction has been reliably performed using δ^{15}N. Unfortunately, for the EDML core δ^{15}N values are only available for the depth intervals 550 m to 1200 m (see Figure 4-4, *Landais et al.,* 2006). For the Holocene δ^{13}C data, a constant value of 0.44‰, derived from the youngest δ^{15}N data of the Early Holocene, was added to the measured δ^{13}C data. This approach is justified since temperature and accumulation rate were pretty stable throughout the Holocene. For the sample depth 1056 m, a value of 0.39‰ is accessible from *Landais et al.* (2006). The standard deviation of the δ^{15}N data is 0.006‰, thus, the attributed error from the gravitational correction is negligible compared to the overall error of the δ^{13}C analysis. The gravitational correction for the CO_2 concentration is analogue to δ^{13}C and scales with δ^{15}N due to the same physical principle (Eqn. 2-2 in Chapter 2.1). Accordingly, Eqn. 3-5 was applied (*Etheridge et al.,* 1996):

$$CO_2(gravity) \quad = \quad CO_2 - \; CO_2 \cdot \frac{\delta^{15}\mathrm{N} \cdot 15.2}{1000} \qquad (3-5)$$

with CO_2(gravity) the corrected concentration, CO_2 the measured data, and the conversion factor 15.2 resulting from the mass difference between CO_2 and the average mass of air. As the absolute value of this correction is only ~1.8 ppmv for Holocene CO_2 concentrations and ~1.3 ppmv for the Glacial the resulting error is again small (~0.02 ppmv) compared to the analytical error.

Only recently, the dating and synchronization of the upper part of the EDML core was completed (*EPICA community members,* 2006). The time scales for the gas-age and ice-age were derived from a synchronization of characteristic fluctuations in the methane concentration between layer-counted Greenland ice cores and the EDML core. The basis of this approach is that a change in the methane concentration constitutes a global atmospheric signal, though its source lies mainly in the Northern Hemisphere. Further, the time scale of the EDC core is based on a glaciological flow model. Via peak matching the two EPICA ice cores were synchronized using either prominent volcanic markers, or high dust concentrations. The final outcome is a common time scale for Greenland and Antarctic ice cores, which will in the future allow to compare gas and ice records on the same time scale. The results of the ice core analyses of this work are reported on this new time scale. However, the records with which they are compared in the following were reported on individual and preliminary time scales, thus, small dating errors between the records are expected to occur.

4.5.2 Comparison with other Antarctic ice core records

First attempts to measure $\delta^{13}C$ on ice cores date back more than 20 years (*Friedli et al.,* 1984; *Friedli et al.,* 1986; *Siegenthaler et al.,* 1988), though, these early data covered very restricted time periods and were not considered for the comparison. A first highly resolved and precise $\delta^{13}C$ data set was measured on the Law Dome ice core, however, it covers only the last 1000 years (*Francey et al.,* 1999). Due to the high accumulation rate of more than 1 m at this coastal site, this core is very precisely dated. In contrast, the Taylor Dome record (*Indermühle et al.,* 1999; *Smith et al.,* 1999) spans more than 25 ka, but it lacks the high temporal resolution of the Law Dome record. The most recent $\delta^{13}C$ results were measured on the two EPICA cores, EDC and EDML (*Eyer,* 2004). Though both the EDC and the EDML $\delta^{13}C$ records possess a high temporal resolution throughout the Holocene, and in case of EDC also the late glacial, these records are difficult to interpret due to their high scatter and internal inconsistency.

Concerning the CO_2 concentration more records are available compared to $\delta^{13}C$, therefore, the most suitable CO_2 records in terms of temporal resolution and precision were selected for the comparison with the results from this study on the EDML core. From the same core, a highly resolved CO_2 concentration record measured by *Siegenthaler et al.* (2005a) covers the last 1000 years and provides an overlap with the uppermost sample depth of this study. A well resolved and precise CO_2 record from the EDC core covering the last 22 ka is used for reference by combining the EDC Holocene record (*Monnin et al.,* 2004) with data from the Last Glacial Termination (*Monnin et al.,* 2001). For the older part, a CO_2 record from Taylor Dome (*Indermühle et al.,* 2000) is used. However, the age scale for the Taylor Dome core is under debate, thus, the alignment of the Taylor Dome records with the other Antarctic ice core records should be made with caution (*Monnin et al.,* 2004).

To compare the results from this study with these records from previous studies covering contrasting time frames and different resolutions, two separate figures are discussed in the following: Figure 4-5 covers the Holocene data from this work, while Figure 4-6 includes also the data from the late glacial period. Within the uncertainty range, the CO_2 concentration measurements from this study agree well with the CO_2 results from previous studies (lower panels in Fig. 4-5 and Fig. 4-6). This is an important precondition to trust in the general suitability of the sublimation extraction technique also for the $\delta^{13}C$ analysis. Note that all CO_2 concentration records shown in Figure 4-5 and Figure 4-6 were retrieved using mechanical extraction devices, which allow for only 60-85% extraction efficiency (see Chapter 3-2).

Generally, low extraction efficiencies are associated with clathrate ice when analyzed with mechanical extraction techniques and special care has to be taken during the extraction of this ice (*Siegenthaler,* 2006).

Problems during the analysis of clathrate ice for $\delta^{13}C$ and CO_2 concentrations were reported by *Eyer* (2004). Using a mechanical cracker device, he noticed surprisingly low CO_2 concentrations for the EDC core already below a depth of 650 m, the onset of the clathrate formation. This issue is shown in Figure 4-6 (filled blue diamonds, lower panel), where the CO_2 concentrations for ages older than 26 ka BP deviate towards lower values. In parallel, the corresponding $\delta^{13}C$ values (filled blue diamonds, upper panel, Fig. 4-6) showed a higher scatter and *Eyer* (2004) reported a linear trend towards more negative $\delta^{13}C$ values with increasing depth, which he corrected from the $\delta^{13}C$ data. The comparison of the Holocene $\delta^{13}C$ data indicates that the values from this study might be shifted towards more negative $\delta^{13}C$ values compared to previous studies (Fig. 4-5). Given the large scatter of the previous studies and the

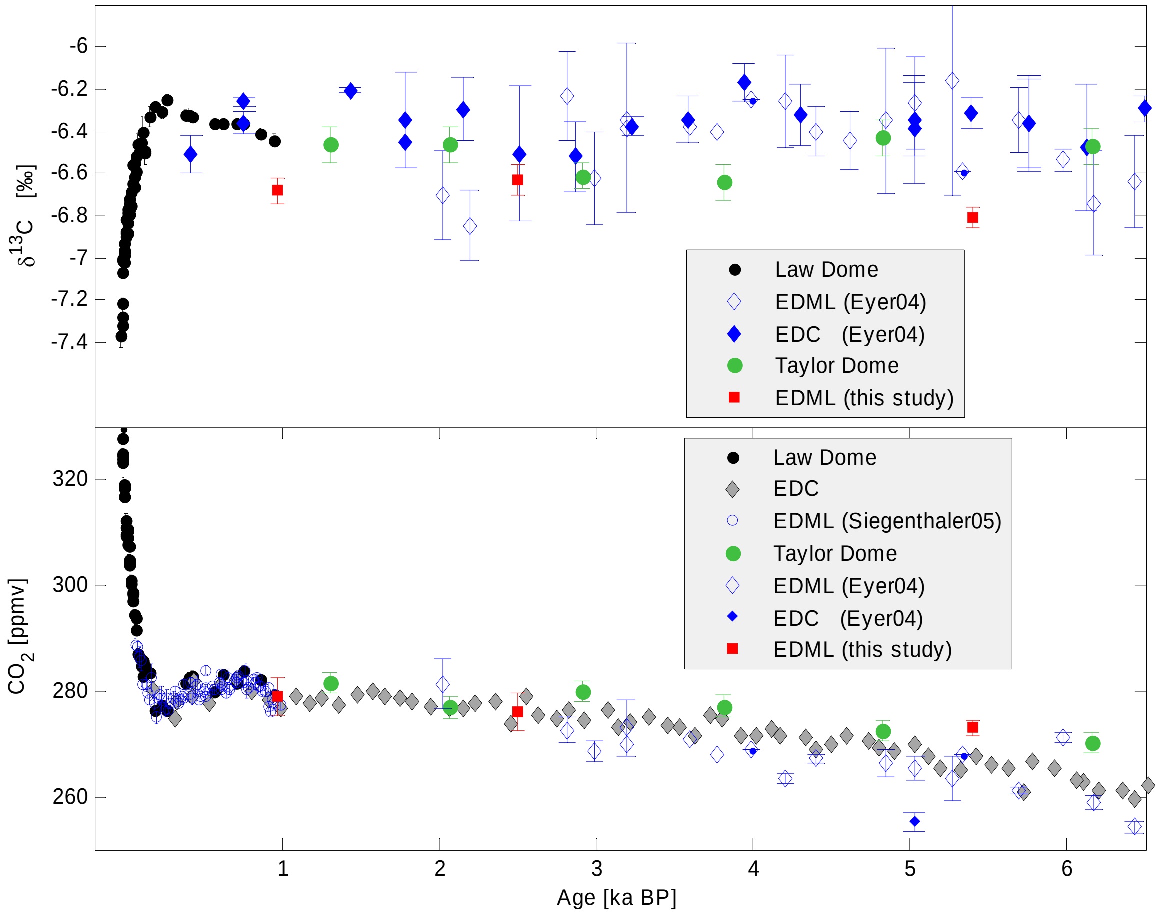

Figure 4-5 Comparison of Holocene $\delta^{13}C$ values and CO_2 concentrations analyzed on the EDML ice core described in this study (red squares) with results from previous ice core studies. Top: $\delta^{13}C$ data from Law Dome (black circles, *Francey et al.,* 1999), from *Eyer* (2004) for the EDML core (blue open diamonds) and the EDC core (blue filled diamonds), Taylor Dome (green circles, *Indermühle et al.,* 1999). Bottom: CO_2 concentrations from Law Dome (black circles, *Francey et al.,* 1999), EDC (grey diamonds, *Monnin et al.,* 2004), EDML (blue open circles, *Siegenthaler et al.,* 2005a), Taylor Dome (green circles, *Indermühle et al.,* 1999), and the corresponding CO_2 concentrations for the $\delta^{13}C$ data from *Eyer* (2004) for the EDML core (blue open diamonds) and EDC (blue filled diamonds).

limited number of $\delta^{13}C$ values of this study, an assumed off-set certainly needs confirmation by further measurements. Nevertheless, a comparison of the shallowest sample depth corresponding to around 1000 years BP, with the $\delta^{13}C$ value from Law Dome at the same age, suggests an off-set of 0.25‰.

There is little doubt in the absolute accuracy of the $\delta^{13}C$ values measured on the Law Dome ice core due to an overlap and good agreement of the ice core results with measurements made on firn air and archived atmospheric air samples (see details in *Francey et al.,* 1999). If

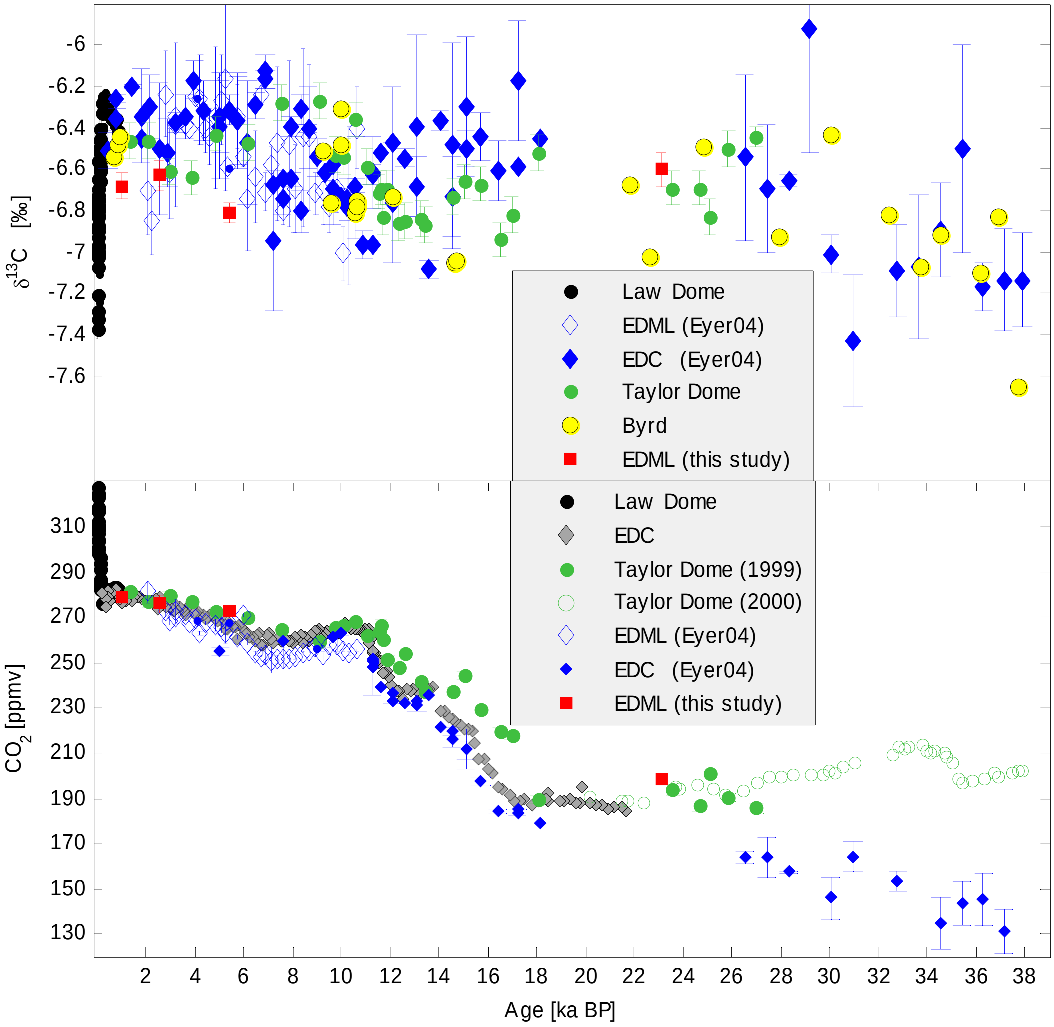

Figure 4-6 Comparison of $\delta^{13}C$ values and CO_2 concentrations from the EDML core analyzed in this study (red squares) with previous studies reaching back to 40 ka BP. Top: $\delta^{13}C$ data from Law Dome (black circles, *Francey et al.,* 1999), from *Eyer* (2004) for the EDML core (blue open diamonds) and EDC (blue filled diamonds), Taylor Dome (green circles, *Indermühle et al.,* 1999; *Smith et al.,* 1999), and Byrd ice core (yellow circles, *Leuenberger et al.,* 1992). Note that for EDC data older than 26 ka BP *Eyer* (2004) used a $\delta^{13}C$ correction to account for the lower extraction efficiency of clathrate ice. Bottom: CO_2 concentrations from Law Dome (black circles, *Francey et al.,* 1999), EDC (grey diamonds, *Monnin et al.,* 2001; *Monnin et al.,* 2004), 'Taylor Dome (1999)' are the corresponding CO_2 values to the $\delta^{13}C$ data in the upper panel (green circles, *Indermühle et al.,* 1999; *Smith et al.,* 1999), 'Taylor Dome (2000)' are additional CO_2 concentration measurements on older sections of the Taylor Dome core (green open circles, *Indermühle et al.,* 2000) and the corresponding CO_2 values for the $\delta^{13}C$ data in the upper panel from *Eyer* (2004) for the EDML core (blue open diamonds) and EDC (blue filled diamonds). Note that the EDC data older than 26 ka BP were measured on ice with clathrate formation resulting in lower CO_2 values (shown are the uncorrected values, see *Eyer* (2004) for details).

all $\delta^{13}C$ data of this work were shifted by around 0.25‰ towards heavier $\delta^{13}C$ values, the three data points within the Holocene would better fit into the envelope of the $\delta^{13}C$ results from previous studies (see Fig. 4-5). However by doing so, the $\delta^{13}C$ data point at 22 ka BP would then be isotopically too heavy and the $\delta^{13}C$ value will be in conflict with basic assumptions concerning the global carbon cycle during the glacial. Besides the multitude of processes involved with the carbon cycle (e.g. *Köhler and Fischer,* 2004), the common understanding of the paleoclimate community assumes lighter $\delta^{13}C$ values for the glacial atmosphere-ocean reservoir compared to the Holocene. Estimations about the reservoir size of the terrestrial carbon stock showed that about 500 Pg less carbon were stored on the continents as organic carbon during the glacial period, thus, isotopically light carbon was transferred to the atmosphere-ocean system (e.g. *Adams and Faure,* 1998; *Joos et al.,* 2004). These assumptions match $\delta^{13}C$ measurements on marine carbonates, which were found to be more isotopically depleted during glacial periods compared to the Holocene (*Hodell et al.,* 2003).
As the available $\delta^{13}C$ information from ice cores for the glacial period is sparse and for ages older than ~20 ka BP highly noisy due to analytical limitations, there is no firm data basis to judge whether the glacial value from his work is plausible or not (upper panel Fig. 4-6). For the Holocene measurements, however, the observed $\delta^{13}C$ discrepancy with the Law Dome record calls for a critical evaluation of a potential off-set due to methodological differences between these two approaches. These differences fall into two main categories: (1) due to the difference in the extraction technique – mechanical vs. sublimation, (2) due the applied referencing procedure.

(1) Besides various technical details in the entire analysis, above all, it is the used extraction technique that makes the largest difference between this study and all previous $\delta^{13}C$ ice core studies. Sublimation under vacuum not only releases the air trapped in bubbles or enclosed in clathrates, but also any additional fraction of CO_2 located within the ice matrix. In contrast, with mechanical techniques CO_2 is only extractable when it is either located in air bubbles, or when the clathrates decompose and release their gases. If the ice contains any additional CO_2, then this fraction should produce an off-set in the CO_2 concentration between the two extraction techniques. Two possible candidates for this 'extra CO_2' were discussed in the past: First, CO_2 produced from chemical in-situ reactions (see Chapter 2.2. for details). Secondly, CO_2 located within so called microbubbles, which, amongst other processes, might be produced during the condensation of snow crystals (*Siegenthaler et al.,* 2005a). While the $\delta^{13}C$ values for the chemically produced in-situ CO_2 might strongly vary as discussed in Chapter 2.2, CO_2 enclosed in these microbubbles should bear a $\delta^{13}C$ value similar to the atmospheric $\delta^{13}C$ signal. However, within the range of the measurement uncertainty (usually 2-3 ppmv), the CO_2 concentrations measured with the sublimation technique do not deviate from the results obtained with mechanical devices (*Siegenthaler et al.,* 2005b). Therefore, the amount of CO_2

added by any of these two processes cannot exceed a few ppmv. Based on isotopic mass balance calculations (see Fig. 2-8 for details), such a small fraction of added carbon can barely explain a $\delta^{13}C$ shift of 0.25‰ assuming reasonable $\delta^{13}C$ values for the added CO_2. A further argument against a possible in-situ contamination being the cause for the measured $\delta^{13}C$ offset is the attained precision of the $\delta^{13}C$ measurement on adjoining replicate samples (see Chapter 4.4). As the chemical species in the EDML ice core show marked annual cycles and the sample replicates cover less than an annual layer, an almost constant in-situ production of CO_2 is very unlikely to occur. From highly resolved CO_2 concentration measurements on Greenland ice cores, which are proven to be contaminated by in-situ CO_2, it is known that this in-situ CO_2 co-varies with the precursor species on a seasonal time scale (*Barnola,* 1999; *Tschumi and Stauffer,* 2000).

(2) As pointed out already, there is no doubt in the overall accuracy of the referencing strategy of the Law Dome measurements due to the convincing overlap with atmospheric air measurements analyzed with the same analytical set-up. Unfortunately, this elegant approach is not feasible with the continuous air release and trapping procedure applied in this work. Additionally, the isotopic composition of the air standard used in this study as reference basis for the ice core results is certainly not optimal because the value of -2.7‰ deviates from the mean value of the ice core samples (-6.7‰). An effect attributed to a difference in the $\delta^{13}C$ value of the air standard to the samples' value is called 'scale compression'. During intercomparison studies of isotopic reference materials it was observed that laboratories using a working standard which deviated grossly from the sample are more likely to show a systematic off-set than others (*Verkouteren,* 1999). This scale compression either results from actual calibration problems of the mass spectrometric measurement, or from an undetected contamination or sorption problem. In any case, the larger the $\delta^{13}C$ difference for sample and standard, the larger is the scale compression. For the ice core measurements planned in the near future, new air standards, calibrated and certified by NOAA/CMDL[21], will be available to improve on the current referencing situation. These two air standards have $\delta^{13}C$ values of -7.9 and -8.4‰, thus, only slightly isotopically lighter than typical samples. In turn, this enables to investigate a potential scale compression effect since air standards of contrasting isotopic composition can then be processed and compared. However, the general matrix difference between an ice sample and the reference standard procedure, being a gas mixture admitted to a cube of pure ice, still remains. To improve on this issue for future ice core measurements, a 'reference ice standard' will be analyzed in conjunction with ice core samples to provide a second reference basis additional to the air standards (see further details below).

---

[21] Climate Monitoring and Diagnostics Laboratory (CMDL) of the National Oceanic and Atmospheric Administration (NOAA) at Boulder, Colorado

4.6 Outlook

The presented analysis technique for ice cores allowed for the first time to link a quantitative extraction technique using sublimation under vacuum with a high-precision $\delta^{13}C$ measurement. It could be shown that the previously postulated small scale $\delta^{13}C$ heterogeneity found in the EDML core, which challenged the $\delta^{13}C$ approach, fortunately, could not be reproduced with this work. The reproducibility of the measured ice core samples was on average 0.06‰, which is considerably smaller than the average scatter of 0.23‰ for EDML ice, or 0.13‰ for EDC ice reported by *Eyer* (2004). Having solved this key question, the next effort will clearly focus on measuring a $\delta^{13}C$ record throughout the Holocene to address the open questions about the Holocene carbon cycle (*Claussen et al.,* 2005; *Ruddiman,* 2005; *Broecker and Stocker,* 2006). The argument is, whether the Holocene CO_2 evolution with its minimum of 260 ppmv at 7 ka BP and its later rise to a preindustrial value of 280 ppmv was due to natural equilibration of the ocean's carbonate system as proposed by *Broecker and Stocker* (2006), or due to early human activities, as proposed by *Ruddiman* (2005). In the latter case, the CO_2 increase would be connected with a decrease in atmospheric $\delta^{13}C$ due a net CO_2 flux from depleted terrestrial biomass into the atmosphere-ocean system. To answer this question, an optimized measurement scheme will be necessary to resolve the expectedly small $\delta^{13}C$ differences among the Holocene samples. With the measurement scheme applied above, which was optimized to address the question of the small scale $\delta^{13}C$ scatter, several replicates of one sample depth were analyzed collectively within a single IRMS session. Though optimized to resolve differences *within* a sample depth, the precision to resolve differences *among* different sample depths was not optimal for this purpose. This results from the fact that for each session an individual off-set from air standard measurement is calculated and subtracted from the ice core samples. Due to the uncertainty involved with this off-set (±0.06‰) and the risk of an undetected bias among different measurement sessions, best results can be obtained when different sample depths are measured within a single session. Further, a 'reference ice standard' should accompany each measurement session in addition to air standards to permit a direct comparison between sample ice and 'reference ice' processed under truly identical conditions. Using an ice core standard as an additional reference basis is now feasible since (1) this work demonstrated that the EDML ice carries a homogenous $\delta^{13}C$ composition on the centimeter-scale, thus, adjoining samples can be regarded to yield identical $\delta^{13}C$ values; (2) a newly drilled shallow ice core close to the EDML drill site allows to set aside a sufficient quantity of young and dated ice for this reference purpose. Due to the gas-age overlap with the $\delta^{13}C$ data set from Law Dome (*Francey et al.,* 1999), being the most trustworthy $\delta^{13}C$ data available so far, the measured Holocene $\delta^{13}C$ data can then be additionally tied to the Law Dome record. Defining a reference ice besides an air standard as a second tie point for $\delta^{13}C$

offers also the advantage that subtle $\delta^{13}C$ drifts of the air standard within the pressure cylinder can be identified and a change in the air standard can be better bridged. Further, it offers the possibility for intercomparison studies among different laboratories and methods.

While measuring a precise $\delta^{13}C$ record in the bubble ice of the Holocene can reveal the riddle of the unresolved CO_2 anomaly of the Early Holocene, the actual strength of this new method lies in the climate history enclosed in clathrate ice. Only a small proportion of the atmosphere's climate history is stored in bubble ice, thus is accessible with current mechanical extraction devices. For the EDML ice core bubble ice covers only the first ~700 m core section or 15 ka from an age of around 150 ka in 2400 m (*EPICA community members,* 2006). The grand questions to be answered with $\delta^{13}C$ data are the identification and quantification of the underlying processes driving the prominent glacial/interglacial CO_2 difference of about 80 ppmv. Further, the EDC ice core reaches back to eight glacial cycles and offers the chance to compare the driving processes between the large 100 ka cycles and the proceeding 40 ka cycles with so called lukewarm interglacials.

References

Adachi Y, Kawamura K, Armi L, Keeling RF. Diffusive separation of the lower atmosphere. *Science* 2006; 311: 1429.

Adams JM, Faure H. A new estimate of changing carbon storage on land since the last glacial maximum, based on global land ecosystem reconstruction. *Global and Planetary Change* 1998; 16-17: 3.

Allison CE, Francey RJ, Meijer HAJ. Recommendations for the reporting of stable isotope measurements of carbon and oxygen in CO_2 gas. Reference and intercomparison materials for stable isotopes in light elements. *In: Proceedings of IAEA consultants' meeting, Vienna, Austria, 1-3 December 1993. IAEA-TECDOC-825, International Atomic Energy Agency, Vienna.* 1995; 155.

Anklin M, Barnola J-M, Schwander J, Stauffer B, Raynaud D. Processes affecting the CO_2 concentrations measured in Greenland ice. *Tellus* 1995; 47: 461.

Archer D, Winguth A, Lea D, Mahowald N. What caused the glacial/interglacial atmospheric pCO_2 cycles? *Reviews of Geophysics* 2000; 38: 159.

Arens NC, Jahren AH, Amundson R. Can C3 plants faithfully record the carbon isotopic composition of atmospheric carbon dioxide? *Paleobiology* 2000; 26: 137.

Arrhenius. On the Influence of Carbonic Acid upon the Temperature of the Ground. *Philosophical Magazine 41* 1896; 237.

Barnes PRF, Wolff EW, Mallard DC, Mader HM. SEM Studies of the Morphology and Chemistry of Polar Ice. *Microscopy Research and Technique* 2003; 62: 62.

Barnola JM. Status of the atmospheric CO_2 reconstruction from ice core analyses. *Tellus, Series B: Chemical and Physical Meteorology* 1999; 51: 151.

Bender M, Sowers T, Barnola J-M, Chappellaz J. Changes in the O_2/N_2 ratio of the atmosphere during recent decades reflected in the composition of air in the firn at Vostok Station, Antarctica. *Geophysical Research Letters* 1994; 21: 189.

Bender M, Sowers T, Lipenkov V. On the concentrations of O_2, N_2, and Ar in trapped gases from ice cores. *Journal of Geophysical Research* 1995; 100:

Bender ML. Orbital tuning chronology for Vostok climate record supported by trapped gas composition. *Earth and Planetary Science Letters* 2002; 204: 275.

Bernard S, Röckmann T, Kaiser J, Barnola JM, Fischer H, Blunier T, Chappellaz J. Constraints on N_2O budget changes since pre-industrial time from new firn air and ice core isotope measurements. *Atmospheric Chemistry and Physics* 2006; 6: 493.

Bintanja R, Van De Wal RSW, Oerlemans J. Modelled atmospheric temperatures and global sea levels over the past million years. *Nature* 2005; 437: 125.

Blunier T, Chappellaz J, Schwander J, Dällenbach A, Stauffer B, Stocker TF, Raynaud D, Jouzel J, Clausen HB, Hammer CU, Johnson SJ. Asynchrony of Antarctic and Greenland climate change during the last glacial period. *Nature* 1998; 394: 739.

Brand WA. High precision isotope ratio monitoring techniques in mass spectrometry. *Journal of Mass Spectrometry* 1996; 31: 225.

Brenninkmeijer CAM. Automated Variable Temperature Liquid Nitrogen Cold Trap. *Analytical Chemistry* 1982; 54: 2622.

Brenninkmeijer CAM, Janssen C, Kaiser J, Röckmann T, Rhee TS, Assonov SS. Isotope Effects in the Chemistry of Atmospheric Trace Compounds. *Chemical Reviews* 2003; 103: 5125.

Broecker WS, Clark E. Holocene atmospheric CO_2 increase as viewed from the seafloor. *Global Biogeochemical Cycles* 2003; 17: 1052.

Broecker WS, Peng T-H. The role of $CaCO_3$ compensation in the glacial to interglacial atmospheric CO_2 change. *Global Biogeochemical Cycles* 1987; 1: 15.

Broecker WS, Stocker TF. The Holocene CO_2 Rise: Anthropogenic or Natural? *EOS* 2006; 87: 26.

Brovkin V, Hofmann M, Bendtsen J, Ganopolski A. Ocean biology could control atmospheric $\delta^{13}C$ during glacial-interglacial cycle. *Geochemistry, Geophysics, Geosystems* 2002; 3: 1.

Brunet F, Gaiero D, Probst JL, Depetris PJ, Lafaye FG, Stille P. $\delta^{13}C$ tracing of dissolved inorganic carbon sources in Patagonian rivers (Argentina). *Hydrological Processes* 2005; 19: 3321.

Buchmann N, Brooks JR, Rapp KD, Ehleringer JR. Carbon isotope composition of C4 grasses is influenced by light and water supply. *Plant, Cell and Environment* 1996; 19: 392.

Caillon N, Severinghaus JP, Barnola JM, Chappellaz J, Jouzel J, Parrenin F. Estimation of temperature change and of gas age - Ice age difference, 108 kyr B.P., at Vostok, Antarctica. *Journal of Geophysical Research D: Atmospheres* 2001; 106: 31893.

Cerling TE, Quade J, Wang Y, Bowman JR. Carbon isotopes in soils and palaeosols as ecology and palaeoecology indicators. *Nature* 1989; 341: 138.

Chappellaz J, Blunier T, Kints S, Dällenbach A, Barnola J-M, Schwander J, Raynaud D, Stauffer B. Changes in the atmospheric CH_4 gradient between Greenland and Antarctica during the Holocene. *Journal of Geophysical Research* 1997; 102: 15987.

Chebbi A, Carlier P. Carboxylic acids in the troposphere, occurrence, sources, and sinks: A review. *Atmospheric Environment* 1996; 30: 4233.

Ciais P, Denning AS, Tans PP, Berry JA, Randall DA, Collatz GJ, Sellers PJ, White JWC, Trolier M, Meijer HAJ, Francey RJ, Monfray P, Heimann M. A three-dimensional synthesis study of $\delta^{18}O$ in atmospheric CO_2 1. Surface fluxes. *Journal of Geophysical Research D: Atmospheres* 1997; 102: 5857.

Ciais P, Tans PP, White JWC, Trolier M, Francey RJ, Berry JA, Randall DR, Sellers PJ, Gollatz JG, Schimel DS. Partitioning of ocean and land uptake of CO_2 as inferred by $\delta^{13}C$ measurements from the NOAA Climate Monitoring and Diagnostics Laboratory Global Air Sampling Network. *Journal of Geophysical Research* 1995; 100: 5051.

Claussen M, Brovkin V, Calov R, Ganopolski A, Kubatzki C. Did humankind prevent a Holocene glaciation? Comment on Ruddiman's hypothesis of a Pre-Historic Anthropocene. *Climatic Change* 2005; 69: 409.

Colbeck SC. Air movement in snow due to windpumping. *Journal of Glaciology* 1989; 35: 209.

Coleman D. Fractionation in inlet system, December 9th 1996. *Archives of ISOGEOCHEM@LIST.UVM.EDU, http://list.uvm.edu/archives/isogeochem.html* 1996;

Coleman DD. Tube Cracker for Opening Samples Sealed in Glass Tubing. *Analytical Chemistry* 1981; 53: 1962.

Craig H. Isotopic standards for carbon and oxygen and correction factors for mass-spectrometric analysis of carbon dioxide. *Geochimica et Cosmochimica Acta* 1957; 12: 133.

Craig H, Horibe Y, Sowers T. Gravitational separation of gases and isotopes in polar ice caps. *Science* 1988; 242: 1675.

Curry WB, Duplessy JC, Labeyrie LD, Shackleton NJ. Changes in the distribution of $\delta^{13}C$ of deep water ΣCO_2 between the last glaciation and the Holocene. *Paleoceanography* 1988; 3: 317.

Dargaville RJ, Doney SC, Fung IY. Inter-annual variability in the interhemispheric atmospheric CO_2 gradient: Contributions from transport and the seasonal rectifier. *Tellus, Series B: Chemical and Physical Meteorology* 2003; 55: 711.

Delmas R. A natural artefact in Greenland ice-core CO_2 measurements. *Tellus* 1993; 45: 391.

Des Marais DJ, Hayes JM. Tube Cracker for Opening Glass-Sealed Ampoules under Vacuum. *Analytical Chemistry* 1976; 48: 1651.

Ding ZL, Yang SL. C3/C4 vegetation evolution over the last 7.0 Myr in the Chinese Loess Plateau: Evidence from pedogenic carbonate $\delta^{13}C$. *Palaeogeography, Palaeoclimatology, Palaeoecology* 2000; 160: 291.

EPICA community members. One-to-one interhemispheric coupling of millennial polar climate variability during the last glacial. *Nature* 2006; submitted.

Etheridge DM, Steele LP, Langenfelds RL, Francey RJ, Barnola J-M, Morgan VI. Natural and anthropogenic changes in atmospheric CO_2 over the last 1000 years from air in Antarctic ice and firn. *Journal of Geophysical Research* 1996; 101: 4115.

Eyer M. Highly resolved $\delta^{13}C$ measurements on CO_2 in air from Antarctic ice cores. *Dissertation University Bern* 2004;

Ferretti DF, Lowe DC, Martin RJ, Brailsford GW. A new gas chromatograph-isotope ratio mass spectrometry technique for high-precision, N_2O-free analysis of $\delta^{13}C$ and $\delta^{18}O$ in atmospheric CO_2 from small air samples. *Journal of the Geophysical Research* 2000; 105: 6709.

Fischer H, Wahlen M, Smith HJ. Reconstruction of glacial/interglacial changes in the global carbon cycle from CO_2 and $\delta^{13}CO_2$ in Antarctic ice cores. *Memoirs of the National Institute for Polar Research* 2003; 57: 121.

Fischer H, Wahlen M, Smith J, Mastroianni D, Deck B. Ice core records of atmospheric CO_2 around the last three glacial terminations. *Science* 1999; 283: 1712.

Flückiger J, Blunier T, Stauffer B, Chappellaz J, Spahni R, Kawamura K, Schwander J, Stocker TF, Dahl-Jensen D. N_2O and CH_4 variations during the last glacial path epoch: Insight into global processes. *Global Biogeochemical Cycles* 2004; 18:

Flückiger J, Dällenbach A, Blunier T, Stauffer B, F. ST, Raynaud D, Barnola J-M. Variations in atmospheric N_2O concentration during abrupt climatic changes. *Science* 1999; 285: 227.

Francey RJ. Tasmanian tree rings belie suggested anthropogenic $^{13}C/^{12}C$ trends. *Nature* 1981; 290: 232.

Francey RJ, Allison CE, Etheridge DM, Trudinger CM, Enting IG, Leuenberger M, Langenfelds RL, Michel E, Steele LP. A 1000-year high precision record of $\delta^{13}C$ in atmospheric CO_2. *Tellus* 1999; 51B: 170.

Francey RJ, Farquhar GD. An explanation of $^{13}C/^{12}C$ variations in tree rings. *Nature* 1982; 297: 28.

Freitag J, Dobrindt U, Kipfstuhl J. A new method for predicting transport properties of polar firn with respect to gases on the pore-space scale. *Annals of Glaciology* 2002; 35: 538.

Freitag J, Wilhelms F, Kipfstuhl S. Microstructure-dependent densification of polar firn derived from X-ray microtomography. *Journal of Glaciology* 2004; 50: 243.

Frey MM, Stewart RW, McConnell JR, Bales RC. Atmospheric hydroperoxides in West Antarctica: Links to stratospheric ozone and atmospheric oxidation capacity. *Journal of Geophysical Research D: Atmospheres* 2005; 110: 1.

Friedli H, Lötscher H, Oeschger H, Siegenthaler U, Stauffer B. Ice core record of the $^{13}C/^{12}C$ ratio of atmospheric CO_2 in the past two centuries. *Nature* 1986; 324: 237.

Friedli H, Moor E, Oeschger H, Siegenthaler U, Stauffer B. $^{13}C/^{12}C$ ratios in CO_2 extracted from Antarctic ice. *Geophysical Research Letters* 1984; 11: 1145.

Ghosh P, Brand WA. Stable isotope ratio mass spectrometry in global climate change research. *International Journal of Mass Spectrometry* 2003; 228: 1.

Ghosh P, Brand WA. The effect of N_2O on the isotopic composition of air-CO_2 samples. *Rapid Communications In Mass Spectrometry* 2004; 18: 1830.

Gillett RW, Van Ommen TD, Jackson AV, Ayers GP. Formaldehyde and peroxide concentrations in Law Dome (Antarctica) firn and ice cores. *Journal of Glaciology* 2000; 46: 15.

Goldstein AH, Shaw SL. Isotopes of Volatile Organic Compounds: An Emerging Approach for Studying Atmospheric Budgets and Chemistry. *Chemical Reviews* 2003; 103: 5025.

Goujon C, Barnola JM, Ritz C. Modelling the densification of polar firn including heat diffusion: Application to close-off characteristics and gas isotopic fractionation for Antarctica and Greenland sites. *Journal of Geophysical Research D: Atmospheres* 2003; 108:

Grachev AM, Severinghaus JP. Laboratory determination of thermal diffusion constants for $^{29}N_2/^{28}N_2$ in air at temperatures from -60 to 0°C for reconstruction of magnitudes of abrupt climate changes using the ice core fossil-air plaeothermometer. *Geochimica et Cosmochimica Acta* 2003; 67: 345.

Guimbaud C, Grannas AM, Shepson PB, Fuentes JD, Boudries H, Bottenheim JW, Domine F, Houdier S, Perrier S, Biesenthal TB, Splawn BG. Snowpack processing of acetaldehyde and acetone in the Arctic atmospheric boundary layer. *Atmospheric Environment* 2002; 36: 2743.

Güllük T, Slemr F, Stauffer B. Simultaneous measurement of CO_2, CH_4, and N_2O in air extracted by sublimation from Antarctica ice cores: Confirmation of the data obtained using other extraction techniques. *Journal of the Geophysical Research* 1998; 103: 15971.

Haan D, Raynaud D. Ice core record of CO variations during the last two millennia: atmospheric implications and chemical interactions within the Greenland ice. *Tellus, Series B: Chemical and Physical Meteorology* 1998; 50B: 253.

Hall JA, Barth JAC, Kalin RM. Routine Analysis by High Precision Gas Chromatography/Mass Selective Detector/Isotope Ratio Mass Spectrometry to 0.1 Parts Per Mil. *Rapid Communications In Mass Spectrometry* 1999; 13: 1231.

Halsted RE, Nier AO. Gas Flow through the Mass Spectrometer Viscous Leak. *The Review of Scientific Instruments* 1950; 21: 1019.

Hobbie EA, Werner RA. Intramolecular, compound-specific, and bulk carbon isotope patterns in C3 and C4 plants: a review and synthesis. *New Phytologist* 2004; 161: 371.

Hodell DA, Venz KA, Charles CD, Ninnemann US. Pleistocene vertical carbon isotope and carbonate gradients in the South Atlantic sector of the Southern Ocean. *Geochemistry Geophysics Geosystems* 2003; 4:

Honig RE. Gas Flow in the Mass Spectrometer. *Journal of Applied Physics* 1945; 16: 646.

Houdier S, Perrier S, Domine F, Cabanes A, Legagneux L, Grannas AM, Guimbaud C, Shepson PB, Boudries H, Bottenheim JW. Acetaldehyde and acetone in the Arctic snowpack during the ALERT2000 campaign. Snowpack composition, incorporation processes and atmospheric impact. *Atmospheric Environment* 2002; 36: 2609.

Huber C, Beyerle U, Leuenberger M, Schwander J, Kipfer R, Spahni R, Severinghaus JP, Weiler K. Evidence for molecular size dependent gas fractionation in firn air derived from noble gases, oxygen, and nitrogen measurements. *Earth and Planetary Science Letters* 2006; 243: 61.

Hutterli MA, McConnell JR, Bales RC, Stewart RW. Sensitivity of hydrogen peroxide (H_2O_2) and formaldehyde (HCHO) preservation in snow to changing environmental conditions: Implications for ice core records. *Journal of Geophysical Research D: Atmospheres* 2003; 108:

Ikeda-Fukazawa T, Fukumizu K, Kawamura K, Aoki K, Nakagawa T, Hondoh T. Effects of molecular diffusion on trapped gas composition in polar ice cores. *Earth and Planetary Science Letters* 2005; 229: 183.

Ikeda-Fukazawa T, Hondoh T, Fukumura T, Fukazawa H, Mae S. Variation in N_2/O_2 ratio of occluded air in Dome Fuji Antarctic ice. *Journal of Geophysical Research* 2001; 106: 17799.

Ikeda-Fukazawa T, Kawamura K, Hondoh T. Mechanism of molecular diffusion in ice crystals. *Molecular Simulation* 2004; 30: 973.

Ikeda T, Fukazawa H, Mae S, Pepin L, Duval P, Champagnon B, Lipenkov VY, Hondoh T. Extreme fractionation of gases caused by formation of clathrate hydrates in Vostok Antarctic ice. *Geophysical Research Letters* 1999; 26: 91.

Indermühle A, Monnin E, Stauffer B, Stocker TF, Wahlen M. Atmospheric CO_2 concentration from 60 to 20 kyr BP from the Taylor Dome ice core, Antarctica. *Geophysical Research Letters* 2000; 27: 735.

Indermühle A, Stocker TF, Joos F, Fischer H, Smith HJ, Wahlen M, Deck B, Mastroianni D, Tschumi J, Blunier T, Meyer R, Stauffer B. Holocene carbon-cycle dynamics based on CO_2 trapped in ice at Taylor Dome, Antarctica. *Nature* 1999; 398: 121.

Joos F, Gerber S, Prentice IC, Otto-Bliesner BL, Valdes PJ. Transient simulations of Holocene atmospheric carbon dioxide and terrestrial carbon since the Last Glacial Maximum. *Global Biogeochemical Cycles* 2004; 18:

Jouzel J, Vimeux F, Caillon N, Delaygue G, Hoffmann G, Masson-Delmotte V, Parrenin F. Magnitude of isotope/temperature scaling for interpretation of central Antarctic ice cores. *Journal of Geophysical Research D: Atmospheres* 2003; 108:

Kaspers KA, van de Wal RSW, van den Broeke MR, Schwander J, van Lipzig NPM, Brenninkmeijer CAM. Model calculations of the age of firn air across the Antarctic continent. *Atmospheric Chemistry and Physics* 2004; 4: 1365.

Kawamura K, Nakazawa T, Aoki S, Sugawara S, Fujii Y, Watanabe O. Atmospheric CO2 variations over the last three glacial-interglacial climatic cycles deduced from the Dome Fuji deep ice core, Antarctica using a wet extraction technique. *Tellus B* 2003; 55: 126.

Kawamura K, Severinghaus JP, Ishidoya S, Sugawara S, Hashida G, Motoyama H, Fujii Y, Aoki S, Nakazawa T. Convective mixing of air in firn at four polar sites. *Earth and Planetary Science Letters* 2006; 244: 672.

Kawamura K, Yokoyama K, Fujii Y, Watanabe O. A Greenland ice core record of low molecular weight dicarboxylic acids, ketocarboxylic acids, and dicarbonyls: A trend from little ice age to the present (1540 to 1989 A.D.). *Journal of Geophysical Research D: Atmospheres* 2001; 106: 1331.

Keeling CD, Whorf TP. Trends: A compendium of data on global change. In Carbon Dioxide Information Analysis Center, Oak Ridge National Laboratory: Oak Ridge, TN, 2000;

Kennedy H, Kennedy DP. Simplified tube cracker for opening samples sealed in glass tubes while under vacuum. *Analytical Proceedings Including Analytical Communications* 1994; 31: 299.

Keppler F, Kalin RM, Harper DB, McRoberts WC, Hamilton JTG. Carbon isotope anomaly in the major plant C1 pool and its global biogeochemical implications. *Biogeosciences* 2004; 1: 123.

Köhler P, Fischer H. Simulating changes in the terrestrial biosphere during the last glacial/interglacial transition. *Global and Planetary Change* 2004; 43: 33.

Köhler P, Fischer H, Munhoven G, Zeebe RE. Quantitative interpretation of atmospheric carbon records over the last glacial termination. *Global Biogeochemical Cycles* 2005a; 19:

Köhler P, Joos F, Gerber S, Knutti R. Simulated changes in vegetation distribution, land carbon storage, and atmospheric CO_2 in response to a collapse of the North Atlantic thermohaline circulation. *Climate Dynamics* 2005b; 25: 689.

Kuhs WF, Chazallon B, Radaelli PG, Pauer F. Cage occupancy and compressibility of deuterated N_2-clathrate hydrate by neutron diffraction. *Journal of Inclusion Phenomena* 1997; 29: 65.

Landais A, Barnola JM, Kawamura K, Caillon N, Delmotte M, Van Ommen T, Dreyfus G, Jouzel J, Masson-Delmotte V, Minster B. Firn-air $\delta^{15}N$ in modern polar sites and glacial-interglacial ice: a model-data mismatch during glacial periods in Antarctica? *Quaternary Science Reviews* 2006; 25: 49.

Leckrone KJ, Hayes JM. Efficiency and Temperature Dependence of Water Removal by Membrane Dryers. *Analytical Chemistry* 1997; 69: 911.

Leckrone KJ, Hayes JM. Water-Induced Errors in Continuous-Flow Carbon Isotope Ratio Mass Spectrometry. *Analytical Chemistry* 1998; 70: 2737.

Leuenberger M, Siegenthaler U, Langway CC. Carbon isotope composition of atmospheric CO_2 during the last ice age from an Antarctic ice core. *Nature* 1992; 357: 488.

Leuenberger MC, Eyer M, Nyfeler P, Stauffer B, Stocker TF. High-resolution $\delta^{13}C$ measurement on ancient air extracted from less than 10 cm^3 of ice. *Tellus* 2003; 55B: 138.

Lichtfouse E. Compound-specific isotope analysis. Application to archaeology, biomedical sciences, biosynthesis, environment, extraterrestrial chemistry, food science, forensic science, humic substances, microbiology, organic geochemistry, soil science and sport. *Rapid Communications In Mass Spectrometry* 2000; 14: 1337.

Linke H, Alemán BJ, Melling LD, Taormina MJ, Francis MJ, Dow-Hygelund CC, Narayanan V, Taylor RP, Stout A. Self-propelled leidenfrost droplets. *Physical Review Letters* 2006; 96:

Lloyd J, Farquhar GD. ^{13}C discrimination during CO_2 assimilation by the terrestrial biosphere. *Oecologia* 1994; 99: 201.

Marino BD, McElroy MB, Salawitch RJ, Spaulding WG. Glacial-to-interglacial variations in the carbon isotopic composition of atmospheric CO_2. *Nature* 1992; 357: 461.

Mariotti A. Atmospheric nitrogen is a reliable standard for natural ^{15}N abundance measurements. *Nature* 1983; 303: 685.

Meier-Augenstein W. Review: Applied gas chromatography coupled to isotope ratio mass spectrometry. *Journal of Chromatography A* 1999; 842: 351.

Meier-Augenstein W, Watt P, Langhans C. Influence of Gas Chromatographic Parameters on Measurement of $^{13}C/^{12}C$ Isotope Ratios by Gas-Liquid Chromatography-Combustion Isotope Ratio Mass spectrometry. *Journal of Chromatography A* 1996; 752: 233.

Merritt DA, Hayes JM. Factors Controlling Precision and Accuracy in Isotope-Ratio-Monitoring Mass Spectrometry. *Analytical Chemistry* 1994; 66: 2336.

Monnin E. CO_2 Konzentrationsmessungen an polaren Eiskernen insbesondere am Eisbohrkern Dome Concordia, Antarktis. *Master thesis, Physikalisches Institut, Universität Bern* 2000;

Monnin E, Indermühle A, Dällenbach A, Flückiger J, Stauffer B, Stocker TF, Raynaud D, Barnola J-M. Atmospheric CO_2 concentration over the last termination. *Science* 2001; 291: 112.

Monnin E, Steig EJ, Siegenthaler U, Kawamura K, Schwander J, Stauffer B, Stocker TF, Morse DL, Barnola JM, Bellier B, Raynaud D, Fischer H. Evidence for substantial accumulation rate variability in Antarctica during the Holocene, through synchronization of CO_2 in the Taylor Dome, Dome C and DML ice cores. *Earth and Planetary Science Letters* 2004; 224: 45.

Mook WG. ^{13}C in atmospheric CO_2. *Netherlands Journal of Sea Research* 1986; 20: 211.

Mook WG. Environmental Isotopes in the Hydrological Cycle; Principles and Applications (Volume I: Introduction - Theory, Methods, Review). *UNESCO/IAEA, Paris,* 2000;

Narukawa M, Kawamura K, Li SM, Bottenheim JW. Dicarboxylic acids in the Arctic aerosols and snowpacks collected during ALERT 2000. *Atmospheric Environment* 2002; 36: 2491.

Norton GA. Improved tube cracker for opening vacuum-sealed glass tubes. *Radiocarbon* 2005; 47: 177.

O'Leary MH. Carbon isotope fractionation in plants. *Phytochemistry* 1981; 20: 553.

Ohno H, Igarashi M, Hondoh T. Salt inclusions in polar ice core: Location and chemical form of water-soluble impurities. *Earth and Planetary Science Letters* 2005; 232: 171.

Ohno H, Igarashi M, Hondoh T. Characteristics of salt inclusions in polar ice from Dome Fuji, East Antarctica. *Geophysical Research Letters* 2006; 33:

Perrier S, Houdier S, Domine F, Cabanes A, Legagneux L, Sumner AL, Shepson PB. Formaldehyde in Arctic snow. Incorporation into ice particles and evolution in the snowpack. *Atmospheric Environment* 2002; 36: 2695.

Petit JR, Jouzel J, Raynaud D, Barkov NI, Barnola J-M, Basile I, Bender M, Chappellaz J, Davis M, Delaygue G, Delmotte M, Kotlyakov VM, Legrand M, Lipenkov VY, Lorius C, Pepin L, Ritz C, Saltzman E, Stievenard M. Climate and atmospheric history of the past 420,000 years from the Vostok ice core, Antarctica. *Nature* 1999; 399: 429.

Ribas-Carbo M, Still C, Berry J. Automated system for simultaneous analysis of ^{13}C, ^{18}O and CO_2 concentrations in small air samples. *Rapid Communications In Mass Spectrometry* 2002; 16: 339.

Rice AL, Gotoh AA, Ajie HO, Tyler SC. High-precision continuous-flow measurement of $\delta^{13}C$ and δD of atmospheric CH_4. *Analytical Chemistry* 2001; 73: 4104.

Riedel K, Allan W, Weller R, Schrems O. Discrepancies between formaldehyde measurements and methane oxidation model predictions in the Antarctic troposphere: An assessment of other possible formaldehyde sources. *Journal of Geophysical Research D* 2005; 110: 1.

Röckmann T, Kaiser J, Brenninkmeijer CAM, Crowley JN, Borchers R, Brand WA, Crutzen PJ. Isotopic enrichment of nitrous oxide ($^{15}N^{14}NO$, $^{14}N^{15}NO$, $^{14}N^{14}N^{18}O$) in the stratosphere and in the laboratory. *Journal of Geophysical Research D* 2001; 106: 10403.

Rommelaere V, Arnaud L, Barnola J-M. Reconstructing recent atmospheric trace gas concentrations from polar firn and bubbly ice data by inverse methods. *Journal of Geophysical Research* 1997; 102: 30.

Ruddiman WF. The anthropogenic greenhouse era began thousands of years ago. *Climatic Change* 2003; 61: 261.

Ruddiman WF. The early anthropogenic hypothesis a year later: An editorial reply. *Climatic Change* 2005; 69: 427.

Salamatin AN, Lipenkov VY, Ikeda-Fukazawa T, Hondoh T. Kinetics of air-hydrate nucleation in polar ice sheets. *Journal of Crystal Growth* 2001; 223: 285.

Santrock J, Studley SA, Hayes JM. Isotopic analyses based on the mass spectrum of carbon dioxide. *Analytical Chemistry* 1985; 57: 1444.

Schaefer H. Stable Carbon Isotopic Composition of Methane from Ancient Ice Samples. *Dissertation, University of Victoria,* 2005;

Schlitzer R. Carbon export fluxes in the Southern Ocean: Results from inverse modeling and comparison with satellite-based estimates. *Deep-Sea Research Part II: Topical Studies in Oceanography* 2002; 49: 1623.

Schmitt J, Glaser B, Zech W. Amount-dependent isotopic fractionation during compound-specific isotope analysis. *Rapid Communications In Mass Spectrometry* 2003; 17: 970.

Schwander J, Barnola J-M, Andrié C, Leuenberger M, Ludin A, Raynaud D, Stauffer B. The age of the air in the firn and the ice at Summit, Greenland. *Journal of Geophysical Research* 1993; 98: 2831.

Schwander J, Stauffer B, Sigg A. Air mixing in firn and the age of the air at pore close-off. *Annals of Glaciology* 1988; 10: 141.

Severinghaus JP, Battle MO. Fractionation of gases in polar ice during bubble close-off: New constraints from firn air Ne, Kr and Xe observations. *Earth and Planetary Science Letters* 2006; 244: 474.

Severinghaus JP, Bender ML, Keeling RF, Broecker WS. Fractionation of soil gases by diffusion of water vapor, gravitational settling, and thermal diffusion. *Geochimica et Cosmochimica Acta* 1996; 60: 1005.

Severinghaus JP, Grachev A, Battle M. Thermal fractionation of air in polar firn by seasonal temperature gradients. *Geochemistry, Geophysics, Geosystems* 2001; 2: 146.

Severinghaus JP, Grachev A, Luz B, Caillon N. A method for precise measurement of argon 40/36 and krypton/argon ratios in trapped air in polar ice with applications to past firn thickness and abrupt climate change in Greenland and at Siple Dome, Antarctica. *Geochimica et Cosmochimica Acta* 2003; 67: 325.

Severinghaus JP, Sowers T, Brook EJ, Alley RB, Bender ML. Timing of abrupt climate change at the end of the Younger Dryas interval from thermally fractionated gases in polar ice. *Nature* 1998; 391: 141.

Siegenthaler U. CO_2-Konzentrationsmessungen an polaren Eisbohrkernen und Tests mit einer neuen Extraktionsmethode, Diplomarbeit, Bern. *unpublished* 2002;

Siegenthaler U. Atmosphärische CO_2-Messungen der letzten 650.000 Jahre anhand von Messungen an Antarktischen Eisbohrkernen. *Dissertation, University of Bern* 2006;

Siegenthaler U, Friedli H, Loetscher H, Moor E, Neftel A, Oeschger H, Stauffer B. Stable-isotope ratios and concentration of CO_2 in air from polar ice cores. *Annals of Glaciology* 1988; 10: 151.

Siegenthaler U, Monnin E, Kawamura K, Spahni R, Schwander J, Stauffer B, Stocker TF, Barnola J-M, Fischer H. Supporting evidence from the EPICA Dronning Maud Land ice core for atmospheric CO_2 changes during the past millennium. *Tellus* 2005a; 57: 51.

Siegenthaler U, Stocker TF, Monnin E, Lüthi D, Schwander J, Stauffer B, Raynaud D, Barnola JM, Fischer H, Masson-Delmotte V, Jouzel J. Atmospheric science: Stable carbon cycle-climate relationship during the late Pleistocene. *Science* 2005b; 310: 1313.

Sigman DM, Boyle EA. Glacial/interglacial variations in atmospheric carbon dioxide. *Nature* 2000; 407: 859.

Smith HJ, Fischer H, Wahlen M, Mastroianni D, Deck B. Dual modes of the carbon cycle since the Last Glacial Maximum. *Nature* 1999; 400: 248.

Smith HJ, Wahlen M, Mastroianni D, Taylor K, Mayewski P. The CO2 concentration of air trapped in Greenland Ice Sheet Project 2 ice formed during periods of rapid climate change. *Journal of Geophysical Research* 1997a; 102: 26577.

Smith HJ, Wahlen M, Mastroianni D, Taylor KC. The CO_2 concentration of air trapped in GISP2 ice from the Last Glacial Maximum-Holocene transition. *Geophysical Research Letters* 1997b; 24: 1.

Sowers T, Bender M, Raynaud D, Korotkevich YS. $\delta^{15}N$ of N_2 in air trapped in polar ice: a tracer of gas transport in the firn and a possible constraint on ice age-gas age differences. *Journal of Geophysical Research* 1992; 97:

Sowers T, Bernard S, Aballain O, Chappellaz J, Barnola JM, Marik T. Records of the $\delta^{13}C$ of atmospheric CH_4 over the last 2 centuries as recorded in Antarctic snow and ice. *Global Biogeochemical Cycles* 2005; 19: 1.

Spahni R, Chappellaz J, Stocker TF, Loulergue L, Hausammann G, Kawamura K, Flückiger J, Schwander J, Raynaud D, Masson-Delmotte V, Jouzel J. Atmospheric science: Atmospheric Methane and Nitrous Oxide of the Late Pleistocene from Antarctic Ice Cores. *Science* 2005; 310: 1317.

Spahni R, Schwander J, Flückiger J, Stauffer B, Chappellaz J, Raynaud D. The attenuation of last atmospheric CH4 variations recorded in polar ice cores. *Geophysical Research Letters* 2003; 30: 25.

Spero HJ, Lea DW. The cause of carbon isotope minimum events on glacial terminations. *Science* 2002; 296: 522.

Stauffer B, Flückiger J, Monnin E, Nakagawa T, Aoki S. Discussion of the reliability of CO_2, CH_4 and N_2O records from polar ice cores. *Mem. Natl Inst. Polar Res., Spec. Issue* 2003; 57: 139.

Stauffer B, Flückiger J, Monnin E, Schwander J, Barnola JM, Chappellaz J. Atmospheric CO_2, CH_4 and N_2O records over the past 60 000 years based on the comparison of different polar ice cores. *Annals of Glaciology* 2002; 35: 202.

Stephens BB, Keeling RF. The influence of antarctic sea ice on glacial-interglacial CO_2 variations. *Nature* 2000; 404: 171.

Stevenson BA, Kelly EF, McDonald EV, Busacca AJ. The stable carbon isotope composition of soil organic carbon and pedogenic carbonates along a bioclimatic gradient in the Palouse region, Washington State, USA. *Geoderma* 2005; 124: 37.

Toggweiler JR. Variation of atmospheric CO_2 by ventilation of the ocean's deepest water. *Paleoceanography* 1999; 14: 571.

Traufetter F, Oerter H, Fischer H, Weller R, Miller H. Spatio-temporal variability in volcanic sulphate deposition over the past 2 kyr in snow pits and firn cores from Amundsenisen, Antarctica. *Journal of Glaciology* 2004; 50: 137.

Trudinger CM, Enting IG, Etheridge DM, Francey RJ, Levchenko VA, Steele LP, Raynaud D, Arnaud L. Modeling air movement and bubble trapping in firn. *Journal of Geophysical Research D: Atmospheres* 1997; 102: 6747.

Tschumi J, Stauffer B. Reconstructing past atmospheric CO_2 concentration based on ice-core analyses: open questions due to in situ production of CO_2 in the ice. *Journal of Glaciology* 2000; 46: 45.

Verkouteren RM. Preparation, characterization, and value assignment of carbon dioxide isotopic reference materials: RMs 8562, 8563, and 8564. *Analytical Chemistry* 1999; 71: 4740.

Wang YQ, Zhang XY, Arimoto R, Cao JJ, Shen ZX. Characteristics of carbonate content and carbon and oxygen isotopic composition of northern China soil and dust aerosol and its application to tracing dust sources. *Atmospheric Environment* 2005; 39: 2631.

Weller R, Traufetter F, Fischer H, Oerter H, Piel C, Miller H. Postdepositional losses of methane sulfonate, nitrate, and chloride at the European Project for Ice Coring in Antarctica deep-drilling site in Dronning Maud Land, Antarctica. *Journal of Geophysical Research D: Atmospheres* 2004; 109:

Werner RA, Brand WA. Referencing strategies and techniques in stable isotope ratio analysis. *Rapid Communications In Mass Spectrometry* 2001; 15: 501.

Werner RA, Rothe M, Brand WA. Extraction of CO_2 from air samples for isotopic analysis and limits to ultra high precision $\delta^{18}O$ determination in CO_2 gas. *Rapid Communications In Mass Spectrometry* 2001; 15: 2152.

Wilson AT, Donahue DJ. AMS carbon-14 dating of ice: progress and future prospects. *Nuclear Instruments and Methods in Physics Research B* 1990; 52: 473.

Wilson AT, Donahue DJ. AMS Radiocarbon dating of Ice; Validity of the Technique and the Problem of Cosmogenic in-situ Production in Polar Ice Cores. *Radiocarbon* 1992; 34: 431.

Wilson AT, Long A. New approaches to CO_2 analysis in polar ice cores. *Journal of the Geophysical Research* 1997; 102: 26601.

Wolff EW, Miners WD, Moore JC, Paren JG. Factors controlling the electrical conductivity of ice from the polar regions - A summary. *Journal of Physical Chemistry B* 1997; 101: 6090.

Yeom CK, Lee SH, Lee JM. Study of transport of pure and mixed CO_2/N_2 gases through polymeric membranes. *Journal of Applied Polymer Science* 2000; 78: 179.

Young ED, Galy A, Nagahara H. Kinetic and equilibrium mass-dependent isotope fractionation laws in nature and their geochemical and cosmochemical significance. *Geochimica et Cosmochimica Acta* 2002; 66: 1095.

Zhang J, Quay PD, Wilbur DO. Carbon isotope fractionation during gas-water exchange and dissolution of CO_2. *Geochimica et Cosmochimica Acta* 1995; 59: 107.

Zumbrunn R, Neftel A, Oeschger H. CO_2 measurements on 1-cm^3 ice samples with IR laserspectrometer (IRLS) combined with a new dry extraction device. *Earth and Planetary Science Letters* 1982; 60: 318.

5 Appendix:

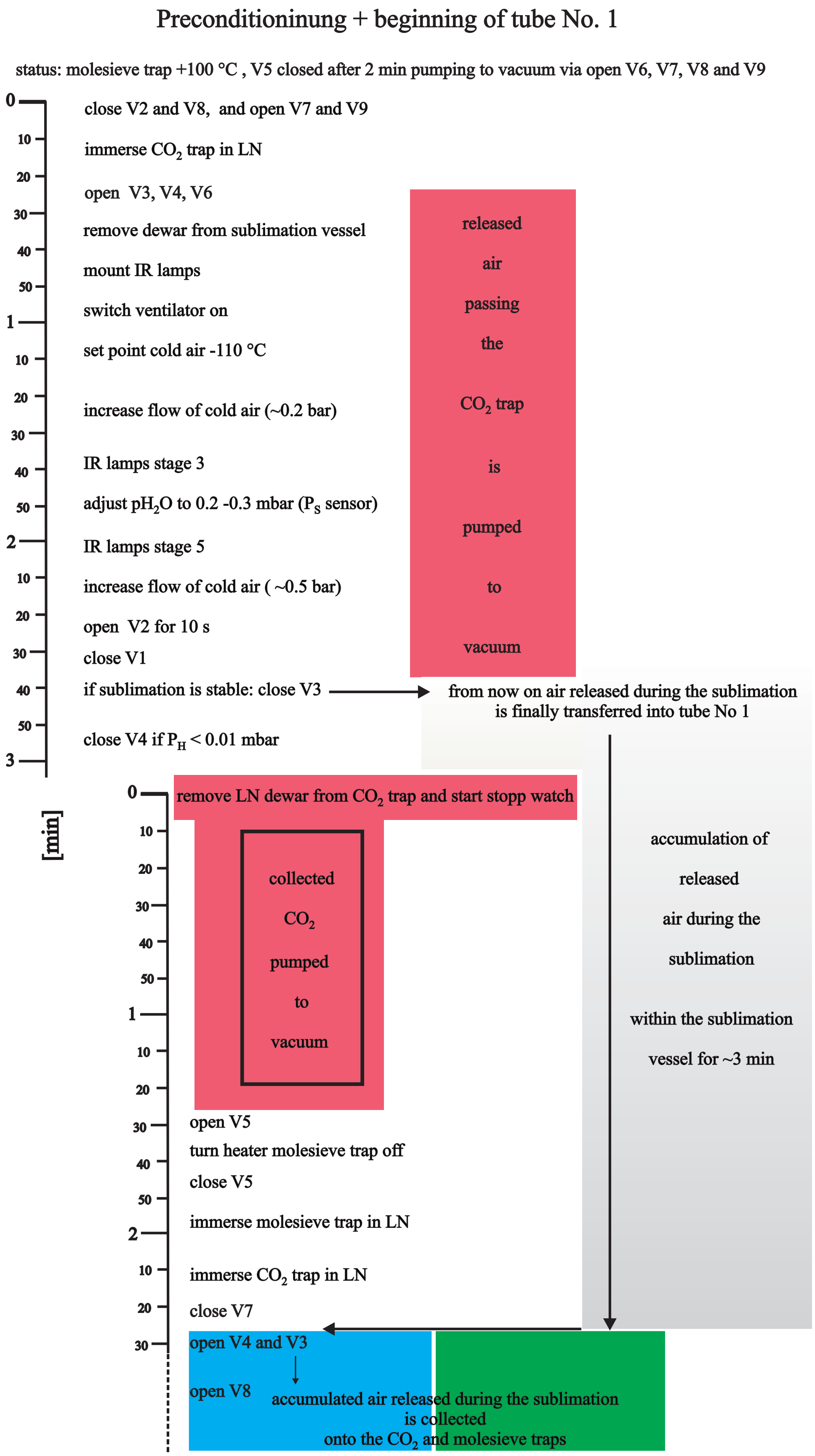

Figure 5-1 Detailed plan of working steps for the sublimation extraction of ice core samples: Part I preconditioning steps and collection of tube No. 1. See general overview of the procedure and used color codes at Figure 3-4.

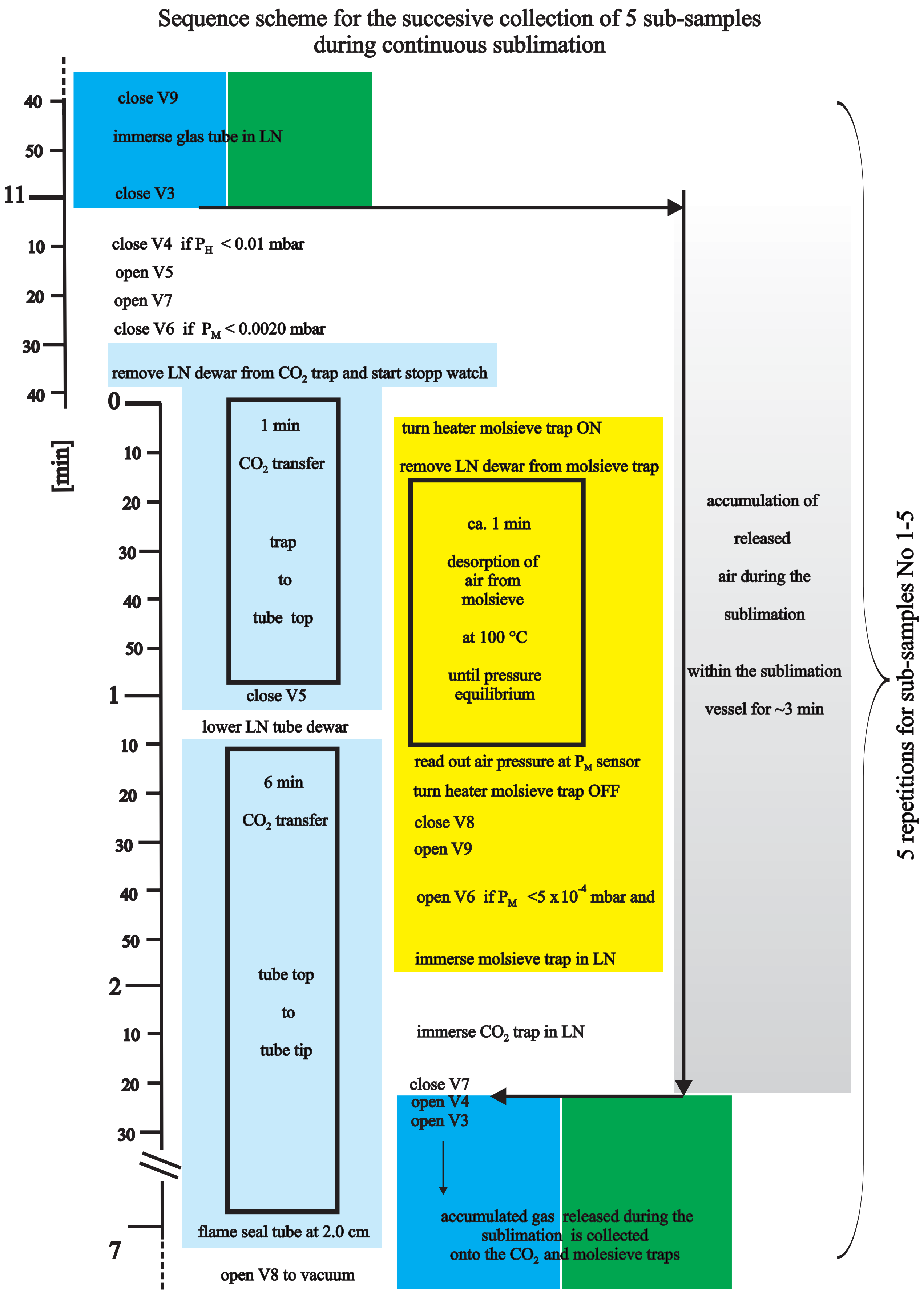

Figure 5-2 Detailed description of the working steps for the sublimation extraction of ice core samples: Part II successive collection of tube No. 1-5. For the general overview of the entire procedure and the used color codes see Figure 3-4.

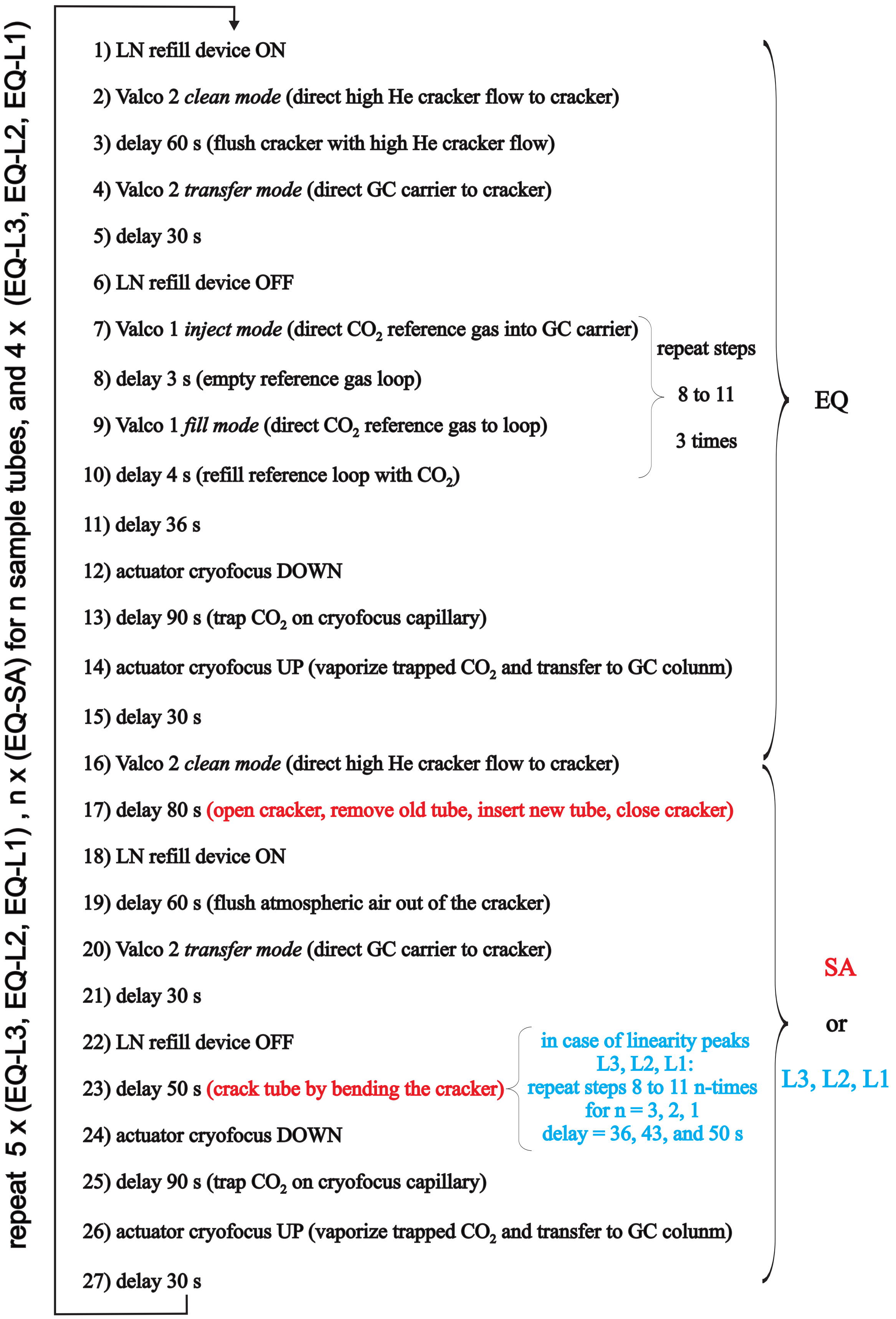

1) LN refill device ON

2) Valco 2 *clean mode* (direct high He cracker flow to cracker)

3) delay 60 s (flush cracker with high He cracker flow)

4) Valco 2 *transfer mode* (direct GC carrier to cracker)

5) delay 30 s

6) LN refill device OFF

7) Valco 1 *inject mode* (direct CO_2 reference gas into GC carrier)

8) delay 3 s (empty reference gas loop)

9) Valco 1 *fill mode* (direct CO_2 reference gas to loop)

10) delay 4 s (refill reference loop with CO_2)

11) delay 36 s

12) actuator cryofocus DOWN

13) delay 90 s (trap CO_2 on cryofocus capillary)

14) actuator cryofocus UP (vaporize trapped CO_2 and transfer to GC column)

15) delay 30 s

16) Valco 2 *clean mode* (direct high He cracker flow to cracker)

17) delay 80 s (open cracker, remove old tube, insert new tube, close cracker)

18) LN refill device ON

19) delay 60 s (flush atmospheric air out of the cracker)

20) Valco 2 *transfer mode* (direct GC carrier to cracker)

21) delay 30 s

22) LN refill device OFF

23) delay 50 s (crack tube by bending the cracker)

24) actuator cryofocus DOWN

25) delay 90 s (trap CO_2 on cryofocus capillary)

26) actuator cryofocus UP (vaporize trapped CO_2 and transfer to GC column)

27) delay 30 s

Figure 5-3 Sequence of valve operation for the tube-cracker GC IRMS system according to the ISODAT script written to produce either EQ-SA pairs, in case of the measurement of sample tubes, or EQ-L1 (L2, L3) in case of linearity pairs to determine the linearity of the tube cracker measurement system (see Fig. 3-2 for the technical details and Fig. 3-8 for an overview of the entire measurement session).

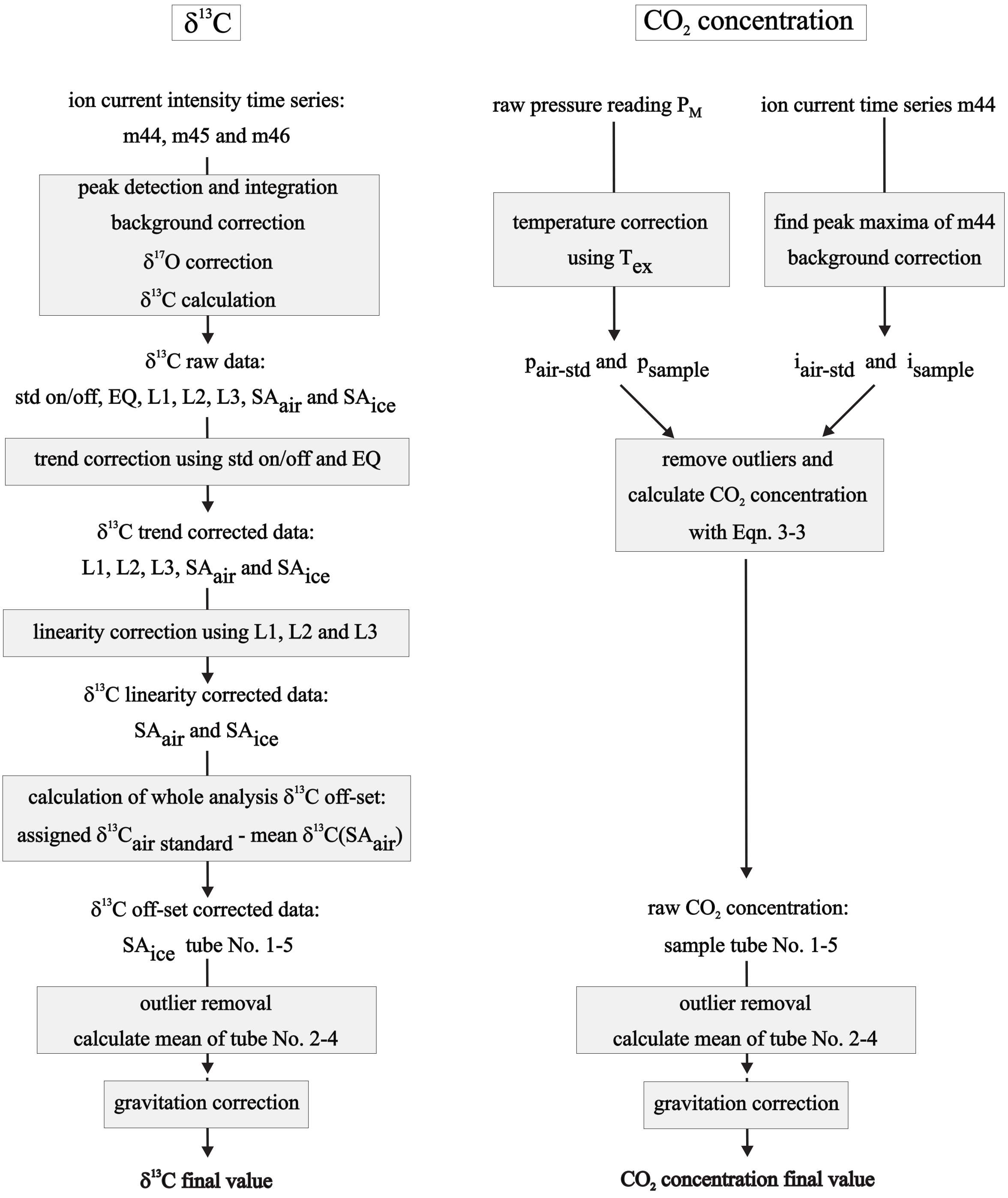

Figure 5-4 Calculation chain for $\delta^{13}C$ and the CO_2 concentration.

Table 5-1 Measured ice core samples with values for δ^{13}C and CO_2 concentration corrected for measurement biases; values for δ^{13}C-gravity and CO_2-gravity were additionally corrected for gravitational settling in the firn column.

EDML bag No.	depth [m]	tube No.	δ^{13}C [‰ VPDB]	δ^{13}C-gravity [‰ VPDB]	CO_2 [ppmv]	CO_2-gravity [ppmv]
151	150.655	1	-6.74	-7.18	283	281
151	150.655	2	-6.45	-6.89	285	283
151	150.655	3	-6.21	-6.65	281	279
151	150.655	4	-6.17	-6.61	278	276
151	150.655	5	-6.36	-6.80	280	278
151	150.610	1	-6.67	-7.11	288	286
151	150.610	2	-6.28	-6.72	282	281
151	150.610	3	-6.17	-6.61	283	281
151	150.610	4	-6.32	-6.76	285	283
151	150.610	5	-6.28	-6.72	275	273
151	150.565	1	-6.66	-7.10	288	286
151	150.565	2	-6.29	-6.73	276	274
151	150.565	3	-6.03	-6.47	279	277
151	150.565	5	-6.30	-6.74	276	274
253	252.700	1	-6.42	-6.86	276	274
253	252.700	2	-6.17	-6.61	275	273
253	252.700	3	-6.15	-6.59	278	276
253	252.700	4	-6.15	-6.59	280	278
253	252.700	5	-6.15	-6.59	277	275
253	252.655	1	-6.62	-7.06	279	277
253	252.655	2	-6.18	-6.62	277	275
253	252.655	3	-6.07	-6.51	277	275
253	252.655	4	-6.18	-6.62	277	275
253	252.655	5	-6.17	-6.61	267	265
253	252.610	1	-6.70	-7.14	283	281
253	252.610	3	-6.19	-6.63	273	271
253	252.610	4	-6.28	-6.72	276	274

to be continued on the next page

continuation from Table 5-1

EDML bag No.	depth [m]	tube No.	$\delta^{13}C$ [‰ VPDB]	$\delta^{13}C$-gravity [‰ VPDB]	CO_2 [ppmv]	CO_2-gravity [ppmv]
253	252.610	5	-6.10	-6.54	271	269
253	252.565	1	-6.48	-6.92	276	274
253	252.565	2	-6.28	-6.72	281	280
253	252.565	3	-6.24	-6.68	282	280
253	252.565	4	-6.20	-6.64	280	278
420	419.700	1	-6.72	-7.16	277	275
420	419.700	2	-6.41	-6.85	275	273
420	419.700	3	-6.42	-6.86	276	274
420	419.700	4	-6.39	-6.83	275	273
420	419.700	5	-6.56	-7.00	274	272
420	419.655	1	-6.70	-7.14	270	268
420	419.655	2	-6.35	-6.79	278	276
420	419.655	3	-6.19	-6.63	275	273
420	419.655	4	-6.36	-6.80	276	274
420	419.655	5	-6.62	-7.06	275	273
420	419.610	1	-6.66	-7.10	274	272
420	419.610	2	-6.40	-6.84	276	274
420	419.610	3	-6.31	-6.75	276	274
420	419.610	4	-6.49	-6.93	272	270
420	419.610	5	-6.51	-6.95	274	272
1056	1055.700	4	-6.24	-6.63	198	197
1056	1055.700	5	-6.53	-6.92	187	186
1056	1055.655	1	-6.41	-6.80	192	191
1056	1055.655	2	-6.23	-6.62	198	197
1056	1055.655	3	-6.17	-6.56	205	203
1056	1055.655	4	-6.30	-6.69	196	195
1056	1055.655	5	-6.36	-6.75	190	189
1056	1055.610	1	-6.50	-6.89	193	192
1056	1055.610	2	-6.23	-6.62	195	193
1056	1055.610	3	-6.18	-6.57	206	205
1056	1055.610	5	-6.39	-6.78	200	199

Paper:

On the application and interpretation of Keeling plots in paleo climate research

—

Deciphering $\delta^{13}C$ of atmospheric CO_2 measured in ice cores

Peter Köhler, Jochen Schmitt, Hubertus Fischer

published in Biogeosciences Discussions, 3, 513-573, 2006

On the application and interpretation of Keeling plots in paleo climate research

—

Deciphering δ^{13}C of atmospheric CO$_2$ measured in ice cores

Peter Köhler, Jochen Schmitt, Hubertus Fischer

Alfred Wegener Institute, Helmholtz Center for Polar and Marine Research
P.O. Box 12 01 61, D-27515 Bremerhaven, Germany

published in *Biogeosciences Discussions, 3, 513-573, 2006*

Abstract

The Keeling plot analysis is an interpretation method widely used in terrestrial carbon cycle research to quantify exchange processes of carbon between terrestrial reservoirs and the atmosphere. Here, we analyse measured data sets and artificial time series of the partial pressure of atmospheric carbon dioxide (pCO$_2$) and of δ^{13}C of CO$_2$ over industrial and glacial/interglacial time scales and investigate to what extent the Keeling plot methodology can be applied to longer time scales. The artificial time series are simulation results of the global carbon cycle box model BICYCLE. Our analysis shows that features seen in pCO$_2$ and δ^{13}C during the industrial period can be interpreted with respect to the Keeling plot. However, only a maximum of approximately half of the signal can be explained by this method. The signals recorded in ice cores caused by abrupt terrestrial carbon uptake or release loose information due to air mixing in the firn before bubble enclosure and limited sampling frequency. For less abrupt changes as occurring during glacial cycles carbon uptake by the ocean cannot longer be neglected. We introduce an equation for the calculation of the effective isotopic signature of long-term changes in the carbon cycle, in which the ocean is introduced as third reservoir. This is a paleo extention of the two reservoir mass balance equations of the Keeling plot approach. Steady state analyses of changes in the terrestrial and marine biosphere lead to similar effective isotopic signatures (-8.6‰) of the carbon fluxes perturbing the atmosphere. These signatures are more positive than the δ^{13}C signals of the sources, e.g. the terrestrial carbon pools themselves (~ -25‰). In all other cases the effective isotopic signatures are larger (-8.2‰ to -0.7‰), and very often indistinguishable in the light of the uncertainties. Therefore, a back calculation from well distinct fluctuations in pCO$_2$ and δ^{13}C to identify their origin using the Keeling plot approach seems not possible.

1 Introduction

In carbon cycle research information on the origin of fluxes between different reservoirs as contained in the ratio of the stable carbon isotopes ^{13}C/^{12}C has become more and more important in the past decades. These isotopic signatures store information about exchange processes because differences in physical properties of atoms and molecules containing different isotopes of an element lead to isotopic fractionation.

Prominent examples in our context of global carbon cycle research are gas exchange between surface ocean and atmosphere or photosynthetic production in both the marine and the terrestrial biosphere. Here, the end member of a carbon flux associated with a given process is in general depleted in the heavier isotope. This is expressed with the fractionation factor ε of the process, which depends on various environmental parameters such as temperature or the biological species (see Zeebe and Wolf-Gladrow (2001) for more basic information on carbon isotopes in seawater).

The isotopic composition of a reservoir is usually expressed in per mil (‰) in the so-called "δ-notation" as the relative deviation from the isotope ratio of a defined standard (VPDP in the case of δ^{13}C):

$$\delta^{13}\mathrm{C}_{\,\mathrm{sample}} = \left(\frac{\frac{[^{13}\mathrm{C}]}{[^{12}\mathrm{C}]}_{\mathrm{sample}}}{\frac{[^{13}\mathrm{C}]}{[^{12}\mathrm{C}]}_{\mathrm{standard}}} - 1 \right) \times 10^3. \qquad (1)$$

The fractionation factor ε (in ‰) between carbon in sample A and in sample B (e.g. before and after some fractionation step) is related to the δ values by

$$\varepsilon_{(A-B)} = \frac{\delta^A - \delta^B}{1 + \delta^B/10^3}. \tag{2}$$

During photosynthesis the carbon taken up by marine primary producers is typically depleted by On land, the type of metabolism determines the fractionation factor during terrestrial photosynthesis. C_3 plants inhibit a higher discrimination against the heavy isotope ($\varepsilon = -15$ to -23‰) than plants with C_4 metabolism ($\varepsilon = -2$ to -8‰) (Mook, 1986).

One prominent interpretation technique of carbon exchange between the atmosphere and other reservoirs, e.g used in carbon flux studies in terrestrial ecosystems, is plotting the δ^{13}C signature of CO_2 as a function of the inverse of the atmospheric carbon dioxide mixing ratio ($\delta^{13}\mathrm{C} = f(1/\mathrm{CO}_2)$). In doing so, the intercept of a linear regression with the y-axis can under certain conditions be understood as the isotopic signature of the flux, which alters the content of carbon in the atmospheric reservoir. This approach is called "Keeling plot" after the very first usage by Charles D. Keeling about 50 years ago (Keeling, 1958, 1961). The application and interpretation of Keeling plots is widely used in terrestrial carbon research and based on some fundamental assumptions (see review Pataki et al., 2003).

Keeling plots have also been used in paleo climate research in the past years (e.g. Smith et al., 1999; Fischer et al., 2003), but it seems that the limitations of this approach have not been adequately taken into account so far to allow for a meaningful interpretation. The aim of this paper therefore is to emphasise what can be learnt from Keeling plots, if applied on slow, but global processes acting on glacial/interglacial time scales, and to discuss their limitations. We emphasise what kind of information can be gained from deciphering the δ^{13}C signal measured in ice cores. For this purpose we extent the Keeling plot approach to a three reservoir system and analyse data sets and artificial time series produced by a global carbon cycle box model, from which we know which processes are operating.

2 The Keeling plot

The principle of the Keeling plot approach is based on the exchange process of carbon between two reservoirs and the conservation of mass. Let C_{new} be the mass of carbon after the addition of carbon with mass C_{add} to an undisturbed reservoir with mass C_{old}.

$$C_{\mathrm{new}} = C_{\mathrm{old}} + C_{\mathrm{add}} \tag{3}$$

With $\delta^{13}C_x$ being the carbon isotope signature of the C component x the conservation of mass thus gives us:

$$C_{\mathrm{new}} \cdot \delta^{13}C_{\mathrm{new}} = C_{\mathrm{old}} \cdot \delta^{13}C_{\mathrm{old}} + C_{\mathrm{add}} \cdot \delta^{13}C_{\mathrm{add}} \tag{4}$$

In combining equations 3 and 4 we obtain a relationship between $\delta^{13}C_{\mathrm{new}}$ and C_{new}:

$$\delta^{13}C_{\mathrm{new}} = C_{\mathrm{old}} \cdot (\delta^{13}C_{\mathrm{old}} - \delta^{13}C_{\mathrm{add}}) \cdot \frac{1}{C_{\mathrm{new}}} + \delta^{13}C_{\mathrm{add}} \tag{5}$$

Thus, the y-intercept y_0 of the linear regression function of equation 5, which describes $\delta^{13}C_{\mathrm{new}}$ as a function of the inverse of the carbon content (1/C_{new}), gives us the isotopic ratio $\delta^{13}C_{\mathrm{add}}$ of the carbon added to the reservoir.

There are two basic assumptions underlying the Keeling plot method: (1) The system consists of a two reservoirs only. (2) The isotopic ratio of the added reservoir does not change during the time of observation. Both assumptions are in a strict sense rarely fulfilled. Furthermore, there are arguments about which linear regression model should be used if one assumes measurement errors in both variables (for details see Pataki et al., 2003). The methodological aspects concerning the choice of a regression model are not the subject of our investigations here.

The Keeling plot approach was used in the past to interprete various different sub-systems of the global carbon cycle. Keeling (1958, 1961) first used it to identify the contribution of terrestrial plants to the background isotopic ratio of CO_2 in a rural area near the Pacific coast of North America. The component of the terrestrial biosphere in the seasonal cycle of CO_2 over Switzerland (Friedli et al., 1986; Sturm et al., 2005) and Eurasia (Levin et al., 2002) was investigated with the Keeling plot. The approach was widely used in terrestrial ecosystem research to identify respiration fluxes (e.g. Flanagan and Ehleringer, 1998; Yakir and Sternberg, 2000; Bowling et al., 2001; Pataki et al., 2003; Hemming et al., 2005). It was used in paleo climate research within the last years to disentangle

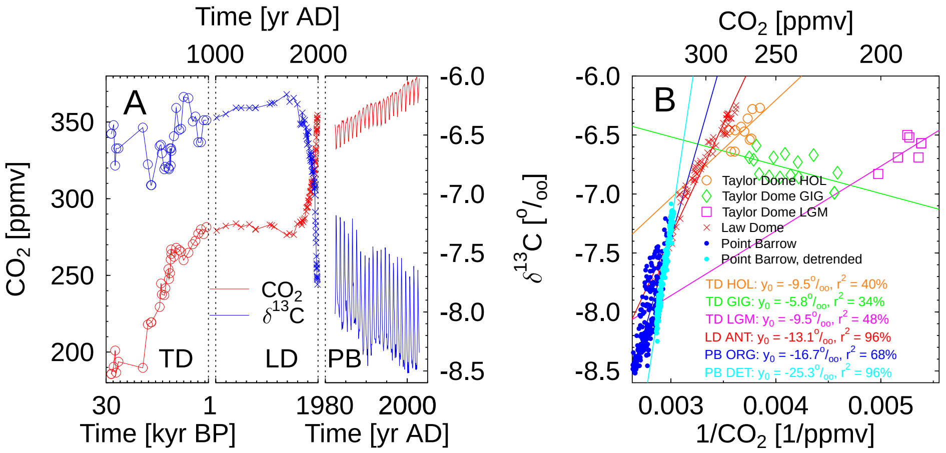

Figure 1: A compilation of data from Point Barrow PB, the Law Dome LD, and the Taylor Dome TD ice cores (A: CO_2, δ^{13}C; B: Keeling plot). Monthly resolved data $(1982-2002)$ from Point Barrow (Keeling and Whorf, 2005; Keeling et al., 2005). Only times where data in both CO_2 and δ^{13}C were available are considered here. For the Keeling plot approach the original data (PB ORG) and detrended time series (PB DET) are plotted and analysed. Data from firn and ice at Law Dome cover the last millenium (Francey et al., 1999; Trudinger et al., 1999) which includes the anthropogenic rise in CO_2 (LD ANT). Data from the Taylor Dome ice core of the last 30 kyr include the glacial/interglacial transition during Termination I (Smith et al., 1999) with the age model of Brook et al. (2000). Taylor Dome data are split into the Holocene (TD HOL), the glacial/interglacial transition (TD GIG), and the LGM (TD LGM).

the processes explaining the subtle changes in CO_2 during the relatively stable LGM and the Holocene as well as the approximately 80 ppmv increase from the Last Glacial Maximum (LGM) to the Early Holocene (Smith et al., 1999; Fischer et al., 2003; Eyer, 2004).

3 Global CO_2 and δ^{13}C times series of different temporal resolution

It has been shown (Fischer et al., 2003), that the seasonal amplitude of CO_2 and δ^{13}C during the last decades, the anthropogenic rise in CO_2 and the corresponding decrease in its δ^{13}C signal since 1750 AD, and the glacial/interglacial variation in these two records exhibit significant different behaviour if analysed with the Keeling plot approach. Data sets showing these dynamics on the three different temporal scales are compiled in Fig. 1. The seasonal signal is measured from 1982 to 2002 AD at Point Barrow, Alaska (Keeling and Whorf, 2005; Keeling et al., 2005). For the anthropogenic variation during the last millennium we use the data measured in air enclosures in the Law Dome ice core (Francey et al., 1999; Trudinger et al., 1999). Glacial/interglacial variations $(1-30$ kyr BP) were detected in the Taylor Dome ice core (Smith et al., 1999). For the interpretation of the seasonal signal measured at Point Barrow both data sets (CO_2, δ^{13}C) need to be detrended to separate the two simultaneous occurring effects of the anthropogenic CO_2 rise and the seasonality from each other. Annual variations are then analysed as perturbations from the mean values during the first year of the measurements. The component $\mathrm{C}_{\mathrm{add}}$ in Equations 3–5 reflects the exchange of carbon of an external reservoir (winter time carbon release from the terrestrial biosphere in the seasonal signal of Point Barrow and anthropogenic emissions in the case of Law Dome) with the atmospheric reservoir. The Point Barrow and Law Dome data can be approximated consistently with the typical Keeling plot linear regression function ($r^2 = 96\%$ in both). The y-axis intercept y_0 declines from the seasonal effects (–25‰) to the anthropogenic impact (–13‰) with the mixed signal of the untreated data at Point Barrow in-between (–17‰) (Fig. 1B). This decline is explained by a larger oceanic carbon uptake and a smaller airborne fraction of any atmospheric disturbance in CO_2 in longer time scales (Fischer et al., 2003).

These two examples based on accurate data sets are already beyond Keelings original idea as they are no longer based on a two reservoir system and highlight the limitations of this approach. While the y-intercept of the detrended data at Point Barrow match the expectations well, the intercept found in the anthropogenic rise in Law Dome does not record the δ^{13}C signal of the carbon released by anthropogenic activity (with δ^{13}C of about -25 to -30‰) to the atmosphere anymore. The seasonal amplitude at Point Barrow can be explained with the

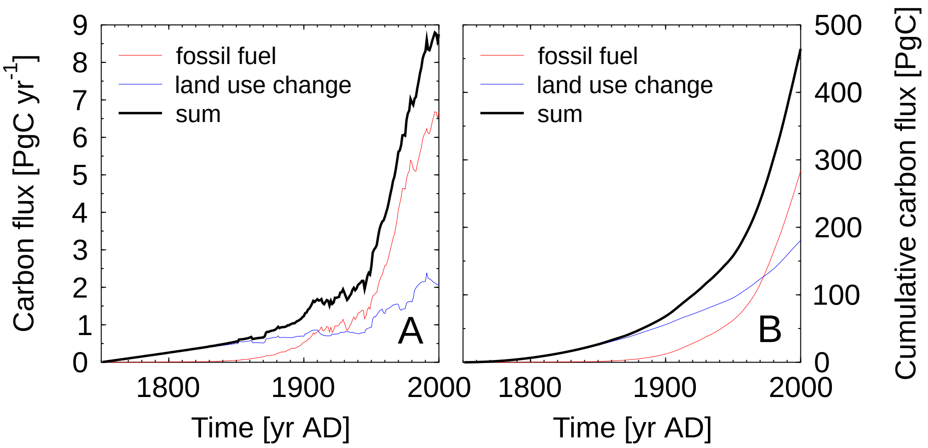

Figure 2: Fossil fuel emissions since 1750 AD (Marland et al., 2005), land use change since 1850 AD (Houghton, 2003), linearly extrapolated to zero in year 1750 AD. A: Annual fluxes; B: Cumulative fluxes.

seasonality of the terrestrial biosphere. Vegetation grows mainly in the northern hemisphere, and thus CO_2 minima occur during maximum photosynthetic carbon uptake by plants during northern summer. The seasonal fluctuation in CO_2 should therefore bear a δ^{13}C signal of the order of $-25‰$ which would account for fractionation during terrestrial photosynthesis (Scholze et al., 2003). This δ^{13}C signal of the seasonal cycle is seen in the detrended Point Barrow data and corresponds well with other studies (e.g. Levin et al., 2002). The anthropogenic rise seen in the Law Dome data set is the residual of the combination of fossil fuel emissions (Marland et al., 2005), land use changes (Houghton, 2003), terrestrial carbon sinks due to CO_2 fertilisation (Plattner et al., 2002), all from which the ocean carbon uptake during that time has to be subtracted. Until about 1910 AD the fossil fuel emissions were smaller than the carbon release caused by land use change (both around 0.8 PgC yr^{-1}). The relation changed thereafter and in the year 2000 fossil fuel emissions were already more than three times larger than carbon fluxes based on land use change (6.7 versus 2.1 PgC yr^{-1}; Fig. 2A). The cumulative release of fossil fuel carbon outcompeted that from land use change only in year 1973 AD. Altogether about 465 Pg of carbon were released by anthropogenic activities during this 250 year period to the atmosphere (Fig. 2B). Without carbon uptake by the ocean and the terrestrial reservoirs this would have led to a rise in atmospheric pCO$_2$ by more than 200 ppmv. The δ^{13}C signal of recent fossil fuel emissions in the USA is around -29 to $-30‰$ (Blasing et al., 2004), while carbon fluxes from land use changes bear the typical δ^{13}C signal of the terrestrial biosphere ($-25‰$). These anthropogenic processes can by no means be inferred from the Keeling plot analysis. The reason for this is that due to the gas exchange between ocean and atmosphere the basic assumption of a two reservoir system is intrinsically violated. This questions the applicability of the Keeling plot approach to carbon change studies on long time scales, where this ocean/atmosphere gas exchange becomes even more significant.

Going further back in time, the glacial/interglacial rise in CO_2 and its accompanied δ^{13}C variations as measured in the Taylor Dome ice core led to a sub-grouping of the δ^{13}C – 1/CO$_2$ data pairs (Smith et al., 1999) with different linear regression functions for the Last Glacial Maximum (LGM), the glacial-interglacial transition (GIG), and the Holocene (HOL) (Fig. 1B). With on average one data point every thousand years the data set is sparse. However, the y-intercepts during LGM and Holocene are similar ($-9.5‰$) and significant different from that during the transition ($-5.8‰$). Thus, it was hypothesised that underlying processes for variations in CO_2 during the relatively stable climates of the LGM and the Holocene might have been the same and might have been mainly based on processes concerning the terrestrial biosphere (Smith et al., 1999; Fischer et al., 2003).

4 Extending the Keeling plot approach to a three reservoir system

A first estimate for the effective carbon isotopic signature in the atmosphere due to an injection of terrestrial carbon into the ocean/atmosphere system can be derived when extending the two reservoirs to a three reservoir system. Here we assume that ocean circulation remained the same and that an equilibrium between ocean and atmosphere is achieved.

We have to extend the carbon and isotopic balance according to

$$A + O = A_0 + O_0 + B \tag{6}$$

and

$$A\delta^A + O\delta^O = A_0\delta_0^A + O_0\delta_0^O + B\delta^B. \tag{7}$$

where $A_0 = 600$ PgC and $O_0 = 38,000$ PgC are the reservoir sizes of the atmosphere and ocean, respectively, before an injection of terrestrial carbon of the size *B*. *A* and *O* are the sizes of the atmospheric and ocean reservoirs after the injection. The δ_0's represent the carbon isotopic signatures of the reservoirs before the injection with $\delta_0^A = -6.5‰$ and $\delta_0^O = +1.5‰$ and the δ's after the injection. The isotopic signature of the terrestrial biosphere $\delta^B = -25‰$ is assumed to be constant. Note, that during the gas exchange and the dissociation of carbonic acid in the seawater fractionation occurs (according to Eq. 2) $\varepsilon_{\mathrm{AO}} \approx \delta_0^A - \delta_0^O \approx \delta^A - \delta^O \approx -8‰$, which is assumed to remain constant in time.

For the oceanic uptake of carbon we have to take the buffering effect of the carbonate system in seawater into account (Zeebe and Wolf-Gladrow, 2001). The ratio between the change in $\mathrm{CO_2}$ concentration and the change in dissolved inorganic carbon (DIC) is described by the Revelle or buffer factor β, which is temperature, alkalinity and DIC dependent:

$$\beta := \left(\frac{d[\mathrm{CO_2}]/[\mathrm{CO_2}]}{d\mathrm{DIC}/\mathrm{DIC}}\right). \tag{8}$$

Any additional carbon injected into the ocean/atmosphere system will be distributed in the two reservoirs according to the ratio of the sizes before the injection, i.e.

$$\frac{A - A_0}{O - O_0} = \beta\frac{A_0}{O_0}. \tag{9}$$

Using the carbon balance in equation 6 we can calculate the size of the ocean and atmosphere reservoir after the injection

$$O = \frac{\beta A_0 + O_0 + B}{\beta A_0/O_0 + 1}. \tag{10}$$

The Revelle factor β in recent surface waters varies between 8 and 16 (Sabine et al., 2004). For the preindustrial setting β in the surface ocean boxes of our box model BICYCLE is on average 11.5, with 9 in equatorial waters and around 12 in the high latitudes. Note that the average Revelle factor of the surface ocean falls to 10 for the climatic conditions of the LGM.

The effective carbon signature of the isotopic change in the atmosphere $\delta^{\Delta A}$ can be estimated according to

$$\delta^{\Delta A} = \frac{A\delta^A - A_0\delta_0^A}{A - A_0}. \tag{11}$$

Using the carbon isotopic balance in equation 7 and replacing $\delta^O = \delta^A - \varepsilon_{\mathrm{AO}}$ we obtain

$$\delta^{\Delta A} = \frac{\frac{A_0+O_0+B-O}{A_0+O_0+B}(A_0\delta_0^A + O_0\delta_0^O + B\delta^B + \varepsilon_{\mathrm{AO}}O) - A_0\delta_0^A}{O_0 + B - O}. \tag{12}$$

When we insert the values for isotopic signatures and reservoir sizes given above and vary the amount of terrestrial carbon added, the isotopic fractionation during gas exchange $\varepsilon_{\mathrm{AO}}$ or the Revelle factor β we obtain varying effective isotopic signatures $\delta^{\Delta A}$ of the change in the atmospheric carbon reservoir as shown in Fig. 3. In a setting for the preindustrial climate conditions, $\delta^{\Delta A}$ varies nearly linearly with B between $-9‰$ and $-10‰$ (Fig. 3A), reflecting the progressive lightening of the overall ocean/atmosphere system the more isotopically depleted terrestrial carbon is added. Note, that these values are similar to the ones derived by Smith et al. (1999) and Fischer et al. (2003) both for the Holocene and the LGM from Taylor Dome ice core data and which have been interpreted as indicative of terrestrial carbon reservoir changes during these periods. However, from the interpretation of other processes changing the global carbon cycle following in section 5.3 it will become apparent that not only terrestrial carbon release can produce this kind of signal.

In the special case with a Revelle factor $\beta = 1$ (no carbonate buffering), and $\varepsilon_{\mathrm{AO}} = 0‰$, (no isotopic fractionation during air/sea transfer), $\delta^{\Delta A}$ records correctly the isotopic signature $\delta^B = -25‰$ of the terrestrial carbon release (Fig. 3B). In all other cases, both the buffering of the ocean and the isotopic fractionation during gas exchange have a significant influence on the calculated $\delta^{\Delta A}$ with the change in the Revelle factor having the strongest effect for typical ocean surface conditions.

This reveals three major findings:

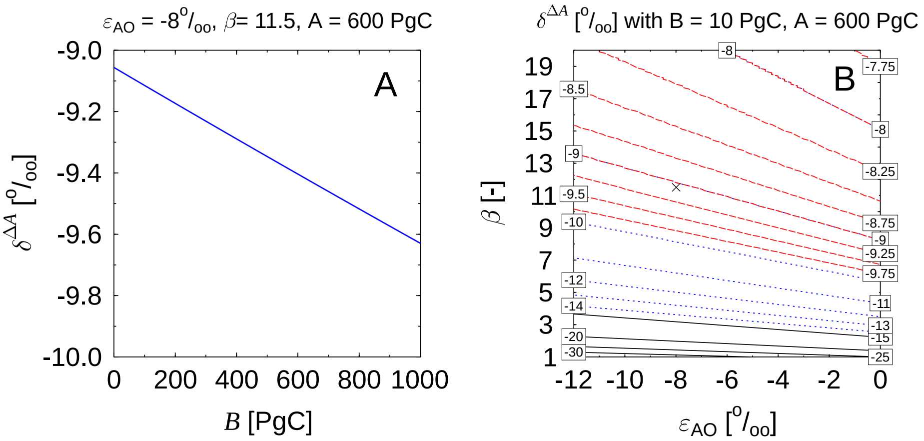

Figure 3: Results of the extended Keeling approach with three reservoirs. Effective isotopic signature of the atmosphere $\delta^{\Delta A}$ as function of (A) the size of the terrestrial release and (B) the Revelle Factor β and the fractionation during gas exchange $\varepsilon_{\mathrm{AO}}$. Other variable as given in the figures. The cross in subfigure B marks the preindustrial state ($\beta = 11.5$, $\varepsilon_{\mathrm{AO}} = -8.0‰$).

1. The isotopic signature $\delta^{\Delta A}$ is dependent on the amount of carbon injected and the setting of the system described by the three reservoirs, their isotopic signatures, the fractionation factors, and the Revelle factor.
2. For realistic settings $\delta^{\Delta A}$ stays between of -8.5 and $-10‰$. The signal which can be detected is therefore much more enriched in ^{13}C than the carbon released from the terrestrial biosphere with $\delta^{B} = -25‰$, which was the origin of the perturbation.
3. There exists a boundary $\delta^{\Delta A}_{\delta\mathrm{C}\rightarrow 0}$ in the effective signature of the isotopic change in atmospheric δ^{13}C which is reached if the amount of carbon released to the atmosphere converges to zero. Note, that $\delta^{\Delta A}$ is not defined for $B = 0$ PgC, because the denominator in Eq. 12 becomes zero. Perturbations in the system will only lead to variations in $\delta^{\Delta A}$ from this boundary.

Only for processes which are faster than the equilibration time of the deep ocean with the atmosphere, substantial amounts of isotopic depleted carbon stay in the atmosphere allowing for more negative effective $\delta^{\Delta A}$ values in the Keeling plot. The latter is seen e.g. for the seasonal variation in CO$_2$ due to the waxing and waning of the biosphere and to a smaller extent also for the input of isotopically depleted anthropogenic carbon into the atmosphere which has a typical time scale of decades to centuries.

The two reservoir system is a special case of these calculation for a three reservoir system when $\beta = 1$ and $\varepsilon_{\mathrm{AO}} = 0‰$, i.e. when the atmosphere and the ocean can be treated as one homogeneous reservoir. The effective carbon isotopic signature $\delta^{\Delta A}$ based on our theoretical consideration as calculated in this section is comparable with the y_0 of a linear regression in a Keeling plot performed on measured or simulated data sets. However, details in the marine carbon cycle, such as spatial variations in the Revelle factor, ocean circulation schemes and the ocean carbon pumps which introduce vertical gradients in DIC and ^{13}C in the ocean prevent us from a direct comparison of the obtained values. Nevertheless, the theoretical exercise above gives us valuable insights for the interpretation of the artificial data sets, which will be discussed in the following.

5 Artificial pCO$_2$ and δ^{13}C times series

Recently, a time-dependent modelling approach was proposing a mechanistic understanding of the dynamics of the atmospheric carbon records over Termination I by forcing the global ocean/atmosphere/biosphere carbon cycle box model BICYCLE forward in time (Köhler et al., 2005a). They identified the impacts of different processes acting on the carbon cycle on glacial/interglacial time scales and proposed a scenario, which provides an explanation the evolution of pCO$_2$, δ^{13}C, and Δ^{14}C over time. The results are in line with various other paleo climatic observations.

In the following we will reanalyse the results of Köhler et al. (2005a) by applying the Keeling plot analysis to study whether this kind of analysis applied on paleo climatic changes in atmospheric CO$_2$ and δ^{13}C can lead to meaningful results. Additionally, further simulations with the BICYCLE model will be performed. The advantage of using model-generated artificial time series is, that we know which processes are operating and which process-dependent isotopic fractionations influence the δ^{13}C signals of the results. We highlight how the Keeling plot approach can gain new insights from these data sets and where its limitations in paleo climatic research seem to be.

Since BICYCLE does not resolve seasonal phenomena we are unable to interprete or reconstruct the dynamics of the Point Barrow data set of the last decades. However, we are able to implement the anthropogenic impacts of the last 250 years as seen in the Law Dome ice core. After a short model description and an interpretation of this data set as a sort of ground truthing for our analysis, we dig into the glacial/interglacial mystery of the carbon cycle and re-evaluate the Taylor Dome ice core data set.

Please note, that atmospheric scientists typically measure carbon dioxide as volume mixing ratio in parts per million and volume (ppmv) in dry air. Marine chemists and the artificial records produced by our model give carbon dioxide as partial pressure (pCO$_2$) given in units of μatm. Only in dry air and at standard pressure, they are numerically equal (Zeebe and Wolf-Gladrow, 2001).

5.1 The global carbon cycle box model BICYCLE

The box model of the global carbon cycle BICYCLE consists of an ocean module with ten homogeneous boxes in three basins (Atlantic, Southern Ocean, Indo-Pacific) and three different vertical layers (surface, intermediate, deep), a globally averaged atmospheric box and a terrestrial module with seven globally averaged compartments representing ground and tree vegetation and soil carbon with different turnover times (Fig. 4). Prognostic variables in the model are DIC, alkalinity, oxygen, phosphate and the carbon isotopes ^{13}C and ^{14}C in the ocean boxes, and carbon and its carbon isotopes in the atmosphere and terrestrial reservoirs. The net difference between sedimentation and dissolution of CaCO$_3$ is calculated from variations of the lysocline and imposes fluxes of DIC and alkalinity between deep ocean and sediment. The model is completely described in Köhler and Fischer (2004) and Köhler et al. (2005a). BICYCLE is based in its architecture on earlier box models used during the past two decades (Emanuel et al., 1984; Munhoven, 1997). It was adapted to be able to answer questions of paleo climate research with its whole parameterisation being updated.

We apply disturbances of the climate system through the use of forcing functions and paleo climate records (e.g. changes in temperature, sea level, aeolian dust input in the Southern Ocean) and prescribe changes in ocean circulation over time based on other data- and model-based studies. BICYCLE is then able to reconstruct the evolution of atmospheric pCO$_2$, δ^{13}C, and Δ^{14}C during the last glacial/interglacial transition (Köhler et al., 2005a).

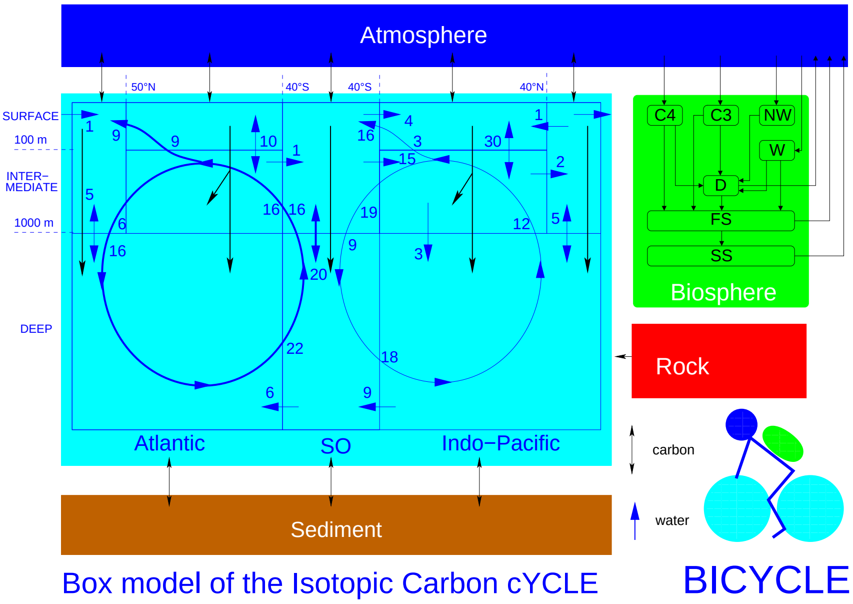

Figure 4: A sketch of the BICYCLE model including boundary conditions and preindustrial ocean circulation fluxes (in Sv = 10^6 m^2 s^{-1}) in the ocean module. The globally averaged terrestrial biosphere distinguishes ground vegetation following different photosynthetic pathways (C4, C3), non-woody (NW), and woody (W) parts of trees, and soil compartments (D, FS, SS) with different turnover times.

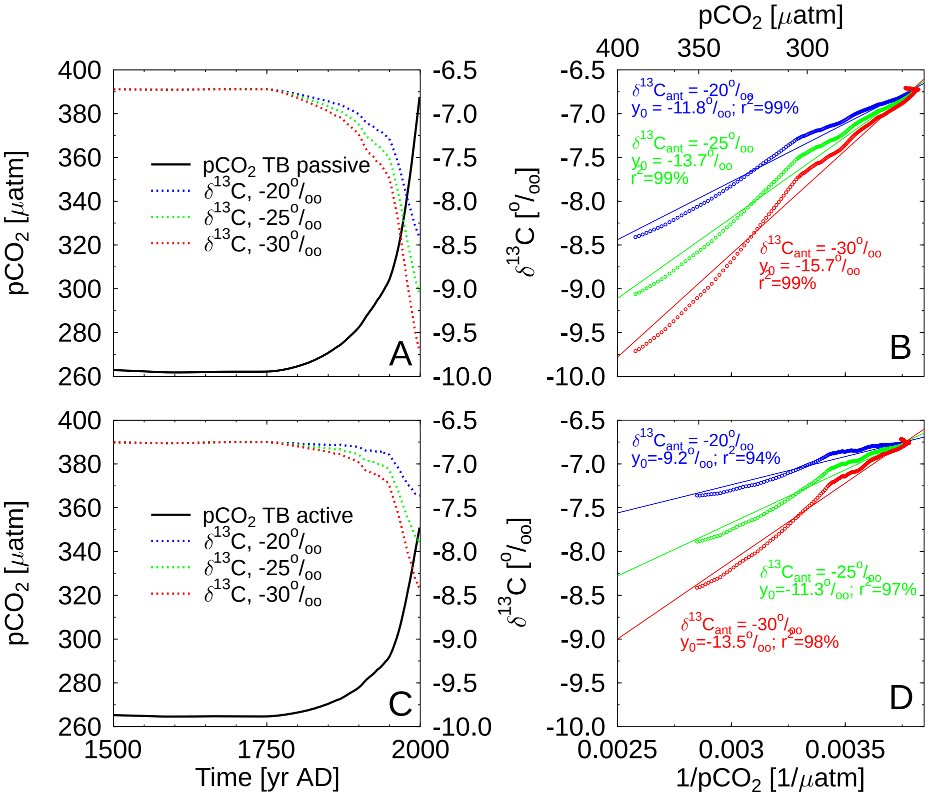

Figure 5: Reconstructions of the rise in $p\mathrm{CO}_2$ during the last 500 years with BICYCLE (left: $p\mathrm{CO}_2$, δ^{13}C; right: Keeling plot). Anthropogenic fluxes were used as plotted in Fig. 2. Two different settings are tested, one with passive terrestrial biosphere TB (top), meaning that carbon storage in the land reservoirs was kept constant, and one with active terrestrial biosphere (bottom), in which a rise in the internal calculated $p\mathrm{CO}_2$ is enhancing terrestrial carbon uptake via its fertilisation effect. Different simulations with different isotopic signatures of the anthropogenic emission ($-20‰$, $-25‰$, $-30‰$).

It was further used to propose a mechanistic understanding of variation in atmospheric CO_2 during the last eight glacial cycles (Wolff et al., 2005; Köhler and Fischer, 2006), and to analyse the implication of changes in the carbon cycle on atmospheric Δ^{14}C and on the ^{14}C production rates (Köhler et al., 2006).

5.2 Anthropogenic emissions — ground truth of the paleo Keeling plot approach

We implement a data-based estimate of the anthropogenic emission since 1750 AD in our model as seen in Fig. 2. BICYCLE calculates $p\mathrm{CO}_2$ depending on the dynamics of the terrestrial biosphere. In the more realistic case of an active terrestrial biosphere, implying an enhanced photosynthesis and thus carbon uptake through CO_2 fertilisation, $p\mathrm{CO}_2$ at year 2000 is calculated to 351 μatm (Fig. 5C). A scenario with passive terrestrial biosphere, meaning a constant carbon storage over time, leads to 388 μatm in the same year (Fig. 5A). The annual mean in year 2000 in the atmospheric CO_2 data at Point Barrow is 371 ppmv, which is approximately half way between the results of the two different simulation scenarios. The scenario with passive terrestrial biosphere is easier to interprete, since we only have to consider the anthropogenic carbon flux to the atmosphere and the effect of the oceanic sink. Both scenarios will be analysed in the following.

The precise value of the δ^{13}C signature of anthropogenic caused carbon release is still uncertain, e.g. land use change has a δ^{13}C of $-25‰$ (Scholze et al., 2003), while δ^{13}C of fossil fuel emissions is around $-30‰$ (Blasing et al., 2004). We therefore varied the isotopic signature of the anthropogenic carbon fluxes between $-20‰$ and $-30‰$ to evaluate the importance of this signature for the simulation results. The simulated atmospheric δ^{13}C in year 2000 AD was $-8.4‰$, $-9.1‰$, $-9.7‰$ and $-7.4‰$, $-7.9‰$, $-8.4‰$ in the scenario with passive and active terrestrial biosphere and for different δ^{13}C signatures ($-20‰$, $-25‰$, $-30‰$), respectively (Fig. 5A,C), reflecting a larger terrestrial fixation of anthropogenic carbon in the active scenario. The annual average δ^{13}C measured at different globally distributed stations varied between -8.0‰ and -8.2‰ (Keeling et al., 2005).

The regression functions of the Keeling approach are still a good approximation of the artificial data sets ($r^2 \geq 94\%$, Fig. 5B,D). However, the y-axis intercept varies depending on the assumed δ^{13}C signal of the anthropogenic carbon flux and the mode of the terrestrial biosphere (active/passive) between -9.2‰ and -15.7‰, while the Law Dome data show -13.1‰ (Table 1). Note, that these numbers are significantly higher than the isotopic signature of the anthropogenic carbon added to the system. Due to the non-negligible effect of a third reservoir, the ocean, the Keeling y-axis intercept deviates from the expected flux signature derived in section 4. Normalised to the δ^{13}C signal of the anthropogenic flux the y-axis intercept amounts to $52 - 59\%$ (passive terrestrial biosphere) and $45 - 46\%$ (active terrestrial biosphere) of the isotopic signal of the anthropogenic flux (Table 1). The difference to an ideal Keeling plot, in which the whole signal would be explained by the y-axis intercept has to be explained purely by oceanic uptake in the case of a passive terrestrial biosphere, and by a mixture of terrestrial and oceanic uptake in simulations with active terrestrial biosphere.

Natural changes in atmospheric CO_2 over the past 650,000 years as recorded in Antarctic ice core records (Petit et al., 1999; Siegenthaler et al., 2005) were always slower and smaller in amplitude than the anthropogenic impact of the last 250 years. Therefore it is conservative to assume that the oceanic uptake of a terrestrial disturbance in the past will always be greater than during the anthropogenic period. The potential of the Keeling plot approach to paleo climate research therefore seems to have an upper limit. No more than about 50% of the isotopic signature of a carbon source to the atmosphere can be explained with it. In fact, due to the longer time scales on which most processes act during glacial cycles it can be expected that much less than this upper limit can be explained by the Keeling plot approach. For steady state situations (the atmosphere and the ocean are in equilibrium) the perturbation of the carbon cycle through terrestrial carbon release with a signature of -25‰ leads to a $\delta^{\Delta A}_{\delta\mathrm{C}\to 0}$ of about -9‰, as shown in section 4. Thus, for this situations only a fraction of $9/25 = 0.36$ is explainable with the Keeling plot approach.

5.3 Glacial/interglacial times

Besides this upper limit of a signal interpretation due to oceanic carbon uptake in long time series two other factors make a comparison of artificial time series with long ice core data sets difficult: First, the air which is enclosed in bubbles in the ice can circulate through the firn down to the depth where bubble close off occurs

Table 1: Analysis of ground truth of the Paleo-Keeling approach: Simulating the anthropogenic rise in $p\mathrm{CO}_2$. Experiments with different $\delta^{13}C_{\mathrm{ant}}$ signatures of the anthropogenic carbon flux and for two different systems including an active and a passive terrestrial biosphere are analysed. Displayed are the y-axis intercepts y_0 of the Keeling plots and the ratio which is explained by this approach (y_0 / $\delta^{13}C_{\mathrm{ant}}$).

Mode of the terrestrial bioshere	$\delta^{13}C_{\mathrm{ant}}$ (‰)		
	-20	-25	-30
	y_0 (‰)		
passive	-11.8	-13.7	-15.7
active	-9.2	-11.3	-13.5
	y_0 / $\delta^{13}C_{\mathrm{ant}}$(-)		
passive	0.59	0.55	0.52
active	0.46	0.45	0.45

($\sim 70 - 100$ m) before it is entrapped in the ice. The bubble close off is a slow process with individual bubbles closing at different times and depth. Accordingly the air enclosed in bubbles and in an ice sample is subject to a wide age distribution acting as an efficient low-pass filter on the atmospheric record. Therefore, all information from the gaseous components of the ice cores is averaged over a time interval of the age of the firn / ice transition zone. This time interval is depending on temperature and accumulation rates, but can roughly be estimated by the ratio of the depth of the firn / ice transition zone divided by the accumulation rate (Schwander and Stauffer, 1984). Thus, the time integral in the gas is small (< 20 years) at Law Dome (Etheridge et al., 1996), varies at Taylor Dome between 150 years in the Holocene and 300 years in the LGM (Steig et al., 1998a,b), and at EPICA Dome C, at which the most recent CO_2 and δ^{13}C measurements were performed (Monnin et al., 2001; Eyer, 2004; Eyer et al., 2004; Siegenthaler et al., 2005), between 300 and 600 years (Schwander et al., 2001). Second, the CO_2 and δ^{13}C records retrieved from ice cores are never continuous records, but consist of single measurements with large, but un-regular data gaps in between. In the Taylor Dome ice core these gaps are on average approximately 1000 years wide. It will be therefore of interest to investigate if the temporal resolution in the data set will be sufficient enough to resolve information potentially retrievable through the Keeling approach.

Anthropogenic activities add carbon via land use change and fossil fuel emissions to the atmosphere, and only subsequently absorbed by the ocean. The causes for natural changes in atmospheric CO_2 and thus the carbon cycle during glacial/interglacial times were to a large extent located in the ocean. Thus, the causes and effects respectively their timing are in principle different. For the natural glacial/interglacial variations the carbon content of the atmosphere is determined by the surface ocean, the atmosphere is also called *slave to the ocean*, while for the anthropogenic impact the opposite is the case: The carbon of the surface ocean is modified by the injection of the anthropogenic rise in atmospheric CO_2.

This situation has also consequences for the investigation of different processes causing natural changes in the carbon cycle. We concentrate in the following on the individual impacts of six important processes. We first investigate the maximum impacts possible from changes in these processes and then analyse variations of realistic amplitude. These processes are changes in terrestrial carbon storage, export production of the marine biota, ocean circulation, gas exchange rates and their variation through variable sea ice cover, and physical effects of variable sea level and ocean temperature. Please note, that in these factorial scenarios all processes can be treated uncoupled in our box model, e.g. changes in the circulation scheme will not lead to temperature variations, which might be the case in general circulation models. A summary of this single process analysis is compiled in Table 2. We end with a combined scenario proposed by Köhler et al. (2005a) which is able the reconstruct the atmospheric carbon records between 20 and 10 kyr BP. Note, that from these different scenarios only the first one (changes in terrestrial carbon storage) strictly resembles the initial idea of a Keeling plot (addition/subtraction of carbon from the atmosphere).

Table 2: Summary of y-axis intercept y_0 and its difference from the terrestrial boundary $\delta^{\Delta A}_{\delta \mathrm{C} \rightarrow 0} = -8.4‰$ of the prior/after Keeling plot analysis for processes changing over Termination I.

Process	y_0 (‰)	$y_0 - \delta^{\Delta A}_{\delta \mathrm{C} \rightarrow 0}$ (‰)	Comment
Linear rise in terrestrial carbon storage	-8.6	-0.2	increase was probably non-linear, steepest slope $-25‰$
Decrease in marine export production	-8.6	-0.2	steeper slope with $y_0 = -9.7‰$ during first 50 years
Rise in NADW formation	-7.8	$+0.6$	varies with time; mixture with changes in marine export production during Heinrich 1 event; during Younger Dryas and resumption in the Holocene $y_0 = -7.15 \pm 0.05‰$, steep slope during first 50 y with $y_0 = -9.5‰$
Rise in Southern Ocean vertical mixing	-8.2	$+0.2$	steep slope during first 50 years with $y_0 = -11.0‰$
Decline in sea ice cover / rise in gas exchange rates	-0.7	$+7.7$	regression over whole data set finds $-3.8‰$ with differences in the North ($-4.8‰$) and the South ($-77.2‰$)
Rise in sea level	-6.4	$+2.0$	
Rise in temperature	-3.6	$+4.8$	
Sediment/ocean interaction	-5.8	$+2.6$	

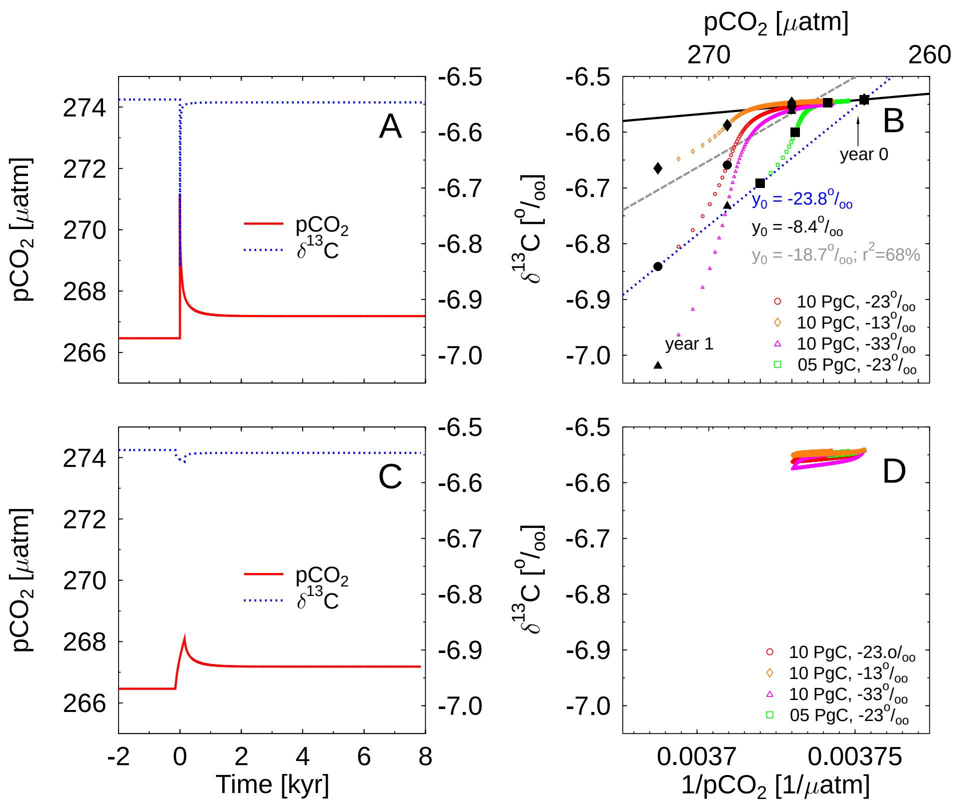

Figure 6: Effect of a pulse of instantaneous release (within one year) of terrestrial carbon with an isotopic signature of $\delta^{13}\text{C} = -23‰$ (left: $p\text{CO}_2$, δ^{13}C; right: Keeling plot). Different carbon release amplitudes (5, 10 PgC) and different δ^{13}C signatures (-13, -23, $-33‰$) are tested. The regression functions seen in B are for the three different regression models for the 10 PgC/$-23‰$ scenario (red circles). Model 1: year 0 and year 1 (short dash); model 2: year 0 and year 8,000 (solid); model 3: regression through 375 years (long dash). Large black markers mark the years 0, 1, 10, 100 in each record. Bottom: Same as above but now the data are smoothed with a 300 yr running mean.

5.3.1 Terrestrial biosphere

There are two opposing changes in terrestrial carbon storage to be investigated: carbon uptake or carbon release. Both might happen very fast in the course of abrupt climate anomalies, such as so-called Dansgaard/Oeschger events (Dansgaard et al., 1982; Johnsen et al., 1992), during which Greenland temperatures rose and dropped by more than 15 K in a few decades during the last glacial cycle (Lang et al., 1999; Landais et al., 2004). Terrestrial carbon storage anomalies during these events were estimated with a dynamic global vegetation model to be of the order of $50 - 100$ PgC (Köhler et al., 2005b). The time scales of these anomalies are of the order of centuries to millenia. We first analyse a scenario in which 10 PgC are released or taken up by the terrestrial pools within one year. This short time frame of one year was chosen to have experiments, in which the whole carbon flux is first altering the atmospheric reservoir, before oceanic uptake or release will set in after year one. The amplitude of the perturbations is optimised to 10 PgC to guarantee still negligible numerical uncertainties ($< 0.01‰$) in the calculation of the δ^{13}C fluxes. We follow with experiments of linear carbon release and three scenarios of carbon uptake during Termination I to investigate the importance of the time scale for the Keeling plot interpretation.

Fast terrestrial carbon release: This would be the scenario closest to the original Keeling plot analysis in terrestrial ecosystem research. There is a source (terrestrial biosphere) which emits CO_2 directly to the atmosphere. In this experiment, the 10 PgC release first increases $p\text{CO}_2$ by more than 4 μatm immediately after the release, and equilibrates less than 1 μatm higher than initially (Fig. 6A). The δ^{13}C signal shows a drop by more than 0.3‰ in year one, and a steady state which is nearly similar to the initial situation (Fig. 6A). Near steady state ($\pm 0.1\%$) in both $p\text{CO}_2$ and δ^{13}C was reached 376 years after the carbon release.

There are several possibilities to draw a regression function through the Keeling plot (Fig. 6B):

Table 3: Terrestrial carbon release of different amplitude and isotopic signature and calculated y-axis intercept based on the original model output, after low-pass filtering of the data with a 300 year running mean, and after data filtering and reducing the data sets to samples every 100 years.

Scenario		y-axis intercept of different regression models (‰) (r^2 in brackets)			
Amplitude of the release (PgC)	isotopic signature $\delta^{13}C_{\mathrm{rel}}$ of release (‰)	model 1 rising[a]	model 2 prior — after[b]	model 3 equilibration[c]	equilibration time (yr) for model 3
original model output					
10	-23.4	-23.8 (100)	-8.4 (100)	-18.7 (68)	375
5	-23.4	-23.6 (100)	-8.4 (100)	-22.3 (75)	189
10	-33.4	-33.9 (100)	-9.3 (100)	-26.0 (68)	375
10	-13.5	-13.6 (100)	-7.5 (100)	-11.4 (70)	375
300 yr running mean					
10	-23.4	-8.9 (93)	-8.4 (100)	-10.4 (85)	241
5	-23.4	-8.9 (93)	-8.4 (100)	-13.8 (89)	71
10	-33.4	-10.2 (92)	-9.3 (100)	-12.6 (84)	241
10	-13.5	-7.7 (95)	-7.5 (100)	-8.4 (86)	241
300 yr running mean + data selection every 100 yr					
10	-23.4	-8.6 (100)	-8.4 (100)	-9.1 (100)	150
5	-23.4	-8.6 (100)	-8.4 (100)	not detectable[d]	50
10	-33.4	-9.6 (100)	-9.3 (100)	-10.5 (100)	150
10	-13.5	-7.5 (97)	-7.5 (100)	-7.7 (100)	150

a: This covers data during rise of atmospheric $p\mathrm{CO}_2$, which are only two points in the original data set, but longer series in smoothed records.
b: Comparing steady state before with new steady state after carbon release.
c: Regression during declining $p\mathrm{CO}_2$ in equilibration time.
d: There is only one data point in the time window spanned by the equilibration process, from which no regression analysis can be performed.

1. A line connecting only the data prior to the start of the carbon release experiment (year 0) and one year later after 10 PgC are released but before any carbon is taken up by the ocean representing the maximum possible slope. Thus, $p\mathrm{CO}_2$ and δ^{13}C after the release can also be calculated following the mass balance equations of a two reservoir system (Eq. 3 and 4).

2. A straight line through two points characterising the states prior to the carbon release and after re-equilibration. This would contain the minimum information retrievable in case of low sampling frequency and would be the analog to the theoretical considerations for a three reservoir system.

3. A regression function through the subset of points covering the equilibration process, in which the main dynamics of the carbon release are represented. We here choose all points after the release (year 1) until both $p\mathrm{CO}_2$ and δ^{13}C were within $\pm 0.1\%$ of their final steady state values.

It is also of interest if and how the amplitude of the carbon release and its isotopic signature influence the Keeling approach. We therefore performed additional simulations (Fig. 6B,D) with smaller amplitude (5 PgC) and different δ^{13}C signature ($-13.5, -23.4, -33.4$‰). These signatures are the result of the variation of the assumed global terrestrial fractionation factor $\varepsilon_{\mathrm{TB}} = -17$‰ by ± 10‰.

If such an event of terrestrial carbon release is to be detected in ice cores, we have to manipulate our artificial data set to account for both the temporal integral during gas enclosures and the limited sampling frequency. We assumed an average mixing time (running average of 300 years), and a regular sampling frequency of 100 years, typical for Antarctic ice core studies.

A summary of calculated y-axis intercepts is found in Table 3. In the original model output the regression model 1 (analysis of the carbon flux in the year of the release) can explain the δ^{13}C signature of terrestrial release very well, independent of amplitude or the δ^{13}C signature itself. The slight overestimation of the regression model of up to 0.5‰ might be due to numerical limitations. Differences in the y-axis intercept between scenarios with varying amplitude and δ^{13}C signature of the released carbon are still large in regression model 3 (y_0 from -18.7‰ to -26.0‰), but a simple functional relationship between y-axis intercept y_0 and the $\delta^{13}\mathrm{C}_{\mathrm{rel}}$ signature of the flux is missing. In model 2 the different δ^{13}C signatures of the carbon release flux are still distinguishable by small differences in the y-axis intercept (y_0 = $-7.5, -8.4, -9.3$‰). These y_0's gained from model 2 are similar to the boundary $\delta^{\Delta A}_{\delta \mathrm{C} \to 0}$ introduced in section 4, which is an embedded feature of the system configuration. Interestingly, the y_0 values derived from the BICYCLE simulations are about 1‰ isotopically heavier than in our equilibrium model in section 4. The reason for this is the establishing of vertical gradients in DIC and δ^{13}C in the ocean due to the ocean carbon pumps (Volk and Hoffert, 1985) leading to an enrichment of δ^{13}C in the surface water by about 1‰.

If we take the signal broadening through temporal mixing in the firn into account (Fig. 6 bottom), the perturbations in $p\mathrm{CO}_2$ and δ^{13}C are largely reduced to 34% and 7% of their original amplitudes, respectively, and the duration of the atmospheric $p\mathrm{CO}_2$ rise of one year in the original data is now spread over the time length of the smoothing filter (300 yr). Even for conditions similar to those found at Law Dome where the air is mixed only over a time interval of 20 years, the amplitudes in $p\mathrm{CO}_2$ and δ^{13}C are reduces to 70% and 47% of their original values, respectively. Y-axis intercepts for the 300 years smoothing filter are reduced significantly for regression models 1 (30% to 57% of y_0 in original data) and 3 (48% to 74% of y_0 in original data).

A further increase of uncertainty arises if we reduce the sampling interval. The effect of a 100 year sampling frequency reduces y-axis intercepts calculated with regression model 1 and 3 further (Table 3). However, the uncertainty introduced by reduced sampling frequency is much smaller than the one based on firn air mixing. Results obtained with regression model 2 (boundary $\delta^{\Delta A}_{\delta \mathrm{C} \to 0}$) were not affected by any of the two post simulation procedures.

From these fast carbon release experiments, several conclusions can be drawn:

1. The results of regression model 1 are in line with the mass balance equations of the two reservoir Keeling approach.
2. In all multi-annual experiments the oceanic uptake of carbon will play an important role.
3. Fast terrestrial carbon release events are in their full extent not recordable in the ice core records due to the time integral introduced by the firn enclosure process.

Slow terrestrial carbon exchange: To understand glacial/interglacial dynamics one has to investigate larger variations in terrestrial carbon storage of several hundreds of PgC, which occurred over longer time intervals. We have therefore performed additional experiments, one in which 500 PgC is released by the terrestrial pools, but now with a constant release rate over a period of 6000 years. In a second set of experiments we mimic in a

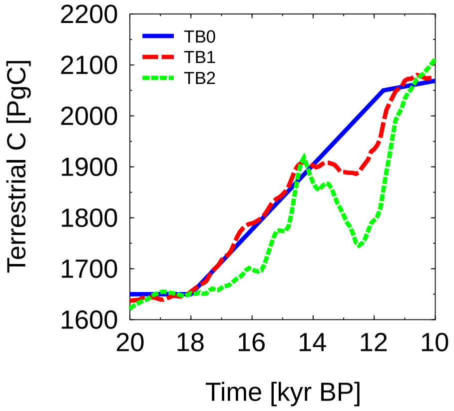

Figure 7: Changes in the terrestrial carbon storage during the last glacial/interglacial transition follows a null-model of linear increase (TB0) or two different dependencies dominated by CO_2 fertilisation (TB1) or climate (TB2). Scenarios taken from Köhler et al. (2005a).

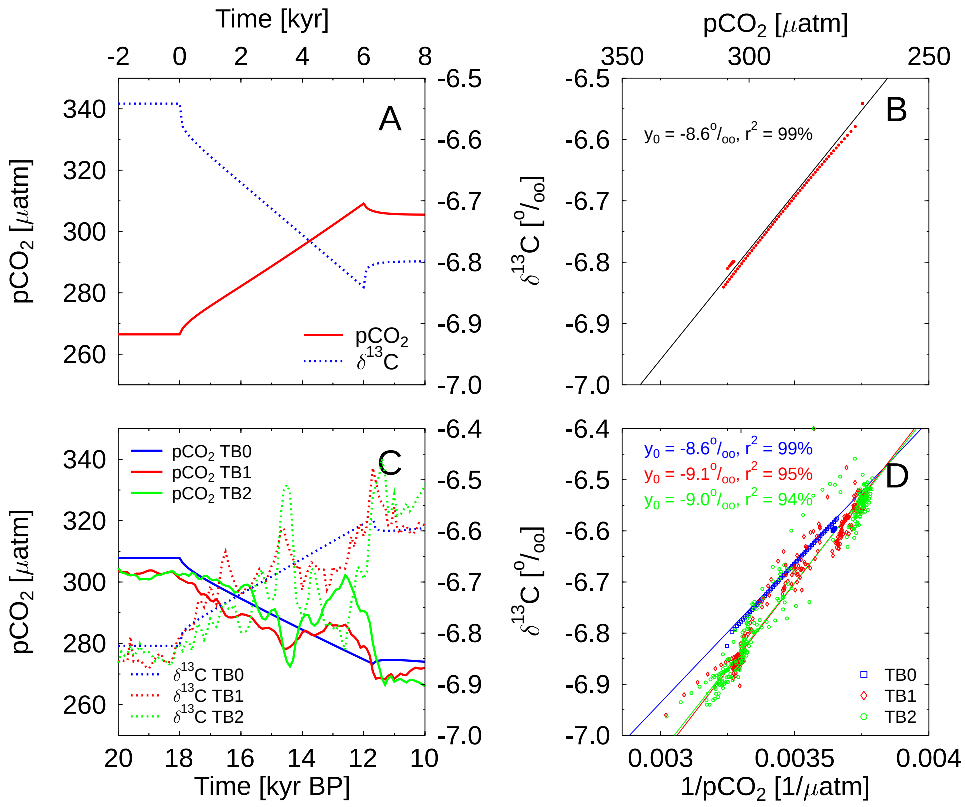

Figure 8: Effects of a gradual change in the carbon storage of the terrestrial biosphere (left: $p\mathrm{CO}_2$, δ^{13}C; right: Keeling plot). Top: Linear decrease in terrestrial carbon storage by 500 PgC. Bottom: Scenarios TB0 (biosphere only, linear increase in terresterial carbon by 400 PgC between 18 and 11.8 kyr BP) TB1 (dominated by CO_2 fertilisation) and TB2 (dominated by climate change) as shown in Fig. 7. Regressions in the Keeling plots are performed over the whole time period.

simplistic way the carbon uptake of approximately 400 PgC over 6000 yr which might have occurred during the last glacial/interglacial transition between 18 and 12 kyr BP as assumed in three different scenarios (TB0, TB1, TB2) in Köhler et al. (2005a). These scenarios differ in functional dependencies of the terrestrial carbon storage on CO_2 fertilisation and climate change (TB0: linear rise in terrestrial carbon; TB1: mainly CO_2 dependent; TB2: mainly climate dependent; Fig. 7).

In both linear experiments (carbon release and TB0) the atmospheric δ^{13}C record shows an relaxation behaviour in the first several hundred years after the beginning and after the end of the carbon release with a gradual change in between (Fig. 8). Atmospheric $p\mathrm{CO}_2$ is changing rather constantly over time, also with small nonlinear responses in the first few hundred years at the beginning and at the end of the experiment. These discontinuities are caused by the time-delayed oceanic carbon uptake. For example, after the end of the experiment ($t = 6$ kyr, Fig. 8A) large parts of the released carbon are taken up by the ocean in the following centuries, similar as in the fast carbon release experiment shown in Fig. 6. In the more complex scenarios TB1 and TB2 the changes in $p\mathrm{CO}_2$ and δ^{13}C are largest in the climate dominated scenarios TB2 with changing rates of up to 30 μatm in $p\mathrm{CO}_2$ and 0.3‰ in δ^{13}C in 1000 years. In the Keeling plots the relaxation behaviour at the beginning and the end of the linear experiments leads to offsets from the well defined linear relationship. A regression over the whole time period leads to a $y_0 = -8.6$‰, only 0.2‰ smaller than the $\delta^{\Delta A}_{\delta \mathrm{C} \to 0}$ boundary for this system. The scatter of the data points is larger in TB1 and TB2, but the regression model through the data is still very good ($r^2 \geq 94\%$) leading to $y_0 = -9.1$ and -9.0‰, respectively. The slope of the regression is steeper here, because the fractionation factor of the terrestrial biosphere $\varepsilon_{\mathrm{TB}}$ is changing over time. The fraction of terrestrial carbon produced by C_4 photosynthesis is decreasing from $\sim 30\%$ during the LGM to $\sim 20\%$ during preindustrial times in the scenarios TB1 and TB2 (Köhler and Fischer, 2004). This leads to a terrestrial fractionation which is more than 1‰ more negative in the preindustrial times than in the LGM.

The range of the δ^{13}C values concluded from our simulation results for a slow terrestrial carbon release agrees

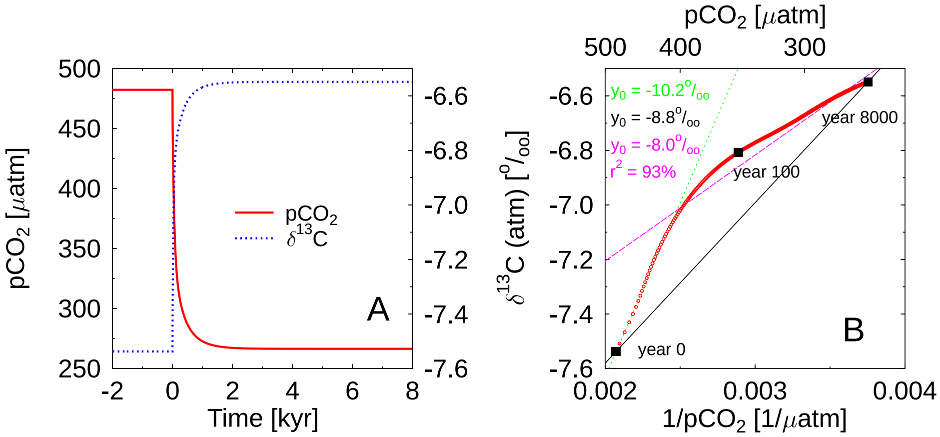

Figure 9: Switching from an abiotic to a biotic ocean at $t = 0$ kyr (A: pCO$_2$, δ^{13}C; B: Keeling plot). Different regression models in B: model 1 (first year only) in green; model 2 (prior/after) in black; model 3 (equilibration time) in magenta.

well with the ones proposed by our theoretical three reservoir approach in section 4 and is very different from the original δ^{13}C of the carbon source. It is especially remarkable that the differences of the y_0's from $\delta^{\Delta A}_{\delta \mathrm{C} \to 0}$ are very small. Furthermore, these slow carbon exchange processes are so slow that the air enclosure procedure with the assumed smoothing filter of 300 years would only marginally alter the records and would not change the y_0 values. Similarly the restricted sampling frequency is of no importance here. These two processes will therefore not be analysed any further in the following, because it is reasonable to assume that their impact on the observed processes can be neglected.

5.3.2 Marine biosphere

While the marine biosphere is in principle a reservoir separate from DIC in the ocean and the atmospheric carbon, it is not independent because the marine export production establishes vertical gradients in DIC and δ^{13}C between the surface and the deep ocean. Accordingly, the following discussion of changes caused by the marine biosphere and other factors later-on represents already a misuse of the Keeling plot approach. Nevertheless it is instructive to study whether the end member analysis can lead to meaningful results and is able to distinguish between different processes.

For the marine biota we again first want to explore the range of possible results before we analyse one scenario which seems to be realistic for the last glacial/interglacial transition. We therefore concentrate first on a switch from an abiotic ocean without any marine biological productivity and no export production to a biotic ocean in year 0 and vice versa. After these biotic/abiotic experiments, the possible effect of an extended glacial marine productivity due to the iron fertilisation in the Southern Ocean is explored. In the biotic ocean a flux of 10 PgC yr^{-1} of organic carbon is exported at 100 m water depth to the deeper ocean. This organic export production is coupled via the rain ratio to an export of 1 PgC yr^{-1} of inorganic CaCO$_3$.

The abiotic/biotic switch leads to a decrease in atmospheric pCO$_2$ of about 220 μatm and a rise in atmospheric δ^{13}C of 1.0‰ (Fig. 9A) and the opposite signals in the biotic/abiotic experiment (not shown). The iron fertilisation experiment decreases glacial pCO$_2$ by 20 μatm, in parallel with a 0.15‰ rise in δ^{13}C (Fig. 10A). Here, both atmospheric records are relaxing to their preindustrial values after the onset of iron limitation around 18 kyr BP. The Keeling plot analysis leads to y-axis intercepts of -8.0 to -10.2‰ for the three different regression models in the abiotic/biotic experiment (Fig. 9B). Comparing only the prior/after model for all three experiments (abiotic/biotic, biotic/abiotic, iron fertilisation) (Fig. 9B, 10B) gives nearly identical results ($y_0 = -8.7 \pm 0.1$‰). If the time window of analysis is reduced to the first 50 years after the beginning of the reduction in export production in the iron fertilisation experiment a steeper slope in the Keeling plot leads to y_0 of -9.7‰ (Fig. 10B).

The marine export production combines two of the three ocean carbon pumps: the organic or soft-tissue pump and the carbonate pump (Volk and Hoffert, 1985). The third one, the solubility pump, operates by the increased solubility of CO$_2$ in downwelling cold water. They all introduce vertical gradients in DIC in the water column, the biological pumps additionally build up a gradient in δ^{13}C. DIC is reduced in the surface layers through marine

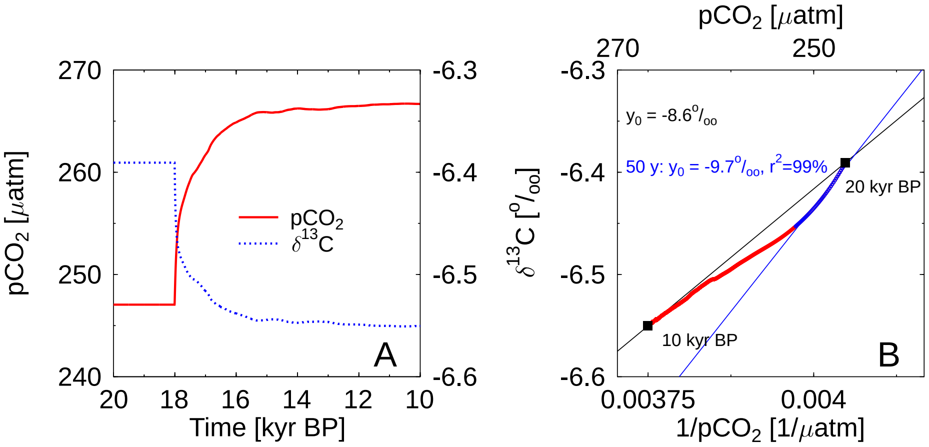

Figure 10: Effects of iron fertilisation in the Southern Ocean on atmospheric carbon records with scenario taken from Köhler et al. (2005a) (A: $p\mathrm{CO}_2$, δ^{13}C; B: Keeling plot). Blue dots and regression in B over the first 50 years during $p\mathrm{CO}_2$ rise only.

production of both organic material (soft-tissues) and CaCO$_3$ and increased in the abyss through carbon released during remineralisation and dissolution. During photosynthesis δ^{13}C is depleted by about $-20‰$, thus leaving carbon enriched in ^{13}C at the surface, while the exported organic matter is depleted. The isotopic fractionation during the production of hard shells slightly enriches ^{13}C in the carbonate ($\varepsilon \in [0, 3]‰$). The vertical gradient in δ^{13}C leads to a difference of about 1.0‰ between surface ($1.5‰$) and abyss ($0.5‰$) in the biotic ocean, while the δ^{13}C signal in the abiotic ocean does not change with depth and is around $0.55‰$. If we now switch on the marine production in a formerly abiotic ocean we merely introduce these gradients to the system. Surface δ^{13}C is rising by 1.0‰ and so is the atmospheric δ^{13}C. The signal seen in the atmospheric record is therefore a mixture of the fractionation during gas exchange and an increased carbon flux from the atmosphere to the ocean. In BICYCLE the flux of CO$_2$ from the surface ocean to the atmosphere has a fractionation factor of $\varepsilon_{\mathrm{O2A}} \approx -10.4‰$ and $\varepsilon_{\mathrm{A2O}} \approx -2.4‰$ in the opposite direction leading to a net fractionation effect of $-8.0‰$ (but both depend also on temperature, and $\varepsilon_{\mathrm{O2A}}$ additionally on DIC, HCO$_3^-$, and CO$_3^{2-}$). Similar as in the previous case of a terrestrial carbon release the system contains a boundary in the effective isotopic signature. Each perturbation of the system leads to a derivation from this boundary. The effects of changes in the marine carbon fluxes on atmospheric $p\mathrm{CO}_2$ and δ^{13}C are not necessary the same as for the terrestrial case. Therefore, the boundary is not identical with $\delta^{\Delta A}_{\delta \mathrm{C}\to 0}$, but seems to be very close. From variations of the global export production one can estimate this marine boundary to be around $-8.5‰$. In year 1, for example, one can understand the signal ($y_0 = -10.2‰$) in the following way: In areas in which marine export production is reducing surface DIC the gross carbon flux from the ocean to the atmosphere is largely reduced. In the most extreme case we would only find a gross carbon flux from the atmosphere to the ocean with the corresponding fractionation factor $\varepsilon_{\mathrm{A2O}} = -2.4‰$. This would be the isotopic signature of the process in action and added to the marine boundary it would lead at maximum to a y_0 of $-10.9‰$. The calculated y_0 is smaller because there is still a small but not negligible gross flux of CO$_2$ from the ocean to the atmosphere. The signal during the first 50 years of the iron fertilisation experiment ($y_0 = -9.7‰$) can be interpreted similarly. During the latter part of the abiotic/biotic switch experiment and over the equilibration period y_0 is $\sim -8.0‰$ and thus more positive than the marine boundary. This might be caused by the increased δ^{13}C of the DIC in the surface waters. After 100 years, $p\mathrm{CO}_2$ has already dropped to 346 μatm, thus nearly 2/3 of the oceanic uptake of carbon happens in this first century. Therefore the carbon fluxes from the atmosphere to the ocean and vice versa are nearly similar thereafter. That means that now the isotopic enriched DIC of the surface waters can enter the atmosphere and is then enriching δ^{13}C and y_0.

If compared with the terrestrial experiments the results from regression model 3 (prior/after analysis) have y_0's which are only $0.2 - 0.4‰$ more negative than $\delta^{\Delta A}_{\delta \mathrm{C}\to 0}$. This is very similar to the experiments with slow carbon exchange between the terrestrial biosphere and the atmosphere.

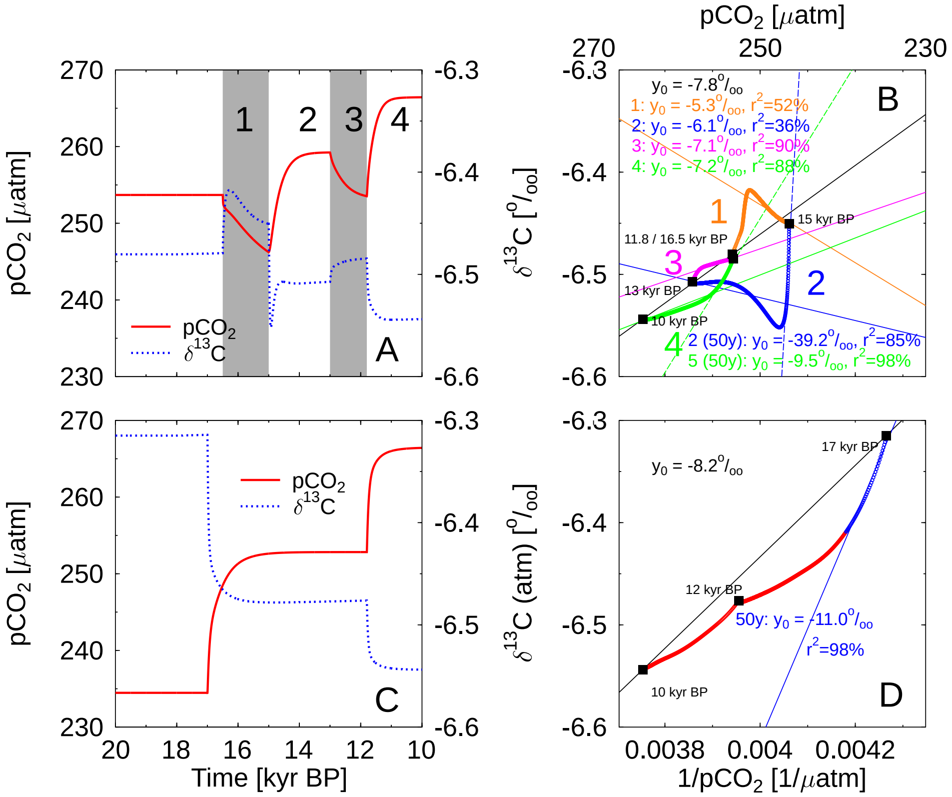

Figure 11: Simulated effects of changes in the strength of the NADW formation (top) and Southern Ocean vertical mixing (bottom) as used in Köhler et al. (2005a) (left: $p\mathrm{CO}_2$, δ^{13}C; right: Keeling plot). Four different time intervals with different strength in NADW formation are identified and labeled in A and B. Regression are performed for the prior/after situation (black, B, D), for these four time intervals (B) and for selected 50 year time windows (B, D).

5.3.3 Ocean circulation

Previously Köhler et al. (2005a) assumed a rise in the strength of the North Atlantic Deep Water (NADW) formation from 10 Sv (10^6 m^3 s^{-1}) during the Last Glacial Maximum (LGM) to intermediate levels of 13 Sv in the Bølling/Allerød warm interval and 16 Sv at the beginning of the Holocene. This rise was punctuated by sharp drops in the NADW formation strength and the subsequent ocean circulation fluxes to 0 Sv and 11 Sv during the Heinrich 1 event and the Younger Dryas, respectively. Repeating this temporal sequence of events over a period of approximately 6000 years leads to drops in $p\mathrm{CO}_2$ by 10 μatm during times of reduced ocean circulation accompanied by rises in δ^{13}C of about 0.05‰. Initial and final values differ by about 15 μatm and -0.05‰ (Fig. 11A).

The prior/after analysis in the Keeling plot leads to a y-axis intercept of -7.8‰, however, the pattern is highly time-dependent and allows a breakdown of the time series into the individual events, which show distinctively different behaviour. These events are marked in Fig. 11A,B (1: decrease in NADW formation during Heinrich 1 event; 2: increase in NADW formation during Bølling/Allerød warm interval; 3: decrease in NADW formation during Younger Dryas; 4: increase in NADW formation towards interglacial levels). The regression analysis over the whole of these four periods, which last between 1200 and 2000 years each, finds y-axis intercepts between -5.3 and -7.2‰. If shorter time windows after the beginning of these changes in ocean circulation are analysed, much steeper regression functions can be found. For example, the regressions through 50 year time windows at the beginning of interval 2 and 4, which show the steepest slopes in the Keeling plot, lead to y-axis intercepts of -39.1 and -9.5‰, respectively (Fig. 11B).

The complete shut-down of the NADW formation during Heinrich 1 event alters also the nutrient availability for the marine biota. The export of organic matter depends on the availability of macro-nutrients in the surface waters and is prescribed to an upper limit of 10 PgC yr^{-1}. In the time interval between 16.5 and 15 kyr BP marine export falls from 10 PgC yr^{-1} to $8.9 - 9.3$ PgC yr^{-1}. Less export production increases atmospheric $p\mathrm{CO}_2$ and decreases atmospheric δ^{13}C. This implies that the peaks in the atmospheric carbon records were both dampened during interval 1. Accordingly, the y_0 derived from the Keeling plot during this time interval is a mixture of ocean circulation and marine biota.

A second ocean circulation process which changed according to Köhler et al. (2005a) over the time of the last transition was the Southern Ocean vertical mixing rate (Fig. 11C,D). It rose from 9 Sv (glacial) to 29 Sv (preindustrial) and led to a rise in pCO$_2$ by about 30 μatm and a drop in δ^{13}C by more than $0.2‰$. Here, the Keeling plot interpretation gives us a y-axis intercept of $-8.2‰$ for the prior/after analysis. The steepest slope during the first 50 years after the start of the change would yield to a y-axis intercept of $-11.0‰$ (Fig. 11D).

The overturning circulation distributes carbon in the ocean. Its effect on the atmospheric carbon reservoirs, however, is opposite to that of the three ocean carbon pumps. While the pumps introduce vertical gradients in DIC and δ^{13}C as described in the subsection about the marine biota, the overturning circulation is reducing these vertical gradients again through the ventilation of the deep ocean which brings water rich in DIC and depleted in ^{13}C back to the surface. A weakening of the ventilation reduces these upwelling processes and leads to lower pCO$_2$ and higher δ^{13}C values as seen in the experiments.

The y_0-values derived from the four intervals for changing NADW formation differ. Between interval 3 and 4 in which opposing changes in ocean circulation occur, the differences in the y_0-values are small. These different circulation patterns can be seen in the Keeling plot in the dynamics of the first years of the intervals: In intervals 1 and 3, in which the strength of the NADW formation is reduced, the analysis of a time window at the beginning of the interval leads to less negative y_0 than over the whole period, while the opposite is the case in the intervals 2 and 4 with a resumption of the NADW formation. These temporal changes over the course of each interval are caused by the equilibration of the model to a new steady state. In interval 1, the shutdown of the NADW and the subsequent fluxes lead first to an enrichment of DIC and of ^{13}C in the North Atlantic surface waters and thus to higher atmospheric δ^{13}C. Later-on, this is over-compensated by decreasing DIC and δ^{13}C in the equatorial surface of the Atlantic Ocean. However, the dynamics during a complete shutdown of the NADW formation might be unrealistic because in the current model configuration the tropical Atlantic surface and intermediate ocean boxes would exchange water with each other but not with any other water masses (Fig. 4). This artefact is also responsible for the dynamics during the first years of interval 2, but is not affecting the latter intervals.

Compared to the terrestrial carbon release we can say that a change in ocean circulation is assigned to a y_0 slightly more positive than the terrestrial boundary $\delta^{\Delta A}_{\delta \mathrm{C} \to 0}$ ($+0.2$ to $1.2‰$). The dynamics during the first years of a abrupt rise/decrease in the strength of the overturning circulation lead to larger offsets (fall/rise) from the terrestrial boundary.

5.3.4 Gas exchange / sea ice

A change in sea ice cover leads to changes in the gas exchange rates with opposing effects for the northern and the southern high latitudes. As the preindustrial North Atlantic Ocean is a sink for CO$_2$ a reduced gas-exchange due to higher sea ice cover leads to rising atmospheric pCO$_2$, while the same happening in the Southern Ocean being a source for CO$_2$ leads to a drop in pCO$_2$. Again, we first explore the maximum amplitudes possible by covering either the whole North Atlantic Ocean or Southern Ocean surface boxes with sea ice, reducing the gas exchange rates in these areas to zero (Fig. 12 top) before we investigate a data-based scenario for Termination I in which sea ice was approximately doubled during glacial times (Fig. 12 bottom).

In the extreme scenarios sea ice cover is relaxed instantaneously from a full coverage of the surface ocean boxes to preindustrial areal distribution in year 0. The experiment in the North Atlantic yields a drop in pCO$_2$ by 35 μatm, a drop in δ^{13}C by $0.04‰$, and a y-axis intercept (prior/after analysis) in the Keeling plot analysis of $-6.1‰$. A similar experiment in the Southern Ocean increases pCO$_2$ by about 15 μatm, δ^{13}C drops by $1.0‰$ leading to a prior/after y-axis intercept of $-23.8‰$.

In the data based scenario across Termination I the annual averaged sea ice area during LGM is approximately doubled (Crosta et al., 1998a,b; Sarnthein et al., 2003; Gersonde et al., 2005) and its evolution is coupled to sea surface temperature changes. pCO$_2$ fluctuates by about 10 μatm and δ^{13}C by $0.15‰$ (Fig. 12C). Due to the different responses in the North and in the South the data plotted as Keeling plot zig-zag quite a lot. Prior/after analysis finds an y-axis intercept of $-0.7‰$. The regression over the whole period finds $y_0 = -3.8‰$ ($r^2 = 38$%). The data based contribution from the North ($y_0 = -4.8‰$) and the South ($y_0 = -77.2‰$) have very different y-axis intercepts (Fig. 12D).

The very negative y_0 caused by changes in sea ice coverage in the Southern Ocean needs further clarification. The changes in sea ice coverage cause variations in the gas exchange rates. In the scenario across Termination I, the global exchange flux rises from 52 PgC yr^{-1} during the LGM to 58 PgC yr^{-1} at $t = 10$ kyr BP in the scenario, which considers only changes in sea ice in the Southern Ocean. The pCO$_2$ of the atmosphere and the Southern

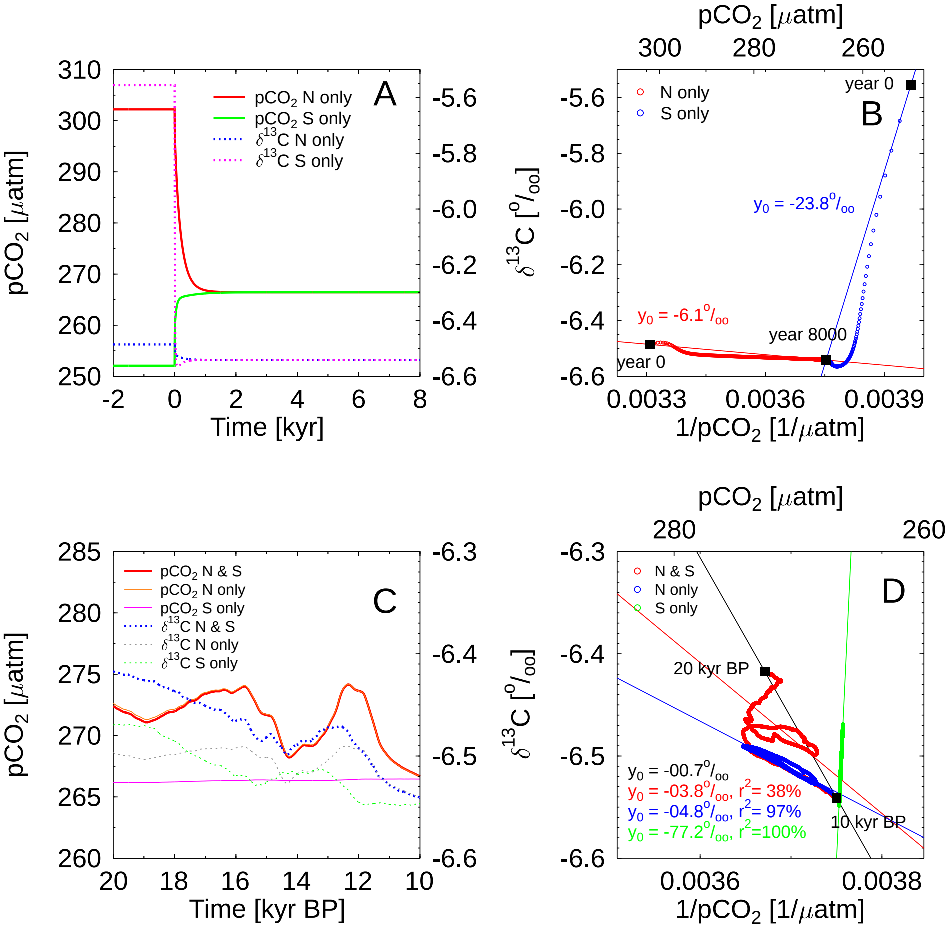

Figure 12: Simulated effects of an instantaneous change in sea ice cover from total coverage to preindustrial values in the North Atlantic (top: N only), or the Southern Ocean (top: S only) and as in the scenario used in Köhler et al. (2005a) (left: pCO$_2$, δ^{13}C; right: Keeling plot). In the Termination I scenario (bottom) the contribution of northern (N only) and southern (S only) sea ice is shown individually and in a combined scenario (N & S). Regressions for the prior/after situation are shown everywhere, in D regressions over the whole period are shown additionally.

Ocean surface box are very close to each other at the beginning of the experiment (270 and 266 μatm, respectively). Therefore, an increase in gas exchange rate in the Southern Ocean is only marginally increasing atmospheric pCO$_2$ (< 1 μatm). However, the stronger gas exchange leads to a significant decrease in atmospheric δ^{13}C by 0.08‰. A y_0 of -77.2‰ is consistent in our modelling environment, but dependent strongly on the model architecture. In general, the effects of sea ice coverage on carbon cycle dynamics have been found to vary between different models (Archer et al., 2003). This example shows, that the Keeling plot is difficult to interpret for experiments without significant net carbon uptake or release of the atmosphere, which lead nevertheless to changes in atmospheric δ^{13}C. The slope of the regression function might in the most extreme case of a constant pCO$_2$ rise to infinity. Besides gas exchange a second example for this situation is a change from C3 grasses to C4 grasses in the terrestrial biosphere.

The difference of these results from $\delta^{\Delta A}_{\delta\mathrm{C}\to 0}$ gives us a comparison with the terrestrial release scenario. The contribution from changing gas exchange in the Arctic carries a y_0 several ‰ heavier than $\delta^{\Delta A}_{\delta\mathrm{C}\to 0}$, while fast changes in the gas exchange in the South lead to lighter y_0.

5.3.5 Sea level and ocean temperature

Changes in sea level and ocean temperature over the last glacial/interglacial transition are documented rather well in the paleo climate archives. We therefore describe in the following only those changes which we propose over Termination I, but do not analyse the maximum range possible by these two processes.

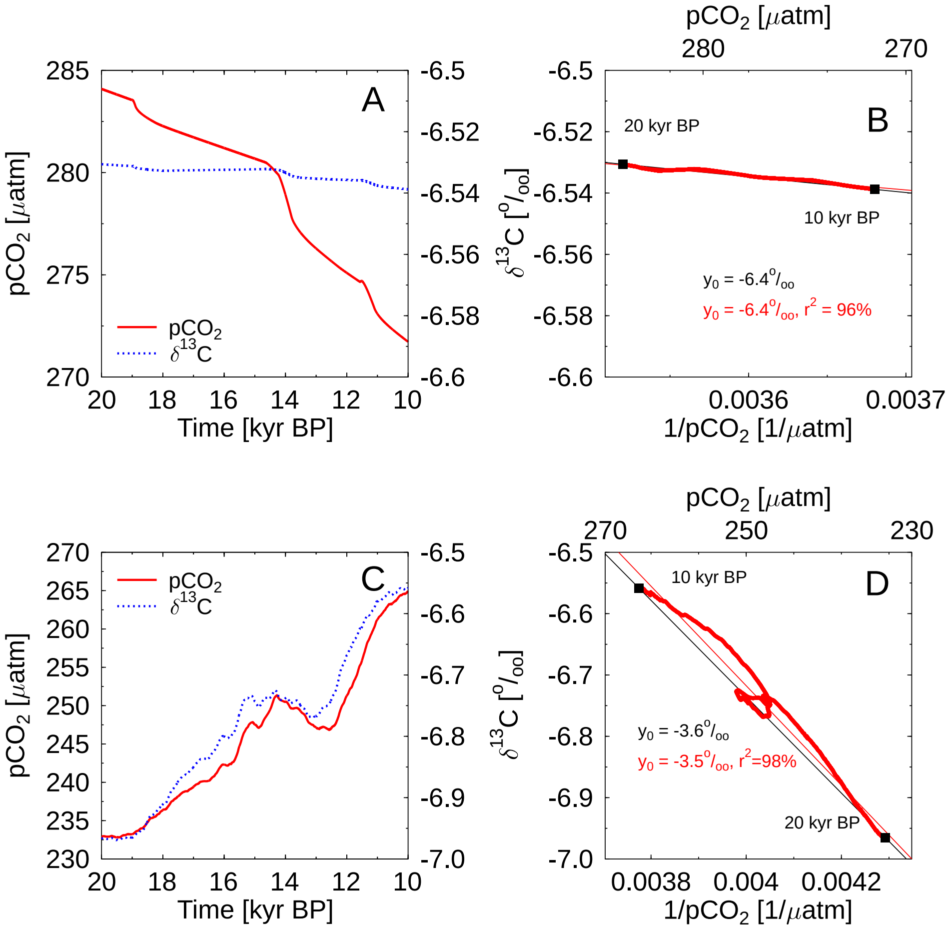

Figure 13: Simulated effects of sea level rise (top) and ocean temperature change (bottom) as used in Köhler et al. (2005a) (left: $p\mathrm{CO}_2$, δ^{13}C; right: Keeling plot). Regression of the prior/after analysis (black) and over the whole period (red) are shown.

Sea level: Sea level rose from 20 kyr BP to 10 kyr BP by about 85 m (Fairbanks, 1990). This leads in our model to a drop in $p\mathrm{CO}_2$ by about 13 μatm and nearly no change in the δ^{13}C. The y-axis intercept in a Keeling plot with prior/after analysis or regression over whole time period is -6.4‰ (Fig. 13 top).

The rising sea level leads to a dilution of the concentration of all species in the ocean and a decrease in salinity by about 2.3%. The ocean can then store more carbon. Again, in the comparison with the terrestrial case this sea level rise is a process with a typical δ^{13}C signature that is about $+2$‰ more positive than $\delta^{\Delta A}_{\delta \mathrm{C}\to 0}$.

Ocean temperature: The rise of the ocean temperature by 3 to 5 K during the simulated 10 kyr (20 to 10 kyr BP) leads to a rise in $p\mathrm{CO}_2$ of 32 μatm, and a rise in δ^{13}C of 0.4‰, the latter leading the first by about 1000 years (Fig. 13 bottom). The Keeling plot analysis gives us y_0's of -3.5 and -3.6‰ for the regression over the whole period and the prior/after analysis, respectively.

Due to the temperature dependent solubility of CO_2 warm water stores less carbon than cold water. A rise in ocean temperature therefore weakens the solubility pump and leads to an out-gassing of CO_2. The rise in δ^{13}C is mainly caused by the temperature-dependent isotopic fractionation during gas exchange between the surface ocean and the atmosphere. The temperature effect has a δ^{13}C signature which is about $+5$‰ heavier than the $\delta^{\Delta A}_{\delta \mathrm{C}\to 0}$ obtained in the terrestrial release case.

5.3.6 Combined scenarios and CaCO_3 chemistry

The previous study (Köhler et al., 2005a) finds that combined scenarios are able to reconstruct the observed dynamics in atmospheric $p\mathrm{CO}_2$ and δ^{13}C during Termination I (Fig. 15). They combine the processes investigated above (terrestrial carbon storage, marine biology, ocean circulation, temperature, sea level, sea ice) together with

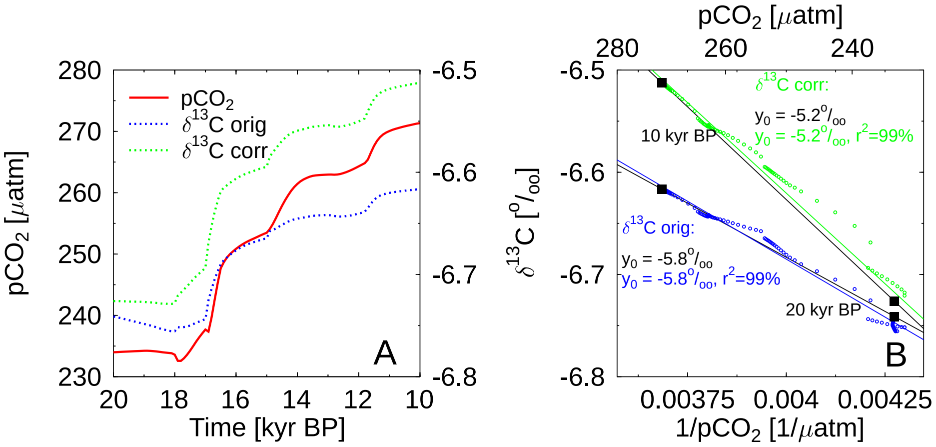

Figure 14: Estimation of the effect of sediment/ocean fluxes of $CaCO_3$ on the atmospheric carbon records by subtracting the results of a scenario with all processes but the $CaCO_3$ effect in operation from the combined scenario. Terrestrial biosphere is following a linear glacial/interglacial rise (TB0 in Fig. 7). A: $p\mathrm{CO}_2$ and δ^{13}C. B: Keeling plot. Regression of the prior/after analysis (black) and over the whole period (blue, green) are shown. The original δ^{13}C (orig) and δ^{13}C corrected (corr) for the trend in the mean δ^{13}C caused by the sedimentation losses are shown.

the consideration of $CaCO_3$ fluxes between sediment and ocean.

The influence of the fluxes of $CaCO_3$ cannot be analysed separately as $CaCO_3$ fluxes between deep ocean and sediment are generated by the model as response to changes in the deep ocean CO_3^{2-} concentration. $CaCO_3$ chemistry is acting as an amplifier of the results of all other processes with respect to the changes in $p\mathrm{CO}_2$. However, we can estimate their impact by subtracting the results of a simulation which includes all processes apart from sediment/ocean fluxes from the results of a scenario including all processes. Over the course of Termination I the sedimentation of $CaCO_3$ is higher than its dissolution, leading to a loss of DIC ($\sim$1000 PgC) and twice as much alkalinity. These changes lower the pH of the ocean, which shifts the distribution of the three different species of DIC (CO_2, HCO_3^-, CO_3^{2-}) in the carbonate system towards CO_2, and leads to its out-gassing and a rise in atmospheric $p\mathrm{CO}_2$ of approximately 35 μatm (Fig. 14A). This loss of carbon is accompanied by a depletion of the mean oceanic δ^{13}C by about 0.1‰, because the $CaCO_3$, which is lost to the sediments bears a δ^{13}C signal of about 3‰. Atmospheric δ^{13}C is therefore falling by approximately the same amount. If the δ^{13}C record is corrected for this effect of sedimentation, it rises by about 0.2‰ (Fig. 14). This residual rise is caused by the fractionation factor of the CO_2 flux from the ocean to atmosphere, which depends on DIC itself and the pH dependent dissociation of DIC into the different species (Ridgwell, 2001). The Keeling plot analysis of these changes (Fig. 14B) leads to y_0 of -5.8 and -5.2‰ for both the prior/after analysis and the regression model of the original and the corrected data, respectively.

Termination I was subdivided into four intervals based on different changing rates in the CO_2 record (Monnin et al., 2001). Depending on the realisation of the variation of the terrestrial carbon storage over time, three different scenarios are discussed (A-TB0, A-TB1, A-TB2; Fig. 7). In the Keeling plot of these combined results the only well distinct feature found in all three scenarios is the sharp drop in δ^{13}C in parallel with rising $p\mathrm{CO}_2$ which occurs during interval I (Fig. 15B). In the Taylor Dome data set this is also the only event in which the signal-to-noise-ratio is high enough to allow a distinct identification. Changes in interval II and III occur during rather small or no variations in $p\mathrm{CO}_2$ leading to features which are rather indistinguishable in the light of their uncertainties in the data sets. The scenario A-TB2 shows a variability in δ^{13}C which is closest to that of the Taylor Dome record, while $p\mathrm{CO}_2$ is best reconstructed in the A-TB0 simulation.

In the following we have a closer look on the Keeling plots of these three combined scenarios and especially on the results of A-TB2 (Fig. 15B, 16). Regression functions are applied to seven time windows in scenario A-TB2 (Table 4, Fig. 16B):

1. The main dynamics of a reduced marine export production due to iron limitation falls in time window 1 ($20.0 - 17.1$ kyr BP). In the combined scenario y_0 is -7.3‰ while the decrease in export production as single process would lead to $y_0 = -8.6$‰ with at maximum -9.7‰ during the first years of the reduced export production.

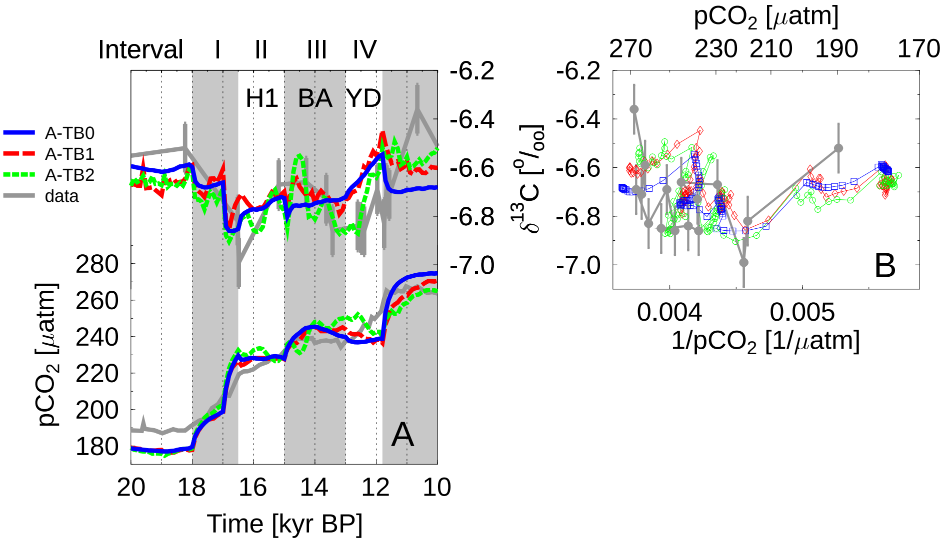

Figure 15: A: Measured and simulated atmospheric carbon records over Termination I: Data: Atmospheric δ^{13}C in the Taylor Dome ice core (Smith et al., 1999); pCO$_2$ in the EPICA Dome C ice core divided in four intervals with different changing rates (Monnin et al., 2001). Both data set are synchronized to the GISP2 age scale (Meese et al., 1997). The intervals II, III, and IV are approximately identical with the Heinrich 1 event (H1), the Bølling-Allerød warm interval (BA), and the Younger Dryas cold event (YD) in the North Atlantic region. Simulation scenarios combine all physical processes (ocean temperature, sea level, sea ice) with changes in ocean circulation (NADW formation, Southern Ocean mixing), marine export production, CaCO$_3$ compensation and terrestrial biosphere. Differences in the scenarios A-TB0, A-TB1, and A-TB2 are the simulated changes the terrestrial carbon storage, which are shown in Fig. 7. B: Keeling plot. Note, that the measured CO$_2$ data are given in volume mixing ratio [ppmv], while the model calculates the partial pressure (pCO$_2$) in units of μatm.

2. The increase in Southern Ocean vertical mixing is mainly happening in window 2 ($17.0 - 16.9$ kyr BP) leading to $y_0 = -10.0$‰ in A-TB2, but to -8.2‰ as single process.
3. There is no specific process in operation in window 3 ($16.8 - 16.6$ kyr BP) which has a y_0 of -5.2‰.
4. In window 4 ($16.5 - 14.9$ kyr BP) covering the Heinrich 1 event the NADW formation is shut-off. Additionally, the marine export production is reduced by ∼10% due to macro-nutrient limitation.
5. NADW formation is resuming to intermediate strength in time window 5 covering the beginning of the Bølling-Allerød warm interval in-between Heinrich 1 and the Younger Dryas ($14.8 - 14.3$ kyr BP). From a comparison of the three scenarios (Fig. 15B) we further know that the changing carbon storage in the terrestrial biosphere is additionally affecting the time windows 4 and 6, and that it is mainly responsible for the dynamics in time window 5. In the scenarios A-TB0 and A-TB1 the time windows 4 and 5 are not distinguishable.
6. In the Younger Dryas (window 6, $14.2 - 11.8$ kyr BP) the NADW formation is partly reduced.
7. No clear regression ($r^2 = 6\%$) is found for window 7 ($11.7 - 10.0$ kyr BP), in which the carbon cycle is organised to a new interglacial equilibrium.

A-TB2 leads to y-axis intercepts of $-11.4, -13.3$, and -13.0‰ in the windows 4, 5, and 6 respectively. For comparison, the single process analysis has found $y_0 = -5.3$ to -7.2‰ for changes in NADW formation between 16.5 and 11.8 kyr BP, but much higher negative values (-39.2‰) in certain times. The rise in the terrestrial carbon storage has $y_0 = -8.6$ to -9.1‰.

This analysis above shows that it seems possible to identify single processes in the Keeling plot of our artificial time series, if they dominate the atmospheric carbon records for a certain time. However, due to the variety of the processes the y-axis intercept which we identify in the combined scenarios is in no case near or close to the expected y_0 values we concluded from our single process analysis.

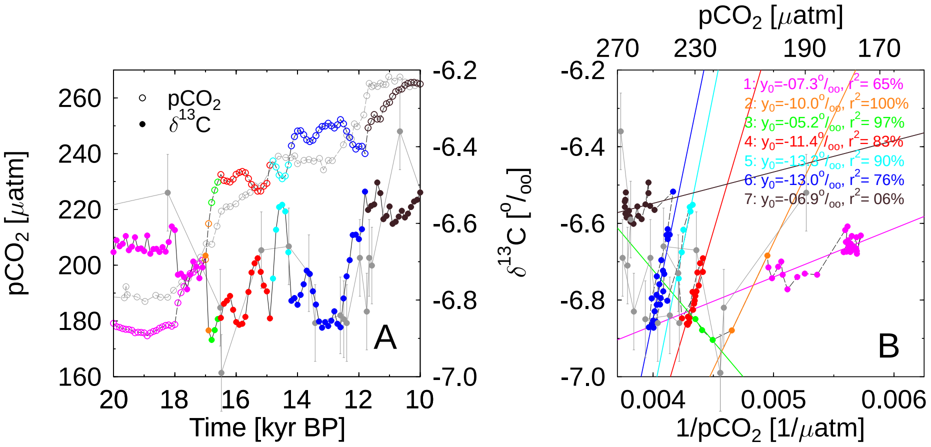

Figure 16: A detailed look at scenario A-TB2 (colors) in comparision to the Taylor Dome δ^{13}C and EPCIA Dome C CO_2 data (grey) during Termination I ($10-20$ kyr BP). A: pCO$_2$ (open circles), δ^{13}C (closed circles); B: Keeling plot. Seven time windows showing different dynamics and their regression functions are marked with different colors. Note, that the measured CO_2 data are given in volume mixing ratio [ppmv], while the model calculates the partial pressure (pCO$_2$) in units of μatm.

6 Discussion and Conclusions

In this study we analysed processes which alter the atmospheric content of carbon dioxide and δ^{13}C of CO_2 using artificial time series produced with a global carbon cycle box model. Although there is evidence that the scenarios investigated here are plausible and they can explain the observations during the last glacial/interglacial transition, alternatives can not be ruled out due to data uncertainties and model simplicity. Nevertheless, for the investigation of these artificial time series and their potential to be interpreted using the Keeling plot approach the absolute validity of these scenarios is not important. By using a simple carbon cycle model we benefit from the fact that individual processes acting on the carbon cycle can be switched on and off and their hypothetical impacts can be analysed individually.

All processes have been analysed with respect to their impact to the Keeling plot analysis. A summary is found in Table 2. The effective isotopic signature $\delta^{\Delta A}$ of terrestrial carbon uptake or release modifying the global carbon cycle can be understood based on theoretical considerations of a three reservoir system which also includes oceanic carbon uptake. These considerations can be understood as the paleo extension of the Keeling plot approach. The effective isotopic signature converts to a boundary $\delta^{\Delta A}_{\delta \mathrm{C} \rightarrow 0}$ of $-8.4‰$ for terrestrial carbon fluxes approaching zero. The $\delta^{\Delta A}_{\delta \mathrm{C} \rightarrow 0}$ obtained from theory is comparable to the y-axis intercept y_0 in a classical Keeling plot. We identified y-axis intercepts of different processes and compared it with the theoretical well understood value of the

Table 4: Regression analysis of time windows in the combined scenario A-TB2 covering carbon cycle dynamics during Termination I. Results in 100 years resolution.

#	Time (kyr BP)	y_0 (‰) r^2 (%) in brackets	Main processes
1	20.0 – 17.1	-7.3 (65)	Reduction in marine export production
2	17.0 – 16.9	-10.0 (100)	Increase in Southern Ocean mixing
3	16.8 – 16.6	-5.2 (97)	nothing special
4	16.5 – 14.9	-11.4 (83)	NADW and export production reduced in Heinrich event 1 and terrestrial carbon storage
5	14.8 – 14.3	-13.3 (90)	NADW rise in Bølling/Allerød and mainly terrestrial carbon storage
6	14.2 – 11.8	-13.0 (76)	NADW reduced in Younger Dryas and and terrestrial carbon storage
7	11.7 – 10.0	-6.9 (6)	nothing special, equilibration to interglacial climate

terrestrial carbon release. The y_0's of the prior/after analysis of our single process analysis vary between -0.7 and -8.6‰. Some processes are compounds of subprocesses which have distinctively different y_0 values (e.g. sea ice cover in different hemispheres, y_0 (north) = -4.8‰; y_0 (south) = -77.2‰), in others the prior/after analysis leads to very different results if a specific narrow time window is observed (e.g. terrestrial carbon storage, NADW formation). Furthermore, the terrestrial carbon storage very likely changed in a non-linear way during the last glacial/interglacial transition and not in a linear way as assumed in scenario TB0 (Fig. 7). This is also supported by a simulation studies using a dynamical global simulation model (Köhler et al., 2005b). High frequency changes on a centennial to millennial time scale are very likely smoothed out in the ice core records due to the average mixing time of the air of several centuries and the limited sampling frequency. The single process analysis of the states prior and after the experiments leads to y_0 different than the boundary caused by terrestrial processes. They vary from $\delta^{\Delta A}_{\delta\mathrm{C}\to 0}$ by a small decline (-0.2‰) to a large increase ($+7.7$‰). Processes in which the biology is involved (marine and terrestrial) have identical y_0's (small decline in comparison to $\delta^{\Delta A}_{\delta\mathrm{C}\to 0}$) and are therefore indistinguishable. In all other cases y_0 is more positive than $\delta^{\Delta A}_{\delta\mathrm{C}\to 0}$.

The Taylor Dome record of atmospheric δ^{13}C shows dynamics, in which a Keeling plot analysis leads to y_0 values around -9.5‰ (Smith et al., 1999; Fischer et al., 2003). This holds, however only for the Holocene and the climatically relatively stable LGM, while during the transition no clear end member could be recognised so far. Unpublished measurements (Eyer, 2004) performed at the EPICA Dome C ice core show evidence for millennial scale variability with fast and large changes in δ^{13}C (more than 0.5‰ in a century). We believe from our analysis that the processes responsible for these variations can not be identified based on a Keeling plot analysis. However, our study gives us some indications which processes are in general able to contribute to fast changes and thus might be responsible for very negative y-axis intercepts in a Keeling plot analysis. From what we have learned from our model of the global carbon cycle fast changes in terrestrial carbon storage, variations in ocean circulation strength (NADW formation) and sea ice coverage in the Southern Ocean are the only processes which can contribute significantly to these δ^{13}C excursions. However, the signal of fast terrestrial carbon release is smoothed by air mixing processes in the firn. In the EPICA Dome C ice core with its small accumulation rate and large mixing time terrestrial processes might therefore not be responsible for these negative δ^{13}C signals.

In the light of these conclusions we have to acknowledge that especially the modelling response to Southern Ocean sea ice extent is highly model dependent. Large variability in pCO$_2$ and δ^{13}C occur especially when the surface ocean box is nearly fully covered with sea ice and thus reducing gas exchange dramatically (Köhler and Fischer, 2006). Thus, our model architecture with a Southern Ocean box ranging from 40°S to the Antarctic continent is probably too simplistic to cover the complete picture of observed dynamics. Other model intercomparisions have already pointed out these model-dependent behaviour (Archer et al., 2003).

From the understanding which emerges here, it seems unlikely, that the interpretation of δ^{13}C measured during glacial/interglacial transitions can be enhanced very much with the Keeling plot approach. The identification of a single process which might be responsible for the observed fluctuations in atmospheric CO$_2$ and δ^{13}C can not be based on a Keeling plot analysis. Most processes acted simultaneously on the global carbon cycle during the transition and the uncertainties in data retrieval, y-axis intercept, and δ^{13}C are too large to come to a sound and unequivocal process identification.

Acknowledgements

We thank J. Severinghaus for ideas on the three box model calculations and J. Freitag for discussions on firnification and bubble close off. This study is funded by the German Ministry of Education and Research through the German Climate Research Programme DEKLIM (project RESPIC).

References

Archer, D. E., Martin, P. A., Milovich, J., Brovkin, V., Plattner, G.-K., and Ashendel, C.: Model sensitivity in the effect of Antarctic sea ice and stratification on atmospheric pCO$_2$, Paleoceanography, 18, 1012, doi: 10.1029/2002PA000 760, 2003.

Blasing, T. J., Broniak, C., and Marland, G.: Estimates of monthly carbon dioxide emissions and associated δ^{13}C values from fossil-fuel consumption in the U.S.A, in Trends: A Compendium of Data on Global Change, Carbon Dioxide Information Analysis Center, Oak Ridge National Laboratory, U.S. Department of Energy,, Oak Ridge, Tenn., USA, 2004.

Bowling, D. R., Tans, P. P., and Monson, R. K.: Partitioning net ecosystem carbon exchange with isotopic fluxes of CO_2, Global Change Biology, 7, 127–145, 2001.

Brook, E. J., Harder, S., Serveringhaus, J., Steig, E. J., and Sucher, C. M.: On the origin and timing of rapid changes in atmospheric methane during the last glacial period, Global Biogeochemical Cycles, 14, 559–572, 2000.

Crosta, X., Pichon, J.-J., and Burckle, L. H.: Application of modern analog technique to marine Antarctic diatoms: Reconstruction of maximum sea-ice extent at the Last Glacial Maximum, Paleoceanography, 13, 284–297, 1998a.

Crosta, X., Pichon, J.-J., and Burckle, L. H.: Reappraisal of Antarctic seasonal sea-ice extent at the Last Glacial Maximum, Geophysical Research Letters, 14, 2703–2706, 1998b.

Dansgaard, W., Clausen, H. B., Gundestrup, N., Hammer, C. U., Johnsen, S. F., Kristinsdottir, P. M., and Reeh, N.: A new Greenland deep ice core, Science, 218, 1273–1277, 1982.

Emanuel, W. R., Killough, G. G., Post, W. M., and Shugart, H. H.: Modeling terrestrial ecosystems in the global carbon cycle with shifts in carbon storage capacity by land-use change, Ecology, 65, 970–983, 1984.

Etheridge, D. M., Steele, L. P., Langenfelds, R. L., Francey, R. J., Barnola, J.-M., and Morgan, V. I.: Natural and anthropogenic changes in atmospheric CO_2 over the last 1000 years from air in Antarctic ice and firn, Journal of Geophysical Research, D101, 4115–4128, 1996.

Eyer, M.: Highly resolved δ^{13}C measurements on CO_2 in air from Antarctic ice cores, Ph.D. thesis, University of Bern, Bern, Switzerland, 2004.

Eyer, M., Leuenberger, M., Nyfeler, P., and Stocker, T.: Comparison of two $\delta^{13}CO_2$ records measured on air from the EPICA Dome C and Kohnen Station ice cores, Geophysical Research Abstracts, 6, 01 990, 2004.

Fairbanks, R. G.: The age and origin of the Younger Dryas climate event in Greenland ice cores, Paleoceanography, 5, 937–948, 1990.

Fischer, H., Wahlen, M., and Smith, J.: Reconstruction of glacial/interglacial changes in the global carbon cycle from CO_2 and $\delta^{13}CO_2$ in Antarctic ice cores, Memoirs of the National Institute for Polar Research, Special Issue, 57, 121–138, 2003.

Flanagan, L. B. and Ehleringer, J. R.: Ecosystem-atmosphere CO_2 exchange: interpretating signals of change using stable isotope ratios, Trends in Ecology and Evolution, 13, 10–14, 1998.

Francey, R. J., Allison, C. E., Etheridge, D. M., Trudinger, C. M., Enting, I. G., Leuenberger, M., Langenfelds, R. L., Michel, E., and Steele, L. P.: A 1000-year high precision record of δ^{13}C in atmospheric CO_2, Tellus, 51B, 170–193, 1999.

Friedli, H., Lötscher, H., Oeschger, H., Siegenthaler, U., and Stauffer, B.: Ice core record of the $^{13}C/^{12}C$ ratio of atmospheric CO_2 in the past two centuries, Nature, 324, 237–238, 1986.

Gersonde, R., Crosta, X., Abelmann, A., and Armand, L.: Sea-surface temperature and sea ice distribution of the Southern Ocean at the EPILOG Last Glacial Maximum — a circum-Antarctic view based on siliceous microfossil records, Quaternary Science Reviews, 24, 869–896, 2005.

Hemming, D., Yakir, D., Ambus, P., Aurela, M., Besson, C., Black, K., Buchmann, N., Burlett, R., Cescatti, A., Clement, R., Gross, P., Granier, A., Grünwald, T., Havrankova, K., Janous, D., Janssens, I. A., Knohl, A., Köstner, B., Kowalski, A., Laurila, T., Mata, C., Marcolla, B., Matteucci, G., Moncrieff, J., Moors, E. J., Osborne, B., Pereira, J. S., Pihlatie, M., Pilegaard, K., Ponti, F., Rosova, U., Rossi, F., Scartazza, A., and Vesala, T.: Pan-European δ^{13}C values of air and organic matter from forest ecosystems, Global Change Biology, 11, 1065–1093, doi: 10.1111/j.1365–2486.2005.00 971.x, 2005.

Houghton, R. A.: Revised estimates of the annual net flux of carbon to the atmosphere from changes in land use and land management 1850-2000, Tellus, 55B, 378–390, 2003.

Johnsen, S. J., Clausen, H. B., Dansgaard, W., Fuhrer, K., Gundestrup, N., Hammer, C. U., Iversen, P., Jouzel, J., Stauffer, B., and Steffensen, J. P.: Irregular glacial interstadials recorded in a new Greenland ice core, Nature, 359, 311–313, 1992.

Keeling, C. D.: The concentration and isotopic abundance of carbon dioxide in rural areas, Geochimica et Cosmochimica Acta, 13, 322–334, 1958.

Keeling, C. D.: The concentration and isotopic abundance of carbon dioxide in rural and marine air, Geochimica et Cosmochimica Acta, 24, 277–298, 1961.

Keeling, C. D. and Whorf, T. P.: Atmospheric CO_2 records from sites in the SIO air sampling network, in Trends: A Compendium of Data on Global Change, Carbon Dioxide Information Analysis Center, Oak Ridge National Laboratory, U.S. Department of Energy,, Oak Ridge, Tenn., USA, 2005.

Keeling, C. D., Bollenbacher, A. F., and Whorf, T. P.: Monthly atmospheric $^{13}C/^{12}C$ isotopic ratios for 10 SIO stations, in Trends: A Compendium of Data on Global Change, Carbon Dioxide Information Analysis Center, Oak Ridge National Laboratory, U.S. Department of Energy,, Oak Ridge, Tenn., USA, 2005.

Köhler, P. and Fischer, H.: Simulating changes in the terrestrial biosphere during the last glacial/interglacial transition, Global and Planetary Change, 43, 33–55, doi: 10.1016/j.gloplacha.2004.02.005, 2004.

Köhler, P. and Fischer, H.: Proposing a mechanistic understanding of changes in atmospheric $\mathbf{CO_2}$ during the last 740 000 years, Climate of the Past Discussions, 2, 1–42, SRef–ID: 1814–9359/cpd/2006–2–1, 2006.

Köhler, P., Fischer, H., Munhoven, G., and Zeebe, R. E.: Quantitative interpretation of atmospheric carbon records over the last glacial termination, Global Biogeochemical Cycles, 19, GB4020, doi: 10.1029/2004GB002 345, 2005a.

Köhler, P., Joos, F., Gerber, S., and Knutti, R.: Simulated changes in vegetation distribution, land carbon storage, and atmospheric CO_2 in response to a collapse of the North Atlantic thermohaline circulation, Climate Dynamics, 25, 689–708, doi: 10.1007/s00 382–005–0058–8, 2005b.

Köhler, P., Muscheler, R., and Fischer, H.: A model-based interpretation of low frequency changes in the carbon cycle during the last 120 kyr and its implications for the reconstruction of atmospheric $\Delta^{14}C$ and the ^{14}C production rates estimates, Geochemistry, Geophysics, Geosystems, p. submitted; doi: 10.1029/2005GC001228, 2006.

Landais, A., Barnola, J. M., Masson-Delmotte, V., Jouzel, J., Chappellaz, J., Caillon, N., Huber, C., Leuenberger, M., and Johnsen, S. J.: A continuous record of temperature evolution over a sequence of Dansgaard-Oeschger events during Marine Isotope Stage 4 (76 to 62 kyr BP), Geophysical Research Letters, 31, L22 211, doi: 10.1029/2004GL021 193, 2004.

Lang, C., Leuenberger, M., Schwander, J., and Johnsen, S.: 16°C rapid temperature variation in central Greenland 70,000 years ago, Science, 286, 934–937, 1999.

Levin, I., Ciais, P., Langenfelds, R., Schmidt, M., Ramonet, M., Sidorov, K., Tchebakova, N., Gloor, M., Heimann, M., Schulze, E.-D., Vygodskaya, N. N., Shibistova, O., and Lloyd, J.: Three years of trace gas observations over the EuroSiberian domain derived from aircraft sampling – a concerted action, Tellus, 54B, 696–712, 2002.

Marland, G., Boden, T., and Andres, R. J.: Global, Regional, and National CO_2 Emissions, in Trends: A Compendium of Data on Global Change, Carbon Dioxide Information Analysis Center, Oak Ridge National Laboratory, U.S. Department of Energy,, Oak Ridge, Tenn., USA, 2005.

Meese, D. A., Gow, A., Alley, R., Zielinski, G., Grootes, P., Ram, M., Taylor, K., Mayewski, P., and Bolzan, J.: The Greenland Ice Sheet Project 2 depth-age scale: Methods and results, Journal of Geophysical Research, 102, 26 411–26 423, 1997.

Monnin, E., Indermühle, A., Dällenbach, A., Flückiger, J., Stauffer, B., Stocker, T. F., Raynaud, D., and Barnola, J.-M.: Atmospheric CO_2 concentrations over the last glacial termination, Science, 291, 112–114, 2001.

Mook, W. G.: ^{13}C in atmospheric CO_2, Netherlands Journal of Sea Research, 20, 211–223, 1986.

Munhoven, G.: Modelling glacial-interglacial atmospheric CO_2 variations: the role of continental weathering, Ph.D. thesis, Université de Liège, Liège, Belgium, 1997.

Pataki, D. E., Ehleringer, J. R., Flanagan, L. B., Yakir, D., Bowling, D. R., Still, C. J., Buchmann, N., Kaplan, J. O., and Berry, J. A.: The application and interpretation of Keeling plots in terrestrial carbon cycle research, Global Biogeochemical Cycles, 17, 1022, doi: 10.1029/2001GB001 850, 2003.

Petit, J. R., Jouzel, J., Raynaud, D., Barkov, N. I., Barnola, J.-M., Basile, I., Bender, M., Chappellaz, J., Davis, M., Delaygue, G., Delmotte, M., Kotlyakov, V. M., Legrand, M., Lipenkov, V. Y., Lorius, C., Pépin, L., Ritz, C., Saltzman, E., and Stievenard, M.: Climate and atmospheric history of the past 420,000 years from the Vostok ice core, Antarctica, Nature, 399, 429–436, 1999.

Plattner, G.-K., Joos, F., and Stocker, T. F.: Revision of the global carbon budget due to changing air-sea oxygen fluxes, Global Biogeochemical Cycles, 16, 1096, doi: 10.1029/2001GB001 746, 2002.

Ridgwell, A. J.: Glacial-interglacial perturbations in the global carbon cycle, Ph.D. thesis, University of East Anglia, Norwich, U.K., 2001.

Sabine, C. L., Feely, R. A., Gruber, N., Key, R. M., Lee, K., Bullister, J. L., Wanninkhof, R., Wong, C. S., Wallace, D. W. R., Tilbrook, B., Millero, F. J., Peng, T.-H., Kozyr, A., Ono, T., and Rios, A. F.: The oceanic sink for anthropogenic CO_2, Science, 305, 367–371, 2004.

Sarnthein, M., Pflaumann, U., and Weinelt, M.: Past extent of sea ice in the northern North Atlantic inferred from foraminiferal paleotemperature estimates, Paleoceanography, 18, 1047, doi: 10.1029/2002PA000 771, 2003.

Scholze, M., Kaplan, J. O., Knorr, W., and Heimann, M.: Climate and interannual variability of the atmosphere-biosphere $^{13}CO_2$ flux, Geophysical Research Letters, 30, 1097, doi: 10.1029/2002GL015 631, 2003.

Schwander, J. and Stauffer, B.: Age difference between polar ice and the air trapped in its bubbles, Nature, 311, 45–47, 1984.

Schwander, J., Jouzel, J., Hammer, C. U., Petit, J.-R., Udisti, R., and Wolff, E.: A tentative chronology for the EPICA Dome Concordia ice core, Geophysical Research Letters, 28, 4243–4246, 2001.

Siegenthaler, U., Stocker, T. F., Monnin, E., Lüthi, D., Schwander, J., Stauffer, B., Raynaud, D., Barnola, J.-M., Fischer, H., Masson-Delmotte, V., and Jouzel, J.: Stable carbon cycle-climate relationship during the late Pleistocene, Science, 310, 1313–1317; doi: 10.1126/science.1120 130, 2005.

Smith, H. J., Fischer, H., Wahlen, M., Mastroianni, D., and Deck, B.: Dual modes of the carbon cycle since the Last Glacial Maximum, Nature, 400, 248–250, 1999.

Steig, E. J., Brook, E. J., White, J. W. C., Sucher, C. M., Bender, M. L., Lehman, S. J., Morse, D. L., Waddington, E. D., and Clow, G. D.: Synchronous climate change in Antarctica and North Atlantic, Science, 282, 92–95, 1998a.

Steig, E. J., Morse, D. L., Waddington, E. D., and Polissar, P. J.: Using the sunspot cycle to date ice cores, Geophysical Research Letters, 25, 163–166, 1998b.

Sturm, P., Leuenberger, M., and Schmidt, M.: Atmospheric O_2, CO_2 and $\delta^{13}C$ observations from the remote sites Jungfraujoch, Switzerland, and Puy de Dôme, France, Geophysical Research Letters, 32, L17 811; doi: 10.1029/2005GL023 304, 2005.

Trudinger, C. M., Enting, I. G., Francey, R. J., Etheridge, D. M., and Rayner, P. J.: Long-term variability in the global carbon cycle inferred from a high-precision CO_2 and $\delta^{13}C$ ice-core record, Tellus, 51B, 233–248, 1999.

Volk, T. and Hoffert, M. I.: Ocean carbon pumps: analysis of relative strengths and efficiencies in ocean-driven atmospheric CO_2 changes, in The carbon cycle and atmospheric CO_2: Natural variations archean and present, edited by E. T. Sundquist and W. S. Broecker, vol. 32 of *Geophysical Monograph*, pp. 99–110, American Geophysical Union, Washington, D.C., USA, 1985.

Wolff, E. W., Kull, C., Chappellaz, J., Fischer, H., Miller, H., Stocker, T. F., Watson, A. J., Flower, B., Joos, F., Köhler, P., Matsumoto, K., Monnin, E., Mudelsee, M., Paillard, D., and Shackleton, N.: Modeling past atmospheric CO_2: results of a challenge, EOS, 86 (38), 341, 345, 2005.

Yakir, D. and Sternberg, L. D. S. L.: The use of stabile isotopes to study ecosystem gas exchange, Oecologia, 123, 297–311, 2000.

Zeebe, R. E. and Wolf-Gladrow, D. A.: CO_2 in Seawater: Equilibrium, Kinetics, Isotopes, vol. 65 of *Elsevier Oceanography Book Series*, Elsevier Science Publishing, Amsterdam, The Netherlands, 2001.

Acknowledgements

My first thank goes to Prof. Heinz Miller, whose long-term effort to bring together an enthusiastic team of specialists from various disciplines to cover the entire deep ice core business, beginning with the reconnaissance of a proper drill site, the deep drilling, a broad spectrum of analytical approaches for physical and chemical aspects of the ice, and towards a climatic interpretation of the these data sets including modeling, made this PhD thesis possible. I thank Prof. Kai-Uwe Hinrichs for being the 'Zweitgutachter' of this thesis.

I'm very indebted to Hubertus Fischer, for supporting me in any aspect of scientific life. He had the scientific curiosity to discuss about all my newest theories, why this and that doesn't work and how it might work - no matter if he were in the field in Antarctica or in New York. And thanks for your optimism, which helped me go further and further.

Many thanks to…..

Anna Wegner and Felix Fundel for being the best room mates and enriching my daily life, especially during the desktop phase, with fun & jokes, cakes, matlab conversations, playing boule at the beach, and for numerous Kefirs and orange juices to keep me healthy.

Melanie Behrens and Ulrike Salzer for their help in the mass spec lab and providing technical support. And above all, thanks for working on similar problems. Klaus-Uwe Richter for his nice help with questions concerning electronic equipment at the beginning. Jens Hefter for collegially sharing the mass spec lab with me. Andreas Frenzel for selecting the right computer for me.

Peter Köhler for fruitful discussions about the global carbon cycle and the opportunity to see how a modeler sees the world. Johannes Freitag for his help to get in touch with the world of firnification and for all the brief philosophical excursions while walking from the 'Café Caspar' back to AWI.

Thanks to the entire glaciology group for the stimulating working atmosphere and especially Hans Oerter. Further, Fernando Valero-Delgado for singing on the floor, taking care of all the ice core boxes, for all the cakes he organized. Sepp Kipfstuhl for always keeping a critical eye on the cold labs and his exceptional scientific spirit and curiosity.

Birthe Twarloh for continuously reminding me to fulfill my social obligations, to decide Monday what to like Friday, and for the feeling to be a real scientist. All the colleagues, who left the group: Wolfgang Rack, Urs Ruth, Olaf Eisen, Anja Lambrecht, Marie-Luise Siggard-Andersen, for their special contribution to enrich life within the glaciology group. Michael Bock for doubling the number of Geoecologists within the glaciology group.

The night porters, especially Heinz, for their nice words when suddenly approaching me during the night in one of my laboratories. The secretaries of the department and also the general administration of AWI for their patience if I repeatedly forgot to sign a form.

The drilling and science team of the field campaign 2003/2004 at the Dronning Maud Land drill site – it was a great experience to be in Antarctica and learn to drill ice cores, thanks especially to Frank Wilhelms. The EPICA community, especially all the nice colleagues from Bern, who shared data and ideas and for the good scientific spirit and social life on all the conferences I could attend.

Sonja Paul for her love and the hundred things which makes life worth living and which helped to forget the isotopes for while. A special thank goes to the beautiful beech forests and the landscape in the surroundings of Göttingen, to which I could escape and who provided me with everything I missed in Bremerhaven.

Finally, I am indebted to my parents and family for their support during my education all the years of my studies and for being the lovely home to which I came back too rarely.

Erklärung

Ich versichere, dass ich die vorliegende Dissertation selbständig verfasst und keine anderen als die angegebenen Quellen und Hilfsmittel verwendet habe.

Ich versichere, dass ich nicht bereits anderweitig eine Dissertation eingereicht oder versucht habe, mich einer Doktorprüfung zu unterziehen.

Bremerhaven, den 02.10.2006

(Jochen Schmitt)